

---

Electronic Thesis and Dissertation Repository

---

8-24-2015 12:00 AM


## Design and Fabrication of Integrated Plasmonic Platforms for Ultra-sensitive Molecular and Biomolecular Detections

Mohammadali Tabatabaei  
*The University of Western Ontario*

Supervisor  
Dr. François Lagugné-Labarthet  
*The University of Western Ontario*

Graduate Program in Chemistry  
A thesis submitted in partial fulfillment of the requirements for the degree in Doctor of Philosophy  
© Mohammadali Tabatabaei 2015

Follow this and additional works at: <https://ir.lib.uwo.ca/etd>

 Part of the [Analytical Chemistry Commons](#), [Materials Chemistry Commons](#), and the [Physical Chemistry Commons](#)

---

### Recommended Citation

Tabatabaei, Mohammadali, "Design and Fabrication of Integrated Plasmonic Platforms for Ultra-sensitive Molecular and Biomolecular Detections" (2015). *Electronic Thesis and Dissertation Repository*. 3161. <https://ir.lib.uwo.ca/etd/3161>

This Dissertation/Thesis is brought to you for free and open access by Scholarship@Western. It has been accepted for inclusion in Electronic Thesis and Dissertation Repository by an authorized administrator of Scholarship@Western. For more information, please contact [wlsadmin@uwo.ca](mailto:wlsadmin@uwo.ca).

DESIGN AND FABRICATION OF INTEGRATED PLASMONIC PLATFORMS FOR  
ULTRA-SENSITIVE MOLECULAR AND BIOMOLECULAR DETECTIONS

(Thesis format: Integrated Article)

by

Mohammadali Tabatabaei

Graduate Program in Chemistry

A thesis submitted in partial fulfillment  
of the requirements for the degree of  
Doctor of Philosophy

The School of Graduate and Postdoctoral Studies  
The University of Western Ontario  
London, Ontario, Canada

©Mohammadali Tabatabaei 2015

## Abstract

One of the major challenges in analytical and biological sciences is to develop a device to obtain unambiguous chemical and structural properties of a material or a probe biomolecule with high reproducibility and ultra-high sensitivity. Moreover, in addition to such a high sensitivity, other cases such as minimum intrusiveness, small amounts of analyte, and short acquisition time and high reproducibility are key parameters that can be valued in any analytical measurements. Among the promising methods to achieve such endeavor, plasmon-mediated surface-enhanced spectroscopic techniques, such as surface-enhanced Raman spectroscopy (SERS), are considered as suitable options. Such techniques take advantage of the interaction between an optical field and a metallic nanostructure to magnify the electromagnetic (EM) field in the proximity of the nanostructure. This results in an amplified signal of the vibrational fingerprints of the adsorbed probe molecules onto the metallic surface. Keys to obtaining ultra-sensitive SERS measurements are the development of rationally-designed plasmonic nanostructures. Besides, a major challenge for controlled and reliable sensitive measurements of probe biomolecules on biological cells gives rise due to the intrinsic random positioning and proliferation of these cells over a substrate such as a glass coverslip.

In this thesis, the rational design and development of a fluorocarbon thin film micropatterned platform is introduced for controlled programming of conventional and transfected cells proliferation over the substrate. They also provided high throughput capability of controlled neuronal network connections towards advanced imaging and sensitive detection of biomolecules of interest at nanoscale resolution. This micropatterned platform was also integrated with optimized plasmonic nanostructures fabricated by nanosphere lithography (NSL) for SERS biosensing of glycans using a Raman reporter over the positionally-controlled single cells surfaces. In addition to providing controlled plasmon-mediated measurements, the fabrications of two newly-developed 3D plasmonic nanostructures have been introduced in this thesis. These are nanopyramids arrays fabricated by NSL and arrays of nanoholes with co-registered nanocones fabricated by electron-beam lithography (EBL). These approaches have been used not only for ultra-sensitive molecular detection at the monolayer level in a variety of configurations, but also towards label-free single molecule detection at sub-femtomolar concentrations.

## Keywords

fluorocarbon polymer, cell micropatterning, neuronal network, plasmon, localized surface plasmon resonance, plasmonic nanostructure, finite-difference time domain, surface-enhanced Raman spectroscopy, nanosphere lithography, electron beam lithography, self-assembled monolayer, biosensing, glycan, 4-mercaptophenyl boronic acid, 4-nitrothiophenol, sub-femtolar detection.

## Dedication

To my beloved family

## Co-Authorship Statement

Dr. François Lagugné-Labarthe was the corresponding author on the presented papers in this thesis and was responsible for the supervision of Mohammadali Tabatabaei over the course of his studies. The thesis includes material from four publications, all of which had contributions from co-authors.

Mohammadali Tabatabaei was the primary author of the published or submitted papers presented in Chapters 4, 5, 6 and 7. He was responsible for the majority of the experimental work in these papers as well as the writing and revision for all drafts, including final manuscripts. Some data were jointly acquired and analyzed by co-authors as summarized below:

**Chapter 4:** Tabatabaei, M.; Caetano, F. A.; Vedraïne, S.; Norton, P. R.; Ferguson, S. S. G.; Lagugné-Labarthe, F.; “Directing GPCR-transfected cells and neuronal projections with nano-scale resolution” *Biomaterials*, (2013), 34, 10065.

Dr. Fabiana Caetano trained Mohammadali Tabatabaei for confocal fluorescence imaging, cell and neuronal cultures, the transfection of cells, as well as the immunostaining of cells and neurons. She was also involved in writing the biological parts of the manuscript and the revision of the final draft along with Dr. Stephen S. G. Ferguson from Robarts research institute at Western University. Dr. Ferguson was also involved in supervising the project. Dr. Sylvain Vedraïne trained Mohammadali Tabatabaei for the AFM imaging and he was involved in the imaging of neuronal projections and the revision of the final draft. Dr. Peter R. Norton was involved in the final revision of the manuscript and he kindly provided the combined AFM-confocal fluorescence instrument for part of the cell and neuronal imaging.

**Chapter 5:** Tabatabaei, M.; Wallace, G. Q.; Caetano, F. A.; Gillies, E. R.; Ferguson, S. S. G.; Lagugné-Labarthe, F.; “Enabling controlled positioning of analytes and cells on a plasmonic platform for surface-enhanced Raman spectroscopy: where surface chemistry meets biology” Submitted to *J. Am. Chem. Soc.*, (2015).

Gregory Q. Wallace was involved in SEM imaging of the final platform and some of SERS experiments and their analysis. The HeLa cells were kindly provided by Dr. Elizabeth R.

Gillies's research laboratory at the department of chemistry at Western University. Dr. Fabiana Caetano was involved in supervising the biological aspect of the project specifically for the studies of HEK and neuronal cells. HEK and neuronal cells were kindly provided by Dr. Stephen S. G. Ferguson's research laboratory at Robarts research institute of Western University. All the authors were involved in revision of all the drafts and also the final manuscript.

**Chapter 6:** Tabatabaei, M.; Sangar, A.; Kazemi-Zanjani, N.; Torchio, P.; Merlen, A.; Lagugné-Labarthe, F.; *J. Phys. Chem. C*, (2013), 117, 14778.

Dr. Alexandre Sangar was involved in fabrication of plasmonic platform. Dr. Nastaran Kazemi-Zanjani was involved in SERS measurements and FDTD calculations. All authors were involved in revisions of manuscript including the final draft.

**Chapter 7:** Tabatabaei, M.; Najiminaini, M.; Davieau, K.; Kaminska, B.; Singh, M. R.; Carson, J. J. L.; Lagugné-Labarthe, F.; "Tunable 3D plasmonic cavity nanosensors for surface-enhanced Raman spectroscopy with sub-femtomolar limit of detection" *ACS Photonics*, (2015), 2, 752.

Dr. Mohamadreza Najiminaini was involved in the fabrication of the plasmonic platform and optical transmission studies. Kiefer Davieau was involved in FDTD calculations and optical transmission simulations. All the authors were involved in the revisions of the manuscript including the final draft.

## Acknowledgments

First of all, I would like to acknowledge, with gratitude, my supervisor: Dr. François Lagugné-Labarthe for his advice and support throughout my years here. He was really supportive during my Ph.D. time here at Western, especially at times when research was not particularly moving forward so well. He was always open to new and creative ideas giving me freedom to work on different projects. Noteworthy, I always felt comfortable to discuss all the aspects of my projects with him including those that I was not necessarily in agreement with. This developed a more complete approach for all steps of the projects. He also gave me the opportunity to train and work with several junior graduate or undergraduate students to enrich my supervision capabilities. This also includes collaborations with national and international research scientists during my studies. I would also like to acknowledge the many people who have had significant impact on my research. The staff at Western's Nanofabrication Facility deserves my gratitude as without them my work would not have been possible: Tim Goldhawk, and Dr. Todd Simpson. To our collaborator at Robarts Research Institute, Dr. Stephen S. G. Ferguson, and Dr. J. J. L. Carson at Lawson Health Research Institute, as well as Dr. Elizabeth R. Gillies and Aneta Borecki at Department of Chemistry for allowing me access to HeLa cells, and the training of their cultures.

Many thanks are extended to all researchers at Dr. Ferguson's research group at Robarts Research Institute in particular Dr. Fabiana A. Caetano not just for her kind efforts and willingness to teach me complex cell/neuron culturing, as well as confocal imaging, but also for her always useful consultations, and of course the fun time outside of the lab with all Ferguson's group. I would also like to thank Dr. Mohamadreza Najiminaini for both his scientific help and also his friendship and fun time outside of the lab. Special thanks to both present and past members of the F.L.L group: Gregory Q. Wallace, Farshid Pashae, Dr. Nastran Kazemi-Zanjani, Renjie Hou, Dr. Kristen Snell, Dr. Sylvain Vedraïne, Dr. Alexandre Garreau, Matt Coady, Shabila Fayaz, and Dr. Betty C. Galarreta for their support, friendship, and all of our adventures both in and out of the lab.

Finally, my deepest appreciation goes to my family and friends for the constant love and unending support you all send my way!



## Table of Contents

Abstract .....	ii
Dedication .....	iv
Co-Authorship Statement.....	v
Acknowledgments.....	vii
List of Tables .....	xiii
List of Figures .....	xiv
List of Abbreviations, Symbols, and Nomenclature.....	xxiii
List of Appendices .....	xxvi
Chapter 1 .....	1
1 General introduction.....	1
1.1 Overview.....	1
1.2 Wide range of applications .....	3
1.3 Scope of thesis .....	3
1.4 References.....	5
Chapter 2.....	10
2 Principles of micropatterning techniques and surface-enhanced spectroscopies.....	10
2.1 Chemically patterning surfaces for cell-based assays.....	10
2.1.1 Photolithography.....	11
2.1.2 Microcontact printing.....	12
2.1.3 Microfluidic patterning .....	13
2.1.4 Stencil patterning .....	14
2.1.5 Inkjet patterning .....	15
2.1.6 Plasma processes.....	16
2.2 Principles and theory of surface-enhanced spectroscopies.....	19
2.2.1 Raman spectroscopy .....	19

2.2.2	Fluorescence spectroscopy.....	21
2.2.3	Plasmonic resonances in metal .....	22
2.2.4	Surface-enhanced Raman spectroscopy (SERS) .....	34
2.3	Summary.....	40
2.4	References.....	41
Chapter 3	.....	50
3	Fabrication techniques of plasmonic platforms .....	50
3.1	Nanosphere lithography (NSL).....	50
3.2	Electron-beam lithography (EBL) .....	57
3.3	Raman setup for SERS measurements.....	60
3.4	Summary.....	61
3.5	References.....	62
Chapter 4	.....	64
4	Directing GPCR-transfected cells and neuronal projections with nano-scale resolution .....	64
4.1	Introduction.....	65
4.2	Materials and methods .....	67
4.2.1	Materials .....	67
4.2.2	Patterned substrate fabrication.....	68
4.2.3	Cells cultures.....	70
4.2.4	Neuronal cultures .....	71
4.2.5	Immunofluorescence staining.....	71
4.2.6	Characterization .....	72
4.3	Results and discussion .....	73
4.3.1	Characterization of fluoropolymer patterned surface .....	73
4.3.2	Non-transfected cell proliferation on patterned substrates .....	77

4.3.3	Micropatterned transfected cells .....	79
4.3.4	Neuronal circuit arrangement on patterned substrates .....	84
4.3.5	Spine localization in isolated neuronal projections .....	86
4.4	Conclusions.....	88
4.5	References.....	88
Chapter 5.....		93
5	Enabling controlled positioning of analytes and cells on a plasmonic platform for surface-enhanced Raman spectroscopy: where surface chemistry meets biology .....	93
5.1	Introduction.....	94
5.2	Experimental section.....	96
5.2.1	Materials .....	96
5.2.2	Fabrication process of FC-patterned platform .....	97
5.2.3	Functionalization of the platform.....	100
5.2.4	SERS setup.....	100
5.2.5	AFM.....	101
5.2.6	Scanning electron microscopy (SEM) .....	101
5.2.7	Cultures of HEK, C2C12, and HeLa cells .....	101
5.2.8	Cultures of neuronal cells .....	101
5.3	Results and discussion .....	102
5.3.1	Characterization of FC-patterned plasmonic substrates .....	102
5.3.2	Controlled micro-defined functionalization with analyte .....	103
5.3.3	Biocompatibility of FC-patterned plasmonic platform.....	105
5.3.4	SERS activity of FC-patterned plasmonic platform .....	107
5.3.5	Glycan expression of different cell lines probed by SERS.....	110
5.4	Conclusions.....	117
5.5	References.....	117

Chapter 6.....	122
6 Optical Properties of Silver and Gold Tetrahedral Nanopyramid Arrays Prepared by Nanosphere Lithography .....	122
6.1 Introduction.....	123
6.2 Experimental section.....	125
6.2.1 Materials .....	125
6.2.2 Preparation of samples by nanosphere lithography .....	125
6.2.3 Metal deposition and characterization .....	126
6.2.4 FDTD simulations.....	126
6.2.5 Azopolymer thin film preparation and photoinduced surface deformation .....	127
6.2.6 Raman SERS measurements.....	128
6.3 Results and discussion .....	128
6.3.1 Characterization of nanopyramid arrays fabricated by NSL .....	129
6.3.2 FDTD calculations .....	131
6.3.3 Mapping individual hot spots on photosensitive self-developing azopolymer.....	137
6.3.4 SERS measurements .....	140
6.4 Conclusion .....	144
6.5 References.....	145
Chapter 7.....	149
7 Tunable 3D plasmonic cavity nanosensors for surface-enhanced Raman spectroscopy with sub-femtomolar limit of detection.....	149
7.1 Introduction.....	150
7.2 Experimental section.....	152
7.2.1 Fabrication of 3D plasmonic cavity nanosensors .....	152
7.2.2 Numerical simulation of 3D plasmonic cavity nanosensors.....	153
7.2.3 Optical characterization setup.....	154

7.2.4	SERS measurements and sample preparation.....	155
7.3	Results and Discussion .....	156
7.3.1	Physical characterization of the fabricated 3D plasmonic cavity nanosensors .....	156
7.3.2	Tunable cavity 3D nanosensors .....	157
7.3.3	Effect of plasmonic tunability on SERS .....	162
7.3.4	SERS mapping of hot spots on 3D plasmonic nanosensors .....	165
7.3.5	Limit of detection for 3D nanosensors.....	166
7.3.6	Estimation of a SERS enhancement factor .....	169
7.4	Conclusions.....	173
7.5	References.....	174
Chapter 8	.....	178
8	Conclusions and outlook.....	178
8.1	References.....	182
Appendix A	.....	185
Curriculum Vitae	.....	201

## List of Tables

Table 2.1 Summary of microfabrication techniques used for cellular patterning.....	18
Table 3.1 Comparing three principle techniques for NSL.....	54
Table 5.1 SERS vibrational frequencies assignment of 4-MPBA and Cell.....	108

## List of Figures

Figure 2.1 Schematic illustration of three selected surface micropatterning techniques.....	14
Figure 2.2 Schematic description of three types of plasma processes. The active species in the plasma are used to: a) chemically modify the surface, b) remove the top layer of the exposed surface, and c) deposit polymerized material on the exposed surface.....	17
Figure 2.3 Jablonski Diagram demonstrating the variety of light-matter interactions.....	21
Figure 2.4 Illustration of propagating surface plasmon at the interface between metal surface and a dielectric. ....	24
Figure 2.5 Real and imaginary dielectric functions of gold and silver according to the Lorentz-Drude model. <sup>69</sup> .....	25
Figure 2.6 (A) Dispersion curves of SP and light line ( $\omega=ck_x$ ), $\omega_{sp}$ is a SP frequency. (B) Two-dimensional grating of a square lattice holes: ( $p$ ) is the spacing between adjacent holes and ( $a$ ) is the width of holes.....	27
Figure 2.7 A 2D sub-wavelength hole array in a metal film on a substrate in a square lattice arrangement. $p$ is the spacing between two adjacent holes, $a$ is a width of each hole, $K_x$ wave vector of the light is along the $x$ -axis, and $(+1,0)$ , $(-1,0)$ , $(0,\pm 1)$ , $(+1,1)$ , and $(-1,1)$ are various $(i, j)$ grating modes.....	29
Figure 2.8 Illustration of localized surface plasmon in metal nanostructures (A) False-colored SEM image of tetrahedral gold nanopyrramids fabricated by nanosphere lithography over an Indium Tin Oxide (ITO) surface (B) finite-difference time-domain (FDTD) simulation of a single hexagonal array showing the confinement of the electric field at the surface of a bowtie and within the gaps between the neighbouring nanopyrramids. The image in part A is adapted from reference 53 with permission from American Chemical Society publishing group. ....	31
Figure 2.9 Localized surface plasmon resonance (LSPR) model for metallic nanosphere. ...	32

Figure 2.10 Illustration of different enhancement mechanism (a)-(c) demonstrate three types of chemical mechanism while (d) shows electromagnetic mechanism. <sup>120</sup> .....	38
Figure 3.1 Schematic illustration of the nanosphere lithography with interface method. A) a monolayer of polystyrene microspheres are spread on water-air interface and the monolayer is transferred onto the surface of a clean microscope coverslip; B) a uniform layer of a metal of choice is deposited by electron-beam evaporation and the microspheres are removed by sonication in ethanol revealing the final plasmonic platform; C) side view of the same process in B. ....	51
Figure 3.2 Representative SEM images of nanotriangles fabricated by different NSL techniques, including A-C) drop casting. D-F) spin casting. G-I) interface method. ....	53
Figure 3.3 SEM images of distinct plasmonic nanostructures obtained on the NSL substrates based on the presence of different layers of the sacrificial template of nanospheres. ....	56
Figure 3.4 Scanning electron micrographs of 2D nanostructures written using EBL. <sup>14</sup> .....	58
Figure 3.5 Schematic illustration of fabrication process for 3D plasmonic cavity nanosensors .....	59
Figure 3.6 Principles of the SERS setup used in this thesis. The linearly polarized laser gets focused onto the sample using a microscope objective (typically $\times 100$ , 0.9 N.A.). The backscattered light from the sample gets collected using the same microscope objective, passes through the notch filter that rejects the incident wavelength and then enters the spectrometer. Prior to entering the spectrometer, a confocal pinhole selects the back-scattered light from a given focal plane. A diffraction grating disperses the light spatially, separating the distinct wavelengths. The dispersed light is then detected by a CCD detector prior to signal acquisition and treatment. ....	60
Figure 4.1 Schematic illustration of the applied method to prepare patterns with fluorocarbon (FC) polymer; Photolithography and plasma deposition of a thin FC film were used prior cell culture over the patterned surface. ....	69



Figure 4.2 Optical images of the photoresist patterned substrates, taken in bright field. A-C) hexagonal grid-like pattern; D-H) isolated and connected reservoirs with different geometries. Scale bar in D-H represents 50 $\mu\text{m}$ . .....	73
Figure 4.3 Bright field optical images of fluoropolymer patterned substrates with different geometries. A-C) hexagonal grid-like pattern; D-H) five different geometries of isolated and connected reservoirs; The scale bar in images D-H represents 50 $\mu\text{m}$ . .....	74
Figure 4.4 Schematic demonstration of different geometries of connected reservoirs on patterned substrates. ....	75
Figure 4.5 AFM height images of A) a node of hexagonal grid-like pattern; B) channels of connected reservoirs C) a reservoir; D) a channel on hexagonal grid-like pattern; E) cross section of a channel showing the thickness ( $25 \pm 5 \text{ nm}$ ) of fluoropolymer thin film deposited on the substrate; A and B are the 3D AFM images. ....	75
Figure 4.6 AFM (A, and B) and wide field fluorescence (B, and D) of micropatterned CF10 cells; E) Overlay fluorescence and AFM image of patterned CF10 cells grown inside the channels. A-D) Transfected CF10 cells with CRF <sub>1</sub> ; E) Non-transfected CF10 cells. B, and D) Green is for YFP and blue for HOECHST. E) Green is for Alexa Fluor <sup>®</sup> 488 Phalloidin, and blue for HOECHST.....	76
Figure 4.7 Confocal fluorescence images of the growth of non-transfected HEK 293 and CF10 cell lines on patterned substrates; A-F) Non-transfected CF10 cells grown on patterned reservoirs substrates; G-J) Non-transfected HEK 293 cells grown on hexagonal grid-like patterned substrates; K, and L) Non-transfected CF10 cells grown on hexagonal grid-like patterned substrates; Blue represents HOECHST nuclear staining in all images; Actin (488 nm) and Alexa Fluor 488 Phalloidin are stained in green for HEK 293 cells and CF10 cells, respectively to show cell body; All scale bars are 50 $\mu\text{m}$ . ....	77
Figure 4.8 Confocal Fluorescence images of control samples on confocal dishes; A) Non-transfected HEK 293 cells B) Non-transfected CF10 cells; C-F) HEK 293 cells transfected with mGluR1, mGluR5, CRF1, and 5HT2A, respectively; number of cells in all dishes: $8 \times 10^5$ cells/dish; Alexa Fluor <sup>®</sup> 488 Phalloidin, Flag, and YFP are stained in green showing cells	

bodies and receptors; HOECHST is used for nuclear staining in blue; All scale bars represent 50  $\mu\text{m}$ . ..... 79

Figure 4.9 Widefield fluorescence images of micropatterned CF10 cells transfected with: row A) mGluR1-Flag; B) mGluR5-Flag; C) CRF1-YFP; D) 5HT2A-YFP receptors on five different geometries of reservoirs; Blue represents HOECHST nuclear staining, receptors tagged with Flag were labeled with Alexa Fluor 488 (green, 488nm); YFP label is also shown as green (514 nm); All the scale bars represent 20  $\mu\text{m}$ . ..... 82

Figure 4.10 Confocal (A-H) and widefield (I-N) fluorescence images of HEK 293 cells transfected with A-D) mGluR1-Flag; E-H) mGluR5-Flag; I-K) CRF-YFP; L-N) 5HT-YFP; Blue represents HOECHST nuclear stain, green is for Flag (488 nm), and YFP (514 nm); red is for actin 633 nm; All scale bars are 50  $\mu\text{m}$ . ..... 83

Figure 4.11 Widefield (B, and D) and confocal (A, and C) fluorescence images of cortical neuron circuit arrangement; A) 7 DIV; B-D) 14 DIV; Synaptic markers: Synaptophysin (red) and PSD-95 (green) were used; Blue represents HOECHST nuclear staining; All scale bars are 50  $\mu\text{m}$ . A-C)  $1 \times 10^6$  cells/dish; D)  $1.5 \times 10^6$  cells/dish. .... 85

Figure 4.12 AFM height images of isolated neuronal projections showing the spines localization A, D) 2D AFM images of isolated neuronal projections; B) AFM image of the selected area shown in A; C) 3D AFM image of the selected area shown in B; E, F) 3D AFM image of the selected area shown in D; G) 3D AFM image of selected area in E showing the spines with higher magnification; Arrows show the spine localizations of isolated neuronal projections. .... 87

Figure 5.1 Schematic illustration of the fabrication process for the FC-patterned plasmonic platform. .... 98

Figure 5.2 AFM topography of A) a node and B) a channel of a hexagonal grid-like FC-patterned substrate on glass coverslip. C) Cross section of the indicated area in B determining the thickness of FC film of  $60 \pm 5$  nm. .... 99

Figure 5.3 SEM images of FC-patterned plasmonic substrates with two different feature patterns: Hexagonal-grid like pattern (A-F) Triangular pattern (G-I) ..... 103

Figure 5.4 Collected confocal SERS spectra and mapping of functionalized 4-NTP on a FC-patterned plasmonic substrate. A) Schematic of the microwell plasmonic platform B) SERS mapping on an isolated triangular pattern C) Chemical structure of 4-NTP and collected SERS spectra of defined regions in B. Region 1 and 2 are located on plasmonic platform and FC polymer, respectively. D) Optical image of a node and channels positioned over the NSL substrate. SERS mappings of selected regions in D representing a node (E) and a channel (F) are shown in the interpolated images of E and F. .... 104

Figure 5.5 SEM images of positionally-controlled cells on FC-plasmonic substrates. A, B) HEK 293 cells; C, D) Cortical neurons; Blue arrows indicate cell nuclei; Red Arrows indicate cell membranes (A, B) and projections of neurons (C, D). .... 106

Figure 5.6 SERS activity of 4-MPBA functionalized FC-patterned plasmonic platform representing 4-MPBA and HEK cell vibrational frequencies (A, C, and D); the non-SERS spectra are obtained on flat Au surface (B, and E) as a control compared to SERS signal obtained on SERS-active plasmonic regions containing nanotriangles within the fluoropolymer. A, B, C are normalized to the same scale. The same process is used for D, and E. Baseline correction is applied to all the spectra. .... 109

Figure 5.7 Confocal SERS mapping of cell compartments and glycan expression on HEK 293, C2C12 and HeLa cells. Optical image of isolated single A) HEK 293, B) C2C12, C) HeLa cell. Confocal SERS map of cell compartments of selected regions in optical images for D) HEK 293 cell, E) C2C12 cell, F) HeLa cell; Confocal SERS map of glycan expression over the selected regions in optical images for G) HEK cell, H) C2C12 cell, I) HeLa cell; J) Overlay of A+G; K) Overlay of B+H; L) Overlay of C+I. .... 111

Figure 5.8 Confocal SERS mapping of a single HeLa cell with nanoscale surface morphology obtained by AFM. A) Optical image of a single HeLa cell; B) SERS mapping of cell compartments; C) Overlay of SERS map in B with AFM morphology shown in D; D) AFM phase of the single cell shown in D. E) Glycan distribution on the same cell; F) Overlay of D and E. .... 113

Figure 5.9 Average SERS spectra of 4MPBA and isolated cells on 4-MPBA functionalized-plasmonic platform; A) HEK 293 cell; B) C2C12 cell; C) HeLa cell. D) Ratios of the average

intensities of 4-MPBA/Cell+4MPBA for 15 cells at  $1074\text{ cm}^{-1}$ . Baseline corrections were applied to all spectra. .... 114

Figure 5.10 Cell SERS analysis representing the ratios of the normalized average SERS (Intensity (4-MPBA)/Intensity (4-MPBA + Cell)) at  $1074$  and  $1574\text{ cm}^{-1}$  for 15 different cells for each cell line. The error bars are generated based on the percent deviation from the median ratio values. The obtained median values are  $0.91 \pm 4\%$  (HEK 293 at  $1074\text{ cm}^{-1}$ ),  $0.98 \pm 3\%$  (HEK 293 at  $1574\text{ cm}^{-1}$ ),  $0.83 \pm 4\%$  (C2C12 at  $1074\text{ cm}^{-1}$ ),  $0.85 \pm 5\%$  (C2C12 at  $1574\text{ cm}^{-1}$ ),  $0.51 \pm 10\%$  (HeLa at  $1074\text{ cm}^{-1}$ ),  $0.71 \pm 10\%$  (HeLa at  $1574\text{ cm}^{-1}$ )..... 116

Figure 6.1 Chemical Structure of p(DR1M-co-MMA) 11% ..... 127

Figure 6.2 A) SEM images of silver-coated polystyrene nanospheres. B) Array of silver nanopyramids. C, D) Individual silver nanopyramids before and after coating with an azopolymer thin film, respectively. E, F) Extinction spectra of the Silver (red) and gold(blue) nanopyramids. Excitation wavelengths as well as the  $[800-1800]\text{ cm}^{-1}$  spectral ranges with respect to both excitations are indicated. .... 129

Figure 6.3 False-colored SEM image showing arrays of gold nanopyramids ..... 130

Figure 6.4 FDTD calculation of the transverse (B,C,F,G) and longitudinal (A,D,E) components of the electric field ( $E/E_0$ , Log scale representation) for silver nanopyramids prepared on ITO and irradiated at  $532\text{ nm}$ . The transverse field shown in C,F) are calculated  $2\text{ nm}$  above the tip(s) of the pyramid(s). The transverse field shown in (B,G) are calculated  $2\text{ nm}$  above the ITO base layer. .... 132

Figure 6.5 FDTD calculation of the transverse (B,C,F,G) and longitudinal (A,D,E) components of the electric field ( $E/E_0$ , Log scale representation) for silver nanopyramids prepared on ITO and irradiated at  $632.8\text{ nm}$ . The transverse field shown in C,F) are calculated  $2\text{ nm}$  above the tip(s) of the pyramid(s). The transverse field shown in (B,G) are calculated  $2\text{ nm}$  above the ITO base layer ..... 133

Figure 6.6 FDTD calculation of the transverse (B,C,F,G) and longitudinal (A,D,E) components of the electric field ( $E/E_0$ , Log scale representation) for gold nanopyramids prepared on ITO and irradiated at  $632.8\text{ nm}$ . The transverse field shown in C,F) are

calculated 2 nm above the tip(s) of the pyramid(s). The transverse field shown in (B,G) are calculated 2 nm above the ITO base layer. .... 134

Figure 6.7 FDTD calculation of the transverse (B,C,F,G) and longitudinal (A,D,E) components of the electric field ( $E/E_0$ , Log scale representation) for gold nanopyramids prepared on ITO and irradiated at 532 nm. The transverse field shown in C,F) are calculated 2 nm above the tip(s) of the pyramid(s). The transverse field shown in (B,G) are calculated 2 nm above the ITO base layer. .... 136

Figure 6.8 A,B) AFM images of Ag nanopyramids prepared on ITO coated with a 80 nm azopolymer thin film layer before (A) and after (B) 15 min of irradiation with a irradiance of  $100 \text{ mW/cm}^2$ . C,D) topographical cross sections along the center of a hexagonal lattice (noted ①) of Ag nanopyramids before and after irradiation. E,F) AFM topographical cross sections along the closest facing silver pyramids (noted ②) before and after irradiation. ... 139

Figure 6.9 Raman spectra of 4-NTP adsorbed on the nanopyramid arrays. The spectra were recorded with same acquisition time (10 s). No baseline correction was performed. Raman spectra acquired on flat metal portions (no structures) and functionalized the same conditions as shown. A) SERS spectra collected on Au nanopyramids with 632.8 and 532 nm irradiations. B) SERS spectra collected on Ag nanopyramids with 632.8 nm excitation under 0.2 mW (initial) and 2mW (final) irradiations. C) SERS spectra collected on Ag nanopyramids with 532 nm excitation under 0.2 mW and 2mW irradiations. D) SERS spectra recorded at 632.8 nm on Ag nanopyramids at 2 mW (initial) and 0.2 mW (final)..... 141

Figure 6.10 Raman spectra of 4-NTP adsorbed on the nanotriangles (30 nm Au), and nanopyramid arrays (400 nm Au). The spectra were recorded with same acquisition time (10 s) and irradiation wavelength was 632.8 nm with  $I=2 \text{ mW}$ . .... 143

Figure 6.11 SERS spectra of 4-NTP adsorbed onto silver nanopyramids recorded initially under 2 mW irradiance followed by a measurement under 0.2 mW with identical acquisition time (10 s). .... 144

Figure 7.1 Layout of FDTD simulation model including boundary conditions for optical properties and electromagnetic field distribution of 3D plasmonic nanosensors with a periodicity of 500 nm..... 154

Figure 7.2 Schematic of 3D plasmonic nanosensor displaying a cavity beneath the Au layer, and truncated nanocones at the bottom of the cavity. .... 156

Figure 7.3 SEM images of 3D plasmonic cavity nanosensors composed of a NHA membrane with co-registered NCA. a) A 230 nm thick Au NHA membrane with 500 nm periodicity and 87 nm hole radius fabricated on a Pyrex substrate with a single 250 nm deep cavity. b) Magnified image shown in (a) representing the dimensions of the truncated Au nanocones with an apex radius of 44 nm, a base radius of 87 nm, and a height of 150 nm. .... 157

Figure 7.4 Optical transmission spectra of 3D plasmonic nanosensors for simulated and experimental results. The periodicities range from 425 nm (green curve) to 500 nm (red curve) with increments of 25 nm. Simulated results for (a) air ( $n = 1.00$ ), (b) water ( $n = 1.33$ ), experimental results for (c) air ( $n = 1.00$ ), and (d) water ( $n = 1.33$ ). .... 159

Figure 7.5 Electric field ( $|E/E_0|^2$ , log scale representation) intensity of a unit cell in a 3D plasmonic nanosensor displayed on the  $xz$  plane. The electric field intensity for air ( $n = 1.00$ ) at (a) (-1,0) peak at 594 nm, (c) 633 nm, and (d) 780 nm. The SEM image of the actual structure represented simulated images has been shown in (b). The electric field intensity for water ( $n = 1.33$ ) at (e) (1,1) peak at 620 nm, (f) (-1,0) peak at 738 nm, (g) 633 nm, and (h) 785 nm. .... 160

Figure 7.6 Simulated optical transmission spectra of 3D cavity plasmonic nanosensors in Ethanol ( $n=1.36$ ). The periodicities range from 425 nm (green curve) to 500 nm (red curve) with increments of 25 nm. .... 161

Figure 7.7 SERS spectra of 4-NTP adsorbed on the 3D nanosensors with different periodicities, medium (air and water) and wavelength of incident light. a) P500 nm and b) P425 nm periodicities at 633 nm incident light in air (red) and water (blue); c) P500 nm and d) P425 nm periodicities at 785 nm in air (red) and water (blue). Acquisition time for each spectrum was 3 s with 5 accumulations. Base line correction was applied to all spectra. A +5000 a.u. offset was applied to both red spectra in a and b. A +1000 a.u. offset was applied to both blue spectra in c and d. These offsets were applied to represent the data in a more comparable fashion. .... 163

Figure 7.8 SERS spectra of 4-NTP adsorbed on the 3D nanosensors with different periodicities, medium (air and water) and wavelength of incident light. a) P475 nm and b) P450 nm periodicities at 633 nm incident light in air (red) and water (blue); c) P475 nm and d) 450 nm periodicities at 785 nm in air (red) and water (blue). All the experimental conditions are the same as Figure 7.7. .... 164

Figure 7.9 Surface-enhanced Raman mapping of 4-NTP adsorbed on the 3D nanosensors with 500 nm periodicity in air with 633 nm incident light. Acquisition time for each spectrum was 1 s with 1  $\mu\text{m}$  step size. a) Transmission optical image of 3D nanosensors with overlaid SERS mapping (inset) for the area outlined with red dashed box. b) Raman mapping of the outlined area in panel (a). c) Spectra of the regions marked (1) and (2) in panel (b). No baseline correction was applied to spectra in panel (c). .... 166

Figure 7.10 Standard error analysis of SERS signals for three main peaks of 4-NTP (100 aM) at 1080 (vs C-H), 1337 (vs  $\text{NO}_2$ ), and 1575 (vs C-C)  $\text{cm}^{-1}$  obtained on 15 spots (average of 3 experiments for each spot) of the P500 nanosensors. The standard error bars are generated based on the obtained mean values of 895.3, 1980.6, 1061.7 (a.u.) for the Raman intensities at 1080, 1337, and 1575  $\text{cm}^{-1}$ , respectively. .... 167

Figure 7.11 SERS spectra of 4-NTP adsorbed onto 3D nanosensors collected by using 633 nm incident laser in air. a) Different concentrations (1 aM-1 mM) of 4-NTP adsorbed on the 3D nanosensors with 500 nm periodicity; b) The effect of numerical aperture and magnification on SERS spectra of 100 aM 4-NTP adsorbed on the 3D nanosensors; c) SERS spectra of 100 aM 4-NTP adsorbed on to the 3D nanosensors. Baseline correction was applied to all spectra. SERS signals of the main  $\text{NO}_2$  peak are shown within each inset in each panel. .... 169

Figure 7.12 Sensitivity of sensors represented by SERS signals of vs  $\text{NO}_2$  with respect to the Log [Concentration] between 1 aM and 1  $\mu\text{M}$ . .... 172

## List of Abbreviations, Symbols, and Nomenclature

$\alpha$	polarizability of a molecule
$\beta$	bending mode
$\epsilon_0$	permittivity constant of free-space
$\epsilon_d$	permittivity constant of a dielectric
$\epsilon_m$	complex dielectric function of a metal
$\lambda$	wavelength of light
$\lambda_{LSPR}$	localized surface plasmon resonance excitation band
$\vec{\mu}$	dipole moment
$\mu\text{CP}$	microcontact printing
$\mu\text{m}$	micrometer
$\mu\text{s}$	microsecond
$\nu$	stretching mode/vibrational level
$\theta$	angle of incidence
$\sigma_{\text{ext/sca/abs}}$	extinction/scattering/absorption cross-section
$\omega$	laser frequency
$\omega_p$	plasma frequency
$\sigma$	scattering cross section
$\sigma_{\text{ext/sca/abs}}$	extinction/scattering/absorption cross section
$\chi$	shape factor of a nanoparticles
2D	two dimensional
3D	three dimensional
4-NTP	4-nitrothiophenol
4-MPBA	4-mercaptophenyl boronic acid
5-HT2A	5-hydroxytryptamine receptor
5HTR	Serotonin
AFM	atomic force microscopy
aM	attomolar
BSA	bovine serum albumin
$c$	speed of light
C2C12	mouse myoblast cells
$\text{C}_4\text{F}_8$	Octafluorocyclobutane
CCD	charge-coupled device
CF10	prion protein neural cell line
CHO	Chinese hamster ovarian
CRHR1/CRF1	corticotropin releasing hormone receptor
$e$	electron charge
$d$	diameter
DIV	days in vitro
DMEM	Dulbecco's modified eagle's medium
$E_o$	incident electromagnetic field
$E_f$	Fermi energy level
$ E ^2$	total electric field intensity
EBL	electron beam lithography
EF	enhancement factor



EM	electromagnetic
EOT	extraordinary optical transmission
FC	fluorocarbon
FDTD	finite-difference time domain
GPCR	G protein-coupled receptor
HEK 293	human embryonic kidney cells
HeLa	Henrietta Lacks cervical cancer cells
hESC	human embryonic stem cells
HOMO	highest occupied molecular orbital
I	light intensity
ICP	inductively coupled plasma
$\text{Im}(\epsilon_m)$	imaginary component of the dielectric function of a metal
$i$	integer of the scattering mode index
IPA	isopropyl alcohol
IR	infrared
ITO	indium tin oxide
$j$	integer of the scattering mode index
$k_0 \sin \theta$	in-plane component of the wavevector of the incident light
$k$	wavevector of incident radiation
$K_d$	dissociation constant
$K_x$	wave vector of light
$k_{SP}$	surface plasmon wave vector
LSPR	localized surface plasmon resonance
LUMO	lowest unoccupied molecular orbital
MDCK	Madin-Darby canine kidney
$m_e$	electron mass
MEM	minimal essential medium
mGluR	metabotropic glutamate receptor
N	number of scattering centers
N.A.	numerical aperture
NCA	nanocones array
$n_e$	number of electrons
NHA	nanoholes array
ns	nanosecond
NSL	nanosphere lithography
$P_i$	polarization induced
$p$	spacing between adjacent nanoholes
PLD	pulsed laser deposition
PDMS	poly(dimethylsiloxane)
PrP	prion protein
ps	picosecond
$\vec{r}$	electron displacement
R	radius vector of a point position in space
$\text{Re}(\epsilon_m)$	imaginary component of the dielectric function of a metal
SE-CARS	surface-enhanced coherent anti-Stokes Raman spectroscopy
SEF	surface-enhanced fluorescence
SE-FSRS	surface-enhanced femtosecond stimulated Raman spectroscopy

SEIRA	surface-enhanced infrared absorption
SEIRS	surface-enhanced infrared spectroscopy
SERS	surface-enhanced Raman spectroscopy
SERRS	surface-enhanced resonance Raman spectroscopy
SMD	single molecule detection
SP	surface plasmon
SPP	surface plasmon polariton
TERS	tip-enhanced Raman spectroscopy
TR-SE-CARS	time-resolved SE-CARS
UV	ultra violet
$\vec{u}_x$	reciprocal lattice wave vector
V	volume
YFP	yellow fluorescence protein

## List of Appendices

Appendix A.....	185
-----------------	-----

## Chapter 1

### 1 General introduction

#### 1.1 Overview

The discovery of Raman scattering was reported in 1920's by Chandrasekhara .V. Raman, resulting from a vast range of studies on inelastic scattering of light in liquids and solids. It was not until 1923 that it was suggested by Adolf Smekal that light also gets scattered inelastically with wavelengths longer or shorter than the initial wavelength of the source excitation.<sup>1,2</sup> The first Raman spectra and the resulting manuscript supporting this effect was published by C.V. Raman in 1928.<sup>3</sup> This brought him the honor of winning a Nobel Prize in Physics in 1930. Further development of Raman spectroscopy was however peripheral for years significantly due to the weakness of typical Raman scattering processes to be detected in absence of a powerful light source and an efficient detector.<sup>4</sup> Upon discovery of laser in 1960 and significant development in optical detection sensitivity, the progressive development of Raman spectroscopy over the past decades has led to a myriad of applications from fundamental research in physics to analytical measurements with extreme sensitivity.

Chemical information about structure,<sup>5,6</sup> symmetry,<sup>7</sup> bonding in molecules or crystals,<sup>8-10</sup> and also the electronic environment<sup>11</sup> of material based upon their vibrational fingerprints can be obtained by Raman spectroscopy as an analytical technique. Raman spectroscopy has emerged applications in multifarious fields such as chemical analysis,<sup>12,13</sup> material sciences,<sup>14,15</sup> biomedical applications<sup>16,17</sup> and also art-related investigations.<sup>18,19</sup> Noticeably, the intrinsic low efficiency of the inelastic scattering in Raman can be surpassed by using plasmonic platforms providing enhanced signals by

several orders of magnitude. In this context, the use of localized surface plasmon resonances play a key role in order to concentrate the light in the proximity of a metallic nanostructure that act as a nanoantenna that locally enhance the electromagnetic (EM) near-field light.<sup>20,21</sup> Upon illumination of the light on a noble metal surface, plasmon resonances occur from the optical response of the free conducting electrons over the surface of the metal. As a result, a confined electric field will be generated within the near-field of the surface of the metallic nanostructure. A molecule of choice located within this confined region of intensified electric field generates an enhanced Raman signal, which it roughly scales with the forth power of the excitation electric field.<sup>22,23</sup> Surface-enhanced Raman spectroscopy (SERS) has been introduced as a consequence of the discovery of this phenomenon as a revolutionary sensitive analytical technique in the early 1970s.<sup>24,25</sup>

In SERS, the Raman scattering is typically enhanced up to a factor of  $10^2$  to  $10^{14}$  through locating the sample in close vicinity of the plasmonic nanostructures.<sup>26-28</sup> SERS has emerged as a powerful technique with applications within multidisciplinary fields and with detection limits down to attomolar concentrations and even further to as-described single molecule detection.<sup>29-32</sup> Beyond the increased sensitivity of molecules adsorbed onto a metallic surface, the use of plasmonic structures is also very useful to improve the spatial resolution in optical microscopy and spectroscopy measurements that are inherently limited by the diffraction limit of light.<sup>33</sup> This limit, known as the Rayleigh criterion, is a function of the excitation wavelength,  $\lambda$ , and the focusing properties of the utilized microscopic objective.<sup>34</sup> This dependence implies that the smallest distance that could be resolved in far-field measurement, including SERS, is in the range of  $\lambda/2$ , which is typically about 200-300 nm under ideal experimental conditions.<sup>35</sup> For this reason, many research groups have been developing new approaches to use efficiently

plasmonic nanostructures with the goal to improve the lateral resolution of the surface-enhanced Raman measurements.

## 1.2 Wide range of applications

The power of SERS originates from its ability to identify chemical species and providing structural information in a wide range of fields. This includes materials science, biochemistry, life sciences, catalysis, and electrochemistry. We highlight here a few exciting applications of SERS in life sciences. SERS has emerged as a highly sensitive and selective method for the detection of a variety of biological samples.<sup>36</sup> SERS biosensing, a wide range topic, has been reviewed in great detail in the literature.<sup>37-39</sup> SERS biosensors have been used for detection of different biological samples and diseases, including various cancers,<sup>40-43</sup> Alzheimer's disease,<sup>44,45</sup> and Parkinson's disease.<sup>46,47</sup> Furthermore, SERS has been utilized in other aspects of life sciences including biomedical applications,<sup>48,49</sup> cellular probing,<sup>50-52</sup> in vivo cell probing,<sup>53-55</sup> in vitro cell analysis,<sup>56,57</sup> imaging of individual cells,<sup>58,59</sup> differentiating cancer cells,<sup>60</sup> imaging of proteins,<sup>61,62</sup> bacteria and virus detection.<sup>54,63</sup>

## 1.3 Scope of thesis

The fabrication of SERS platforms have been developed using a variety of techniques for involving both top-down and bottom-up methodologies depending on the desired application. In top-down methods, the focus was mostly on 2D structures, which lacks the capability of trapping low concentration of a probe molecule within nano-scale regions of hot spots. Therefore, an approach towards developing a 3D plasmonic platform as a possible biosensor with high affinity of trapping low concentrations of a target molecule is of great interest and demand. In the case of bottom-up approaches, the studies that have been reported are mainly focused on using synthetic metallic colloidal nanoparticles

which provide an intrinsic random assortment of hot spots within the nanoparticles and over a substrate. More specifically, when dealing with biological cells, the random growth of cells over the substrate diminishes the accuracy of probing a molecule of interest over the cells using such plasmonic platforms. As a result, an approach towards organized programming of the biological cells growth on a plasmonic platform as a biosensor is of high interest. This provides controlled positioning of these cells on highly sensitive plasmonic windows on the substrate for further investigations of a molecule of interest over the cells using plasmon-mediated surface-sensitive spectroscopic techniques such as SERS. In this thesis, I propose original approaches by integrating plasmonic platforms into controlled biocompatible micropatterns for biosensing applications. I also provide distinct approaches for the fabrication of 3D plasmonic nanostructures for highly sensitive detections.

A summary of the covered subjects in each chapter is as follows:

In Chapter 2, the principles of chemical patterning of a surface for cell-based assays and also the theoretical background that is essential for thorough understanding of the SERS underlying principles are developed. Major surface patterning techniques and their comparison are first presented. The principles of Raman and fluorescence spectroscopy are briefly explained while the plasmonic properties of noble metals with the focus on localized surface plasmon are described theoretically. Principles of SERS have also been approached theoretically followed by a discussion of the proposed enhancement mechanisms.

The experimental procedure of fabricating plasmonic platforms and experimental setup for performing SERS measurements are discussed in Chapter 3. This Chapter details the principles of the fabrication of 2D and 3D plasmonic nanostructures using two commonly used techniques of nanosphere and electron-beam lithographies.

The presented results in this thesis are organized in two categories. In Chapter 4, a developed cell micropatterning technique has been introduced with subsequent demonstration of integrated plasmonic sensors into these micropatterns in Chapter 5 for biosensing applications. In Chapters 6 and 7, the fabrication of two distinct plasmonic platforms has been described with the purpose of significantly improving the detection limit. The development of a 3D structure for ultra-sensitive SERS measurements with a higher affinity of trapping molecules at a low concentration is provided together with SERS measurements for a selected model molecule.

Finally, I provide a summary of the presented works in Chapter 8 and critically review some of the emerging fields, where SERS can be of interest as well as the possible technical improvements yielding better reproducibility and better sensitivity of the SERS platforms for ultra-sensitive detections. I also discuss the potential future works for the projects presented in this thesis.

## 1.4 References

- (1) Long, D. A. The Raman Effect: A Unified Treatment of the Theory of Raman Scattering by Molecules; John Wiley & Sons, Inc.: Chichester, 2002.
- (2) Smekal, A.; Naturwissenschaften, **(1923)**, 11, 873.
- (3) Raman, C. V.; Krishnan, R. S.; Nature, **(1928)**, 121, 501.
- (4) Hibben, J. H. The Raman Effect and Its Chemical Applications; Reinhold Publishing Corp.: New York, 1939.
- (5) Acharya, S. A.; Maheshwari, N.; Tatikondewar, L.; Kshirsagar, A.; Kulkarni, S. K.; Cryst. Growth Des. , **(2013)**, 13, 1369.
- (6) Fu, Q.; Lu, J.; Lin, N.; Zheng, S.; Rom. Biotechnol. Lett. , **(2012)**, 17, 7557.
- (7) Heckel, J. C.; Weisman, A. L.; Schneebeli, S. T.; Hall, M. L.; Sherry, L. J.; Stranahan, S. M.; DuBay, K. H.; Friesner, R. A.; Willets, K. A.; J. Phys. Chem. A **(2012)**, 116, 6804.



- (8) Matz, K. G.; Mtei, R. P.; Leung, B.; Nieter-Burgmayer, S. J.; Kirk, M. L.; *J. Am. Chem. Soc.*, **(2010)**, 132, 7830.
- (9) Nurulhuda, I.; Johari, M. A.; Mazatulikhma, M. Z.; Rusop, M.; *Adv. Mater. Res.*, **(2013)**, 667, 464.
- (10) Zalamova, K.; Georgiev, M. D.; Georgiev, G. K.; *Proc. SPIE-Int. Soc. Opt. Eng.*, **(2003)**, 5226, 179.
- (11) Schatschneider, B.; Monaco, S.; Tkatchenko, A.; Liang, J.-J.; *J. Phys. Chem. A*, **(2013)**, 117, 8323.
- (12) Stair, P. C.; *Adv. Catal.* , **(2007)**, 51, 75.
- (13) Chen, Y.; Jin, Z.; Pan, Z.; *J. Supercrit. Fluids*, **(2012)**, 72, 22.
- (14) Dresselhaus, M. S.; Dresselhaus, G.; Saito, R.; Jorio, A.; *Phys. Rep.*, **(2005)**, 409, 47.
- (15) Torres, A.; Martin-Martin, A.; Martinez, O.; Prieto, A. C.; Hortelano, V.; Jimenez, J.; Rodriguez, A.; Sangrador, J.; Rodriguez, T.; *Appl. Phys. Lett.*, **(2010)**, 96, 0119041.
- (16) Choo-Smith, L. P.; Edwards, H. G. M.; Endtz, H. P.; Kros, J. M.; Heule, F.; Barr, H.; Robinson, J. S.; Bruining, H. A.; Puppels, G. J.; *Biopolymers* **(2002)**, 67, 1.
- (17) Thomas, G. J., Jr.; *Annu. Rev. Biophys. Biomol. Struct.*, **(1999)**, 28, 1.
- (18) Bersani, D.; Madariaga, J. M.; *J. Raman Spectrosc.*, **(2012)**, 43, 1523.
- (19) Tournie, A.; Prinsloo, L. C.; Paris, C.; Colomban, P.; Smith, B.; *J. Raman Spectrosc.*, **(2011)**, 42, 399.
- (20) Kawata, S.; *Appl. Spectrosc.*, **(2013)**, 67, 117.
- (21) Kawata, S.; Inouye, Y.; Verma, P.; *Nat. Photonics*, **(2009)**, 3, 388.
- (22) Morton, S. M.; Silverstein, D. W.; Jensen, L.; *Chem. Rev.* , **(2011)**, 111, 3962.
- (23) Novotny, L.; Hecht, B. *Principles of nano-optics*; 1st ed.; Cambridge University Press: Cambridge, England, 2006.
- (24) Haynes, C. L.; Yonzon, C. R.; Zhang, X.; Van Duyne, R. P.; *J. Raman Spectrosc.*, **(2005)**, 36, 471.

- (25) Van Duyne, R. P.; Moore, C. B. *Chemical and Biochemical Applications of Lasers*; Academic Press: New York, 1979; Vol. 4.
- (26) Albrecht, M. G.; Creighton, J. A.; *J. Am. Chem. Soc.*, **(1977)**, 99, 5215.
- (27) Fleischmann, M.; Hendra, P. J.; McQuillan, A. J.; *Chem. Phys. Lett.*, **(1974)**, 26, 163.
- (28) Jeanmaire, D. L.; Van Duyne, R. P.; *J. Electroanal. Chem. Interfacial Electrochem.*, **(1977)**, 84, 1.
- (29) Dieringer, J. A.; Lettan, R. B., II; Scheidt, K. A.; Van Duyne, R. P.; *J. Am. Chem. Soc.*, **(2007)**, 129, 16249.
- (30) Kneipp, K.; Wang, Y.; Kneipp, H.; Perelman, L. T.; Itzkan, I.; Dasari, R.; Feld, M. S.; *Phys. Rev. Lett.*, **(1997)**, 78, 1667.
- (31) Xu, H.; Bjerneld, E. J.; Kall, M.; Borjesson, L.; *Phys. Rev. Lett.*, **(1999)**, 83, 4357.
- (32) Tabatabaei, M.; Najiminaini, M.; Davieau, K.; Kaminska, B.; Singh, M. R.; Carson, J. J. L.; Lagugné-Labarthe, F.; *ACS Photonics*, **(2015)**, 2, 752.
- (33) Rayleigh, L.; *Philos. Mag.*, **(1879)**, 8, 261.
- (34) Abbe, E.; *Archiv für mikroskopische Anatomie* **(1873)**, 9, 413.
- (35) Hartschuh, A.; Sanchez, E. J.; Xie, X. S.; Novotny, L.; *Phys. Rev. Lett.*, **(2003)**, 90, 0955031.
- (36) Sharma, B.; Frontiera, R. R.; Henry, A.-I.; Ringe, E.; Van Duyne, R. P.; *Mater. Today*, **(2012)**, 15, 16.
- (37) El-Ansary, A.; Faddah, L. M.; *Nanotechnol., Sci. Appl.*, **(2010)**, 3, 65.
- (38) Hudson, S. D.; Chumanov, G.; *Anal. Bioanal. Chem.*, **(2009)**, 394, 679.
- (39) Tripp, R. A.; Dluhy, R. A.; Zhao, Y.; *Nano Today*, **(2008)**, 3, 31.
- (40) Grubisha, D. S.; Lipert, R. J.; Park, H.-Y.; Driskell, J.; Porter, M. D.; *Anal. Chem.*, **(2003)**, 75, 5936.

- (41) Mohs, A. M.; Mancini, M. C.; Singhal, S.; Provenzale, J. M.; Leyland-Jones, B.; Wang, M. D.; Nie, S.; *Anal. Chem.*, (2010), 82, 9058.
- (42) Sha, M. Y.; Xu, H.; Natan, M. J.; Cromer, R.; *J. Am. Chem. Soc.*, (2008), 130, 17214.
- (43) Stevenson, R.; Ingram, A.; Leung, H.; McMillan, D. C.; Graham, D.; *Analyst* (2009), 134, 842.
- (44) Beier, H. T.; Cowan, C. B.; Chou, I. H.; Pallikal, J.; Henry, J. E.; Benford, M. E.; Jackson, J. B.; Good, T. A.; Cote, G. L.; *Plasmonics*, (2007), 2, 55.
- (45) Benford, M. E.; Chou, I. H.; Beier, H. T.; Wang, M.; Kameoka, J.; Good, T. A.; Cote, G. L.; *Proc. SPIE*, (2008), 6869, 68690W/1.
- (46) An, J.-H.; El-Said, W. A.; Yea, C.-H.; Kim, T.-H.; Choi, J.-W.; *J. Nanosci. Nanotechnol.*, (2011), 11, 4424.
- (47) Shi, C.; Zhang, Y.; Gu, C.; Seballos, L.; Zhang, J. Z.; *Proc. SPIE*, (2008), 6852, 685204/1.
- (48) Reyes-Goddard, J. M.; Barr, H.; Stone, N.; *Photodiagn. Photodyn. Ther.*, (2005), 2, 223.
- (49) Farquharson, S.; Gift, A. D.; Shende, C.; Maksymiuk, P.; Inscore, F. E.; Murrin, J.; *Vib. Spectrosc.* (2005), 38, 79.
- (50) Jarvis, R. M.; Goodacre, R.; *Anal. Chem.*, (2004), 76, 40.
- (51) Kneipp, J.; Kneipp, H.; McLaughlin, M.; Brown, D.; Kneipp, K.; *Nano Lett.*, (2006), 6, 2225.
- (52) Cao, Y. C.; Jin, R.; Mirkin, C. A.; *Science* (2002), 297, 1536.
- (53) Kneipp, K.; Kneipp, H.; Kneipp, J.; *Acc. Chem. Res.*, (2006), 39, 443.
- (54) Premasiri, W. R.; Moir, D. T.; Klempner, M. S.; Krieger, N.; Jones, G., II; Ziegler, L. D.; *J. Phys. Chem. B*, (2005), 109, 312.

- (55) Talley, C. E.; Jusinski, L.; Hollars, C. W.; Lane, S. M.; Huser, T.; Anal. Chem., **(2004)**, 76, 7064.
- (56) Dijkstra, R. J.; Scheenen, W. J. J. M.; Dam, N.; Roubos, E. W.; ter Meulen, J. J.; J. Neurosci. Methods, **(2006)**, 159, 43.
- (57) Chow, R. H.; Von Rueden, L.; Neher, E.; Nature **(1992)**, 356, 60.
- (58) Vo-Dinh, T.; Yan, F.; Wabuyele, M. B.; J. Raman Spectrosc., **(2005)**, 36, 640.
- (59) Vo-Dinh, T.; Kasili, P.; Wabuyele, M.; Nanomedicine, **(2006)**, 2, 22.
- (60) Lee, S.; Kim, S.; Choo, J.; Shin, S. Y.; Lee, Y. H.; Choi, H. Y.; Ha, S.; Kang, K.; Oh, C. H.; Anal. Chem., **(2007)**, 79, 916.
- (61) Souza, G. R.; Christianson, D. R.; Staquicini, F. I.; Ozawa, M. G.; Snyder, E. Y.; Sidman, R. L.; Miller, J. H.; Arap, W.; Pasqualini, R.; Proc. Natl. Acad. Sci. U. S. A., **(2006)**, 103, 1215.
- (62) Hu, Q.; Tay, L.-L.; Noestheden, M.; Pezacki, J. P.; J. Am. Chem. Soc., **(2007)**, 129, 14.
- (63) Bell, S. E. J.; Mackle, J. N.; Sirimuthu, N. M. S.; Analyst **(2005)**, 130, 545.

## Chapter 2

### 2 Principles of micropatterning techniques and surface-enhanced spectroscopies

The design and development of an efficient controlled plasmonic platform for ultra-sensitive molecular and biomolecular applications requires a thorough understanding of various micropatterning and surface-enhanced spectroscopic techniques. Major chemical patterning methods for cell-based studies as well as optical and spectroscopic principles of plasmonic-mediated surface-enhanced techniques, in particular SERS are presented in this Chapter as a basis to support the research work that follows in this thesis.

#### 2.1 Chemically patterning surfaces for cell-based assays

Advanced microfabrication techniques combined with chemical surface modifications have become widely used for investigations of cell interaction with their environment. There is a vast range of methodologies for patterning chemical and biological functionalities to a surface. Among them, many are based upon generating patterns of biologically active areas that promote protein and cell adhesion, surrounded by a protein resistant background to prevent cell adhesion.<sup>1</sup> Some of the most conventional patterning methods are introduced here, along with recent applications in cellular studies. Cell micropatterning has been greatly explored over the past several years. This includes many different techniques emerging towards patterning combinations of adhesive or inhibitive materials or the direct immobilization of biomolecules. However, most of these techniques are limited to the type of substrate, and to their compatibility with inverted microscopes due to a lack of transparency. This is problematic for visualization and analysis of cells using optical microscopy.<sup>2</sup> In addition, the adhesion promoting molecules or biomolecules present can potentially interfere in the analysis of the cells

while investigating cell interactions using spectroscopic techniques. Furthermore, direct patterning of biomolecules can have critical drawbacks: proteins can denature with time, and serum proteins can damage the pattern fidelity, likely due to protein replacement. Therefore, using a serum-free media would reduce the invasiveness of the investigations and would increase the durability, and stability of the produced patterns yielding better imaging or spectroscopic analysis.<sup>3</sup> In this thesis, the development of a new cell patterning platform is introduced on a glass substrate, keeping it compatible for further integration of plasmonic sensors. Glass is an optimal substrate due to its optical transparency in the visible spectral range, its inherent hydrophilicity, and it is widely used in traditional cell culturing and optical microscopy studies. It also supports healthy cell function, and does not require any additional chemical or biological modifications to promote cell adhesion. Instead, the adhesion proteins essential for cell adhesion originates directly from the serum of the media. As opposed to mechanical positioning, this allows for natural cell adhesion, helping to maintain cell viability.<sup>4</sup>

### 2.1.1 Photolithography

Photolithography, also termed as optical or UV lithography, is perhaps the most conventional microfabrication technique. It generates patterned features that can be precisely controlled down to micron dimensions.<sup>5</sup> This is used to transfer a desired pattern depicted on a mask to a substrate by UV irradiation of a photo-sensitive polymer called a photoresist. The photoresist can be either of “positive” or “negative” type. In positive resist the UV-exposed area of the polymer is soluble in the developing solvent while it is the opposite in negative resist. The photoresist is first spin-coated onto the surface of a flat substrate to create a homogeneous thin film, and is then brought into contact with the mask. In a second step, the accessible areas of the photoresist are exposed by the UV source. These will be removed in a developing solvent to create a

patterned structure of photoresist revealing “windows” that provide access to the underlying substrate for further modifications. The patterned photoresist features can be used as a lift-off mask for patterning chemical species or biomolecules, in order to create amendable cell-repellent and cell-adhesive surfaces. Limitations and drawbacks to using photolithography to pattern cells include the use of organic solvent leading to denaturation of most biomolecules, and the substrates that can be patterned. Furthermore, there is always the concern about inefficiency of lift-off process leading to left-over photoresist residues after cleaning.<sup>6,7</sup>

### 2.1.2 Microcontact printing

Microscale stamps made of silicone elastomer poly(dimethylsiloxane) (PDMS) are used as templates in a group of methods known as soft lithography to create ordered functionalization patterns over large surface areas. The most common technique used is microcontact printing ( $\mu$ CP), for its simplicity, cost effectiveness, flexibility, and the ability to replicate submicron features with high fidelity on numerous types of substrates.<sup>8</sup> PDMS is a liquid prepolymer at room temperature due to its low melting point ( $\sim -50$  °C) and glass transition temperature ( $\sim -120$  °C).<sup>9</sup> The stamp is produced by pouring the silicone rubber over a master mold generated by UV photolithography.<sup>10</sup> After curing, the rubber stamp is peeled off the master, creating a complementary replica of the pattern. Subsequently, the stamp is “inked” with the molecules of interest by adsorption to the PDMS stamp. After being dried, the stamp is placed into contact with the substrate. This transfers the molecular layer directly from the stamp to the substrate.<sup>11</sup> In cell micropatterning applications, the used ink is a material that promotes cell adhesion and extracellular matrix proteins. However, the excavated regions can be backfilled with a passivating layer to prevent cell adhesion.<sup>8</sup> The main drawback of  $\mu$ CP is the transfer efficiency is often less than 100%, with significant variations between experiments. Due

to the physisorption of most molecules stamped to the surface, exchange and degradation processes are likely in the cell culture environment. This results in diminished pattern resolution. Moreover, the biological activity of some biomolecules may be lost during the stamping process.<sup>12,13</sup>

### 2.1.3 Microfluidic patterning

Microfluidic patterning is a soft lithographic technique where an elastomeric stamp is employed. The designed stamp with desired microchannels is pressed into contact with the surface to be patterned. The areas in contact with the stamp are protected from the patterning solution, while fluid is delivered into the channels and transferred to sites that are unprotected by the stamp. This technique offers the easiest approach towards producing multi-molecule patterns in parallel. This gives ones an opportunity to use numerous materials placed in separate channels. As this method is performed in the liquid state, live cells can also be patterned in addition to adhesion components and biomolecules. In the meantime, it also provides a tool to investigate in-vitro dynamic conditions of the experiment.<sup>14,15</sup> The beneficial aspect of conducting the experiment in a liquid state highlights the ability to precisely control the ligand density while the functionality of the biomolecules is preserved. However, there are certain disadvantages. These patterns often lose integrity over time once the stamp is removed, since the pattern geometries are limited to open network structures.<sup>16,17</sup> Also, the solvent that circulates in the channels must be compatible with the chemical nature of the microfluidic pattern.



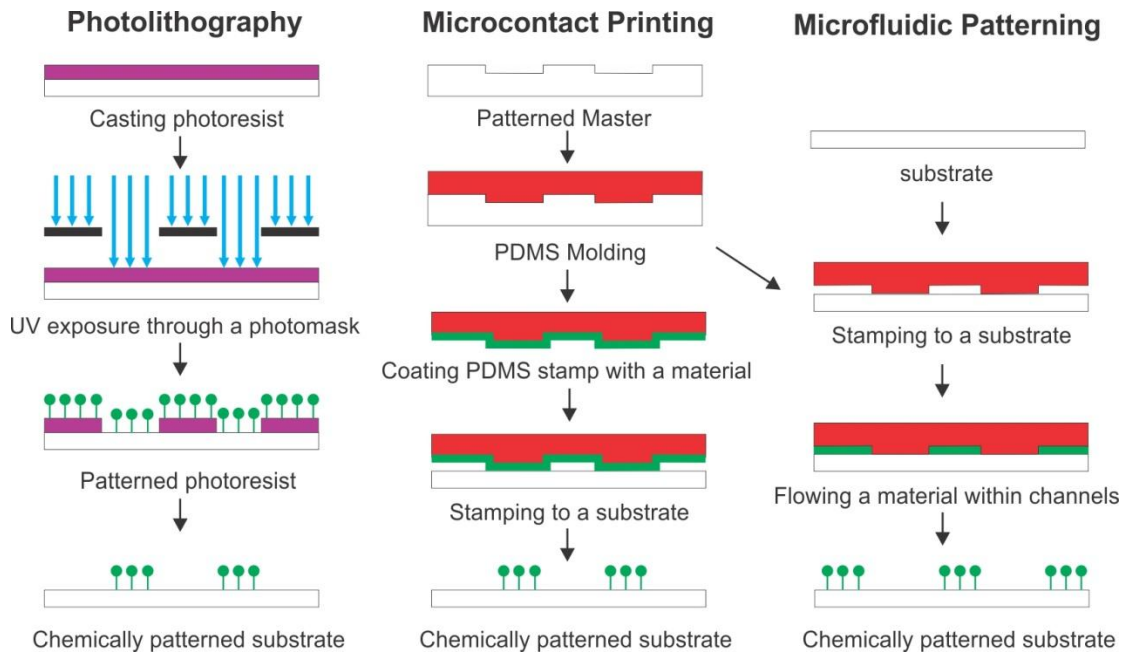


**Figure 2.1 Schematic illustration of three selected surface micropatterning techniques.**

Aside from these three major techniques, there are other patterning methods with quite similarities to usual aforementioned ones, but also with distinct alterations depending on the application of interest. These techniques are introduced as follows.

#### 2.1.4 Stencil patterning

This technique mimics the similar process of microcontact patterning depicted in **Figure 2.1** with slight differences.<sup>18</sup> A stencil is a thin membrane with empty spaces of a specific geometry and size. This acts as a template for the selective modification of the surface to be brought into contact with the surface to be patterned. In stencil patterning, the stencil is attached onto a substrate for direct patterning by deposition, etching or implantation of the substrate through the stencil apertures without any resist.<sup>19</sup> The stencil itself protects

the substrate while the solutions enter the empty spaces to locally modify the surface. The patterning can be performed by the functionalization of different molecules or cell seeding directly to the substrate, without the use of solvents. After plating the cells on the stencil protected regions, the stencil is then manually peeled off, and the cell islands are in the same shape as the stencil. Traditionally, metallic materials were used for the membranes, despite the fact that they produced a loose seal with the substrate. In contrast, elastomeric stencils of PDMS have been introduced, and are far superior as they form seals with many types of surfaces. Aside from the many benefits and simplicity of this method, there are a few disadvantages including the fabrication complexity of high resolution patterns, the difficulty of handling the thin membranes, and the removal of the stencil could detach the cells. In addition, while the stencil is removed, the cells are free to migrate, sacrificing pattern fidelity.<sup>2,20,21</sup> There are two major reasons reported in the literature for using stencil patterning. The first reason is the need for non-contaminated surfaces. Novel nanoscale structures and materials such as nanowires or nanodots deposited on ultra-clean surfaces require non contaminated environment by photoresists and solvents. The second reason is the need for high temperature process such as pulsed laser deposition (PLD) of ferroelectric materials used in cells for mass-storage applications and the variety of substrate materials including plastics, or other flexible materials for biological and chemical systems.<sup>22</sup>

### 2.1.5 Inkjet patterning

Commercial inkjet printers have been modified and combined with computer-aided design software in order to directly print adhesive molecules, proteins, molecules for electronic applications and even cell solutions on surfaces. The printer is equipped with a stage and a micropipette nozzle to dispense liquid in the programmed pattern. The amount of material that is deposited can be varied by changing the number of droplets

printed per spot, and features such as lines, dots, arrays, and gradients have been printed. Also, with the use of a multiple nozzle device, a multifunctional pattern is possible. The spot size and resolution of the patterns is greatly limited by the resolution of the printer, the nozzle diameter, as well as the liquid/solid interfacial tensions. The smallest spot size is still hundreds of microns, so it is only compatible for large arrays of cells. Moreover, when patterning cell suspensions, cells have been observed to die, likely due to dehydration of the drop, as well as damage occurring during the delivery.<sup>23-25</sup>

### 2.1.6 Plasma processes

Plasmas have been utilized for the surface modification of many types of materials and a wide range of applications. The properties of the plasma can be readily guided towards a specific objective simply by altering different conditions such as composition of the feed gas, and the properties of the substrate.<sup>26</sup> Plasma is a gas which consists of a high population of charged particles, supplying a highly ionized gas. This medium includes both positive and negatively charged particles, despite maintaining macroscopic neutrality. Due to the number of charge-carrier particles, the plasma has a high electrical conductivity. Other than ions, the reactive species found in a plasma include neutral and radical molecules, both are which take part in plasma modifications.<sup>27</sup>

There are three major areas where plasmas can be utilized for surface modifications and patterning. The first is the use of the reactive environment to chemically modify the surface of a material. By altering the surface functionalities using plasma bombardment, many different reactions can be performed providing new functional groups such as amino- or hydroxyl- functionalities, which are proficient for immobilizing biomolecules.<sup>28</sup>

A second capability of plasma treatment is to use the species generated in the plasma to remove or etch material off the surface. This is similar to a sputtering mechanism, wherein the species bombarding the surface exchanges momentum with atoms in the surface upon collision. If the energy of the impinging particle is greater than the surface binding energy, an atom will be ejected from the surface.<sup>29</sup> The final mode of plasma modifications is the use of a polymerizable gaseous or vaporizable monomer to deposit material. The plasma supplies sufficient energy to the monomer fragment in order to initiate polymerization, and a polymer thin film is deposited. Based on the properties of the feed gas, either cell-adhesive or cell-repellent functionality can be introduced to the surface.<sup>30,31</sup>

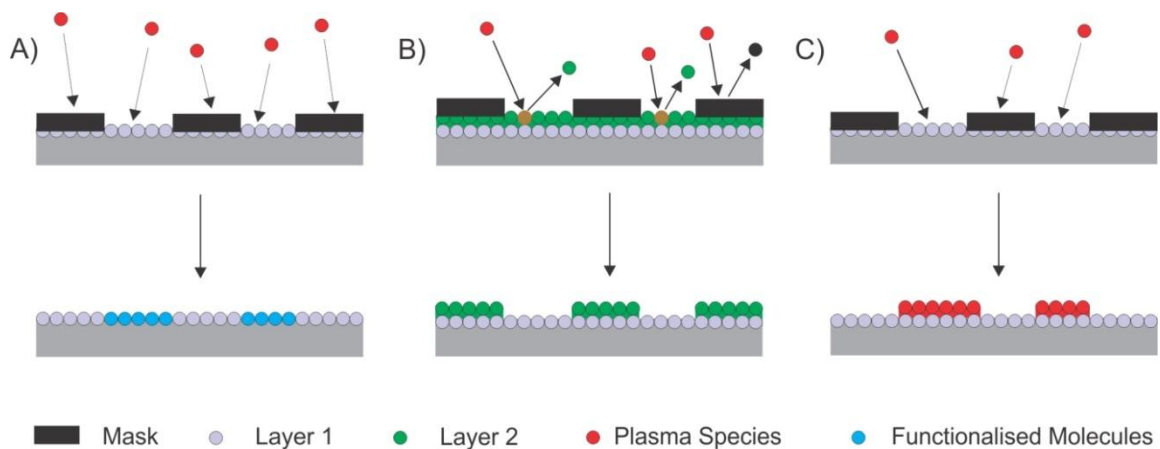


**Figure 2.2 Schematic description of three types of plasma processes. The active species in the plasma are used to: a) chemically modify the surface, b) remove the top layer of the exposed surface, and c) deposit polymerized material on the exposed surface.**

Plasma surface modifications can also be combined with a physical mask in order to pattern the surface. A thin metallic mask with empty regions shaped in the desired feature is placed in contact with the substrate, and then exposed to the plasma. The active species

will therefore only interact with the substrate in areas that are unprotected by the mask.<sup>32</sup> The three aforementioned methods can be used to (i) chemically modify the exposed regions with different functional groups (**Figure 2.2A**) (ii) reveals a bi-layered substrate by removal of the top layer (**Figure 2.2B**), (iii) selective deposition of a new material using plasma polymerization (**Figure 2.2C**).

**Table 2.1 Summary of microfabrication techniques used for cellular patterning**

Technique	Recent Selected Applications
Photolithography	Patterning of 3D-formed polycarbonate films for targeted cell guiding. <sup>34</sup> Cracking-assisted photolithography for mixed-scale patterning and nanofluidic applications. <sup>35</sup>
Microcontact Printing	Protein patterning on hydrogels for application in cardiac differentiation. <sup>36</sup> Tuning cell–surface affinity to direct cell specific responses to patterned proteins. <sup>37</sup>
Microfluidic Patterning	Anisotropic crystalline protein nanolayers for patterned co-cultures of adherent and non-Adherent cells. <sup>38</sup> Differentiation of neuroepithelial stem cells into functional dopaminergic neurons. <sup>39</sup> Rapid quantification of live cell receptors. <sup>40</sup>
Stencil Patterning	Assessment of multidrug resistance on cell co-culture patterns. <sup>41</sup> Control of collective cell migration in epithelial monolayers. <sup>42</sup> Patterning and interrogating neural circuitry. <sup>43</sup>
Inkjet Patterning	Inkjet-printed silk nest arrays for cell hosting. <sup>44</sup> Complex heterogeneous tissue constructs containing multiple cell types. <sup>45</sup>
Plasma Processes	Directed positioning of single and connected transfected and non-transfected cells and neuronal projections using surface patterning by plasma-deposited fluorocarbon (FC) thin films. <sup>46,47</sup> Fibroblast/myoblast co-cultures by selective fibronectin adsorption <sup>32</sup>

As with any of the techniques mentioned, there still are certain limitations to plasma processes. The etch rates of different etchant gases are highly variable, and it can be difficult to produce a highly stable plasma polymer layer. It also requires another step to determine the optimal conditions for each method as compared to the simple dip and rinse process of the other techniques. Finally, close contact with the physical mask is crucial for pattern production, and the lateral and vertical resolution is limited by the mask.<sup>33</sup> A summary of the recent applications in cellular patterning reported for the introduced microfabrication methods are shown in **Table 2.1**.

## 2.2 Principles and theory of surface-enhanced spectroscopies

The design and development of an efficient nanostructure for surface-enhanced Raman spectroscopy (SERS) requires a clear understanding of the principles of spectroscopy, in particular Raman spectroscopy, and also associated plasmonic enhancement processes that yield ultra-sensitive Raman measurements. The optical and spectroscopic principles of SERS and plasmonic structures are thus presented in this chapter as a base of support to the research work that follows in this thesis.

### 2.2.1 Raman spectroscopy

The required energy for vibrational and electronic transitions in a molecule is dependent on the interaction between light and matter. This is depicted in the Jablonski energy diagram shown in **Figure 2.3**. Matter can absorb the impinging light to its surface.

Absorption of infrared (IR) light in the mid-infrared range (4-20  $\mu\text{m}$  wavelength range) excites molecular vibrations within the ground electronic states. UV-visible light (280-700 nm) excites electrons to higher energy levels followed by relaxation through distinct

pathways including non-radiative relaxations and radiative fluorescence and phosphorescence emissions.<sup>48</sup> Light gets scattered by the exposed molecules when the energy of an electronic transition does not match the wavelength of the incident light. Rayleigh scattering is the process when the majority of the scattered photons are elastically scattered with energies equal to the energy of the incoming light. However, one out of  $10^6$ - $10^8$  photons approximately are scattered inelastically with distinct optical frequencies from the incident light.<sup>49,50</sup> This inelastic light scattering occurred by molecular vibrations is called Raman scattering.<sup>49</sup>

Upon Raman scattering, quantized energy states of the scattering molecules interact with the incident light, yielding a scattered photon with either less or more energy relative to the incident photon. These processes are defined as Stokes and anti-Stokes Raman scattering respectively.<sup>49,51</sup> In Stokes Raman scattering, the photons undergo a transition from lower to higher energy level and *vice-versa* for anti-Stokes Raman scattering. Based upon Boltzmann distribution, excited vibrational energy levels are less populated than the ground state. Therefore, anti-Stokes is less intense due to the occurred scattering from a less populated state. These three modes of Raman scattering are shown in **Figure 2.3**. For Raman scattering, (excluding resonance Raman), the scattering process begins from an intermediate state. This is a time-dependent superposition of molecular electronic states called virtual energy level or state. The energies of these states do not match the energy of the present excited electronic levels in the scattering system. In resonance Raman scattering, however, the energy of the incoming source of irradiation matches an existing electronic transition.

The theory of Raman spectroscopy is extended from classical view to fully quantum mechanical approach.<sup>50,52-55</sup> The presented background of Raman in this section is,

however, adjusted to the level of knowledge which is required to understand the work in this thesis.

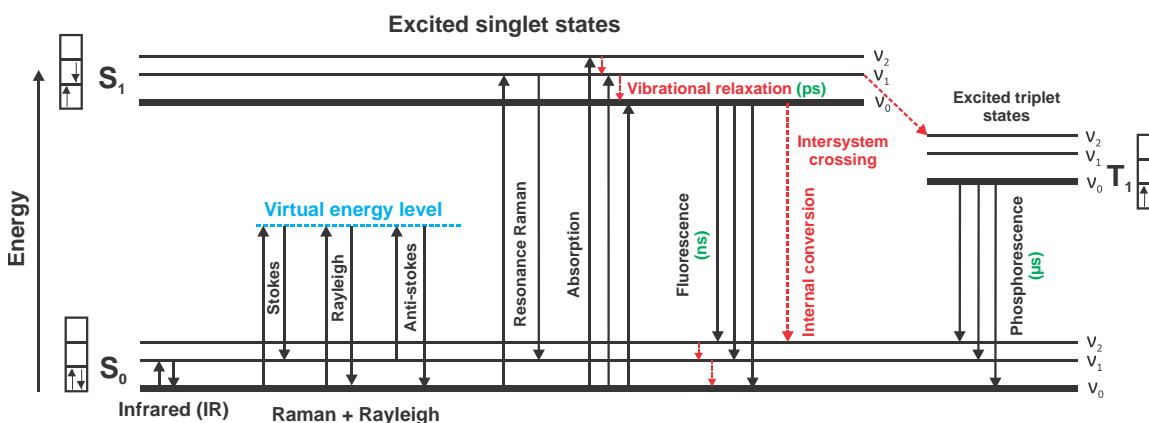


**Figure 2.3 Jablonski Diagram demonstrating the variety of light-matter interactions**

### 2.2.2 Fluorescence spectroscopy

Fluorescence spectroscopy is of great interest due to its vast applications in the field of chemistry, life sciences, photonics, and materials science.<sup>56-59</sup> Fluorescence occurs when a fluorescent capable material (fluorophore) is excited into a higher electronic state by absorbing an incident photon. The excited photon can return to the ground state by radiative relaxation through emission of a photon, which is called fluorescence.

Fluorescence occurs when there is no change of spin multiplicity between the two levels of the transition. The emission usually occurs from the ground vibrational level of the excited electronic state and goes to an excited vibrational state of the ground electronic state. Thus, fluorescence signals occur at longer wavelengths compared to absorption. This is due to the energy loss in the excited state through vibrational relaxation. The relative intensities of the fluorescence signals provide information about structure and environments of the fluorophores. Noteworthy, the absorption is very fast while lifetime of fluorescence is approximately 0.1-100 ns with respect to other processes such as



radiative relaxation from triplet excited state to the singlet ground state so-called phosphorescence, which occurs in a microsecond time scale.<sup>60</sup>

### 2.2.3 Plasmonic resonances in metal

The field of plasmonics is described as the general area that aims at controlling the coupling between an EM wave and the free electrons of a metal. Its application to spectroscopy is numerous and is often referred to as molecular plasmonics and aims at benefitting from the local EM field enhancements that occur in nanostructured metals. To better understand the mechanism at work behind the surface-enhanced techniques, we introduce in the next chapters the underlying principles of a surface plasmon (SP) and localized surface plasmon resonance (LSPR).

#### 2.2.3.1 Plasmon

The interaction of EM radiation with a metallic nanostructure yields the oscillation of the free conduction electrons of the metal out-of-phase relative to the driving electric field of the incident radiation.<sup>61</sup> A plasmon is therefore a collective oscillation of the conduction electrons in a metal in response to an EM disturbance, such as an optical field. A displacement of the free electrons with respect to the positively charged lattice in metal occurs by this oscillation. As a result, at defined optical frequencies, the free electrons can sustain surface and volume charge density oscillations. The free motion of the metal conduction electrons within the bulk of the metal is included in the physical process involved in plasmon resonance. Upon irradiation by a laser with angular frequency of  $\omega$ , the free conduction electrons go through a displacement  $\vec{r}$  ( $\vec{r}(t) = \vec{r}_0 e^{-i\omega t}$ ) that generates a dipole moment  $\vec{\mu}$  through  $\vec{\mu} = e\vec{r}$  where  $e$  and  $\vec{r}_0$  denotes the electron charge and position in absence of an incident EM field, respectively. The generated dipole moment proceeds to a macroscopic  $\vec{p} = n_e \vec{\mu}$  where  $n_e$  is the number of electrons per unit of

volume. For materials with dimensions larger than the wavelength of the incident light ( $d \gg \lambda$ ), these oscillations occur at the plasma frequency ( $\omega_p$ ), as described in (1).

Oscillation of the metal free electrons occur at a certain frequency,  $\omega_p$ , which is termed as plasmon frequency and is defined as:<sup>62</sup>

$$\omega_p = \frac{1}{2\pi} \sqrt{\frac{n_e e^2}{m_e \epsilon_0}} \quad (1)$$

where  $\epsilon_0$  is the permittivity or the dielectric constant of free space and  $m_e$  represents the effective mass of an electron. The complete characterization of the electron oscillation requires solving the equation of motion for electrons under the incident EM field which is beyond the scope of this thesis and has been studied in detail in the literature.<sup>61,63,64</sup>

### 2.2.3.2 Surface Plasmon (SP)

Plasmon takes place in the form of an SP at the interface between a metal surface and a dielectric material such as air or glass.<sup>62</sup> These are light waves that are trapped on the surface because of their interaction with the free electrons of the conductor, usually a metal. Strictly speaking, they should be called surface plasmon polaritons (SPPs) to reflect this hybrid nature. The term "surface plasmon polariton" explains that the wave includes both charge motion in the metal called SP, and EM wave in the air or dielectric, which is termed polariton.<sup>65</sup> Originally, SPs derive from collective oscillations of the electron density at the metal surface. Higher angles of incidence (which implies that the wavevector  $k$  of the incident radiation is nearly parallel to the surface) couple most efficiently as a consequence of excited SP by the oscillating electric field of the incident

light.<sup>62</sup> Plasmonic oscillations at the metal-dielectric interface can significantly enhance the optical near-field in the vicinity of the metal surface. As mentioned, SPP appears as a combination of an EM wave and surface charges as depicted in **Figure 2.4**.

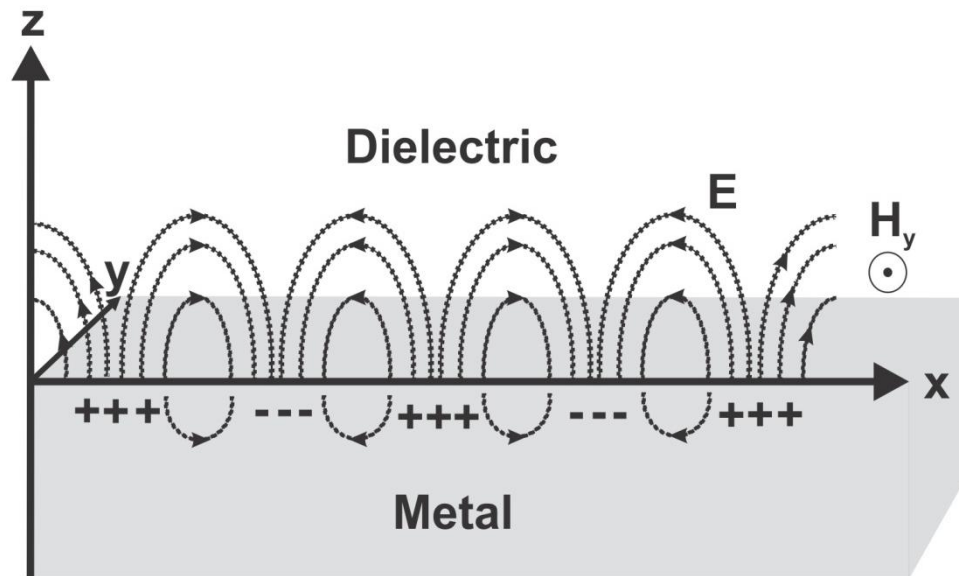


**Figure 2.4 Illustration of propagating surface plasmon at the interface between metal surface and a dielectric.**

The generated EM field at the metal surface consists of transverse magnetic field parallel to the interface. More importantly, the surface charge generation requires the presence of an electric field normal to the surface. As a consequence, there will be an evanescent SP field component perpendicular to the surface. This gets enhanced near the interface and decays rapidly with distance away from it into the two media.<sup>66</sup> For an SP to be detectable at the metal-dielectric interface, the complex dielectric constant of the metal has to have a negative real and a positive imaginary part, which is the case for noble metals.<sup>67,68</sup>

Of different available metals, gold and silver are widely used as their plasmon frequency is in the UV-Visible-Near IR range, making them ideal candidates for applications in

vibrational spectroscopy. The dielectric complex function of gold and silver are shown in **Figure 2.5**. The real and imaginary parts of the dielectric constants are calculated using the Lorentz-Drude model which is commonly used to characterize the motion of the free electrons inside an EM field.<sup>61</sup>

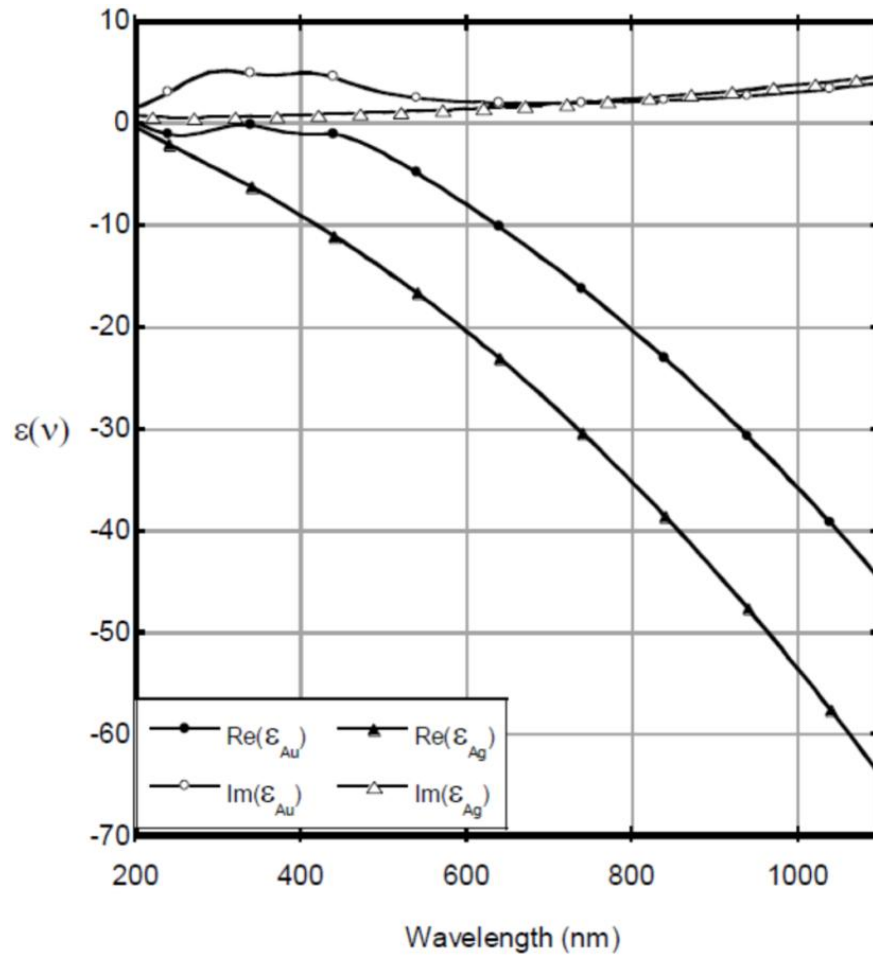


**Figure 2.5** Real and imaginary dielectric functions of gold and silver according to the Lorentz-Drude model.<sup>69</sup>

As shown in **Figure 2.5**, the imaginary part of the dielectric constant for gold and silver are quite similar, however, small differences between these values at each wavelength leads to a significant differences in the plasmonic behavior of the two metals.

### 2.2.3.3 Surface plasmon excitation

SP excitation occurs by impinging photons on the surface of a metal. However, this phenomenon does not simply occur optically. On a smooth metal-air interface, light cannot excite or couple to SPs. This owes to the fact that light momentum is not sufficient to couple to SP. Based upon energy conservation, the dispersion relation of SP on a smooth metal film can be expressed by:

$$|\vec{k}_{sp}| = |\vec{k}_0| \sqrt{\frac{\epsilon_m \epsilon_d}{\epsilon_m + \epsilon_d}} \quad (2)$$

where  $\epsilon_d$  and  $\epsilon_m$  are the dielectric constant and function of dielectric and metal, respectively. The free space wavenumber of the incident excitation photon describes as  $\vec{k}_0 = \frac{\omega}{c}$ . The dispersion curves of light and SP are shown in **Figure 2.6A**.

As shown in **Figure 2.6A**, light cannot excite SPs at the interface between metal and dielectric since SP curve is located outside the accessible region surrounded by the light line. Features such as prisms, gratings, or surface roughness are necessary to increase the momentum of light to excite SPs, since at any specific wavelength, SPs have higher momentum than incident light at the dielectric-metal interface.<sup>66,70</sup> In the case of an array of periodic holes in a metal film, such as a two-dimensional grating in a metal film, the grating structure provides an increase in light momentum, which results in coupling of light to SP. When a plane wave impinges on a grating structure with a square lattice arrangement, the dispersion relation between light and SP on a metallic grating structure is expressed by:

$$\vec{k}_{sp} = \vec{k}_0 \sin \theta \pm i\vec{u}_x \pm j\vec{u}_y \quad (3)$$

where  $\vec{k}_0 \sin \theta$  is the in-plane component of the wave vector of the incident light,  $k_0 = \frac{\omega}{c}$ .<sup>66,71</sup> The reciprocal lattice wave vectors  $\vec{u}_x$  and  $\vec{u}_y$  describe a square lattice when  $|\vec{u}_x| = |\vec{u}_y| = \frac{2\pi}{p}$ , where  $p$  is the spacing between adjacent nanoholes, and  $i$  and  $j$  are integers expressing the scattering mode indices (some examples of  $i$  and  $j$  are illustrated in **Figure 2.7**). Inserting equation (2) into equation (3) results in the dispersion relation between light and SP, which is formulated as:

$$|\vec{k}_{sp}| = \left[ \left( \frac{2\pi}{\lambda} \sin(\theta) + i \frac{2\pi}{p} \right)^2 + \left( j \frac{2\pi}{p} \right)^2 \right]^{1/2} = |\vec{k}_0| \sqrt{\frac{\epsilon_m \epsilon_d}{\epsilon_m + \epsilon_d}} \quad (4)$$

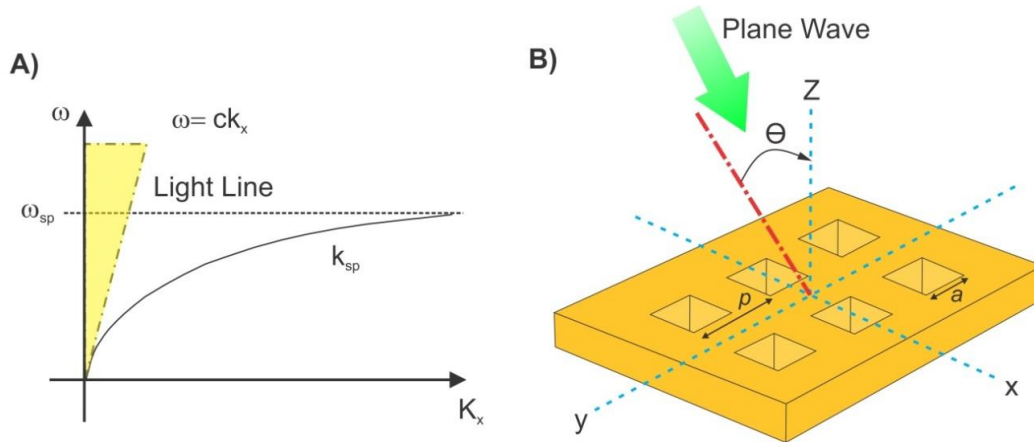


**Figure 2.6 (A) Dispersion curves of SP and light line ( $\omega=ck_x$ ),  $\omega_{sp}$  is a SP frequency. (B) Two-dimensional grating of a square lattice holes: ( $p$ ) is the spacing between adjacent holes and ( $a$ ) is the width of holes.**

### 2.2.3.4 Extraordinary optical transmission of sub-wavelength hole arrays

An array of periodic sub-wavelength holes fabricated in an optically thick metal film results in an extraordinary optical transmission (EOT) phenomena described by Thomas W. Ebbesen in 1988.<sup>71</sup> His observation was that light was transmitted by sub-wavelength structures significantly more than what it should have been considering solely the diffraction limit of light. This unique optical property surpasses the diffraction limit of light owing to the excitation of SP waves occur at the metal-dielectric interface. This excitation occurs because of momentum matching between the SP and the light as a consequence of the periodic arrangement of the sub-wavelength holes.<sup>71</sup> As a result, the coupling of the light to the SP and evanescent transmission occurs through the sub-wavelength hole array. This ends up to radiation of the decoupled light from SP to free space. For a normally incident plane wave on an array of periodic sub-wavelength holes or a grating with square lattice arrangement, the wavelength at the SP excitation modes is expressed by:

$$\lambda_{\max} \cong \frac{p}{\sqrt{i^2+j^2}} \sqrt{\frac{\epsilon_m \epsilon_d}{\epsilon_m + \epsilon_d}} \quad (5)$$

This equation can then be used to estimate the EOT positions of sub-wavelength hole arrays for various SP excitation modes (i ,j) when incident light is normal to the surface of hole arrays.<sup>71</sup> Noteworthy, the various SP excitation modes are mainly dependent on the direction of the light wave vector ( $K_x$ ). For instance, as shown in **Figure 2.7**, when the wave vector of the light ( $K_x$ ) is along the x-axis, various (i, j) SP excitation modes related to metal/air or metal/substrate interfaces can be described. The (+1,0), (-1,0), (0,±1), (+1,1), and (-1,1) are different grating modes, resulting in a variety of SP excitation modes from metal/air or metal/substrate sides by the light as shown in **Figure**

**2.7.** Although, there are other grating modes such as  $(+2,0)$  and  $(-2,0)$  which are not illustrated in **Figure 2.7**. In this example, the  $(\pm 1,0)$  SP excitation modes are parallel to the wave vector of the light ( $K_x$ ) while the  $(0,\pm 1)$  SP excitation modes are perpendicular to the  $K_x$ . However, when the light is normal to the surface of the sub-wavelength hole array, the  $(\pm 1,0)$  and  $(0,\pm 1)$  SP excitation modes lead to a spectral overlap in the optical transmission spectra of the structure and a single resonance called  $(1,0)$  EOT peak. This is similar for  $(+1,1)$ , and  $(-1,1)$  when the light is normal to the surface of the sub-wavelength hole array.

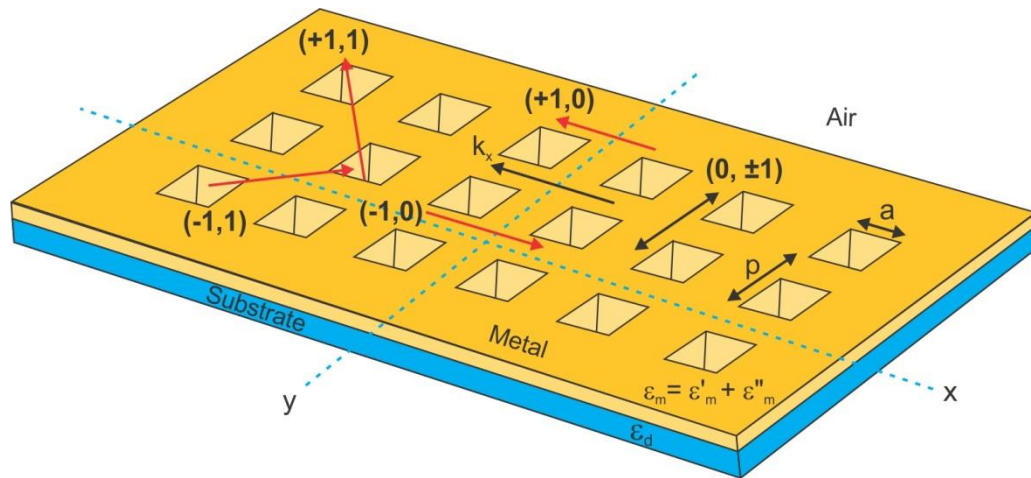


**Figure 2.7** A 2D sub-wavelength hole array in a metal film on a substrate in a square lattice arrangement.  $p$  is the spacing between two adjacent holes,  $a$  is a width of each hole,  $K_x$  wave vector of the light is along the x-axis, and  $(+1,0)$ ,  $(-1,0)$ ,  $(0,\pm 1)$ ,  $(+1,1)$ , and  $(-1,1)$  are various  $(i, j)$  grating modes.

Similar to the calculation of EOT positions, a transmission minimum (Wood's anomaly) happens before each EOT at a shorter wavelength. The transmission minimum is caused by the diffraction of light by the grating and its propagation in the dielectric. The diffracted wave becomes tangent to the grating and propagates within the dielectric when



the transmission minimum occurs. As a consequence, the diffracted wave matches the grating periodicity:

$$K_{\text{diff}} = \frac{\omega}{c} \sqrt{\varepsilon_d} = i \vec{u}_x \pm j \vec{u}_y \quad (6)$$

where  $\varepsilon_d$  is the dielectric constant of propagation medium. The position of the transmission minimum for a sub-wavelength hole array is expressed by

$$\lambda_{\text{min}} = \frac{p}{\sqrt{i^2 + j^2}} (\varepsilon_d)^{1/2} \quad (7)$$

The EOT or resonance properties of sub-wavelength hole arrays can be characterized by the resonance position, resonance transmission efficiency, resonance steepness, resonance bandwidth, and enhanced electric field at the edges of sub-wavelength holes at the resonance wavelengths. All these properties of a sub-wavelength hole array play a key role in the efficiency of its applications. However, resonance properties depend greatly on composition of the metal and dielectric materials, sub-wavelength hole shapes, and different geometrical arrangements of sub-wavelength holes. Many studies have reported the effect of the geometrical parameters of sub-wavelength hole arrays in various metal films by means of simulation, experiments, and theoretical calculation.<sup>72-74</sup> The equations developed above are of great importance to understand the device described in Chapter 7.

### 2.2.3.5 Localized surface plasmon resonance (LSPR)

LSPR gets excited when an SP is confined to a nanostructure with dimensions comparable to the wavelength of the light.<sup>62</sup> In LSPR, incident light promotes the free electrons of the metal nanostructure to oscillate collectively with respect to the incident electric field upon which they experience a change in their momentum. The collective oscillations create

charge accumulation at the surface. In addition, when these oscillations are coupled between neighbouring nanostructures, the electric field is locally enhanced inside the interparticle gaps. An example of LSPR generated within the gaps between gold nanopyramids in hexagonal arrays is illustrated in **Figure 2.8**.<sup>75</sup>

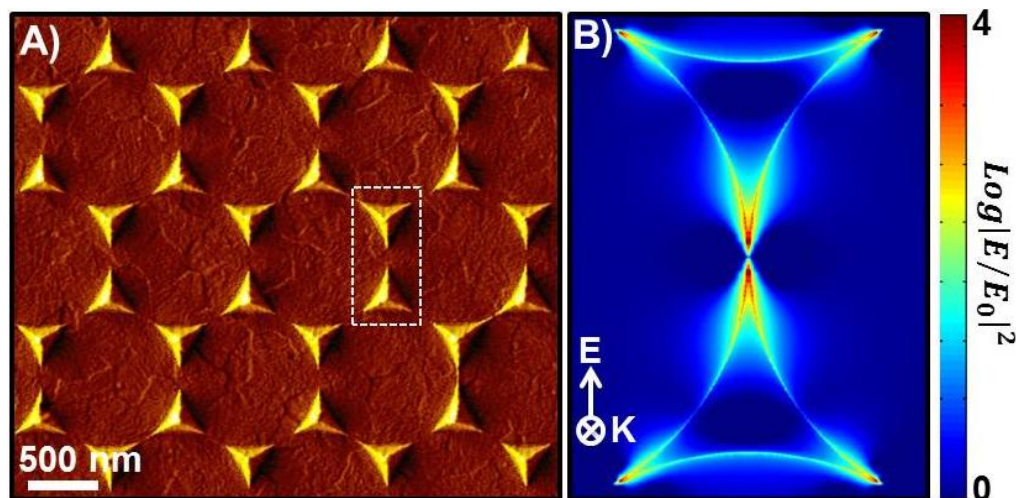


**Figure 2.8** Illustration of localized surface plasmon in metal nanostructures (A) False-colored SEM image of tetrahedral gold nanopyramids fabricated by nanosphere lithography over an Indium Tin Oxide (ITO) surface (B) finite-difference time-domain (FDTD) simulation of a single hexagonal array showing the confinement of the electric field at the surface of a bowtie and within the gaps between the neighbouring nanopillars. The image in part A is adapted from reference 53 with permission from American Chemical Society publishing group.

There are two critical parameters related to LSPR that should be taken into account in the case of metallic nanostructures, with a particle size comparable to the incident EM wavelength of light ( $d < \lambda$ ). The first parameter arises from the fact that LSPR is sensitive to the dielectric environment and the complex permittivity of the metal, similar to SP.<sup>68</sup>

In the meantime, the EM field can penetrate the nanoparticle. As a result, a shift occurs in the metallic electron cloud with respect to the center of the nanostructure generating an oscillator, as illustrated in **Figure 2.9**.

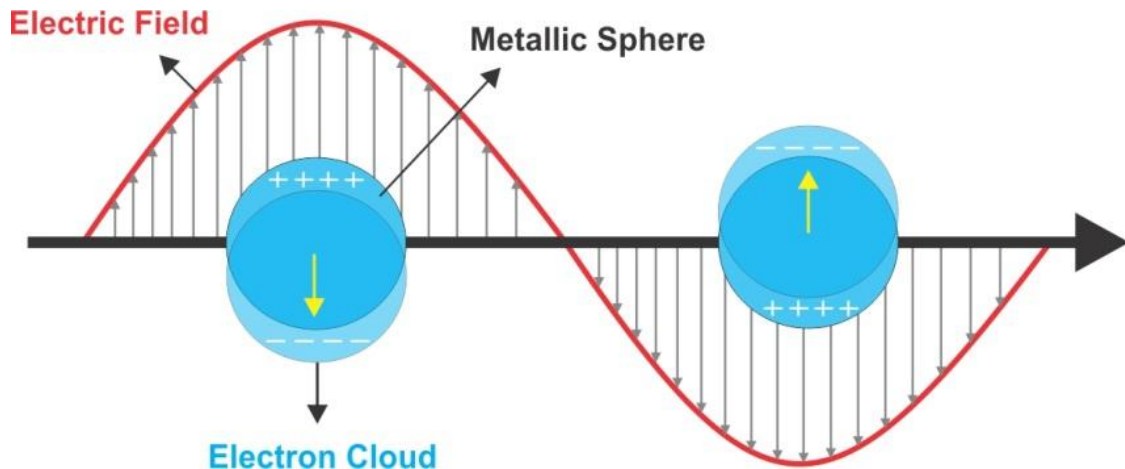


**Figure 2.9** Localized surface plasmon resonance (LSPR) model for metallic nanosphere.

This leads to an LSPR frequency that is typically found in the Visible-NIR range in noble metals.<sup>62,68,76</sup> The second effect of LSPR refers to a change in amplitude of the EM field. This is greatly enhanced by several orders of magnitude at nanoscale regions on the surface, known as “hot spots.” These regions present an evanescent nature, as the intensity of the field rapidly decays with distance.<sup>62,76</sup> Mie’s analytical solution to Maxwell’s equations in the scattering and absorption of light by spherical particles is usually utilized for the characterization of LSPR.<sup>77</sup>

According to the Mie theory, if the diameter of the nanoparticles are considerably smaller than incident EM wavelength of light ( $d \ll \lambda$ ), total scattering ( $\sigma_{\text{sca}}$ ), extinction ( $\sigma_{\text{ext}}$ ), and absorption cross-sections ( $\sigma_{\text{abs}}$ ) of a nanosphere are defined as:<sup>62,63,68,78</sup>

$$\sigma_{\text{ext}} = \frac{18\pi\epsilon_d^{3/2}V}{\lambda^4} \times \frac{\text{Im}(\epsilon_m)}{[\text{Re}(\epsilon_m)\chi\epsilon_d]^2 + [\text{Im}(\epsilon_m)]^2} \quad (8)$$

$$\sigma_{\text{ext}} = \frac{32\pi^4\epsilon_d^2V^2}{\lambda^4} \times \frac{[\text{Re}(\epsilon_m) - \epsilon_d]^2 + [\text{Im}(\epsilon_m)]^2}{[\text{Re}(\epsilon_m)\chi\epsilon_d]^2 + [\text{Im}(\epsilon_m)]^2} \quad (9)$$

$$\sigma_{\text{abs}} = \sigma_{\text{ext}} - \sigma_{\text{sca}} \quad (10)$$

According to the equations (8-10), optical properties of metallic nanoparticles are described as a function of the dielectric constants of the metal and the environment, as well as the geometrical parameters including the shape factor ( $\chi$ ) and volume ( $V$ ) of the nanoparticles. These equations are typically used for estimating the optical response of systems to LSPR. In addition, LSPR can be accumulatively enhanced when the interparticle distances between the nanoparticles are small enough to allow for coupling of the neighboring hot spots.<sup>78,79</sup>

In summary, a fundamental understanding of plasmon and in particular localized surface plasmon (LSP) is essential for the fabrication of active SERS platforms in order to improve the sensitivity of Raman scattering. Any controlled way to confine a plasmon with defined features including frequency, amplitude and phase of the field at the

extremity of the sharp nanostructures to generate nanoantennas is of great benefit specifically in the field of highly sensitive spectroscopic techniques.

## 2.2.4 Surface-enhanced Raman spectroscopy (SERS)

More than forty years ago, Fleischmann *et. al* observed an enhancement of the Raman signal (around  $10^5$  times) of pyridine adsorbed onto the surface of a roughened silver electrode.<sup>80</sup> This enhancement was attributed to the increase in the surface area of the roughened electrode. It was not until 1977, when the groups of both Van Duyne and Creighton performed similar experiments to that of Fleischmann, that the nature of the enhancement was determined.<sup>81,82</sup> However, three years later, both groups found that the enhancement of the Raman signal could not occur with just an increase in surface area, and SERS was subsequently proposed.<sup>78</sup> In doing so, the field of surface-enhanced spectroscopies, such as surface-enhanced Raman (SERS), surface-enhanced fluorescence (SEF), and surface-enhanced infrared absorption (SEIRA) were born. A substantial interest has emerged in SERS subsequent to the unraveling of the possibility of using SERS for single molecule detection (SMD), reported in 1990s.<sup>83-85</sup> This has reinforced SERS as a powerful analytical tool and a broad active research field due in part to the development of nanofabrication methods.

### 2.2.4.1 SERS enhancement mechanisms

The essential localized enhancement of electric field to enhance the weak inelastic scatterings in Raman and increasing the sensitivity of this spectroscopy, originates from different sources. This includes the power of the incident light, enhancement of the Raman scattering, and also the modification of the scattering process. The first two mentioned factors are known to have an EM mechanism,<sup>86-97</sup> while the third is usually categorized as a chemical mechanism.<sup>96-99</sup> These mechanisms, involved in SERS, are

very well described in the literature by Moskovits and other researchers and will be briefly reviewed in the following sections.<sup>62,78,86,91,92,100</sup>

#### 2.2.4.1.1 Electromagnetic Mechanism

The EM mechanism arises from the plasmon resonance generated on a metallic nanostructure upon illumination by a light source, for example, a laser.<sup>101,102</sup> This mechanism has the greatest contribution with enhancement factors (EFs) of 4 to 8 orders of magnitude.<sup>100</sup> The sharp metallic plasmonic nanostructures act as optical nanoantennas that convert freely propagating optical radiation into localized energy and vice versa.<sup>103</sup> When a sample or a molecule of interest is located in the vicinity of the nanoantenna, both incident light and Raman scattering are enhanced the same way. As a result, both the incident and the Raman scattering are both enhanced equally yielding a Raman intensity enhancement that scales with the fourth power of the local electric field. The optimum enhancement occurs if both the incident and the scattered light are in resonance with the antenna. At larger distances from the antenna, the resonance is damped.<sup>104</sup> The enhancement of the electric field in SERS is therefore, a combination of three different effects. These include the lightning rod effect, the excitation of LSP, and the antenna resonance effect.

The dielectric function changes from metal to metal as outlined in **Figure 2.5**. As such, the intensity of the EM field from LSPR is highly sensitive to a change in the wavelength of light ( $E_{\text{LSPR}}(\lambda)$ ). Therefore, once a molecule is adsorbed onto the surface of a metallic nanostructure and is irradiated with an excitation source, the intensity of the incident field ( $E_0(\lambda)^2$ ) is enhanced with respect to ( $E_{\text{LSPR}}(\lambda)$ ), as well as the Raman scattering light ( $E_{\text{LSPR}}(\lambda \pm \lambda_R)$ ), as described below:

$$EF_{EM}(\lambda) = \frac{|E_{LSPR}(\lambda)|^2 |E_{LSPR}(\lambda \pm \lambda_R)|^2}{|E_0(\lambda)|^4} \quad (11)$$

When both the incident beam and the scattered Raman signals are near that of the LSPR resonance wavelength ( $\lambda_{LSPR}$ ), the maximum enhancement due to the EM mechanism will occur.<sup>68,105</sup>

The lightning rod effect is influenced by the shape of the nanostructure or the nanoantenna. The very sharp apex or edges of the metallic nanostructure called nanoantenna, generates highly localized surface charge densities that enhance the electric field locally at the sharp end of the metallic nanoantenna. This can be attributed to the gap size of the two facing nanoantennas such as facing bow-tie assemblies of nanotriangles or nanoparticles in close proximity. By decreasing the gaps between nanoantennas, this effect can be enhanced. The incident light drives the metal free electrons along the polarization direction. Because the charge density is zero inside a metal at any instant of time, charges accumulate on the surface of the metal.<sup>106</sup>

As mentioned earlier in section 2.2.3.2, the SP is efficiently excited if the wavelength of the laser matches the plasmon resonance(s) of the metal. Such plasmon resonances depend on the material property and the shape of the nanoantennas. Sharper objects with a higher aspect ratio generate stronger confined fields.<sup>107,108</sup> Excitation of the antenna resonance depends on the wavelength of the incident light. In this case, a highly localized and enhanced electric field is observed at sharp edges of the nanostructures, so called nanoantennas.<sup>109</sup> The polarization of the incident light with respect to the shape of the nanostructure is also playing a pivotal role.<sup>75,110</sup> A more detailed description of the EF and the experimental method to estimate the values in complex nanostructures are described in Chapter 6 and 7.

Despite the fact that the EM mechanism dominates the enhancement mechanism at work for SERS, there are some observations that cannot be explained by this theory, suggesting there are other factors. This includes (i) the difference observed for the SERS spectrum of a molecule and its normal Raman spectrum, (ii) the inconsistent EF obtained when different molecules have been studied such as non-resonant and resonant molecules under the same experimental conditions, and finally (iii) the discrimination in the enhancement of the different bands in a SERS spectrum. Such observations can be better addressed by the chemical mechanism as explained in the following section.<sup>111,112</sup>

#### 2.2.4.1.2 Chemical Mechanism

The presence of the chemical mechanism was evidenced when enhancement of the Raman scattering was observed even without using metallic plasmonic nanostructures in the plasmonic region of interest or using flat metal surfaces.<sup>113,114</sup> Under the described conditions, no EM enhancement is expected to be observed. Therefore, a different mechanism has to be involved for the enhancement of the Raman scattering. These mechanisms typically induce 1-4 orders of magnitude of enhancement and are categorized under chemical mechanisms. Three different sub-mechanisms involved in chemical mechanism are depicted in **Figure 2.10 A-C** along with EM mechanism for the purpose of comparison.<sup>115</sup>

Studies on non-EM enhancement mechanisms suggested that the resonance between the metal nanostructure and the incident laser induces a charge transfer between the metallic nanostructure and the adsorbed molecules.<sup>97,116</sup> For charge transfer to happen, the metal and the probe molecule must be in close enough proximity for the corresponding wave functions to overlap. However, the exact mechanism at work for charge transfer is not fully understood.



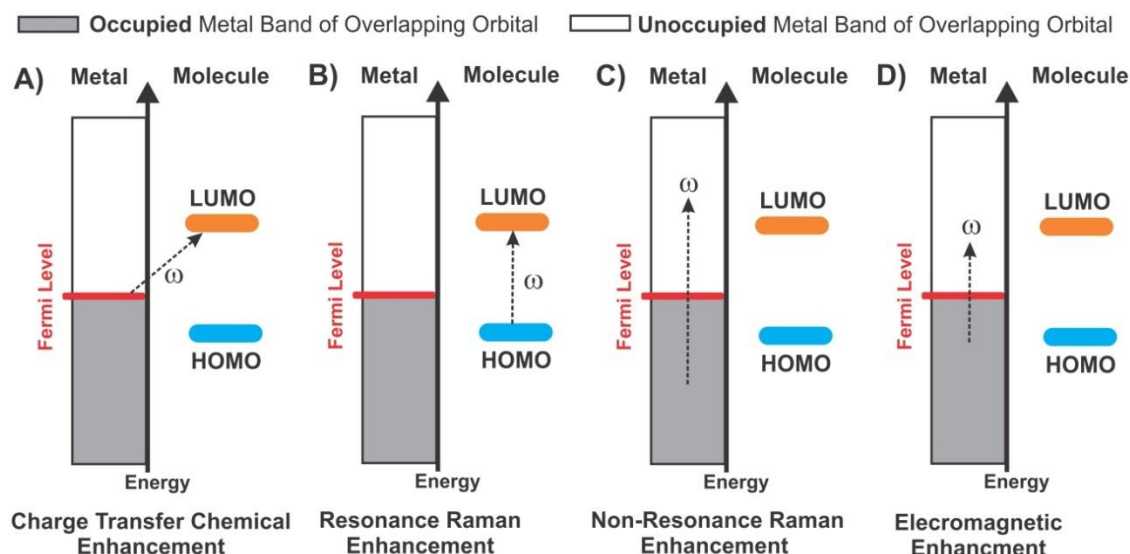


**Figure 2.10 Illustration of different enhancement mechanism (a)-(c) demonstrate three types of chemical mechanism while (d) shows electromagnetic mechanism.<sup>120</sup>**

A mechanism was proposed by Pettinger in 1986.<sup>117</sup> He suggested that the plasmon resonances in the metal can be excited by radiation through which an electron-hole pair is generated. As a result, the energy of resonant metal is transferred to the molecule to promote it to an excited state. The energy will then be sent back inelastically by the molecule to the metal after its relaxation to the ground state. At this stage, the excited SP emits a photon. The HOMO and LUMO energy states of the metal and the adsorbent should be taken into account to explain the charge transfer. Initially, the energy level between the HOMO and LUMO of the probe molecule is too high to be reached upon illumination by laser. However, the HOMO and LUMO of the metal are at the same Fermi energy level. It is proposed in the literature that a sample-metal complex is formed when the sample is in direct contact with the metal surface.<sup>118,119</sup> This formation expedites a charge transfer from the HOMO of the molecule to the LUMO of metal and

from there to the LUMO in the molecule eventually as depicted in **Figure 2.10A**. By this means, the Raman scattering cross-section is enhanced through decreasing the energy gaps between the bands and enabling an electronic transition of the molecule.

Resonance Raman is another source for chemical enhancement in addition to the charge transfer effect.<sup>115,121</sup> Resonance Raman is very similar to the molecular resonance mechanism. The only difference is that the presence of a metal tip induces the resonance by altering the excitation energy of the molecule and consequently through the nanoantennas of the nanostructure altering the resonance conditions. Therefore, although the resonance Raman is not a surface effect, it should be considered due to the impact of the metallic nanoantennas on resonance Raman enhancement.<sup>100</sup> Resonance phenomenon could generate 3-6 orders of magnitude of the total enhancement, when the incident Raman beam matches or is close to an allowed electronic transition of the studied molecules.<sup>100</sup> Herein, the presence of metallic nanostructure alters the excitation energies of the molecule, leading to the formation of surface-enhanced resonance Raman spectroscopy (SERRS).<sup>100,115,118</sup>

Non-resonant chemical mechanism is the third source for chemical enhancement providing 2 orders of magnitude or less contribution to total enhancement. Non-resonant chemical mechanism is due to interaction between the ground state of the probe molecules and the metal upon placing the sample in the vicinity of a noble metal. Quantum mechanical calculations suggest that this phenomenon is greatly dependent to size, charge, binding site and the molecule's orientation with respect to the metal cluster and also the separation between the two.<sup>115,122,123</sup> Depending on the orientation of the molecule with respect to the nanoantennas on the nanostructure, certain Raman modes could or could not be excited while charge transfer or resonance conditions are absent.

The charge transfer effect is typically much more pronounced in SERS measurements as compared to tip-enhanced Raman spectroscopy (TERS), another Raman-based advanced optical and spectroscopic technique with nanoscale spatial resolution.<sup>124</sup> For instance, the charge transfer has only been observed in previously published TERS study of adenine nucleobases and has not been detected for other nucleobases such as cytosine and thymine.<sup>125-128</sup> Chemical enhancement is excluded from the work presented in this thesis because of two main reasons: (i) First, chemical enhancement is very dependent on the sample and (ii) the molecules used in this thesis are all non-resonant molecules. It is worthwhile to mention that the chemical and EM mechanisms can both be present to generate further enhancement of the Raman scattering. Both effects are typically used in single molecule Raman spectroscopy. Molecules such as dyes (Rhodamine, malachite green, methylene blue) are often used to further increase the Raman signal under resonance conditions. The contribution of each mechanism varies depending on the electronic transitions in the molecular systems of interest for a selected irradiation wavelength.<sup>100</sup>

## 2.3 Summary

The underlying principles of micropatterning and SERS were reviewed in this Chapter. First, distinct major micropatterning methods including photolithography, microcontact printing, and microfluidic patterning along with other widely-used patterning approaches of stencil, inject and plasma-assisted patterning were discussed thoroughly. Second, Raman scattering was introduced as the inelastic scattering of light caused by laser induced molecular vibrations in a medium. The low cross-section of this inelastic scattering would be improved within plasmonic fields generated at the surface of a noble metal upon illumination by a proper laser wavelength. The phenomenon includes the basis for surface-enhanced Raman spectroscopy providing a highly sensitive analytical method

to detect very low concentrations of a wide range of samples. It was further discussed that the dielectric function of noble metals and also the dimension and size of the metallic nanostructures play substantial roles in excitation of their plasmon resonances. The enhancement of the Raman scattering in SERS was analyzed on the basis of two mechanisms termed as the EM enhancement and chemical enhancement. The former is believed to play a dominant role in the accessible enhancement in SERS while the latter is more pronounced in surface-enhanced method where the molecules come to direct contact with the metal surface. Keys to obtaining ultra-sensitive SERS measurements are the development of novel plasmonic platforms. The principles of two major techniques used in this thesis to fabricate such developed plasmonic platforms along with SERS experimental setup has been discussed in detail in the following chapter.

## 2.4 References

- (1) Falconnet, D.; Csucs, G.; Michelle Grandin, H.; Textor, M.; *Biomaterials*, **(2006)**, *27*, 3044.
- (2) Frimat, J.-P.; Menne, H.; Michels, A.; Kittel, S.; Kettler, R.; Borgmann, S.; Franzke, J.; West, J.; *Anal. Bioanal. Chem.*, **(2009)**, *395*, 601.
- (3) Folch, A.; Toner, M.; *Biotechnology Progress*, **(1998)**, *14*, 388.
- (4) Asphahani, F.; Thein, M.; Veiseh, O.; Edmondson, D.; Kosai, R.; Veiseh, M.; Xu, J.; Zhang, M.; *Biosens. Bioelectron.*, **(2008)**, *23*, 1307.
- (5) Madou, M. J. in *Fundamentals of microfabrication: the science of miniaturization*; 2nd ed.; CRC Press LLC, 2002.
- (6) Healy, K. E.; Thomas, C. H.; Rezanian, A.; Kim, J. E.; McKeown, P. J.; Lom, B.; Hockberger, P. E.; *Biomaterials*, **(1996)**, *17*, 195.
- (7) Lee, J. Y.; Shah, S. S.; Zimmer, C. C.; Liu, G.-y.; Revzin, A.; *Langmuir*, **(2008)**, *24*, 2232.

- (8) Kane, R. S.; Takayama, S.; Ostuni, E.; Ingber, D. E.; Whitesides, G. M.; *Biomaterials*, **(1999)**, *20*, 2363.
- (9) Clarson; S. J.; Semlyen, J. A., Siloxane polymers. Prentice Hall: 1993.
- (10) Ruiz, S. A.; Chen, C. S.; *Soft Matter* , **(2007)**, *3*, 1.
- (11) Mrksich, M.; Whitesides, G. M.; *Trends Biotechnol.*, **(1995)**, *13*, 228.
- (12) Graber, D. J.; Zieziulewicz, T. J.; Lawrence, D. A.; Shain, W.; Turner, J. N.; *Langmuir*, **(2003)**, *19*, 5431.
- (13) Nelson, C. M.; Raghavan, S.; Tan, J. L.; Chen, C. S.; *Langmuir*, **(2003)**, *19*, 1493.
- (14) Booth, R.; Kim, H.; *Ann. Biomed. Eng.*, **(2014)**, *42*, 2379.
- (15) Hegde, M.; Jindal, R.; Bhushan, A.; Bale, S. S.; McCarty, W. J.; Golberg, I.; Usta, O. B.; Yarmush, M. L.; *Lab Chip*, **(2014)**, *14*, 2033.
- (16) Tan, W.; Desai, T. A.; *Tissue Eng.*, **(2003)**, *9*, 255.
- (17) Delamarche, E.; Bernard, A.; Schmid, H.; Bietsch, A.; Michel, B.; Biebuyck, H.; *J. Am. Chem. Soc.*, **(1998)**, *120*, 500.
- (18) Nakanishi, J.; Takarada, T.; Yamaguchi, K.; Maeda, M.; *Anal. Sci.*, **(2008)**, *24*, 67.
- (19) Vazquez-Mena, O.; Villanueva, G.; Savu, V.; Sidler, K.; van den Boogaart, M. A. F.; Brugger, J.; *Nano Lett.*, **(2008)**, *8*, 3675.
- (20) Folch, A.; Jo, B.-H.; Hurtado, O.; Beebe, D. J.; Toner, M.; *J. Biomed. Mater. Res.* , **(2000)**, *52*, 346.
- (21) Veiseh, M.; Wickes, B. T.; Castner, D. G.; Zhang, M.; *Biomaterials*, **(2004)**, *25*, 3315.
- (22) Shin, H.-J.; Choi, J. H.; Yang, H. J.; Park, Y. D.; Kuk, Y.; Kang, C.-J.; *Appl. Phys. Lett.*, **(2005)**, *87*, 113114.
- (23) Roth, E. A.; Xu, T.; Das, M.; Gregory, C.; Hickman, J. J.; Boland, T.; *Biomaterials*, **(2004)**, *25*, 3707.
- (24) Xu, T.; Jin, J.; Gregory, C.; Hickman, J. J.; Boland, T.; *Biomaterials*, **(2005)**, *26*, 93.

- (25) Yamazoe, H.; Tanabe, T.; *J. Biomed. Mater. Res. A*, **(2009)**, 91A, 1202.
- (26) Ohl, A.; Schröder, K.; *Surf. Coat. Tech.*, **(1999)**, 116–119, 820.
- (27) Gurnett, D. A.; Bhattacharjee, A. *Introduction to plasma physics: with space and laboratory applications*; Cambridge University Press, 2005.
- (28) Lhoest, J. B.; Detrait, E.; Dewez, J. L.; Van Den Bosch De Aguilar, P.; Bertrand, P.; *J. Biomater. Sci. Polym. Edn.*, **(1996)**, 7, 1039.
- (29) Flounders, A. W.; Brandon, D. L.; Bates, A. H.; *Biosens. Bioelectron.*, **(1997)**, 12, 447.
- (30) Goessl, A.; Garrison, M. D.; Lhoest, J.-B.; Hoffman, A. S.; *J. Biomat. Sci.-Polym. E.*, **(2001)**, 12, 721.
- (31) Siow, K. S.; Britcher, L.; Kumar, S.; Griesser, H. J.; *Plasma. Process. Polym.*, **(2006)**, 3, 392.
- (32) Tourovskaia, A.; Barber, T.; Wickes, B. T.; Hirdes, D.; Grin, B.; Castner, D. G.; Healy, K. E.; Folch, A.; *Langmuir*, **(2003)**, 19, 4754.
- (33) Sardella, E.; Favia, P.; Gristina, R.; Nardulli, M.; d'Agostino, R.; *Plasma Process. Polym.*, **(2006)**, 3, 456.
- (34) Hirschbiel, A. F.; Geyer, S.; Yameen, B.; Welle, A.; Nikolov, P.; Giselbrecht, S.; Scholpp, S.; Delaittre, G.; Barner-Kowollik, C.; *Adv. Mater.*, **(2015)**, 27, 2621.
- (35) Kim, M.; Ha, D.; Kim, T.; *Nat. Commun.*, **(2015)**, 6.
- (36) Castano, A. G.; Hortiguela, V.; Lagunas, A.; Cortina, C.; Montserrat, N.; Samitier, J.; Martinez, E.; *RSC Adv.*, **(2014)**, 4, 29120.
- (37) Ricoult, S. G.; Thompson-Steckel, G.; Correia, J. P.; Kennedy, T. E.; Juncker, D.; *Biomaterials*, **(2014)**, 35, 727.
- (38) Rothbauer, M.; Ertl, P.; Theiler, B. A.; Schlager, M.; Sleytr, U. B.; Küpcü, S.; *Adv. Mater. Interf.*, **(2015)**, 2, n/a.

- (39) Moreno, E. L.; Hachi, S.; Hemmer, K.; Trietsch, S. J.; Baumuratov, A. S.; Hankemeier, T.; Vulto, P.; Schwamborn, J. C.; Fleming, R. M. T.; *Lab Chip*, **(2015)**, *15*, 2419.
- (40) Ramji, R.; Cheong, C. F.; Hirata, H.; Rahman, A. R. A.; Lim, C. T.; *Small*, **(2015)**, *11*, 943.
- (41) Kuss, S.; Polcari, D.; Geissler, M.; Brassard, D.; Mauzeroll, J.; *Proc. Natl. Acad. Sci.*, **(2013)**, *110*, 9249.
- (42) Cohen, D. J.; James Nelson, W.; Maharbiz, M. M.; *Nat. Mater.*, **(2014)**, *13*, 409.
- (43) Li, W.; Xu, Z.; Huang, J.; Lin, X.; Luo, R.; Chen, C.-H.; Shi, P.; *Sci. Rep.*, **(2014)**, *4*.
- (44) Suntivich, R.; Drachuk, I.; Calabrese, R.; Kaplan, D. L.; Tsukruk, V. V.; *Biomacromolecules*, **(2014)**, *15*, 1428.
- (45) Xu, T.; Zhao, W.; Zhu, J.-M.; Albanna, M. Z.; Yoo, J. J.; Atala, A.; *Biomaterials*, **(2013)**, *34*, 130.
- (46) Leclair, A. M.; Ferguson, S. S. G.; Laguné-Labarthe, F.; *Biomaterials*, **(2011)**, *32*, 1351.
- (47) Tabatabaei, M.; Caetano, F. A.; Vedraïne, S.; Norton, P. R.; Ferguson, S. S. G.; Laguné-Labarthe, F.; *Biomaterials*, **(2013)**, *34*, 10065.
- (48) Schrader, B. *Infrared and Raman Spectroscopy: Methods and Applications*; John Wiley & Sons: Verlag, 1995.
- (49) Petry, R.; Schmitt, M.; Popp, J.; *Chem. Phys. Chem.*, **(2003)**, *4*, 14.
- (50) Madey, T. E.; Yates, J. T. *Vibrational Spectroscopy of Molecules on Surfaces*; Plenum Press: New York, 1987.
- (51) Meyers, R. A. *Encyclopedia of Analytical Chemistry*; John Wiley & Sons: New York, 2000; Vol. 21.
- (52) Ferraro, J. R.; Nakamoto, K.; Brown, C. W. *Introductory Raman Spectroscopy*; 2nd ed.; Academic Press, 2003.

- (53) Long, D. A. *Raman Spectroscopy*; McGraw-Hill: New York, 1977.
- (54) Long, D. A. *The Raman Effect: A Unified Treatment of the Theory of Raman Scattering by Molecules*; John Wiley & Sons, Inc.: Chichester, 2002.
- (55) Matthäus, C.; Chernenko, T.; Newmark, J. A.; Warner, C. M.; Diem, M.; *Biophys. J.*, **(2007)**, *93*, 668.
- (56) Haes, A.; Van Duyne, R.; *Anal. Bioanal. Chem.*, **(2004)**, *379*, 920.
- (57) Rand, B. P.; Peumans, P.; Forrest, S. R.; *J. Appl. Phys.*, **(2004)**, *96*, 7519.
- (58) Wiederrecht, G. P.; *Eur. Phys. J. Appl. Phys.*, **(2004)**, *28*, 3.
- (59) Okamoto, K.; Niki, I.; Shvartser, A.; Narukawa, Y.; Mukai, T.; Scherer, A.; *Nat. Mater.*, **(2004)**, *3*, 601.
- (60) Le Ru, E. C. E., P. G. *Principles of Surface-Enhanced Raman Spectroscopy: and related plasmonic effects*; Elsevier, Oxford, U.K, 2009.
- (61) Novotny, L.; Hecht, B. *Principles of nano-optics*; 1st ed.; Cambridge University Press: Cambridge, England, 2006.
- (62) Mayer, K. M.; Hafner, J. H.; *Chem. Rev.*, **(2011)**, *111*, 3828.
- (63) Bohren, C. F.; Huffman, D. R. *Absorption and Scattering of Light by Small Particles*; John Wiley & Sons: New York, 1983.
- (64) Born, M.; Wolf, E. *Principles of Optics*; 6th ed.; Cambridge University Press: Cambridge, England, 1980.
- (65) Zeng, S.; Baillargeat, D.; Ho, H.-P.; Yong, K.-T.; *Chem. Soc. Rev.*, **(2014)**, *43*, 3426.
- (66) Barnes, W. L.; Dereux, A.; Ebbesen, T. W.; *Nature*, **(2003)**, *424*, 824.
- (67) Banholzer, M. J.; Millstone, J. E.; Qin, L.; Mirkin, C. A.; *Chem. Soc. Rev.*, **(2008)**, *37*, 885.
- (68) Willets, K. A.; Van Duyne, R. P.; *Annu. Rev. Phys. Chem.*, **(2007)**, *58*, 267.



- (69) Galarreta, B. C., "Rational Design and Advanced Fabrication of Metallic Nanostructures for Surface-Enhanced Raman Spectroscopy" (2011). *University of Western Ontario - Electronic Thesis and Dissertation Repository*. Paper 220.
- (70) Raether, H. *Surface plasmons*; Springer-Verlag: Berlin, 1988.
- (71) Ebbesen, T. W.; Lezec, H. J.; Ghaemi, H. F.; Thio, T.; Wolff, P. A.; *Nature*, (1998), 391, 667.
- (72) Przybilla, F., Degiron, A., Laluet, J., Genet, C., & Ebbesen, T. W.; *J. Opt. A: Pure Appl. Opt.*, (2006), 8, 458.
- (73) Rodrigo, S. G.; García-Vidal, F. J.; Martín-Moreno, L.; *Phys. Rev. B*, (2008), 77, 075401.
- (74) Zayats, A. V.; Smolyaninov, I. I.; Maradudin, A. A.; *Phys. Reports*, (2005), 408, 131.
- (75) Tabatabaei, M.; Sangar, A.; Kazemi-Zanjani, N.; Torchio, P.; Merlen, A.; Lagugné-Labarthet, F.; *J. Phys. Chem. C*, (2013), 117, 14778.
- (76) Konstantatos, G.; Sargent, E. H.; *Nat. Nanotechnol.*, (2010), 5, 391.
- (77) Mie, G.; *Ann. Phys.*, (1908), 25, 377.
- (78) Moskovits, M.; *J. Raman Spectrosc.*, (2005), 36, 485.
- (79) Hohenau, A.; Leitner, A.; Aussenegg, F. R.; *Springer Ser. Opt. Sci.*, (2007), 131, 11.
- (80) Fleischmann, M.; Hendra, P. J.; McQuillan, A. J.; *Chem. Phys. Lett.*, (1974), 26, 163.
- (81) Albrecht, M. G.; Creighton, J. A.; *J. Am. Chem. Soc.*, (1977), 99, 5215.
- (82) Jeanmaire, D. L.; Van Duyne, R. P.; *J. Electroanal. Chem.*, (1977), 84, 1.
- (83) Moskovits, M. T., L. L.; Yang, J.; Haslett, T. *SERS and the single molecule. In Optical properties of Nanostructured Random Media*; Springer: Berlin, 2002; p 215.
- (84) Kneipp, K.; Wang, Y.; Kneipp, H.; Perelman, L. T.; Itzkan, I.; Dasari, R.; Feld, M. S.; *Phys. Rev. Lett.*, (1997), 78, 1667.
- (85) Emory, S. R.; Haskins, W. E.; Nie, S.; *J. Am. Chem. Soc.*, (1998), 120, 8009.
- (86) Moskovits, M.; *Rev. Mod. Phys.*, (1985), 57, 783.

- (87) Gersten, J.; Nitzan, A.; *J. Chem. Phys.*, **(1980)**, *73*, 3023.
- (88) Gersten, J. I.; *J. Chem. Phys.*, **(1980)**, *72*, 5779.
- (89) McCall, S. L.; Platzman, P. M.; *Phys. Rev. B*, **(1980)**, *22*, 1660.
- (90) McCall, S. L.; Platzman, P. M.; Wolff, P. A.; *Phys. Lett. A*, **(1980)**, *77A*, 381.
- (91) Moskovits, M.; *J. Chem. Phys.*, **(1978)**, *69*, 4159.
- (92) Moskovits, M.; *Solid State Commun.*, **(1979)**, *32*, 59.
- (93) Schatz, G. C.; *Acc. Chem. Res.*, **(1984)**, *17*, 370.
- (94) Schatz, G. C.; Van Duyne, R. P.; *Surf. Sci.*, **(1980)**, *101*, 425.
- (95) Weitz, D. A.; Garoff, S.; Gersten, J. I.; Nitzan, A.; *J. Chem. Phys.*, **(1983)**, *78*, 5324.
- (96) Adrian, F. J.; *J. Chem. Phys.*, **(1982)**, *77*, 5302.
- (97) Billmann, J.; Otto, A.; *Solid State Commun.*, **(1982)**, *44*, 105.
- (98) Burstein, E.; Chen, Y. J.; Chen, C. Y.; Lundquist, S.; Tosatti, E.; *Solid State Commun.*, **(1979)**, *29*, 567.
- (99) Lombardi, J. R.; Birke, R. L.; Lu, T.; Xu, J.; *J. Chem. Phys.*, **(1986)**, *84*, 4174.
- (100) Morton, S. M.; Silverstein, D. W.; Jensen, L.; *Chem. Rev.*, **(2011)**, *111*, 3962.
- (101) Kelly, K. L.; Coronado, E.; Zhao, L. L.; Schatz, G. C.; *J. Phys. Chem. B* **(2003)**, *107*, 668.
- (102) McCall, S. L.; Platzman, P. M.; *Phys. Rev. B: Condens. Matter*, **(1980)**, *22*, 1660.
- (103) Bailo, E.; Deckert, V.; *Chem. Soc. Rev.*, **(2008)**, *37*, 921.
- (104) Woods, D. A.; Bain, C. D.; *Analyst*, **(2012)**, *137*, 35.
- (105) McFarland, A. D.; Young, M. A.; Dieringer, J. A.; Van Duyne, R. P.; *J. Phys. Chem. B*, **(2005)**, *109*, 11279.
- (106) Hartschuh, A.; Qian, H.; Meixner, A. J.; Anderson, N.; Novotny, L.; *Surf. Interface Anal.*, **(2006)**, *38*, 1472.
- (107) Krug Ii, J. T.; Sanchez, E. J.; Xie, X. S.; *J. Chem. Phys.*, **(2002)**, *116*, 10895.

- (108) Orendorff, C. J.; Gole, A.; Sau, T. K.; Murphy, C. J.; *Anal. Chem.* , **(2005)**, 77, 3261.
- (109) Novotny, L.; van Hulst, N.; *Nat. Photon.* , **(2011)**, 5, 83.
- (110) Fayyaz, S.; Tabatabaei, M.; Hou, R.; Lagugné-Labarthe, F.; *J. Phys. Chem. C*, **(2012)**, 116, 11665.
- (111) Campion, A.; Kambhampati, P.; *Chem. Soc. Rev.*, **(1998)**, 27, 241.
- (112) Hering, K.; Cialla, D.; Ackermann, K.; Dorfer, T.; Moller, R.; Schneidewind, H.; Mattheis, R.; Fritzsche, W.; Rosch, P.; Popp, J.; *Anal. Bioanal. Chem.*, **(2008)**, 390, 113.
- (113) Jiang, X.; Campion, A.; *Chem. Phys. Lett.* , **(1987)**, 140, 95.
- (114) Udagawa, M.; Chou, C.-C.; Hemminger, J. C.; Ushioda, S.; *Phys. Rev. B: Condens. Matter* **(1981)**, 23, 6843.
- (115) Jensen, L.; Aikens, C. M.; Schatz, G. C.; *Chem. Soc. Rev.* , **(2008)**, 37, 1061.
- (116) Otto, A.; *J. Raman Spectrosc.* , **(2005)**, 36, 497.
- (117) Pettinger, B.; *J. Chem. Phys.*, **(1986)**, 85, 7442.
- (118) Kambhampati, P.; Child, C. M.; Foster, M. C.; Campion, A.; *J. Chem. Phys.*, **(1998)**, 108, 5013.
- (119) Kneipp, K.; Kneipp, H.; Itzkan, I.; Dasari, R. R.; Feld, M. S.; *J. Phys.: Condens. Matter*, **(2002)**, 14, R597.
- (120) Kazemi Zanjani, N., "Tip-Enhances Raman Spectroscopy, Enabling Spectroscopy at the Nanoscale" **(2014)**. *University of Western Ontario - Electronic Thesis and Dissertation Repository*. Paper 2079.
- (121) Lombardi, J. R.; Birke, R. L.; *Acc. Chem. Res.*, **(2009)**, 42, 734.
- (122) Morton, S. M.; Ewusi-Annan, E.; Jensen, L.; *Phys. Chem. Chem. Phys.*, **(2009)**, 11, 7424.
- (123) Saikin, S. K.; Olivares-Amaya, R.; Rappoport, D.; Stopa, M.; Aspuru-Guzik, A.; *Phys. Chem. Chem. Phys.*, **(2009)**, 11, 9401.

- (124) Fromm, D. P.; Sundaramurthy, A.; Kinkhabwala, A.; Schuck, P. J.; Kino, G. S.; Moerner, W. E.; *J. Chem. Phys.*, **(2006)**, *124*, 0611011.
- (125) Stöckle, R. M.; Suh, Y. D.; Deckert, V.; Zenobi, R.; *Chem. Phys. Lett.* , **(2000)**, *318*, 131.
- (126) Watanabe, H.; Ishida, Y.; Hayazawa, N.; Inouye, Y.; Kawata, S.; *Phys. Rev. B Condens. Matter Mater. Phys.* , **(2004)**, *69*, 1554181.
- (127) Verma, P.; Yamada, K.; Watanabe, H.; Inouye, Y.; Kawata, S.; *Phys. Rev. B Condens. Matter Mater. Phys.* , **(2006)**, *73*, 0454161.
- (128) Rasmussen, A.; Deckert, V.; *J. Raman Spectrosc.*, **(2006)**, *37*, 311.

## Chapter 3

### 3 Fabrication techniques of plasmonic platforms

Surface-enhanced Raman spectroscopy (SERS) is a promising technique for chemical analysis and surface characterization offering a highly sensitive tool down to single molecule. Nevertheless, several challenges limit the widespread application of this technique. Fabrication of efficient and uniform SERS platforms is indeed one of the most critical challenges.<sup>1</sup> This is limited by the material as well as the size of the nanoscale features that are responsible for generating localized enhanced nanoscale regions of so-called hot spots. An optimized fabrication method is thus the key to prepare efficient and reproducible plasmonic platforms. Moreover, the plasmonic optical properties of the platform are key factors to optimize the enhancement in SERS measurements. The efficient excitation of the plasmonic resonances occurs when the incident light has a polarized component along the nanoantennas direction. This Chapter summarizes the optimal parameters to achieve high sensitive SERS measurements using 2D and 3D plasmonic platforms and also the experimental setup to perform sensitive SERS measurements.

#### 3.1 Nanosphere lithography (NSL)

Design, fabrication and characterization of versatile nanostructured surfaces using different techniques, such as immobilized colloid deposition,<sup>2</sup> nanoimprint lithography,<sup>3</sup> chemical etching,<sup>4</sup> on-wire lithography,<sup>5</sup> and many others<sup>6-10</sup> are reported in the literature. Of those techniques, lithography provides one of the simplest methods to control the geometry, size and spacing of the nanostructures.<sup>7</sup> NSL,<sup>7,11,12</sup> is a technique of choice to

simplify and reduce the costs of production of these substrates and is scalable for the production of large surfaces.

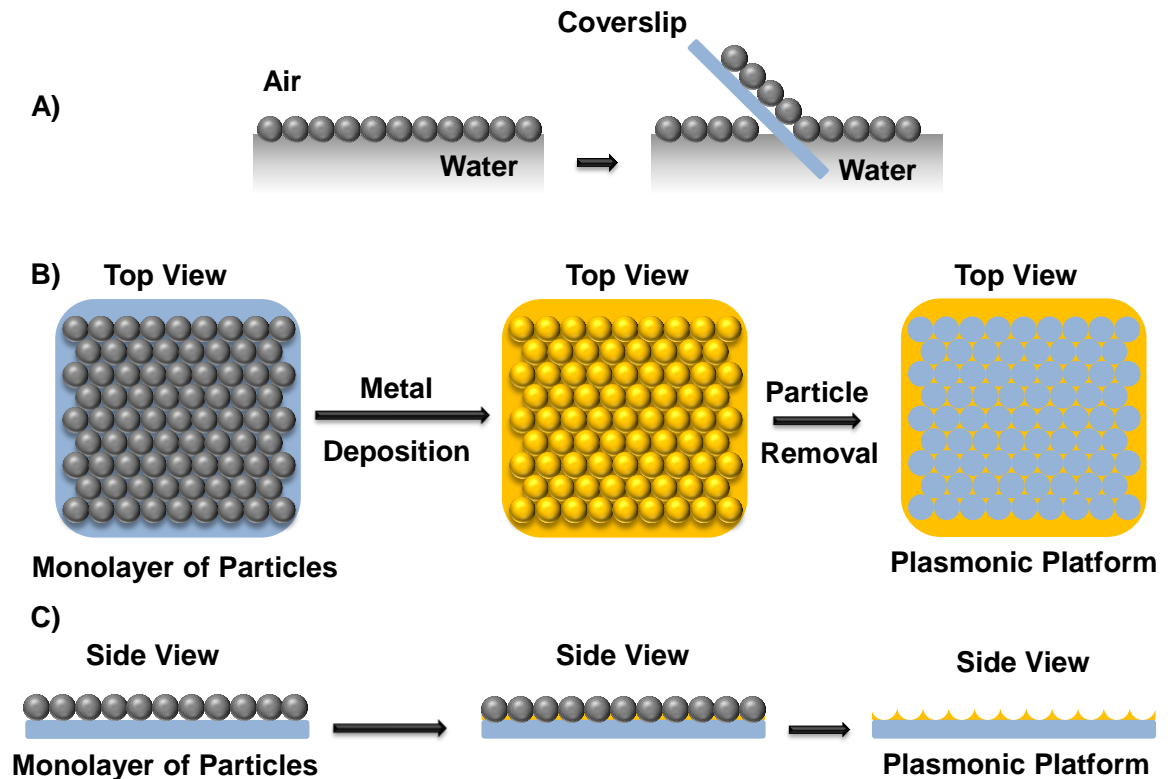


**Figure 3.1** Schematic illustration of the nanosphere lithography with interface method. **A)** a monolayer of polystyrene microspheres are spread on water-air interface and the monolayer is transferred onto the surface of a clean microscope coverslip; **B)** a uniform layer of a metal of choice is deposited by electron-beam evaporation and the microspheres are removed by sonication in ethanol revealing the final plasmonic platform; **C)** side view of the same process in B.

NSL, a derivative of natural lithography<sup>13</sup> uses colloidal polystyrene or silica nanospheres (or microspheres) to create a hexagonal closed packed array. The gap between the spheres enables researchers to design different structures. Simple structures such as nanotriangles and nanopyramids can be produced simply by varying the amount of material that is deposited onto the surface.<sup>12</sup> By etching the spheres prior to deposition, it is possible to create nanohole and nanobowl arrays. More details associated with design of producing nanotriangles and tetrahedral nanopyramids are presented in Chapters 5 and 6, respectively.

A schematic for the principle of NSL is illustrated in **Figure 3.1**. In order to perform NSL, microscope coverslips are sonicated in acetone for 5 min followed by cleaning in Nochromix solution in concentrated sulphuric acid for 15 min. Subsequently, the slides are rinsed in Milli-Q ultrapure water (18.2 M $\Omega$ ·cm) several times. These are sonicated for 1 h in mixture of ammonium hydroxide/hydrogen peroxide/ultrapure water in ratio of 1:1:5. Afterward, the glass slides are rinsed and stored in MilliQ water. Polystyrene nanosphere suspension was equilibrated to room temperature before use. The size of polystyrene nanospheres varies in different experiments. The size that was used in this thesis is 1000 nm polystyrene spheres as shown in Chapter 5 and 6, however, the protocol can be used for other sizes including 650 and 438 nm polystyrene spheres. 20  $\mu$ L aliquot of polystyrene suspension was mixed with 20  $\mu$ L of ethanol (100%). 20  $\mu$ L of the prepared solution was deposited atop a dried coverslip. This was immediately introduced in the air-water interface of a 6 cm Petri dish filled with ultrapure water. The coverslip floated on the air-water interface and the solution spread out from the coverslip to the air-water interface. After the dispersion of the solution, the coverslip sank to the bottom of the Petri dish. A drop of 2% (w/v) sodium dodecyl sulfate solution in water was added to further group the nanospheres into an ordered monolayer. The nanosphere solution was

finally picked up using a wet coverslip and was allowed to dry under a Petri dish undisturbed. After the samples dried, 3 nm of Ti and 30 nm of Au were deposited using electron beam evaporation (Hoser, Ottawa, Canada). The polystyrene particles were removed by sonicating the sample in ethanol for about a minute. The sample was then dried with nitrogen. By adding a dielectric layer such as SiO<sub>2</sub>, these platforms can also be used for surface-enhanced fluorescence SEF, since it requires this layer to prevent the quenching of a chosen fluorophore in the vicinity of the metal surface.<sup>11,12</sup> NSL can also be performed multiple times with different sized spheres on the same substrate in order to create even more different patterns.

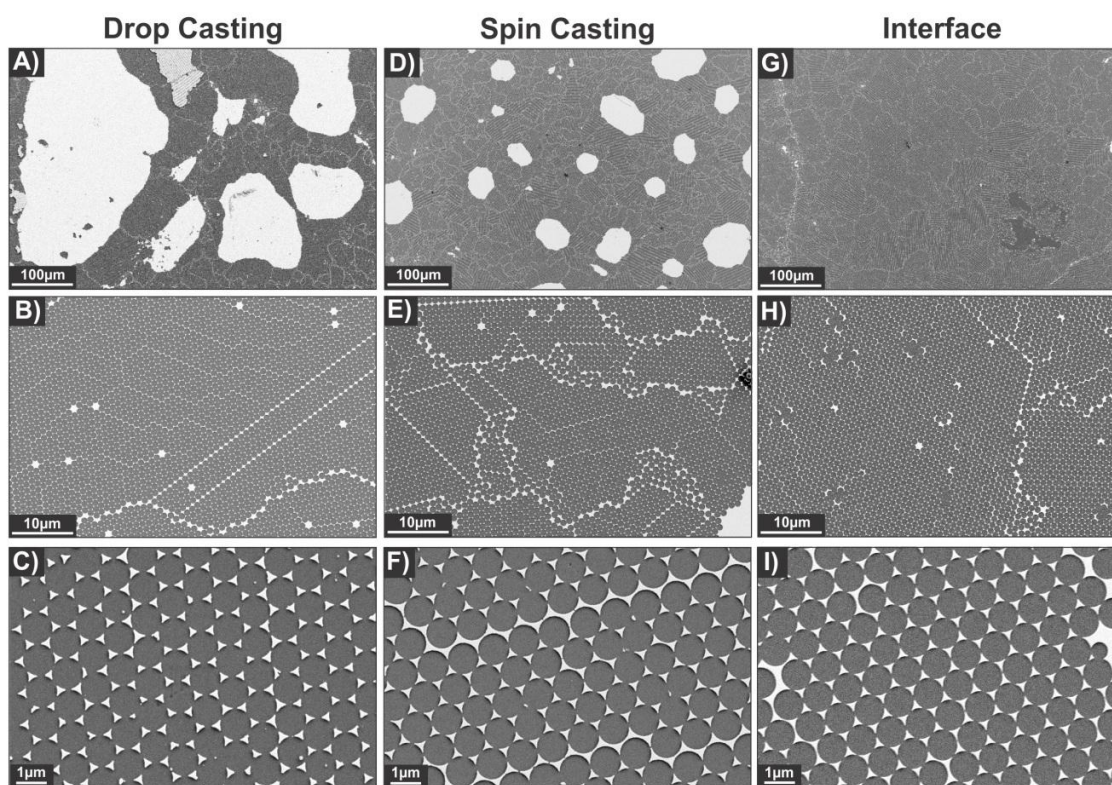


**Figure 3.2** Representative SEM images of nanotriangles fabricated by different NSL techniques, including A-C) drop casting. D-F) spin casting. G-I) interface method.



**Table 3.1 Comparing three principle techniques for NSL.**

<b>NSL Techniques</b>	<b>Drop Casting</b>	<b>Spin Casting</b>	<b>Interface</b>
<b>Advantages</b>	<ol style="list-style-type: none"> <li>1. Easiest method</li> <li>2. Relatively uniform macroscopic regions of monolayers of particles</li> </ol>	<ol style="list-style-type: none"> <li>1. Fastest method</li> <li>2. Quick solvent evaporation</li> <li>3. Greater coverage than drop casting over the substrate</li> </ol>	<ol style="list-style-type: none"> <li>1. Greatest coverage of compact regions of particles over the entire substrate.</li> <li>2. Greatest adaptability to micropatterning techniques</li> <li>3. Best use of particles</li> </ol>
<b>Limitations</b>	<ol style="list-style-type: none"> <li>1. Small coverage on the entire substrate</li> <li>2. Requires solvent to evaporate over a prolonged period</li> <li>3. Large regions of multilayers are formed</li> </ol>	<ol style="list-style-type: none"> <li>1. Produces uniform defects of metal islands within the compact regions of particles</li> <li>2. Negative effect of surfactant on final structures</li> <li>3. Requires specific equipment</li> </ol>	<ol style="list-style-type: none"> <li>1. Requires solvent to evaporate overnight</li> <li>2. Requires Skill</li> <li>3. Limited to the size of particles</li> </ol>

There are three principle techniques that can and have been used to create substrates using NSL (**Figure 3.2**). Of the three, drop casting is by far the easiest. In this technique, an aliquot of a solution containing the polystyrene nanospheres is placed onto the center of the cover slip. As the solvent evaporates, compact and organized layers form on the surface, as shown in **Figure 3.2**. Potentially, the greatest drawback of drop casting is that it only covers a small portion of the entire substrate as shown in **Figure 3.2 A**. However, drop casting does provide macroscopic regions of relative uniformity which can be observed by visual inspection (**Figure 3.2 B and D**). In SERS, experiments are conducted majorly using a confocal microscope requiring small structures area (i.e.  $100 \mu\text{m}^2$ ), whilst in SEIRA, a macroscopic measurement is usually performed, thereby requiring a larger homogeneous structured surface of typically  $25 \text{ mm}^2$ . As such, the ability to select a region of uniformity by visual inspection is a necessity.

The next simplest technique requires the use of a spin coater. Here, the particles are dispersed from the center of the cover slip outwards due to the spinning of the cover slip. Unlike drop casting which requires the solvent to evaporate over a prolonged period, the solvent evaporates quicker. Spin coating may not create the macroscopically large areas as drop casting does, but it does provide considerably greater coverage than drop casting as shown in **Figure 3.2 D**. Based on the time it takes for each step to occur, it is possible to go from unclean cover slips to substrates that are ready to be functionalized, in less than 8 hours (**Figure 3.2 E and F**).

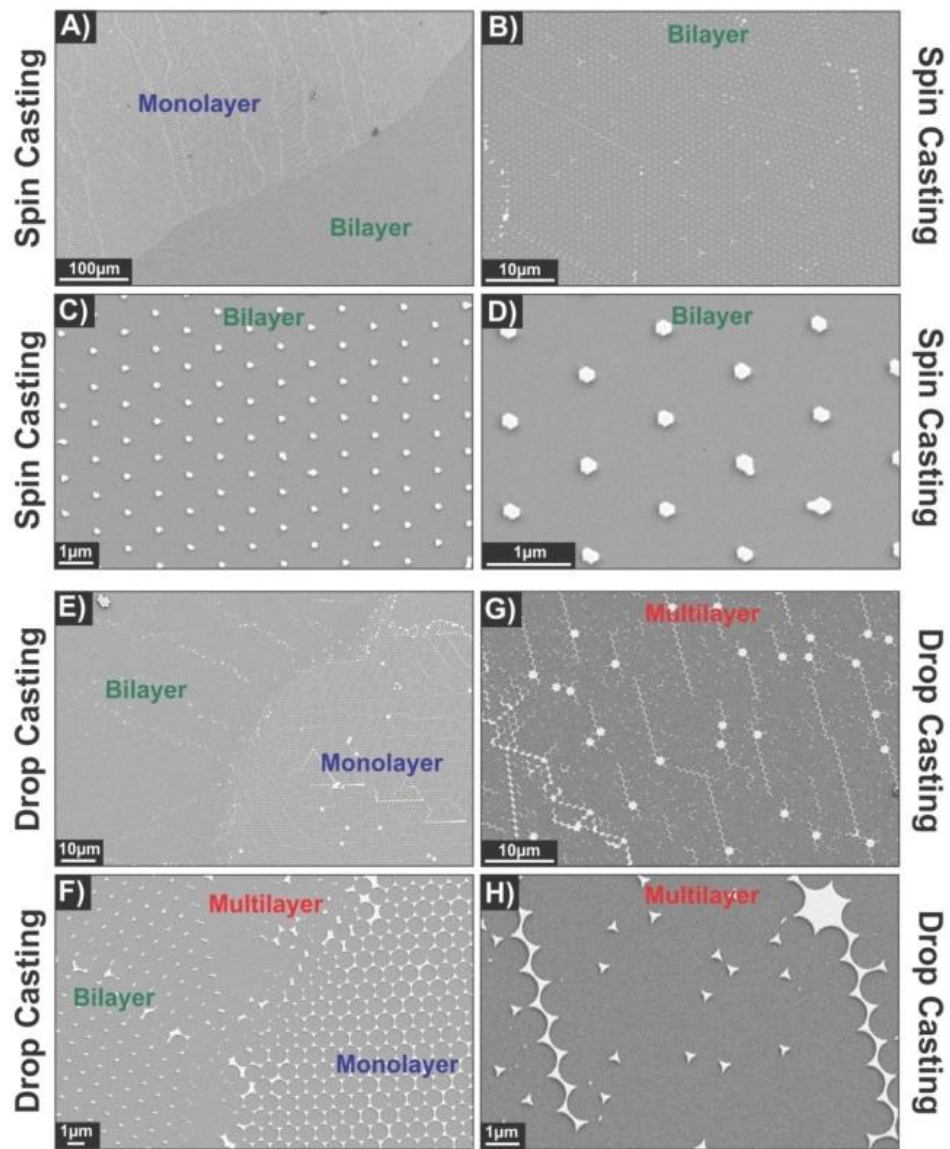


**Figure 3.3 SEM images of distinct plasmonic nanostructures obtained on the NSL substrates based on the presence of different layers of the sacrificial template of nanospheres.**

The more challenging technique is the air-water interface method. In this method, the particles must be grabbed from the surface of the water by a clean hydrophilic cover slip. This method takes considerably more time than the others. The benefit though is that it offers the greatest potential for coverage on a cover slip (**Figure 3.2 G-I**) Other than time, this technique is limited to particles that are at least 0.4  $\mu\text{m}$  in diameter. Below this diameter, it is very difficult if not impossible to see any floating structure in which to grab with a clean cover slip. Brief advantages and limitations of these three methods are shown in **Table 3.1**. In addition to the limitations mentioned in **Table 3.1**, the possibility of producing bilayer and multilayer of particles over the substrates using drop casting and spin casting techniques is significantly higher than air-water interface method as shown in **Figure 3.3**. The presence of bilayer leads to producing nanodots after the metal deposition and removing the particles. In the meantime, the creation of multilayers results in producing empty regions after removing particles. This effect can create microscopic regions of defects through homogenous regions of nanotriangles or nanodots.

### 3.2 Electron-beam lithography (EBL)

In contrast of NSL, EBL allows full control over the design of different features with a high reproducibility and with excellent resolution and homogeneity.<sup>1</sup> EBL can be used to create patterns that go well beyond that of NSL in terms of complexity, reproducibility and homogeneity. Complex shapes and patterns, such as nanosnowflakes, and nanoflowers, can be readily fabricated. These types of structures allow for control over the locations of the “hot spots” on the surface of the substrate as well as on the extinction wavelength of the structured platform. Of these two methods, both have their strengths and weaknesses. In the case of NSL, it is the limited types of structures that can be fabricated, whereas for EBL, the limitation lies in the inability to effectively and efficiently produce the structure over the entire surface of the substrate at a reasonable cost.

EBL requires first a substrate coated with an electron beam photosensitive polymer, known as a photoresist. Using a scanning electron microscope equipped with a lithographic system, a design can be written on the surface by exposing the photoresist with the electron beam scans the surface according to 2D geometric design. Then, in the case of a positive photoresist, the coated sample has to be developed to remove the exposed polymer revealing the non-exposed photoresist that shows the desired patterns. The next step involves metal deposition followed by a lift-off procedure to remove the residual polymer. The final sample shows metallic structures that follow exactly the desired pattern with a 10-20 nm resolution. Some patterns made in our group using this technique are shown in **Figure 3.4**, where it can be appreciated that EBL offers a high control of the size, shape and spacing of the features.<sup>6</sup> Using EBL, it is also possible to fabricate 3D plasmonic nanostructures such as 3D nanocavities consisting of arrays of nanoholes and co-registered nanocones that are shown in detail in Chapter 7.

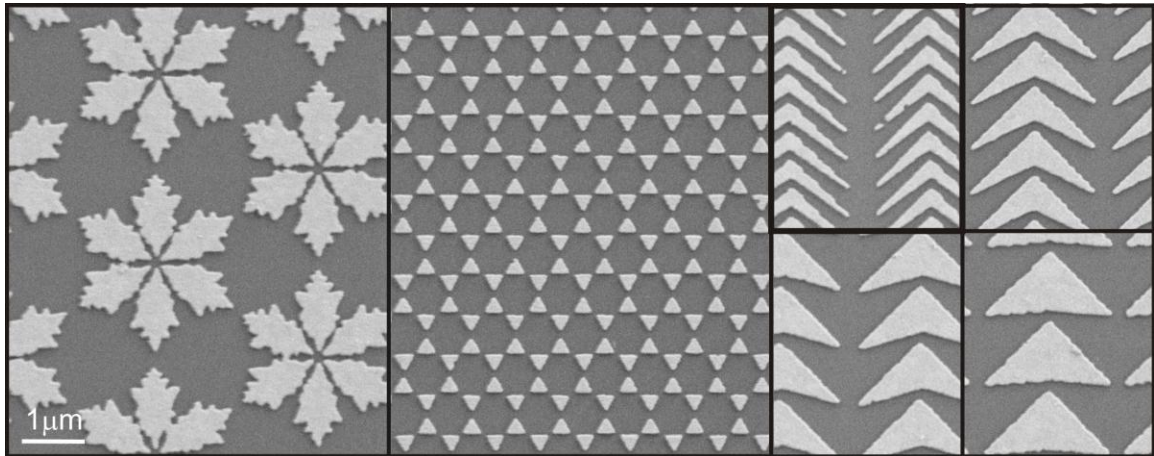


**Figure 3.4** Scanning electron micrographs of 2D nanostructures written using EBL.<sup>14</sup>

In the present thesis, EBL was used to develop a 3D nanostructure for ultra-sensitive detections. A schematic representation of the fabrication process of these structures has been shown in **Figure 3.5**.

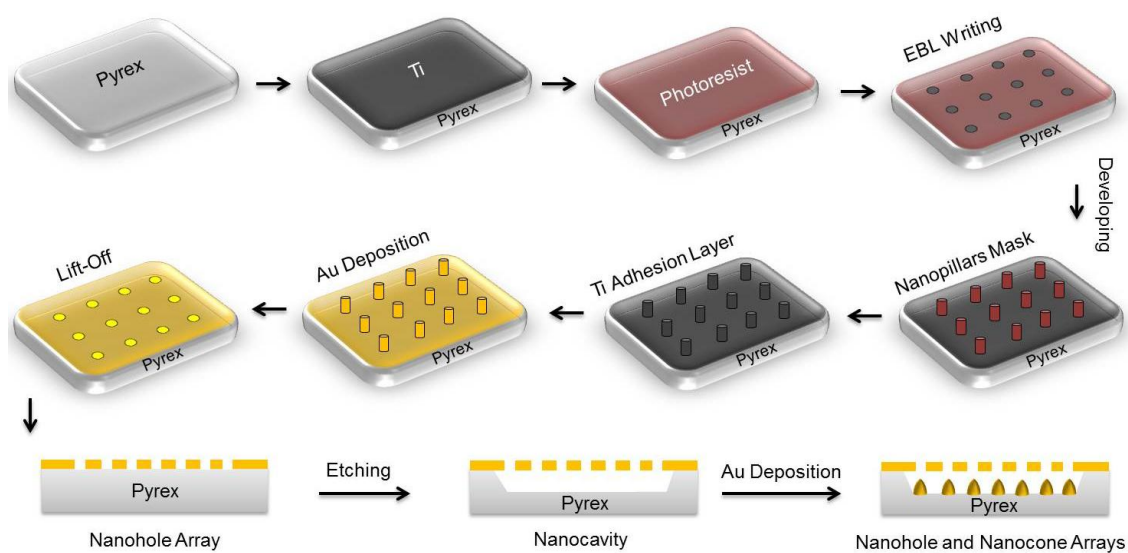


**Figure 3.5 Schematic illustration of fabrication process for 3D plasmonic cavity nanosensors**

Complete details of the fabrication procedure has been discussed in chapter 7 representing an ultra-sensitive detection of 4-nitrothiophenol (4-NTP) down to 100 aM on these plasmonic structures.<sup>15</sup> Briefly, a thin layer of Ti has been deposited on the Pyrex substrate using electron-beam physical evaporation to produce a conductive layer for further EBL writing process. After spin-coating of a photoresist on the substrate, a pattern of choice (nanoholes array) has been written on the substrate using EBL instrument. By developing the photoresist, an array of nanopillars is revealed and is used as a mask for the fabrication of nanoholes array. Subsequently, a thin layer of Ti is deposited on the substrate as an adhesion layer prior to Au deposition. After the metal

deposition, the nanopillars are lifted-off to reveal the nanoholes arrays on the substrate. In the next step, a Ti etchant is used to etch away both Ti and Pyrex to create a nanocavity beneath the nanoholes array. Subsequent to that, another layer of Au is deposited to produce the co-registered truncated nanocones array under the nanoholes array.

### 3.3 Raman setup for SERS measurements

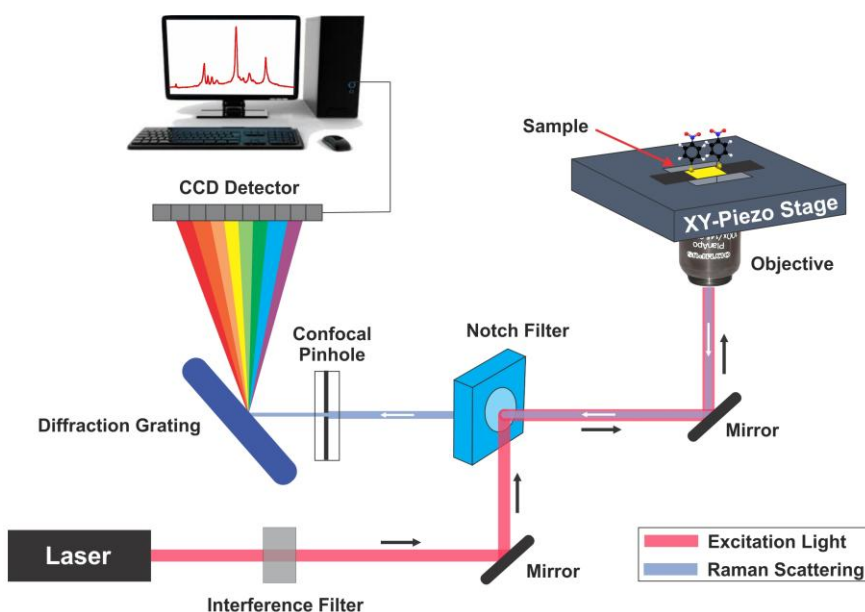


**Figure 3.6 Principles of the SERS setup used in this thesis. The linearly polarized laser gets focused onto the sample using a microscope objective (typically  $\times 100$ , 0.9 N.A.). The backscattered light from the sample gets collected using the same microscope objective, passes through the notch filter that rejects the incident wavelength and then enters the spectrometer. Prior to entering the spectrometer, a confocal pinhole selects the back-scattered light from a given focal plane. A diffraction grating disperses the light spatially, separating the distinct wavelengths. The dispersed light is then detected by a CCD detector prior to signal acquisition and treatment.**

In the present thesis, the SERS setup is based on a commercial Raman spectrometer (600 gr/mm grating, HR LabRam, Horiba-Jobin-Yvon, Kyoto, Japan, focal length of 800 mm) connected to an inverted optical microscope (IX71, Olympus, Tokyo, Japan) and interfaced with a 5 axis atomic force microscope system (AFM, NanoWizard II Bioscience, JPK Instruments Inc., Berlin, Germany) to perform measurements in the bottom illumination configuration and back-scattering collection geometry as shown in **Figure 3.6**. The setup is equipped with three different excitation sources including 532, 632.8, and 785 nm. The excitation source was selected based upon the extinction wavelengths of the SERS substrates and also the probe molecules. The acquisition time used for each experiment was also dependent on obtained signal/noise ratio for the probe molecule.

### 3.4 Summary

There is a vast variety of techniques of generating plasmonic nanostructures for SERS. Of those, lithography includes the two major techniques namely NSL and EBL. These techniques provide simple methods to control the geometry, size and spacing of the nanostructures to generate strong LSPR leading to high SERS enhancements. However, there are certain limitations for both techniques as discussed in this chapter. In order to provide a simple, high-throughput and low-cost method, NSL is the best choice. However, the capability of EBL to create versatile nanostructures in particular for 3D structures is beneficial compared to limited nanostructures that can be provided by NSL. Depending on the application, both techniques provide powerful plasmonic structures that can be used for ultra-sensitive detections of molecules and biomolecules leading to a broad interest in different disciplines including life, material, and environmental sciences.



### 3.5 References

- (1) Guicheteau, J. A.; Farrell, M. E.; Christesen, S. D.; Fountain, A. W.; Pellegrino, P. M.; Emmons, E. D.; Tripathi, A.; Wilcox, P.; Emge, D.; *Appl. Spectrosc.*, **(2013)**, *67*, 396.
- (2) Wang, H.; Levin, C. S.; Halas, N. J.; *J. Am. Chem. Soc.*, **(2005)**, *127*, 14992.
- (3) Li, K.; Clime, L.; Cui, B.; Veres, T.; *Nanotechnology*, **(2008)**, *19*, 145305.
- (4) Cui, B.; Clime, L.; Li, K.; Veres, T.; *Nanotechnology*, **(2008)**, *19*, 145302.
- (5) Qin, L.; Zou, S.; Xue, C.; Atkinson, A.; Schatz, G. C.; Mirkin, C. A.; *Proc. Natl. Acad. Sci. U. S. A.*, **(2006)**, *103*, 13300.
- (6) Banholzer, M. J.; Millstone, J. E.; Qin, L. D.; Mirkin, C. A.; *Chem. Soc. Rev.*, **(2008)**, *37*, 885.
- (7) Hulteen, J. C.; Treichel, D. A.; Smith, M. T.; Duval, M. L.; Jensen, T. R.; Van Duyne, R. P.; *J. Phys. Chem. B*, **(1999)**, *103*, 3854.
- (8) Guieu, V.; Lagugné-Labarthe, F.; Servant, L.; Talaga, D.; Sojic, N.; *Small*, **(2008)**, *4*, 96.
- (9) Marquestaut, N.; Martin, A.; Talaga, D.; Servant, L.; Ravaine, S.; Reculosa, S.; Bassani, D. M.; Gillies, E.; Lagugné-Labarthe, F.; *Langmuir*, **(2008)**, *24*, 11313.
- (10) Bolduc, O. R.; Live, L. S.; Masson, J.-F.; *Talanta*, **(2009)**, *77*, 1680.
- (11) Fayyaz, S.; Tabatabaei, M.; Hou, R.; Lagugné-Labarthe, F.; *J. Phys. Chem. C*, **(2012)**, *116*, 11665.
- (12) Tabatabaei, M.; Sangar, A.; Kazemi-Zanjani, N.; Torchio, P.; Merlen, A.; Lagugné-Labarthe, F.; *J. Phys. Chem. C*, **(2013)**, *117*, 14778.
- (13) Deckman, H. W.; Dunsmuir, J. H.; *Appl. Phys. Lett.*, **(1982)**, *41*, 377.
- (14) Galarreta, B. C., "Rational Design and Advanced Fabrication of Metallic Nanostructures for Surface-Enhanced Raman Spectroscopy" **(2011)**. *University of Western Ontario - Electronic Thesis and Dissertation Repository*. Paper 220.

(15) Tabatabaei, M.; Najiminaini, M.; Davieau, K.; Kaminska, B.; Singh, M. R.; Carson, J. J. L.; Lagugn -Labarthe, F.; *ACS Photonics*, (2015), 2, 752.

## Chapter 4

### 4 Directing GPCR-transfected cells and neuronal projections with nano-scale resolution<sup>1</sup>

Surface modification technology has made significant advances in recent years towards the miniaturization and organization of traditional cell culture systems. However, the capability of directing transfected cells and neuronal connections to probe small structures such as spines is still under development. This chapter presents the capability of cell micropatterning technology not only to direct conventional cell lines, but also transfected cells by different receptors and also small structures such as neuronal connections called spines. Firstly, interactions of different micropatterned substrates with HEK 293, CF10 cell lines, and primary neuronal cultures are evaluated. Using conventional and confocal fluorescence microscopies, several morphological and behavioral aspects of all three cell types are investigated. The immortalized cell lines were able to attach to the substrate and interact with neighboring cells. Similarly, cortical neurons formed connections guided by the micropatterns. Transfection of HEK 293 or CF10 cell lines with specific members of the G protein-coupled receptor (GPCR) family did not alter the behavior of these cells in the micropatterns. Secondly, neuronal projections were efficiently isolated by the patterns, simplifying the localization of spines with nano-scale resolution probed by atomic force microscopy. This presents a valuable approach to isolate cells or to constrain important cell structures to grow along a desired pattern, thus facilitating advanced biological studies.

---

<sup>1</sup> A version of this chapter has been published in [*Biomaterials*, (2013), 34, 10065.]. Reproduced with permission of the Elsevier publishing group.

<sup>2</sup> A version of this chapter has been submitted

## 4.1 Introduction

Cell micro/nanopatterning has become a widely used approach for many different applications such as fundamental biological studies, cell-based biosensors, and tissue engineering.<sup>1-8</sup> With the ability to precisely control the size, shape, and spatial arrangement of the cell adhesive areas, basic cell functions including adhesion, proliferation, migration, motility, and differentiation can be studied.<sup>9-20</sup> Cells plated on adhesive areas typically adopt the size and shape of the pattern, thus allowing the manipulation of cell shape, extension, and spreading.<sup>21-25</sup> In addition, processes such as cell-cell and cell-substrate interactions can be studied.<sup>26-28</sup> Currently, most of these patterning technologies are limited to the type of substrate suitable, and many are not compatible with inverted microscopes due to a lack of transparency. This is a significant disadvantage, as the visualization and analysis of living cells using techniques such as optical or fluorescence microscopies, typically require transparent substrates.<sup>29</sup> Similarly, when investigating cell interactions using spectroscopic techniques, the adhesion promoting molecules or biomolecules present would interfere in the analysis of the cells. In addition, constraining cells to grow flat over a surface offers better quality of imaging using optical microscopy, in particular when complex ensemble of cells such as neural networks are studied.

Modifying the topography of a surface is a non-invasive and non-biological approach towards regulating cell function and it can be effective as a cell-stimulating cue, as cells *in vivo* interact with textured and rough surfaces.<sup>30</sup> Topographical features have been studied at the micro- and nano-scale. However, investigating cell response to topography alone is complicated, because the wettability of the surface is variable with topographical changes.<sup>31</sup> Despite this difficulty, there are some results that suggest an association of cell response to feature pattern.<sup>32</sup> For instance, Fu et al. reported that smooth glass surfaces

support cell adhesion, proliferation, and long-term self-renewal of human embryonic stem cells (hESCs), while rough glass surfaces tended to induce a spontaneous differentiation.<sup>15</sup> They also showed that NIH/3T3 fibroblasts are intrinsically sensitive to nano-scale topological cues, as evidenced by reduced cell spread area, enhanced cell adhesion, proliferation, and migration on nanoscale-rough glass surfaces compared to smooth surfaces.<sup>11</sup> Furthermore, it has been shown that micropatterns with different widths and divergence angles passively direct the locomotion and the migration of NIH/3T3 fibroblasts cells.<sup>21</sup> However, generally speaking, the cellular response to patterns is highly dependent on the specific pattern and also on the type of the cell. For instance, other studies have shown that Madin-Darby canine kidney (MDCK) epithelial cells show approximately the same behavior and growth on various micropatterned features.<sup>26</sup>

One important challenge in cell biology is related to the ability of isolating cells and small structures, such as spines, in order to study protein localization and interaction in those sites. For example, more understanding about neuronal communication would be acquired in a system where the cell projections could be efficiently isolated and tracked. Furthermore, the isolation of spines, important structures involved in synaptic transmission,<sup>33</sup> would be very helpful to further elucidate their role in pathological conditions such as neurodegenerative diseases. Immortalized cell lines are other important models used in cell biology. These cells are extensively used in biological studies due to their availability, low maintenance and cost, compared to primary cultures. Overexpression of G protein-coupled receptors (GPCRs) has brought solid understanding about function and regulation of these receptors.<sup>34</sup> GPCRs, constitute by far the largest receptor family in mammals and are involved in the regulation of virtually all cellular and physiological functions in the body.<sup>35,36</sup> Owing to their ability to bind to ligands with a high specificity and affinity, GPCRs are preferentially targeted for the development of

new therapeutics and account for about 40% of all modern medicinal drugs.<sup>37</sup> Although studies using transfected cells in micropatterned substrates are rare, evaluating the capability of these substrates to guide the GPCR-transfected cells is of great importance.

We previously reported plasma-deposited fluorocarbon patterned substrates as a candidate to pattern single and connected cells.<sup>16,17</sup> In the present work, in addition to the newly optimized fabrication process, we demonstrate the capability of these substrates for controlled growth of cells transfected with different GPCRs. Amongst the receptors used are two members of group 1 metabotropic glutamate receptors (mGluRs), mGluR1 and 5, as well as 5-hydroxytryptamine receptor (5-HT<sub>2A</sub>), and corticotropin releasing hormone receptor (CRHR1), also known as CRF1. The objectives of this study were to: i) direct the GPCR-transfected cells using patterned substrates to determine their cellular response to pattern shape and size compared to non-transfected cells, ii) show the capability of the patterned substrates to isolate the neuronal projections, and finally iii) unravel the spines localization of isolated neuronal projections with nano-scale resolution by the combination of cell micropatterning and atomic force microscopy.

## 4.2 Materials and methods

### 4.2.1 Materials

Standard glass microscope coverslips (22 × 22 × 0.15 mm) and microscope slides (25 × 75 × 1 mm) were purchased from VWR International and Fisher Scientific, respectively. The 35 mm plastic dishes with glass bottom of 0.16-0.19 mm of thickness were purchased from MatTek Corporation. Nanostrip™ (90% sulfuric acid, 5% peroxymonosulfuric acid, <1% hydrogen peroxide, and 5% water) was purchased from Cyantek Corporation. The materials used in the photolithography process, Microposit™ SC1805™ positive photoresist and Microposit™ MF™ 319 developer, were purchased

from Rohm & Haas Electronic Materials, and the NANO<sup>TM</sup> Remover PG was purchased from MicroChem Corporation. Octafluorocyclobutane gas (C<sub>4</sub>F<sub>8</sub>) was purchased from BOC Edwards. The wafer mounting media Crystalbond<sup>TM</sup> 509 was purchased from Aremco Products, Inc., and finally, the isopropyl alcohol (IPA) and acetone were purchased from Sigma-Aldrich and used as received.

#### 4.2.2 Patterned substrate fabrication

Microscope coverslips were cleaned in Nanostrip for 5 min and rinsed thoroughly with de-ionized (DI) water prior to use. The fabrication process, as outlined in **Figure 4.1**, is a combination of three main steps: photolithography, plasma polymerization, followed by a lift-off process. The first step of the fabrication process includes patterning the glass using optical lithography, in order to create a patterned photoresist mask to protect regions of the glass substrate. For this purpose, positive photoresist was spin-coated onto the cleaned glass slide, with a thickness of approximately 500 nm, as measured by atomic force microscopy. For the smaller features in range of 5  $\mu\text{m}$  or less, using a thinner layer of photoresist will lead to sharper pattern. The photoresist was then softbaked at 115 °C for 1 min to evaporate the solvent, followed by baking in an oven at 90 °C for 20 min. It was then exposed to ultra-violet light through a chrome mask that had the desired pattern designed on it. For this purpose, a Karl Suss MA6 contact mask aligner (Suss MicroTech) was used for 8 s at an intensity of 12 mW cm<sup>-2</sup>. The exposed photoresist was then removed by developing in Microposit MF-319 developer for 1 min. It was then washed with DI water and dried under nitrogen.

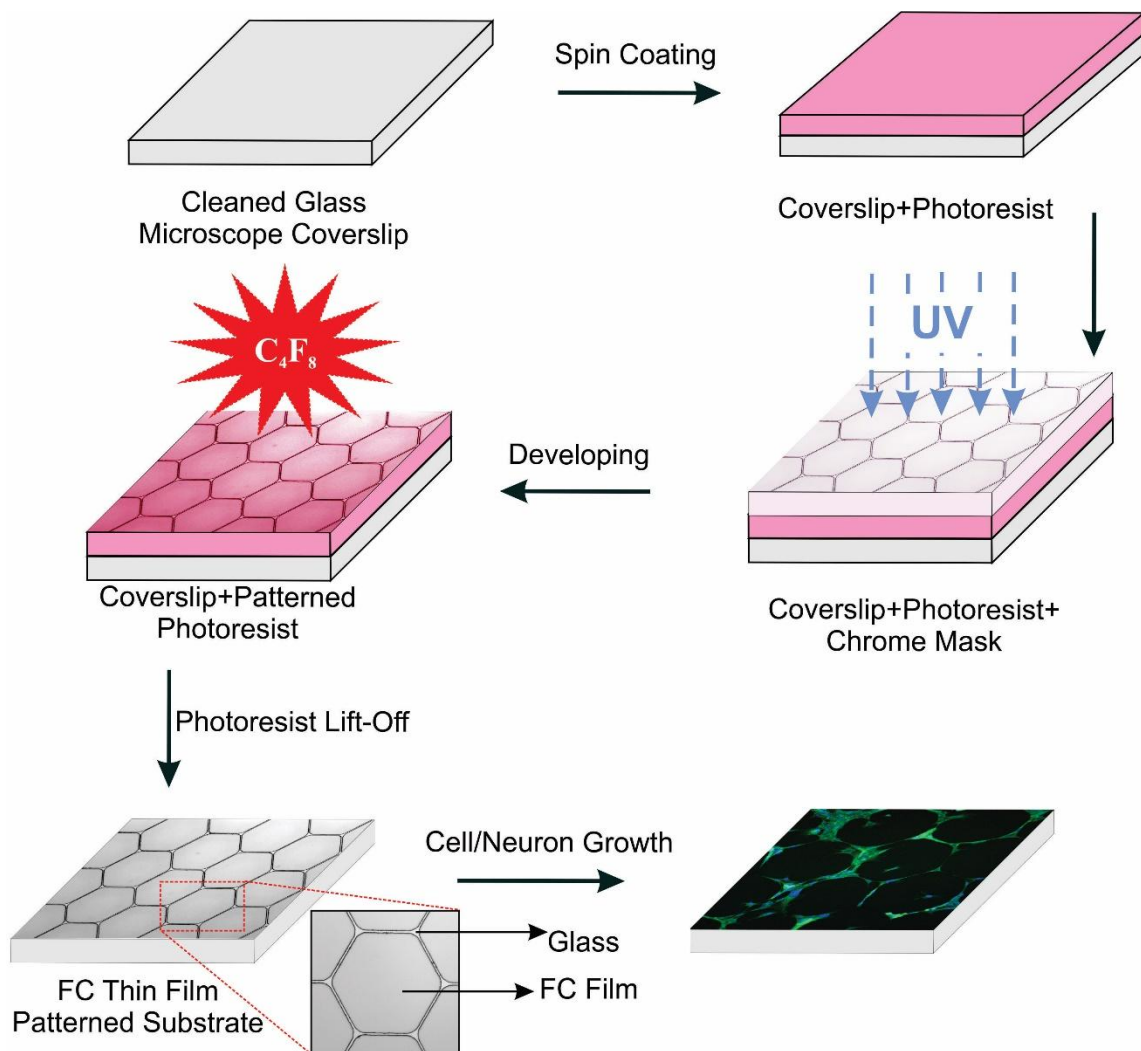


**Figure 4.1 Schematic illustration of the applied method to prepare patterns with fluorocarbon (FC) polymer; Photolithography and plasma deposition of a thin FC film were used prior cell culture over the patterned surface.**

The photoresist mask left on the surface is a replication of the original optical mask. In the second step, the plasma deposition of the fluorocarbon polymer was carried out using a deep reaction ion etching instrument, and inductively coupled plasma (ICP) reactor,



(Alcatel 601E). The source power and substrate bias were set to 1,800 and 80 W, respectively. The feed gas supplied was C<sub>4</sub>F<sub>8</sub>, controlled at a flow of 150 sccm [standard cubic centimeters per minute] with a total process time of 10 s at a temperature of 20 °C. The coverslips were mounted onto silicon wafers for the plasma deposition and were subsequently removed prior to the lift-off process. Finally, the protective photoresist was removed by a lift-off process in a photoresist solvent (NANO™ Remover PG) for 10 min at 80 °C, followed by sonication in the solvent for 30 s. The sample was then rinsed thoroughly with iso-propyl alcohol (IPA) and dried under nitrogen. The final architecture of the substrate is a thin fluoropolymer film with regions wherein the glass substrate is revealed. The process for the preparation of the patterned surfaces is shown in **Figure 4.1**.

#### 4.2.3 Cells cultures

HEK 293, and CF10 cells were maintained in Eagle's Minimal Essential Medium (MEM) and Dulbecco's Modified Eagle's Medium (DMEM, Invitrogen), respectively. They were then supplemented with 2 mM glutamine (used just for CF10), 50 µg ml<sup>-1</sup> gentamicin (Invitrogen), and 10% Fetal Bovine Serum (Invitrogen). The cultures were kept in an incubator at 37 °C, 5% CO<sub>2</sub>, 100% humidity, and were replicated every 3 days by trypsinization (0.25% trypsin-EDTA, Invitrogen). The cells were seeded onto the patterned substrates at a density of 8×10<sup>5</sup> cells/dish and incubated for 48 or 72 h before fixation. Alternatively, the cells were transfected with different DNAs at the concentration of 3 µg per 100 mm plastic dish for mGluR1-Flag, mGluR5-Flag, CRF1, and 5-HT<sub>2A</sub> receptors and 1µg per 100 mm plastic dish for the other constructs used. The cells were transfected using the calcium phosphate method as described previously by Ferguson et al.<sup>38</sup>

#### 4.2.4 Neuronal cultures

Cortical neuron cells (CD-1 strain mice, 14-15 day embryonic age) were also investigated. Primary cortical neurons were dissociated in Neurobasal™ media supplemented with 0.5 mM L-glutamine, 2% B<sub>27</sub> and 0.8% N<sub>2</sub> supplements, and 50 units mL<sup>-1</sup> penicillin-streptomycin (Invitrogen). Cultures were then plated onto the patterned surfaces at a density of 1-1.5×10<sup>6</sup> cells/dish. The cultures were incubated at 37 °C for 7-14 days. The media was also changed every 2-3 days. Animal handling protocol was in accordance with Western University (The University of Western Ontario) Animal Care Committee.

#### 4.2.5 Immunofluorescence staining

HEK and CF10 cells were fixed using a solution of 4% paraformaldehyde prepared in phosphate buffered saline (PBS, pH 7.4, Invitrogen). The cells were then permeabilized in 0.5% Triton-X (Triton®X100, Sigma-Aldrich) prepared in PBS for 5 min. Non-specific binding of proteins and antibodies was prevented by incubation with a blocking solution of 1% bovine serum albumin (BSA, Sigma-Aldrich) + 2.5% goat serum (Invitrogen) in PBS. The cells were incubated over night with different primary antibodies prepared in 0.1% BSA + 0.1% Triton-X solution. The dilution used was: mouse anti-beta actin IgG1 (1:100, Abcam® Inc.), rabbit anti-Flag (1:100, Sigma-Aldrich). The next day, the cells were rinsed 3 times with PBS, and incubated for 1 hour with different secondary antibodies at the dilution of 1:1000 in the same solution as primary antibodies. The secondary antibodies used were goat anti-mouse - Alexa Fluor® 633, goat anti-rabbit Alexa Fluor® Rhodamine and goat anti-mouse Alexa Fluor® 488. Alexa Fluor® Phalloidin 488/633 is also used for non-transfected CF10 and HEK cells. Thereafter, the cells were stained for nucleus by using HOECHST (1:1000) in PBS for 10 min. The cells were rinsed again three times with PBS and the coverslips mounted to glass slides with

IMMU.MOUNT mounting media from Thermo Scientific<sup>®</sup>. Neuronal cells also stained with synaptosin-rabbit (1:100 Molecular Probes) and PSD 95-mouse (1:100 Millipore MAB1596) following the same protocol as described above for the immortalized cell lines.

## 4.2.6 Characterization

### 4.2.6.1 Optical and widefield imaging

Images of the patterned substrates and the fixed cells were carried out in the bright field mode using Zeiss Axioskop2 MAT microscope with a QImaging Retiga 1300 CCD digital camera. Widefield images are also obtained by Zeiss LSM 510 META Multiphoton Confocal Laser Scanning Microscope with an AxioCam HRm CCD camera, respectively.

### 4.2.6.2 Atomic force microscopy (AFM)

AFM images were collected with a Bioscope Catalyst (Bruker), operating in tapping mode. A silicon cantilever with a spring constant of  $40 \text{ N m}^{-1}$  and an oscillating frequency of 325 kHz (NSC-15, Micromasch) was used.

### 4.2.6.3 Fluorescence microscopy

Fluorescence imaging of the cell/neuron components was performed with Zeiss LSM 510 META Multiphoton Confocal Laser Scanning Microscope.

## 4.3 Results and discussion

### 4.3.1 Characterization of fluoropolymer patterned surface

#### 4.3.1.1 Optical imaging

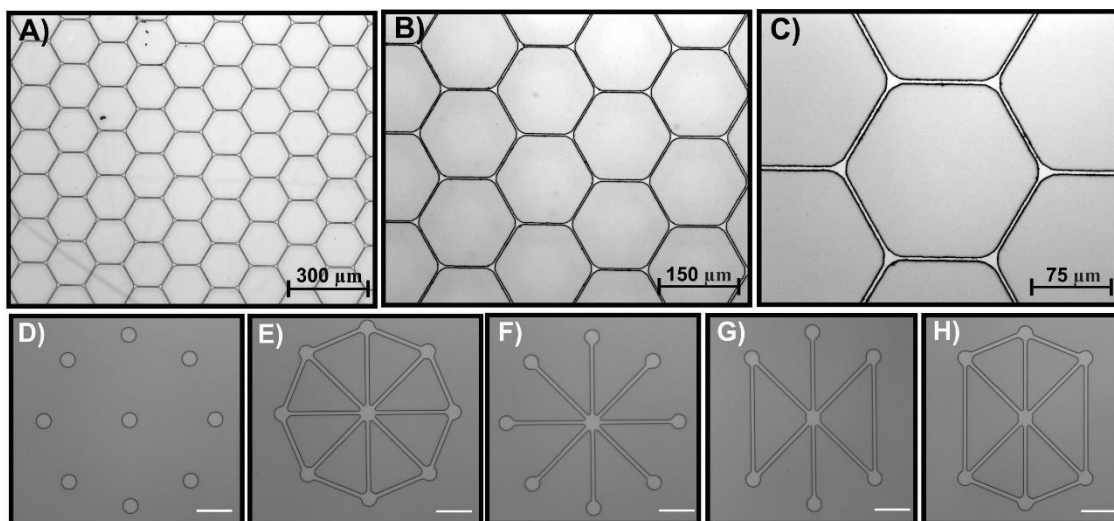


**Figure 4.2** Optical images of the photoresist patterned substrates, taken in bright field. A-C) hexagonal grid-like pattern; D-H) isolated and connected reservoirs with different geometries. Scale bar in D-H represents 50 μm.

The shape, size, and separation of the patterned features for the fabricated substrates were easily controlled due to the versatility and high resolution of the photolithography process. A hexagonal grid-like pattern with triangular shaped nodes (20 μm) and slender channels (100 μm long, 5 μm wide) connecting them (**Figure 4.2 A-C**) were designed to provide simple connections between cells and more specifically to create circuits of neuronal cells at synapses. In addition, patterned connected reservoirs with different geometries (**Figure 4.2 D-H**) were fabricated in order to study the effect of geometry on cell growth. **Figure 4.2** shows the photoresist patterned substrates before fluoropolymer

deposition. The optical images of the final fluoropolymer patterned substrates are shown in **Figure 4.3**. The lack of optical contrast is due to the very thin fluoropolymer thin film (~25 nm),

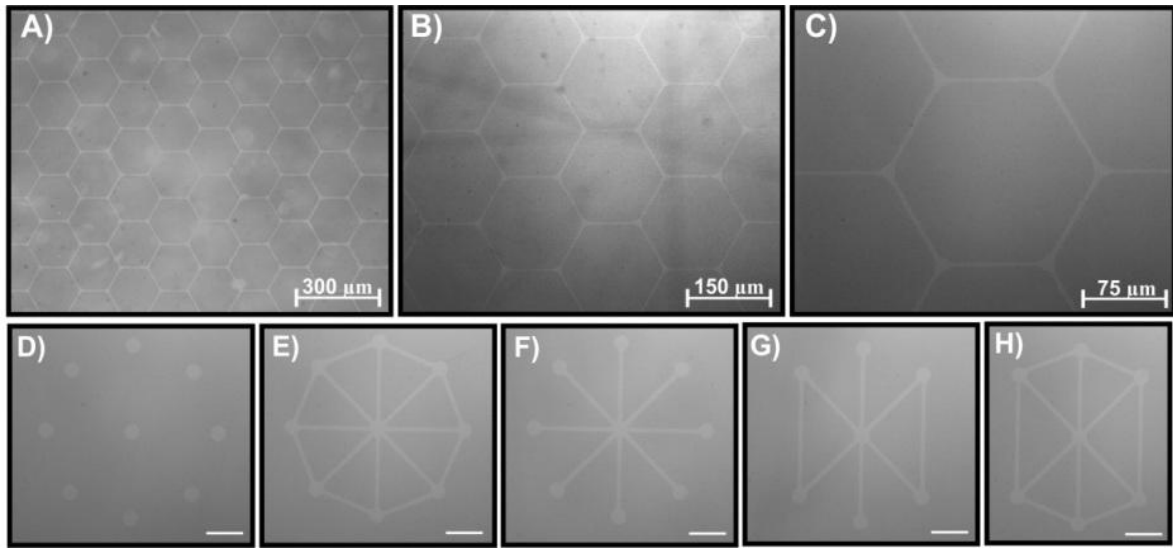


**Figure 4.3** Bright field optical images of fluoropolymer patterned substrates with different geometries. A-C) hexagonal grid-like pattern; D-H) five different geometries of isolated and connected reservoirs; The scale bar in images D-H represents 50  $\mu\text{m}$ .

**Figure 4.4** shows the unit cell of the utilized mask on the left side of image which includes five different geometries from isolated reservoirs (A) to connected reservoirs (B-E) with different distances and numbers of connections. As shown in **Figure 4.4**, the length of channel between two green reservoirs is 70  $\mu\text{m}$ , whereas the distances between two blue or two red reservoirs are 100 and 200  $\mu\text{m}$ , respectively. The diameters of all reservoirs and the widths of the channels are 20 and 5  $\mu\text{m}$ , respectively. These different geometries give one an opportunity to study single cells and also connected cells on the

same sample simultaneously under identical conditions. Furthermore, it helps to reveal cell-cell interactions with respect to the numbers and lengths of connections.

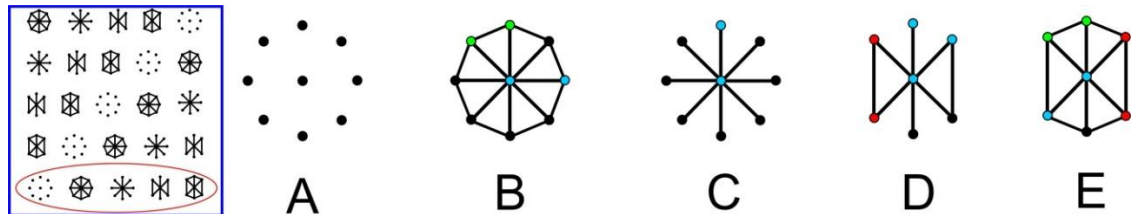


**Figure 4.4** Schematic demonstration of different geometries of connected reservoirs on patterned substrates.

#### 4.3.1.2 AFM

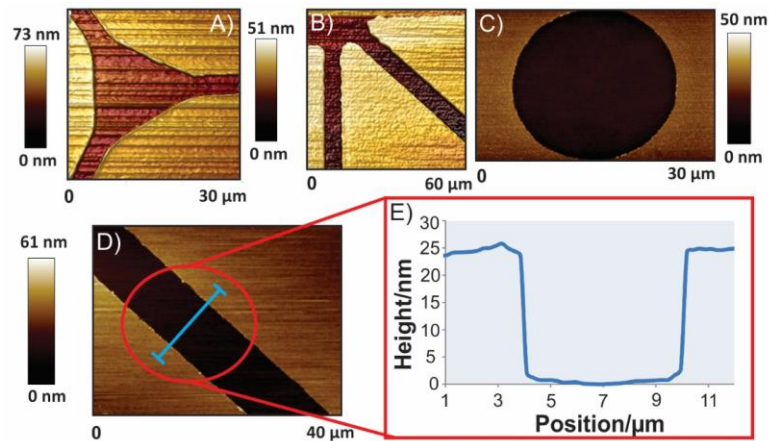


**Figure 4.5** AFM height images of A) a node of hexagonal grid-like pattern; B) channels of connected reservoirs; C) a reservoir; D) a channel on hexagonal grid-like pattern; E) cross section of a channel showing the thickness ( $25 \pm 5$  nm) of fluoropolymer thin film deposited on the substrate; A and B are the 3D AFM images.

AFM imaging was used to evaluate the qualities of fabricated channels and the thickness of the fluoropolymer thin film. **Figure 4.5 A-D** clearly demonstrates the integrities of the different fluoropolymer patterned substrates. The thin film of fluoropolymer was measured to have a thickness of  $25 \pm 5$  nm (**Figure 4.5 E**).

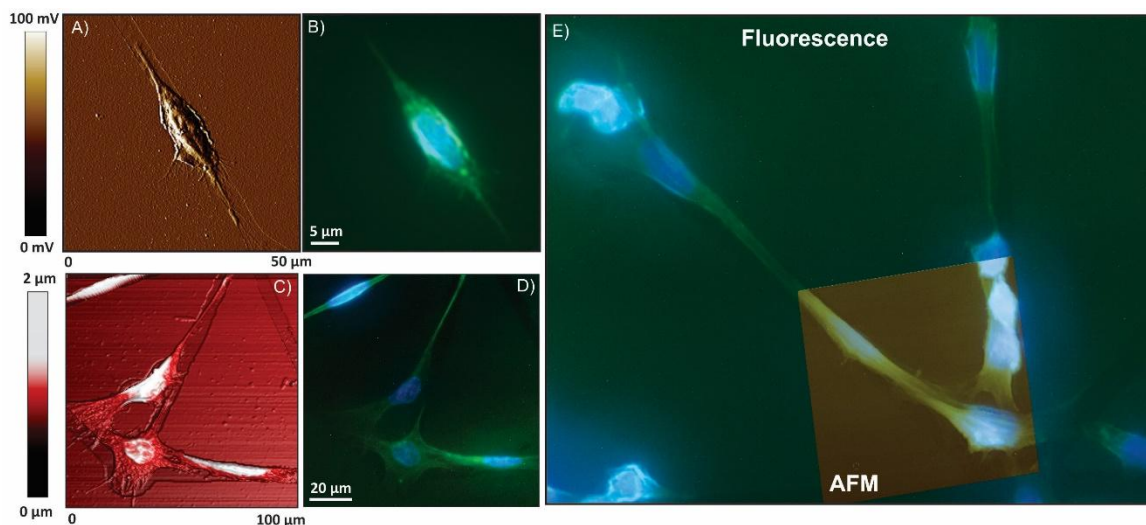


**Figure 4.6** AFM (A, and B) and wide field fluorescence (B, and D) of micropatterned CF10 cells; E) Overlay fluorescence and AFM image of patterned CF10 cells grown inside the channels. A-D) Transfected CF10 cells with CRF<sub>1</sub>; E) Non-transfected CF10 cells. B, and D) Green is for YFP and blue for HOECHST. E) Green is for Alexa Fluor<sup>®</sup> 488 Phalloidin, and blue for HOECHST.

It is observed that some defects of the edges of channels did not affect the cell/neuron growth negatively (**Figure 4.6**). Thus, cells can grow easily through channels while they are repelled by fluoropolymer surface.<sup>16</sup> Overall, the characterization of these new patterns demonstrates that the combination of photolithography and plasma deposition is a promising fabrication technique to prepare patterned surfaces possessing different

geometries. Combined AFM with fluorescence also gives one much detailed morphological information of the cell membrane (**Figure 4.6**).

#### 4.3.2 Non-transfected cell proliferation on patterned substrates

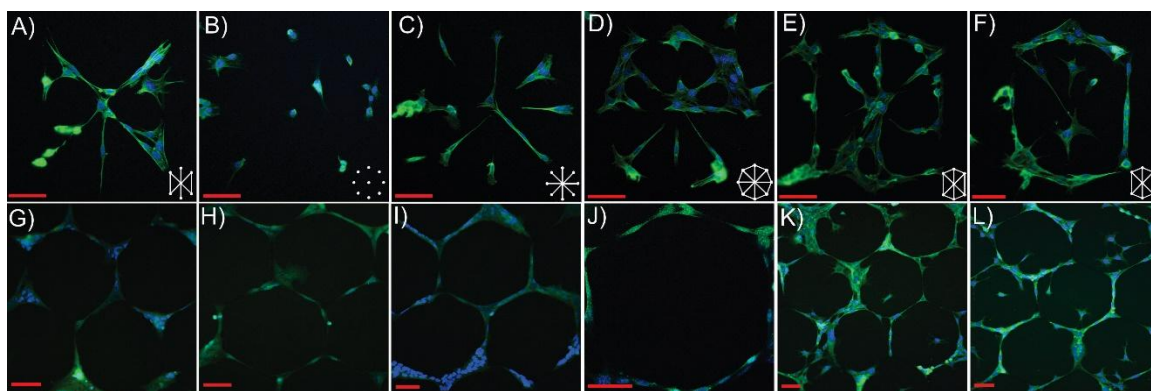


**Figure 4.7** Confocal fluorescence images of the growth of non-transfected HEK 293 and CF10 cell lines on patterned substrates; A-F) Non-transfected CF10 cells grown on patterned reservoirs substrates; G-J) Non-transfected HEK 293 cells grown on hexagonal grid-like patterned substrates; K, and L) Non-transfected CF10 cells grown on hexagonal grid-like patterned substrates; Blue represents HOECHST nuclear staining in all images; Actin (488 nm) and Alexa Fluor 488 Phalloidin are stained in green for HEK 293 cells and CF10 cells, respectively to show cell body; All scale bars are 50  $\mu\text{m}$ .

Prior to studying the growth of more challenging cell lines on the patterned substrates, it was first of interest to assess the behavior of two common cell lines, human embryonic kidney (HEK) 293 and CF10 cells on the patterns. HEK 293 cells have been widely-used in cell biology research for many years and are a well-known and established cellular model.<sup>39,40</sup> The widespread use of this cell line is due to its rapid growth rate, easy maintenance and readily transfectability by the various techniques, including calcium



phosphate method.<sup>38</sup> CF10 cells are a prion protein (PrP<sup>C</sup>-null) neural cell line derived from PrP<sup>0/0</sup> mice.<sup>41</sup> Due to the difficulty of cultivating primary cultures, this cell line was used in this work as a model of neuronal cells. The results obtained for CF10 cells on the patterned substrates were compared with the ones for HEK 293 cells.

**Figure 4.7** shows that both cell lines were able to attach to the substrates, forming different arrays according to the geometry of the pattern. The cells were able to survive and form connections in all the geometries tested. In some locations of the patterned substrates, it was observed that a few cells extended across a fluoropolymer area to interact with cells placed within channels. During the plating of cells on the substrate, they were placed everywhere, even on the fluoropolymer surface. Most cells that were on the fluoropolymer surface could not adhere and survive due to the hydrophobicity of the fluoropolymer surface. Thus, they were easily washed away during the staining process. Despite this, a few cells that formed tight connections with the ones located in the channels remained in the fluoropolymer areas.

In comparison with the HEK 293 cells, the CF10 cells grew and spread better on the patterns (**Figure 4.7**). As shown in **Figure 4.7 K and L**, they formed more hexagonal grid-like patterns on the substrates. This can likely be attributed to their inherent size and morphology, which more closely matches the relatively narrow width (5  $\mu\text{m}$ ) of the channels. Due their high growth rate, the number of CF10 cells plated had to be optimized to prevent the substrate from being overloaded with those cells. This was the key point for CF10 cells, as they grew readily and massively when they were plated on the micropatterned substrates or even on regular confocal dishes. These results suggest that these patterns can also be used for neural cells in order to study the neural communication. The control dishes represent the growth and transfections of cells on

regular confocal dishes (**Figure 4.8**). Glass bottom confocal dishes from MatTek were used for control samples.

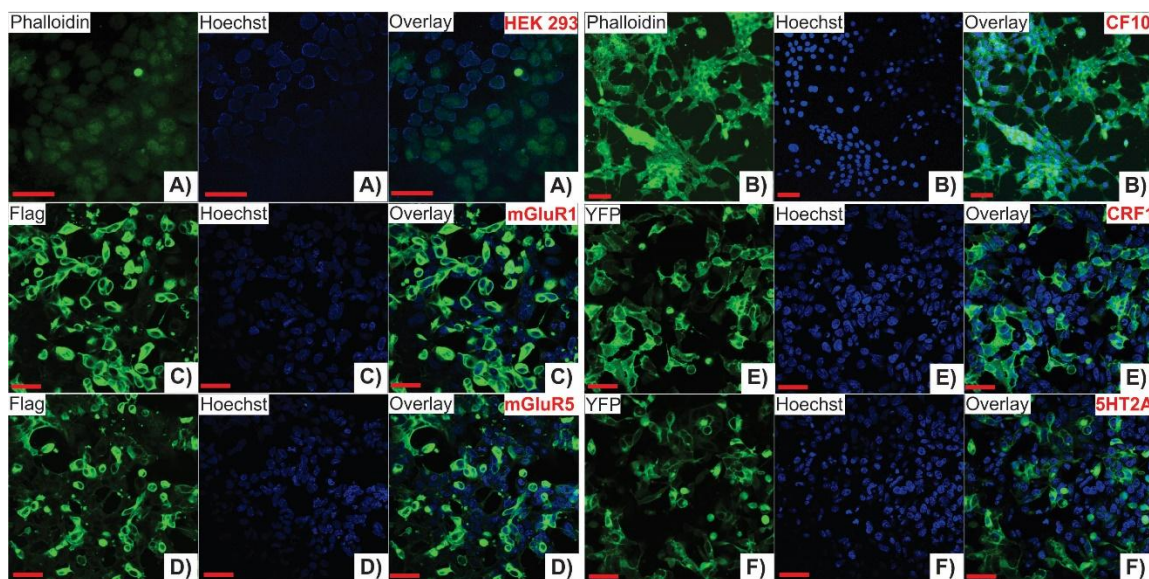


**Figure 4.8 Confocal Fluorescence images of control samples on confocal dishes; A) Non-transfected HEK 293 cells B) Non-transfected CF10 cells; C-F) HEK 293 cells transfected with mGluR1, mGluR5, CRF1, and 5HT2A, respectively; number of cells in all dishes:  $8 \times 10^5$  cells/dish; Alexa Fluor<sup>®</sup> 488 Phalloidin, Flag, and YFP are stained in green showing cells bodies and receptors; HOECHST is used for nuclear staining in blue; All scale bars represent 50  $\mu\text{m}$ .**

### 4.3.3 Micropatterned transfected cells

Glutamate is the major excitatory neurotransmitter in the brain and is essential for integrative brain functions and neuronal cell development. Glutamate exerts its actions by interacting with two major types of receptors: ionotropic and metabotropic. mGluRs are a type of glutamate receptor that is active through an indirect metabotropic process. Unlike ionotropic receptors, mGluRs are not ion channels. They are indirectly linked with ion-

channels on the plasma membrane of the cell through signal transduction mechanisms, often G proteins. They are members of the group C family of GPCRs. Like all glutamate receptors, mGluRs bind glutamate, an amino acid that functions as an excitatory neurotransmitter. Group I mGluRs (mGluR 1 and 5) are implicated in a number of brain disorders and a clearer understanding of mGluR signalling in different neurological pathologies will be important for understanding the underlying molecular aspects of the disease as well as to develop pharmacotherapies. mGluRs play a key role in studying different types of neurological disorders such as Epilepsy's, Huntington's, Alzheimer's, Parkinson's diseases or even in drug addiction. These receptors have also been implicated in cell proliferation and cancer. It has been shown that mGluR5 regulates proliferation, differentiation and guidance of migration of neuronal progenitor cells.<sup>42,43</sup> In addition, altered mGluR1 signaling has been associated with specific types of lung cancer.<sup>44</sup>

Serotonin (5HT<sub>2</sub>R) and CRF (CRFR) receptors are other members of the GPCR family used in this work. 5HT<sub>2</sub> receptors are involved in diverse mental illnesses such as schizophrenia, depression, anxiety, obsessive-compulsive disorder and others.<sup>45,46</sup> CRFR has an important role in stress-mediated responses. Interaction between 5HT<sub>2</sub>R and CRF1R has been shown to regulate anxiety behavior.<sup>47</sup> Both receptors are important targets for the development of drugs treating anxiety and depression. Due to the importance of these GPCRs as therapeutic targets, cells transfected with mGluR1, mGluR5, CRF1, and 5HT<sub>2</sub>A were selected to study on the micropatterns. We evaluated if after transfection the cells would still survive when plated in the micropatterns, and if the expression of different GPCRs would influence their behavior on those patterns. Based on the compatibility of CF10 cells with the patterns as described above, they were selected as the transfected cell type.

We compared the cell proliferation/survival of normal cells to those that were transfected with the DNAs for the expression of the different GPCRs. **Figure 4.9** shows images of GPCR-transfected CF10 cells patterned in five different geometries. The CF10 cells transfected with the aforementioned receptors grew on the substrates readily and were directed with a good agreement to the patterned features. As transfection is a stressful process for the cells, they are more susceptible to death than non-transfected cells. It can be clearly seen in **Figure 4.9** that fewer transfected cells attached to the substrates compared with the non-transfected cells (**Figure 4.7**), even though the same number of cells were plated in both cases. In addition, the morphologies of the transfected cells did not look as healthy.

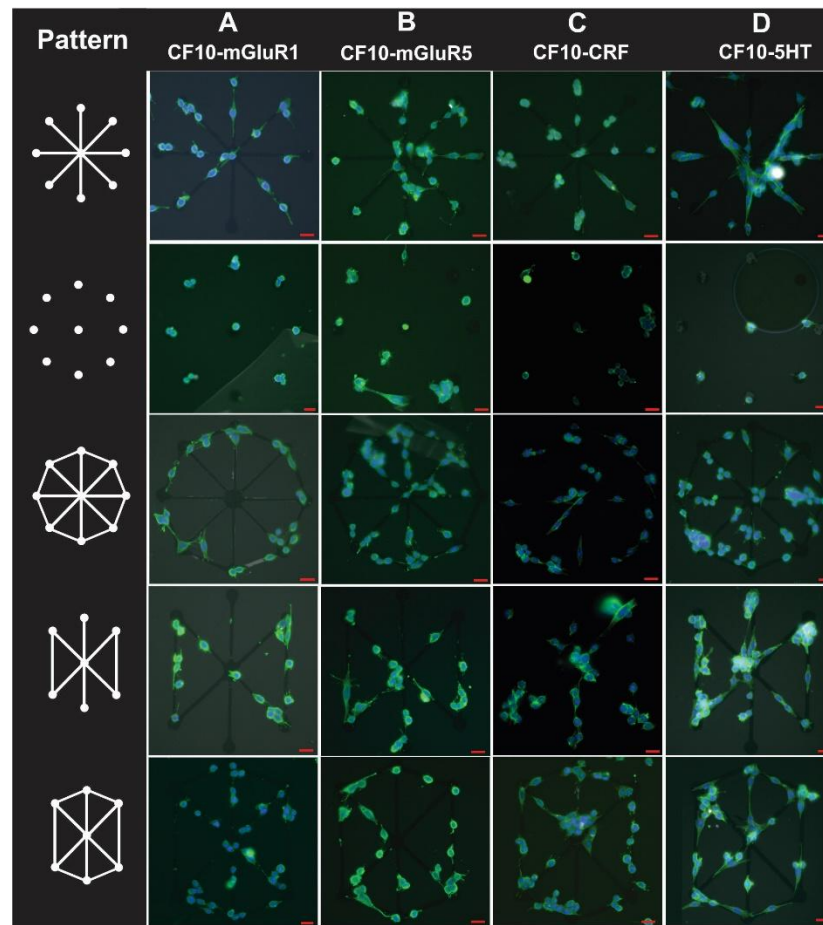


**Figure 4.9** Widefield fluorescence images of micropatterned CF10 cells transfected with: row A) mGluR1-Flag; B) mGluR5-Flag; C) CRF1-YFP; D) 5HT2A-YFP receptors on five different geometries of reservoirs; Blue represents HOECHST nuclear staining, receptors tagged with Flag were labeled with Alexa Fluor 488 (green, 488nm); YFP label is also shown as green (514 nm); All the scale bars represent 20  $\mu\text{m}$ .

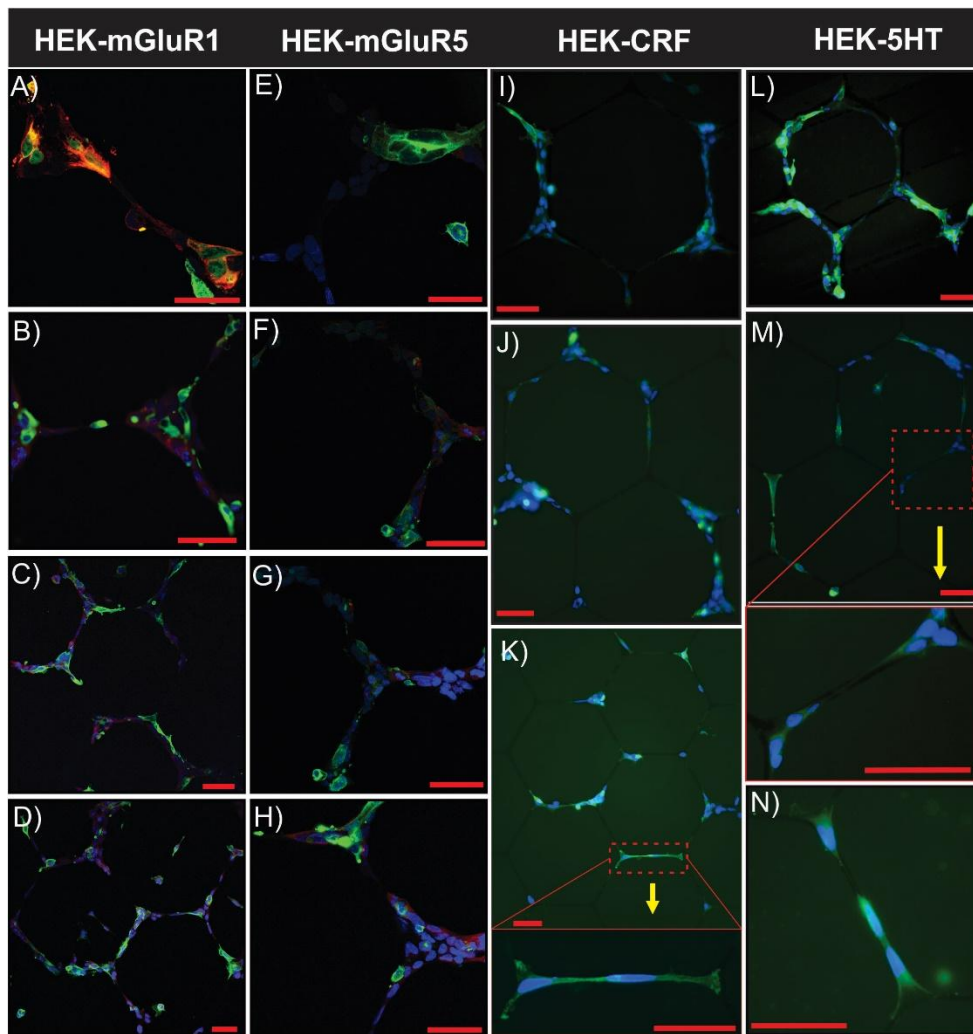


**Figure 4.10** Confocal (A-H) and widefield (I-N) fluorescence images of HEK 293 cells transfected with A-D) mGluR1-Flag; E-H) mGluR5-Flag; I-K) CRF-YFP; L-N) 5HT-YFP; Blue represents HOECHST nuclear stain, green is for Flag (488 nm), and YFP (514 nm); red is for actin 633 nm; All scale bars are 50  $\mu$ m.

The proliferation rates were also smaller in the transfected cells, independent of the receptor used. Thus, the most significant factor was the transfection itself and not the

expression of the specific receptor. Despite these differences compared to non-transfected cells, all of transfected cells were able to form the five geometries on the substrates. As described above, although the HEK cells did not conform to the patterns as readily as the CF10 cells, they exhibit higher transfection efficiency than the CF10 cells.

Therefore, HEK 293 cells transfected with the same receptors as above were also studied on the micropatterned substrates (**Figure 4.10**). Similar to the results obtained for CF10 cells, the transfection process in HEK 293 cells also reduced their survival on the substrates. In addition, there was again no significant difference in terms of how the cells transfected with the different receptors interacted with the substrates. Again, the results with the transfected cells suggested that these patterns were better platforms for neuronal cells. The results obtained here for the immortalized cell lines constitute the basis for advanced studies using transfected cells in micropatterned substrates.

#### 4.3.4 Neuronal circuit arrangement on patterned substrates

Primary mice neuronal cells were cultured on the samples patterned with the hexagonal grid-like substrates and then fixed after 7-14 days in vitro (DIV). **Figure 4.11** shows the fluorescence images of neurons arranged within the hexagonal grids. It was observed that in most cases, the cell bodies were located within the triangular nodes as desired, with the projections extending along the channels to create circuits with other neurons (**Figure 4.11**). Furthermore, by increasing the incubation time from 7 to 14 days, the number of projections increased, as the circuitous patterns were completely filled with numerous projections, even to the point of overlapping significantly (**Figure 4.11D**). There were occasions where projections were observed to extend across a fluoropolymer area to interact with neurons at the other side (**Figure 4.11C**). During imaging acquisition, it was easy to observe that those bridging projections were loose and not physically attached to the fluoropolymer area. Thus, the projections were merely tethered at either end, and it is

believed that this is further indication that projections do not have adherence complexes along the entire length, only in certain locations. The ability to pattern neurons into networks may be very useful to study synapse transmission.

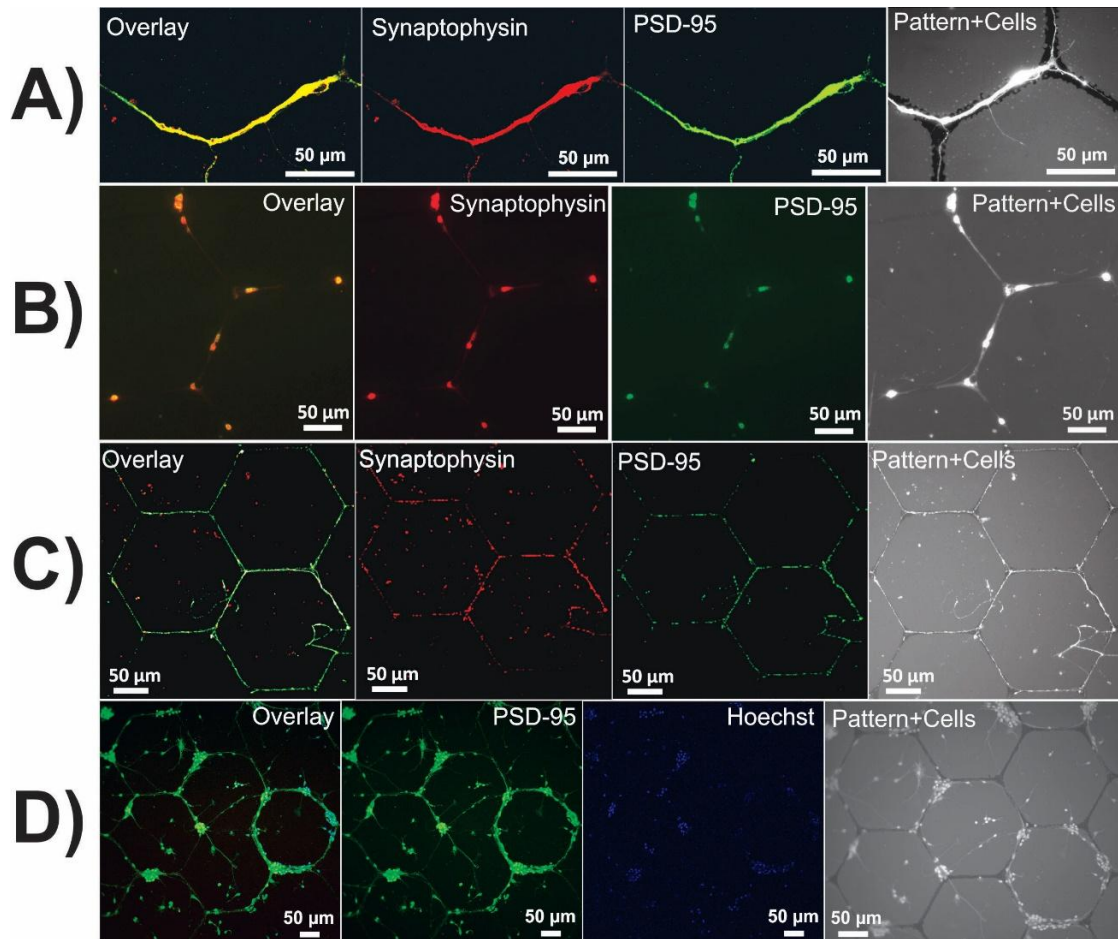


**Figure 4.11** Widefield (B, and D) and confocal (A, and C) fluorescence images of cortical neuron circuit arrangement; A) 7 DIV; B-D) 14 DIV; Synaptic markers: Synaptophysin (red) and PSD-95 (green) were used; Blue represents HOECHST nuclear staining; All scale bars are 50 µm. A-C)  $1 \times 10^6$  cells/dish; D)  $1.5 \times 10^6$  cells/dish.



Neurons are particularly useful as sensing elements as the electrical activity can be monitored in response to chemical influences in the culture environment, and so the networks can be organized on the microelectrodes for optimal contact. Moreover, the ability to isolate neurons has always been a challenge for biologists, as they aggregate once cultured. Hence, these patterns provide the opportunity to study the communication between neurons in a well-controlled architecture.

Finally, immunofluorescence staining was used to image synaptic markers. We could also visualize the cell body by using nuclear staining, which provided an indication of where they were located and the number of cells/channel. Both synaptic markers, synaptophysin and PSD-95, were visible as fluorescent puncta along the projections and around the cell bodies (**Figure 4.11**). These are synaptic sites and are indicative of neuronal communication. There is no preferential location for the synapses, as the projections all along the channels display the same behaviour.

#### 4.3.5 Spine localization in isolated neuronal projections

Different micropatterning techniques have recently been developed for in vitro neural studies.<sup>48-55</sup> However, it is still challenging to isolate the projections of connected neurons. In this study, we combined the cell micropatterning with atomic force microscopy to investigate the localization of spines in isolated projections of cortical neurons. Atomic force microscopy has the ideal spatial resolution to probe small features with sub nano-scale dimensions. It is especially useful for biological samples in which the small structures cannot be easily probed using conventional fluorescence microscopies. The isolated projections of neurons are clearly shown in **Figure 4.12**. By decreasing the number of cells, the probability of having single isolated neurons connected together through their projections is increased (**Figure 4.12 A-C**). **Figure 4.12 A and D** show the 2D AFM images of isolated neuronal projections with 1 and 1.5

million cells/dish, respectively. However, even with higher number of cells, it was still possible to isolate the neuronal projections using these patterns as well as probing the localization of spines (**Figure 4.12 D-G**).

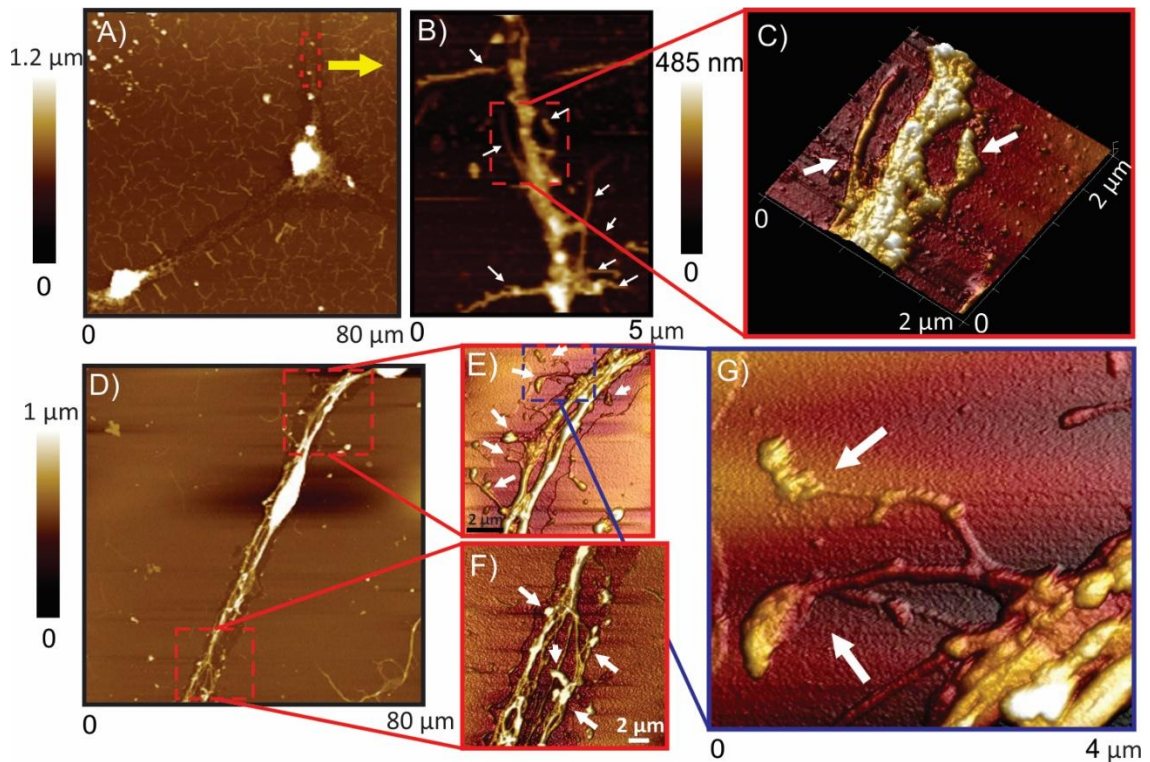


**Figure 4.12** AFM height images of isolated neuronal projections showing the spines localization A, D) 2D AFM images of isolated neuronal projections; B) AFM image of the selected area shown in A; C) 3D AFM image of the selected area shown in B; E, F) 3D AFM image of the selected area shown in D; G) 3D AFM image of selected area in E showing the spines with higher magnification; Arrows show the spine localizations of isolated neuronal projections.

## 4.4 Conclusions

In the present work, we showed the capability of newly optimized fluoropolymer patterned substrates to direct neuronal projections and transfected cells with specific members of GPCRs. It is shown that transfection of two different immortalized cell lines with GPCRs did not alter the behaviour of cells in the micropatterns and their level of growth was affected just due to the cellular stress during transfection process. Aside from that, these patterns provide a well-organized condition to isolate neuronal projections. This provides the possibility of investigating the cellular and neuronal connections in well-controlled positions in high uniformity, thus providing a useful tool for in vitro cellular research. Finally, atomic force microscopy is employed to reveal the localization and morphology of spines with nano-scale resolution for well-isolated neuronal projections compared to conventional and confocal fluorescence microscopies. The combination of this method with fluorescence microscopy provides a promising tool for advanced studies using in vitro immortalized cell lines and neurons; specifically in works focusing at spines. This approach would also be ideal to study synapse events under physiological and pathological conditions.

## 4.5 References

- (1) Fujie, T.; Ahadian, S.; Liu, H.; Chang, H.; Ostrovidov, S.; Wu, H.; Bae, H.; Nakajima, K.; Kaji, H.; Khademhosseini, A.; *Nano Lett.*, (2013), 13, 3185.
- (2) Schwarzenbacher, M.; Kaltenbrunner, M.; Brameshuber, M.; Hesch, C.; Paster, W.; Weghuber, J.; Heise, B.; Sonnleitner, A.; Stockinger, H.; Schutz, G. J.; *Nat. Meth.*, (2008), 5, 1053.
- (3) Karnik, R.; Hong, S.; Zhang, H.; Mei, Y.; Anderson, D. G.; Karp, J. M.; Langer, R.; *Nano Lett.*, (2008), 8, 1153.

- (4) Engelmayr, G. C.; Cheng, M.; Bettinger, C. J.; Borenstein, J. T.; Langer, R.; Freed, L. E.; *Nat. Mater.*, **(2008)**, 7, 1003.
- (5) Kurpinski, K.; Chu, J.; Hashi, C.; Li, S.; *Proc. Natl. Acad. Sci. U. S. A.*, **(2006)**, 103, 16095.
- (6) Khademhosseini, A.; Langer, R.; Borenstein, J.; Vacanti, J. P.; *Proc. Natl. Acad. Sci. U. S. A.*, **(2006)**, 103, 2480.
- (7) Yamamura, S.; Kishi, H.; Tokimitsu, Y.; Kondo, S.; Honda, R.; Rao, S. R.; Omori, M.; Tamiya, E.; Muraguchi, A.; *Anal. Chem.*, **(2005)**, 77, 8050.
- (8) Gauvin, R.; Khademhosseini, A.; *ACS Nano*, **(2011)**, 5, 4258.
- (9) Marcon, L.; Addad, A.; Coffinier, Y.; Boukherroub, R.; *Acta Biomater.*, **(2013)**, 9, 4585.
- (10) Hughes, M. A.; Bunting, A. S.; Cameron, K.; Murray, A. F.; Shipston, M. J.; *J. Biomed. Mater. Res. A*, **(2013)**, 101A, 349.
- (11) Chen, W.; Sun, Y.; Fu, J.; *Small*, **(2013)**, 9, 1.
- (12) Zhu, M.; Baffou, G.; Meyerbröcker, N.; Polleux, J.; *ACS Nano*, **(2012)**, 6, 7227.
- (13) Kushiro, K.; Asthagiri, A. R.; *Langmuir*, **(2012)**, 28, 4357.
- (14) Choi, J.-C.; Doh, J.; *Lab Chip*, **(2012)**, 12, 4964.
- (15) Chen, W.; Villa-Diaz, L. G.; Sun, Y.; Weng, S.; Kim, J. K.; Lam, R. H. W.; Han, L.; Fan, R.; Krebsbach, P. H.; Fu, J.; *ACS Nano*, **(2012)**, 6, 4094.
- (16) Leclair, A. M.; Ferguson, S. S. G.; Lagugné-Labarthe, F.; *Biomaterials*, **(2011)**, 32, 1351.
- (17) Varma, S.; McLachlan, J.; Leclair, A.; Galarreta, B.; Norton, P.; Lagugné-Labarthe, F.; *Anal. Bioanal. Chem.*, **(2010)**, 396, 1159.
- (18) Lu, S.; Bansal, A.; Soussou, W.; Berger, T. W.; Madhukar, A.; *Nano Lett.*, **(2006)**, 6, 1977.

- (19) Huang, J.; Gräter, S. V.; Corbellini, F.; Rinck, S.; Bock, E.; Kemkemer, R.; Kessler, H.; Ding, J.; Spatz, J. P.; *Nano Lett.*, **(2009)**, *9*, 1111.
- (20) Cha, C.; Liechty, W. B.; Khademhosseini, A.; Peppas, N. A.; *ACS Nano*, **(2012)**, *6*, 9353.
- (21) Yoon, S.-H.; Kim, Y. K.; Han, E. D.; Seo, Y.-H.; Kim, B. H.; Mofrad, M. R. K.; *Lab Chip*, **(2012)**, *12*, 2391.
- (22) Pan, Z.; Yan, C.; Peng, R.; Zhao, Y.; He, Y.; Ding, J.; *Biomaterials*, **(2012)**, *33*, 1730.
- (23) Cheng, Q.; Li, S.; Komvopoulos, K.; *Biomaterials*, **(2009)**, *30*, 4203.
- (24) Liu, Y.; Sun, S.; Singha, S.; Cho, M. R.; Gordon, R. J.; *Biomaterials*, **(2005)**, *26*, 4597.
- (25) Co, C. C.; Wang, Y.-C.; Ho, C.-C.; *J. Am. Chem. Soc.*, **(2005)**, *127*, 1598.
- (26) Yang, C.-Y.; Liao, T.-C.; Shuai, H.-H.; Shen, T.-L.; Yeh, J. A.; Cheng, C.-M.; *Biomaterials*, **(2012)**, *33*, 4988.
- (27) Wang, J.; Tham, D.; Wei, W.; Shin, Y. S.; Ma, C.; Ahmad, H.; Shi, Q.; Yu, J.; Levine, R. D.; Heath, J. R.; *Nano Lett.*, **(2012)**, *12*, 6101.
- (28) Yap, F. L.; Zhang, Y.; *Biosens. Bioelectron.*, **(2007)**, *22*, 775.
- (29) Falconnet, D.; Csucs, G.; Michelle Grandin, H.; Textor, M.; *Biomaterials*, **(2006)**, *27*, 3044.
- (30) Lim, J. Y.; Donahue, H. J.; *Tissue Eng.*, **(2007)**, *13*, 1879.
- (31) Martines, E.; Seunarine, K.; Morgan, H.; Gadegaard, N.; Wilkinson, C. D. W.; Riehle, M. O.; *Nano Lett.*, **(2005)**, *5*, 2097.
- (32) Curtis, A. S. G.; Casey, B.; Gallagher, J. O.; Pasqui, D.; Wood, M. A.; Wilkinson, C. D. W.; *Biophys. Chem.*, **(2001)**, *94*, 275.
- (33) Hering, H.; Sheng, M.; *Nat. Rev. Neurosci.*, **(2001)**, *2*, 880.
- (34) Magalhaes, A. C.; Dunn, H.; Ferguson, S. S. G.; *Br. J. Pharmacol.*, **(2012)**, *165*, 1717.

- (35) Blad, C. C.; Tang, C.; Offermanns, S.; *Nat. Rev. Drug Discov.*, **(2012)**, *11*, 603.
- (36) Rosenbaum, D. M.; Rasmussen, S. G. F.; Kobilka, B. K.; *Nature*, **(2009)**, *459*, 356.
- (37) Overington, J. P.; Al-Lazikani, B.; Hopkins, A. L.; *Nat. Rev. Drug Discov.*, **(2006)**, *5*, 993.
- (38) Ferguson, S. G.; Caron, M. In *G Protein Signaling*; Smrcka, A., Ed.; Humana Press: 2004; Vol. 237, p 121.
- (39) Graham, F. L.; Smiley, J.; Russel, W. C.; Nairn, R.; *J. Gen. Virol.*, **(1977)**, *36*, 59.
- (40) Maus, L.; Dick, O.; Bading, H.; Spatz, J. P.; Fiammengo, R.; *ACS Nano*, **(2010)**, *4*, 6617.
- (41) Manson, J. C.; Clarke, A. R.; Hooper, M. L.; Aitchison, L.; McConnell, I.; Hope, J.; *Mol. Neurobiol.*, **(1994)**, *8*, 121.
- (42) Xiao, X. L.; Ma, D. L.; Wu, J.; Tang, F.-R.; *Brain Res.*, **(2013)**, *1493*, 1.
- (43) Jansson, L. C.; Louhivuori, L.; Wigren, H.-K.; Nordström, T.; Louhivuori, V.; Castrén, M. L.; Åkerman, K. E.; *Euro. J. Neurosci.*, **(2013)**, *37*, 1369.
- (44) Esseltine, J. L.; Willard, M. D.; Wulur, I. H.; Lajiness, M. E.; Barber, T. D.; Ferguson, S. S. G.; *Mol. Pharmacol.*, **(2013)**, *83*, 770.
- (45) Roth, B.; Hanizavareh, S. M.; Blum, A.; *Psychopharmacology*, **(2004)**, *174*, 17.
- (46) Gray, J. A.; Roth, B. L.; *Brain. Res. Bull.*, **(2001)**, *56*, 441.
- (47) Magalhaes, A. C.; Holmes, K. D.; Dale, L. B.; Comps-Agrar, L.; Lee, D.; Yadav, P. N.; Drysdale, L.; Poulter, M. O.; Roth, B. L.; Pin, J.-P.; Anisman, H.; Ferguson, S. S. G.; *Nat. Neurosci.*, **(2010)**, *13*, 622.
- (48) Roy, J.; Kennedy, T. E.; Costantino, S.; *Lab Chip*, **(2013)**, *13*, 498.
- (49) Odawara, A.; Gotoh, M.; Suzuki, I.; *Lab Chip*, **(2013)**, *13*, 2040.
- (50) Scott, M. A.; Wissner-Gross, Z. D.; Yanik, M. F.; *Lab Chip*, **(2012)**, *12*, 2265.
- (51) Kang, K.; Choi, S. E.; Jang, H. S.; Cho, W. K.; Nam, Y.; Choi, I. S.; Lee, J. S.; *Angew. Chem. Int. Ed.*, **(2012)**, *51*, 2855.

- (52) Fan, Y.; Xu, F.; Huang, G.; Lu, T. J.; Xing, W.; *Lab Chip*, **(2012)**, *12*, 4724.
- (53) Choi, J. H.; Lee, H.; Jin, H. K.; Bae, J.-s.; Kim, G. M.; *Lab Chip*, **(2012)**, *12*, 5045.
- (54) Baek, N. S.; Kim, Y. H.; Han, Y. H.; Offenhäusser, A.; Chung, M.-A.; Jung, S.-D.; *J. Neurosci. Methods.*, **(2012)**, *210*, 161.
- (55) Wissner-Gross, Z. D.; Scott, M. A.; Ku, D.; Ramaswamy, P.; Fatih Yanik, M.; *Integr. Biol.*, **(2011)**, *3*, 65.

## Chapter 5

### 5 Enabling controlled positioning of analytes and cells on a plasmonic platform for surface-enhanced Raman spectroscopy: where surface chemistry meets biology<sup>2</sup>

The rise of molecular plasmonics and its application to ultrasensitive spectroscopic measurements has been enabled by the rational design and fabrication of a variety of metallic nanostructures. Advanced nano and microfabrication methods are key to the development of such structures, allowing one to tailor optical fields at the sub-wavelength scale, thereby optimizing excitation conditions for ultrasensitive detection. In this work, the control of both analyte and cell positioning over a plasmonic platform is enabled using nanofabrication methods involving patterning of fluorocarbon (FC) polymer ( $C_4F_8$ ) thin films over a plasmonic platform fabricated by nanosphere lithography (NSL). This provides the possibility to probe biomolecules of interest in the vicinity of cells using plasmon-mediated surface-enhanced spectroscopies. In this context, we demonstrate the surface-enhanced biosensing of glycan expression in different cell lines by surface-enhanced Raman spectroscopy (SERS) on these plasmonic platforms functionalized with 4-mercaptophenylboronic acid (4-MPBA) as the Raman reporter. These cell lines include human embryonic kidney (HEK 293), C2C12 mouse myoblasts, and HeLa (Henrietta Lacks) cervical cancer cells. A distinct glycan expression is observed for cancer cells compared to other cell lines by confocal SERS mapping. This suggests the potential application of these versatile SERS platforms for differentiating cancerous from non-cancerous cells.

---

<sup>2</sup> A version of this chapter has been submitted



## 5.1 Introduction

Discovered almost four decades ago, surface-enhanced Raman spectroscopy (SERS)<sup>1</sup> and subsequent techniques such as surface-enhanced fluorescence (SEF)<sup>2</sup> and surface-enhanced infrared spectroscopy (SEIRS)<sup>3-5</sup> have developed into mature methods to give unprecedented levels of sensitivity. SERS in particular provides ultra-high sensitivity down to attomolar concentrations and even further to a single molecule level.<sup>3,6-10</sup> More importantly, the use of these surface-enhanced techniques has enabled biosensing and biomolecular recognition with ultra-high sensitivity, opening a wealth of applications to probe intimate biological processes with minimized intrusion, better specificity and higher reproducibility.<sup>10-14</sup> The interactions between biomolecules and their changes in conformation in response to stimuli are processes that can be probed at the monolayer level with lower light irradiance and shorter acquisition time, thereby reducing experimental invasion and physiological stress.

Key to the success of high spatial resolution optical spectroscopy is advances in micro and nanofabrication techniques that allow one to rationally design and reproducibly fabricate plasmonic platforms with controlled opto-geometric parameters.<sup>15-17</sup> The metallic platforms can be tailored, so that the localized surface plasmon resonance can be accurately tuned to a selected probe wavelength. In particular, highly reproducible plasmonic platforms with feature dimensions and inter-structure distances on the order of 10 nm are achieved by electron beam lithography and focused ion beam milling.<sup>18,19</sup> Among nanofabrication techniques to produce plasmonic platforms, NSL is an inexpensive and high-throughput technique capable of generating well-organized 2D and 3D periodic nanostructures.<sup>2,20,21</sup> Using NSL, the shape of the plasmonic platform can be

feasibly tuned based on the application to produce different features such as nanoscale triangles, pyramids, rings, overlaps, gaps, rod chains, and holes.<sup>21-24</sup>

To study monolayers at surfaces such platforms are ideal as the functionalization of the platform is homogeneous at the scale of the local measurement. In addition, SERS has been widely used for the detection of various biomolecules. For example, SERS platforms functionalized with aptamers have been successfully used for toxin and protein recognition.<sup>25,26</sup> Antibody functionalization of SERS surfaces to detect biomarkers of endocrine disrupting compounds was also described.<sup>27</sup> Furthermore, enzymatic processes such as histone demethylase activity have been probed using SERS assays.<sup>28</sup> However, using such platforms, significant challenges are still encountered in the study of biological processes, such as intracellular sensing,<sup>29</sup> chemical exchanges between cells or responses of cells to endogenous or exogenous stimuli.<sup>30,31</sup> One significant challenge arises from the inherently random growth of cells over most surfaces.<sup>32</sup> The positional control of cell growth over an array of plasmonic platforms would open possibilities for multiplexed parallel screening using SERS, SEF or other optical techniques involving a plasmon resonance that has been tuned to enhance a specific spectral region. Each cell position over a plasmonic platform would be defined by a set of spatial coordinates, allowing automated measurements over a large number of individual cells. Such an approach would in turn be the key to the acquisition of large data sets and thus statistically relevant information concerning biological processes. The control of cell density over the surface would provide the possibility to control and study cell-substrate and cell-cell interactions.<sup>33,34</sup> Our group has previously introduced a new method for cell positioning using plasma deposition of fluoropolymer thin film.<sup>32</sup> However, a plasmonic platform was not incorporated, so it was not possible to perform optical studies of analytes or cells mediated by surface-enhanced methods.

Herein, we introduce the development of the first platform that involves embedded plasmonic platforms organized in micro-scale patterns that direct cell adhesion and growth. This allows one to locate the analyte in defined microwell positions, depending on the feature pattern within the plasmonic sensing areas, to perform controlled plasmon-mediated surface-enhanced measurements. NSL is used to fabricate the SERS platform,<sup>35,36</sup> then a photolithographic method with a plasma induced fluorocarbon (FC)-polymer thin film deposition is used to provide windows over specific areas on the plasmonic platform for cell growth. In the second step, we demonstrate that different cell lines such as immortalized cells and neurons can accurately be positioned and grown over a plasmonic platform of interest. The application of this device in biosensing is also demonstrated by mapping the glycan expression in cell lines including human embryonic kidney (HEK 293), C2C12 mouse myoblasts, and cervical cancer cells (HeLa).

## 5.2 Experimental section

### 5.2.1 Materials

Standard glass microscope coverslips (22×22×0.15 mm) and microscope slides (25×75×1 mm) were purchased from VWR International and Fisher Scientific, respectively. Plastic dishes (35 mm) with glass bottoms (thickness of 0.16-0.19 mm) were purchased from MatTek Corporation. Nanostrip<sup>TM</sup> (90% sulfuric acid, 5% peroxymonosulfuric acid, <1% hydrogen peroxide, and 5% water) was purchased from Cyantek Corporation. The materials used in the photolithography process, Microposit<sup>TM</sup> SC1805<sup>TM</sup> positive photoresist and Microposit<sup>TM</sup> MF-319 developer were purchased from Rohm & Haas Electronic Materials, and the NANO<sup>TM</sup> Remover PG was purchased from MicroChem Corporation. Octafluorocyclobutane gas (C<sub>4</sub>F<sub>8</sub>) was purchased from BOC Edwards. The wafer mounting medium Crystalbond<sup>TM</sup> 509 was purchased from Aremco Products, Inc.,

and finally, the isopropyl alcohol (IPA) and acetone were purchased from Sigma Aldrich and used as received. 1  $\mu\text{m}$  polystyrene microspheres (10% w/w) were purchased from ThermoScientific Co (California, US). Sodium dodecyl sulfate, 4-nitrothiophenol (4-NTP) (80% purity) and 4-mercaptophenylboronic acid (90% purity) were obtained from Sigma-Aldrich (Missouri, US).

### 5.2.2 Fabrication process of FC-patterned platform

Microscope coverslips were cleaned in Nanostrip<sup>TM</sup> for 5 min and rinsed thoroughly with de-ionized (DI) water prior to use. The fabrication process, as outlined in **Figure 5.1**, was performed in four main steps. This includes NSL using an interface method, photolithography, plasma polymerization, followed by a lift-off process. NSL using the interface method was previously described in detail.<sup>2,21,37</sup>

Patterning of the plasmonic platform using optical lithography employed a patterned photoresist mask to protect regions of the plasmonic substrate. A positive photoresist was spin-coated onto the cleaned plasmonic substrate, with a thickness of approximately 500 nm, as measured by atomic force microscopy.<sup>32</sup> For the smaller features in range of 5  $\mu\text{m}$  or less, use of a thinner layer of photoresist led to sharper patterns. The photoresist was then soft-baked at 115 °C for 1 min to evaporate the solvent, followed by baking in an oven at 90 °C for 20 min. It was then exposed to ultra-violet light through a chrome mask that had the desired pattern designed on it. For this purpose, a Karl Suss MA6 contact mask aligner (Suss MicroTech) was used for 8 s at an intensity of 12 mW cm<sup>-2</sup>.

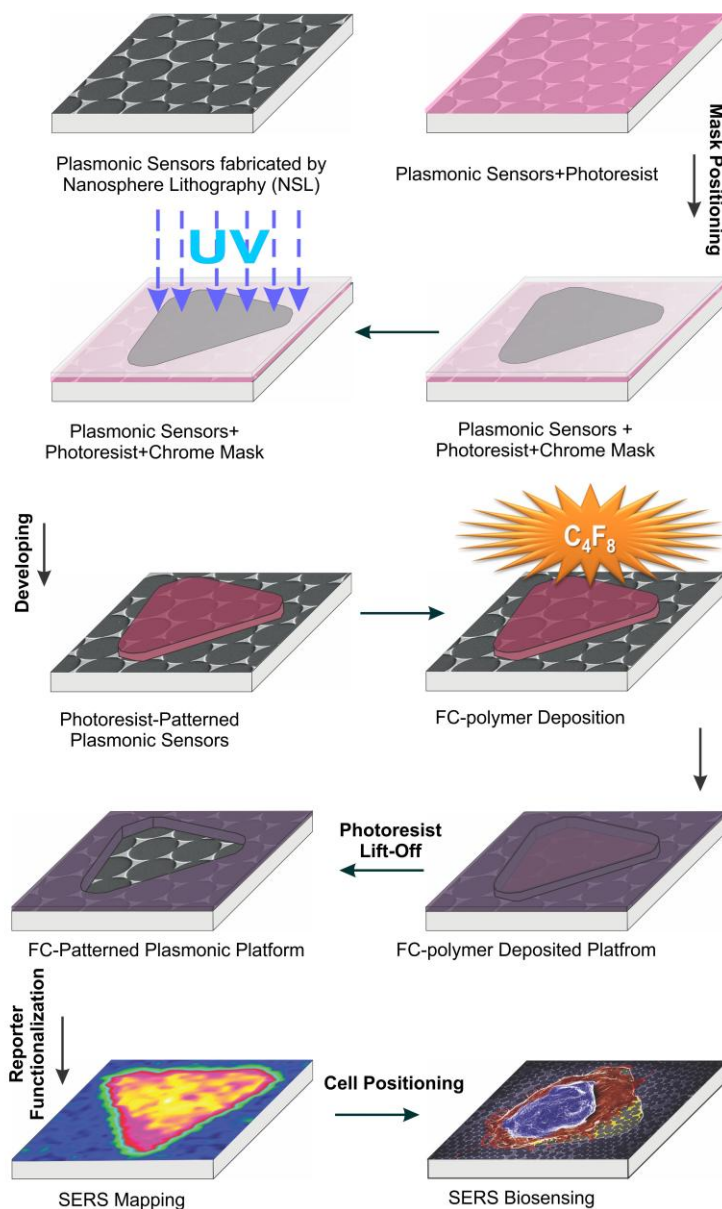


**Figure 5.1 Schematic illustration of the fabrication process for the FC-patterned plasmonic platform.**

The exposed photoresist was then removed by developing in Microposit MF-319 developer for 1 min. It was then washed with DI water and dried under nitrogen. The

photoresist mask left on the surface is a replication of the original optical mask. Subsequently, the plasma deposition of the fluorocarbon polymer was carried out using a deep reaction ion etching instrument, and inductively coupled plasma (ICP) reactor, (Alcatel 601E). The source power and substrate bias were set to 1,800 and 80 W, respectively. The feed gas supplied was  $C_4F_8$ , controlled at a flow of 150 sccm [standard cubic centimeters per minute] with a total process time of 20 s at a temperature of 20 °C. The photoresist-patterned plasmonic platform fabricated on coverslips were mounted onto silicon wafers for the plasma deposition and were subsequently removed prior to the lift-off process.

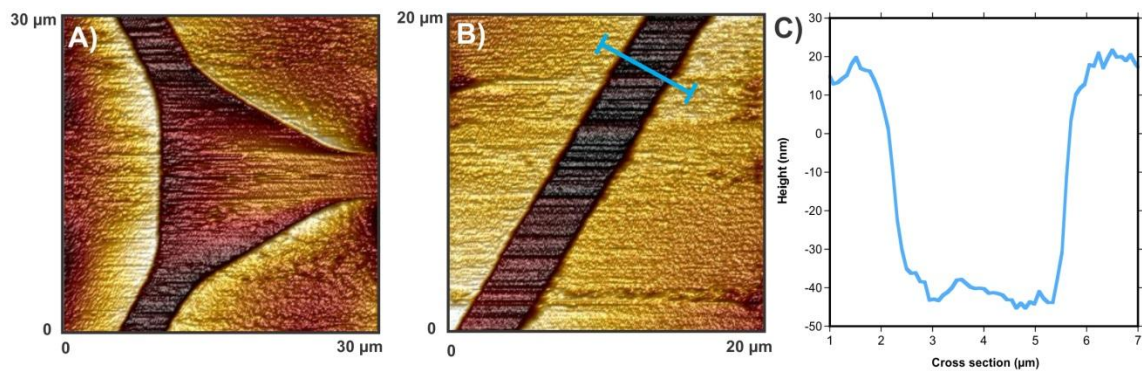


**Figure 5.2** AFM topography of A) a node and B) a channel of a hexagonal grid-like FC-patterned substrate on glass coverslip. C) Cross section of the indicated area in B determining the thickness of FC film of  $60 \pm 5$  nm.

A uniform layer of approximately  $60 \pm 5$  nm (see **Figure 5.2**) of fluorocarbon polymer was deposited on the plasmonic platform. Finally, the protective photoresist was removed by a lift-off process in a photoresist solvent (NANO<sup>TM</sup> Remover PG) for 10 min at 80 °C, followed by sonication in the solvent for 30 s. The sample was then rinsed thoroughly with isopropyl alcohol and dried under nitrogen. The final architecture of the

substrate is a thin fluoropolymer film ( $60 \pm 5$  nm) with regions wherein the nanotriangular plasmonic platform is revealed.

### 5.2.3 Functionalization of the platform

A stock solution of  $10^{-3}$  M 4-nitrothiophenol (4-NTP) in ethanol was prepared. This solution was then diluted to  $10^{-6}$  M. From this solution, two 40  $\mu$ L aliquots were drop casted onto the surface of a substrate that had been placed into a Petri dish. A clean coverslip was then gently placed onto the top of the substrate to sandwich the uniformly dispersed solution between the substrate and a coverslip. The Petri dish was covered with parafilm and left in the refrigerator to functionalize the surface for 24 hours. After 24 hours, the coverslip was removed, and the substrate was dipped 5 times in 3 beakers of ethanol and then dried under nitrogen. 4-Mercaptophenylboronic acid (4-MPBA) was also dissolved in ethanol to form a 10 mM solution for functionalization of the platform as the Raman reporter for glycan study with the same procedure as 4-NTP.

### 5.2.4 SERS setup

The SERS measurements were performed using a Horiba Jobin-Yvon Labram HR Raman microspectrometer equipped with a 600 grooves/mm grating and a 632.8 nm excitation. The intensity was set to 1 mW at the sample. A microscope objective of 100X, 0.9 N.A. was used for all experiments. The pinhole of the spectrometer was opened to 200  $\mu$ m. An acquisition time of 30 s with 5 accumulations was used for spectra shown in **Figure 5.6**. SERS maps ranged in size from as small as 5  $\mu$ m  $\times$  5  $\mu$ m to as large as 30  $\mu$ m  $\times$  30  $\mu$ m. A step-size of 1  $\mu$ m was used for the SERS maps as this corresponds to the approximate size of the laser spot. For the construction of the SERS map shown in **Figure 5.4**, the acquisition time of each individual spectrum was set to 1 s. An acquisition time of 10 second/spectrum is used for all the other SERS maps. SERS mapping was conducted on 15 cells for each cell line for statistical purposes.

### 5.2.5 AFM

AFM images were collected with a Bioscope Catalyst instrument (Bruker), operating in contact mode. A silicon cantilever with a spring constant of  $40 \text{ N m}^{-1}$  and an oscillating frequency of 325 kHz (NSC-15, Micromasch) was used.

### 5.2.6 Scanning electron microscopy (SEM)

SEM images were obtained using a LEO Zeiss 1530 (Zeiss, Oberkochen, Germany). Prior to imaging, substrates were coated with a 5 nm thick layer of osmium.

### 5.2.7 Cultures of HEK, C2C12, and HeLa cells

HEK 293, C2C12, and HeLa cells were maintained in Eagle's Minimal Essential Medium (MEM, Invitrogen). They were then supplemented with 2 mM glutamine (used just for C2C12),  $50 \mu\text{g mL}^{-1}$  gentamicin (Invitrogen), and 10% Fetal Bovine Serum (Invitrogen). The cultures were kept in an incubator at  $37 \text{ }^\circ\text{C}$ , 5%  $\text{CO}_2$ , 100% humidity, and were passaged every 3 days by trypsinization (0.25% trypsin-EDTA, Invitrogen). The cells were seeded onto the patterned substrates at a density of  $8 \times 10^5$  cells/dish and incubated for 48 h before fixation.

### 5.2.8 Cultures of neuronal cells

Cortical neuron cells (CD-1 strain mice, 14-15 day embryonic age) were also used. Primary cortical neurons were dissociated in Hank's balanced salt solution (HBSS) and plated in Neurobasal<sup>TM</sup> media supplemented with 0.5 mM L-glutamine, 2% B<sub>27</sub> and 0.8% N<sub>2</sub> supplements, and 50 units  $\text{mL}^{-1}$  penicillin-streptomycin (Invitrogen). Cultures were then plated onto the patterned surfaces at a density of  $1 \times 10^6$  cells/dish. The cultures were incubated at  $37 \text{ }^\circ\text{C}$  for 14 days. The media was also changed every 2-3 days. Animal handling protocol was in accordance with Western University (The University of Western Ontario) Animal Care Committee. All of the cell lines and cortical neurons were fixed



using a solution of 4% paraformaldehyde and sucrose prepared in phosphate buffered saline (PBS, pH 7.4, Invitrogen).

## 5.3 Results and discussion

### 5.3.1 Characterization of FC-patterned plasmonic substrates

Patterning over the plasmonic platforms was performed in hexagonal grid-like (**Figure 5.3 A-F**) and triangular arrays (**Figure 5.3 G-I**). The FC-patterned plasmonic platform provides multiple organized sensing nodes that can be tailored, depending on the application. For example, triangular patterns can provide single isolated cells for further biological sensing applications as shown in this work and the organized hexagonal grid like channels can be utilized for interconnected cells such as neurons.

**Figure 5.3** shows that sensing windows are surrounded by the thin FC polymer film (thickness of  $60 \pm 5$  nm; see **Figure 5.2**). The typical sizes of the features are limited to few microns in photolithography. Here we demonstrate in the hexagonal grids that it is possible to fabricate features as small as  $4 \mu\text{m}$  as shown by the width of the channels in **Figure 5.3 C-E**. In the case of the triangular patterns, **Figure 5.3 G-I** shows that the plasmonic platforms are homogeneously distributed within the FC-polymer patterned regions. Here, the Au nanotriangles serve two purposes. First, the Au surface of the structures can be used for functionalization with a Raman reporter for a target molecule. Second, the bow-tie assemblies of nanotriangles serve as nanoscale antennas confining EM fields in the hot spot regions formed by the facing nanotriangles. Such localized enhancement of the EM field is critical to further enhance the Raman signal, providing monolayer sensitivity as well as surface detection of cells placed on nanotriangular plasmonic platform.

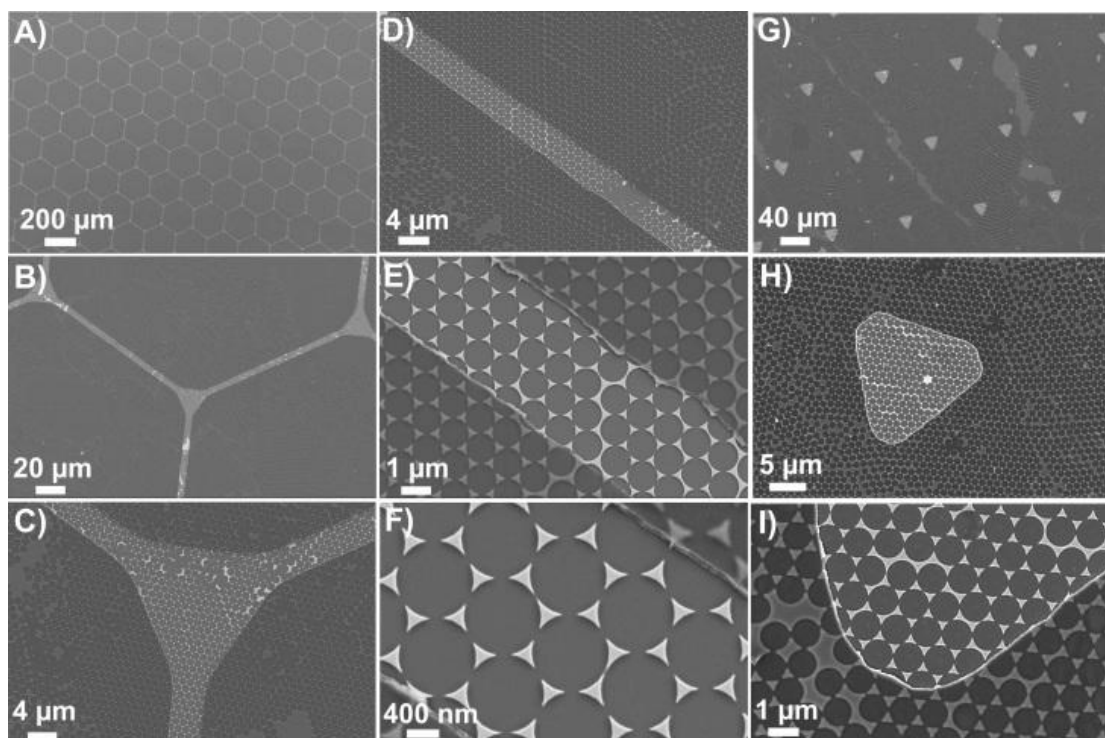


**Figure 5.3 SEM images of FC-patterned plasmonic substrates with two different feature patterns: Hexagonal-grid like pattern (A-F) Triangular pattern (G-I)**

### 5.3.2 Controlled micro-defined functionalization with analyte

In order to evaluate the confinement of the analyte by the patterned fluoropolymer thin film, as well as the SERS activity of the embedded plasmonic platform, the sensing device was functionalized with 4-nitrothiophenol (4-NTP). A schematic representation of the functionalized platform is shown in **Figure 5.4A**. 4-NTP binds specifically to gold, but not to the FC film. After a 24 h functionalization in a 1  $\mu\text{M}$  solution of 4-NTP in ethanol, the substrates were gently rinsed with ethanol.

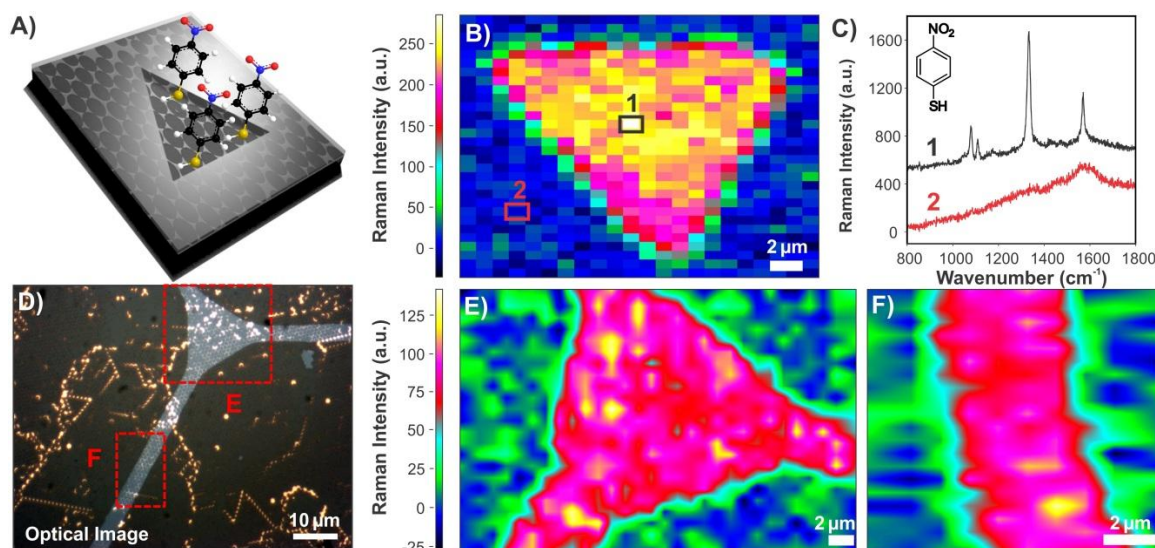


**Figure 5.4** Collected confocal SERS spectra and mapping of functionalized 4-NTP on a FC-patterned plasmonic substrate. A) Schematic of the microwell plasmonic platform B) SERS mapping on an isolated triangular pattern C) Chemical structure of 4-NTP and collected SERS spectra of defined regions in B. Region 1 and 2 are located on plasmonic platform and FC polymer, respectively. D) Optical image of a node and channels positioned over the NSL substrate. SERS mappings of selected regions in D representing a node (E) and a channel (F) are shown in the interpolated images of E and F.

SERS mapping was performed over the sensing area to evaluate the surface-enhanced activity on the gold nanotriangles and the FC polymer-coated regions. A SERS map of 4-NTP on a single triangular pattern is shown in **Figure 5.4B**. This map corresponds to the  $\text{NO}_2$  peak ( $1337\text{ cm}^{-1}$ ) of 4-NTP and was obtained from the integration over the region from  $1300\text{--}1350\text{ cm}^{-1}$ . Selected steps of  $1\text{ }\mu\text{m}$  and an acquisition time of  $1\text{ s/spectrum}$  under  $632.8\text{ nm}$  excitation were sufficient to probe the monolayer of 4-NTP. The SERS spectrum from a pixel found within the nanotriangles inside the pattern (labelled as 1 in

**Figure 5.4B**) shows a well-defined SERS spectrum of 4-NTP (**Figure 5.4C**).<sup>38,39</sup> On the other hand, the SERS spectrum of the fluoropolymer region (labelled as 2 in **Figure 5.4B**) shows only broad background peaks. The optical image of a hexagonal grid-like pattern on the plasmonic substrate is shown in **Figure 5.4D**. The selected regions for mapping are shown in red. SERS mapping areas were selected around the features of interest as  $22 \times 30$ ,  $30 \times 30$ , and  $10 \times 10 \mu\text{m}^2$  for **Figure 5.4 B, E, and F**, respectively. **Figures 5.4E and F** show SERS maps for 4-NTP that were obtained using the same procedure described above.

These results demonstrate the ability of the patterned plasmonic platforms to provide positionally-controlled functionalization with specific molecules for sensitive detection. This is consistent with previous results demonstrating the ability of plasmonic platforms to provide ultra-sensitive detection down to sub-femtomolar concentration.<sup>9,37,40,41</sup> It is also noteworthy that such surfaces can also be tuned to probe different fluorophores over the entire surface with confined positioning, by adding a thin layer of protection such as silica before fluorocarbon patterning.<sup>2</sup>

### 5.3.3 Biocompatibility of FC-patterned plasmonic platform

The biocompatibility of the FC polymer has been demonstrated in previous work, where it was also shown that FC-polymer patterning can be efficiently used for controlled cell isolation and proliferation.<sup>32</sup> To ensure that these desirable properties were retained on the FC-patterned plasmonic platform, a culture of human embryonic kidney (HEK 293) cells and mice cortical neurons (14 DIV) were used. As shown in **Figures 5.5A and B**, HEK 293 cells were efficiently isolated in the triangular windows on the plasmonic platform. It was also observed that these cells easily proliferated on the plasmonic nanotriangles.

Similar results were also obtained for the cortical neurons that were grown for 14 days on the hexagonal grid-like patterns. As shown in **Figures 5.5C and D**, the neuronal cell body and its projections were efficiently adapted within the channels on the plasmonic platform. This demonstrates the capability of these substrates to enable controlled cell positioning on the plasmonic platform for further surface-enhanced spectroscopic measurements of biomolecules of interest within the cells. Moreover, one can tune the feature patterns and interconnection dimensions with regards to the size of the specific cell line to optimize the sensing conditions.

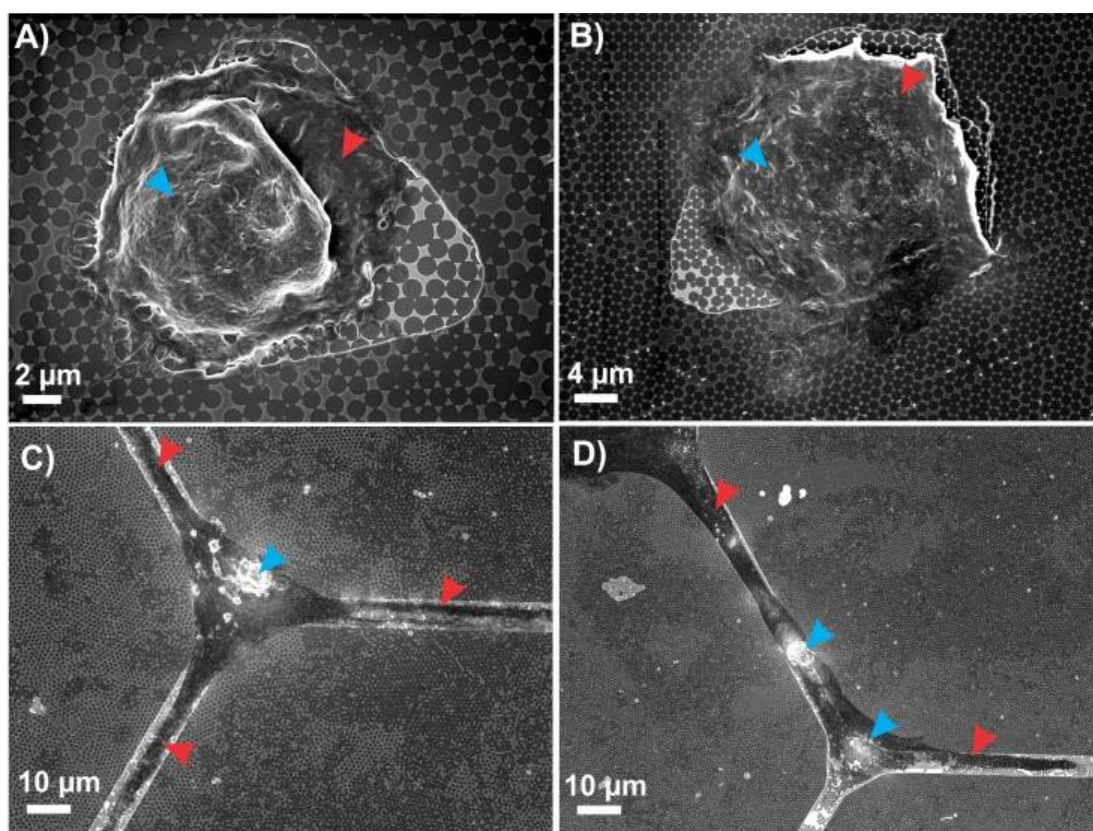


**Figure 5.5** SEM images of positionally-controlled cells on FC-plasmonic substrates. A, B) HEK 293 cells; C, D) Cortical neurons; Blue arrows indicate cell nuclei; Red Arrows indicate cell membranes (A, B) and projections of neurons (C, D).

### 5.3.4 SERS activity of FC-patterned plasmonic platform

With the aim of detecting glycans as described below, the Raman reporter molecule was changed to 4-MPBA. To investigate the SERS activity of the plasmonic platform with respect to this reporter molecules and cells, SERS spectra of 4-MPBA and HEK 293 cells were collected on FC-patterned plasmonic platforms and on a flat Au surface as a reference and are shown in **Figure 5.6**. The SERS activity of the platform for 4-MPBA is shown in **Figure 5.6A**, where characteristic peaks corresponding to the vibrational fingerprint of 4-MPBA are clearly observed. As shown in **Figure 5.6B**, the spectrum of 4-MPBA bound to the flat Au used as the control surface lacks the spectral features of the reporter. By introducing the cell over the platform, spectral features of both the Raman reporter and cell were detected as shown in **Figure 5.6C**. Clear spectral features of cellular components appeared on the SERS spectrum obtained on the plasmonic platform as shown in **Figure 5.6D** without any Raman reporter. In contrast, when the cell was located on a flat Au surface functionalized with the Raman reporter, the fingerprint of the reporter was absent as shown in **Figure 5.6E**, thereby deactivating the plasmonic platform for further sensing over the cell surface.

Although the flat Au surface is SERS inactive, a diminished Raman fingerprint of the cell was detected as shown in **Figure 5.6E**. This is due to the thickness of the cell on the Au surface, but the signal is not generated from the surface. However, in the case of a monolayer of the Raman reporter, it is not possible to obtain the signal. The peaks obtained for the cell at 1003, 1091, and 1651  $\text{cm}^{-1}$ , and the group of 2845, 2875, 2932  $\text{cm}^{-1}$  can be assigned to the phenylalanine of proteins and lipids, symmetric dioxy stretch of the phosphate backbone, amide I C=O and C=C stretching, and CH<sub>2</sub> stretching of protein and lipid functional groups (See **Table 5.1**).<sup>42</sup> The changes in two main peaks (labelled

with red star in **Figure 5.6C**) of 4-MPBA are assigned to B-OH stretching ( $1074\text{ cm}^{-1}$ ) and C-S stretching ( $1074$  and  $1574\text{ cm}^{-1}$ ). These two peaks have been well documented to undergo changes upon interaction with saccharides such as glucose.<sup>58</sup> This interaction is the same one responsible for the proposed binding between the 4-MPBA on the SERS platform and the glycan on the cell surface. The peak at  $1074\text{ cm}^{-1}$  representing the B-OH stretching undergoes the most significant change due to the interaction with glycans. Therefore, the change of signal for this peak was used for the glycan mapping over cell surfaces. The full assignment of 4-MPBA vibrational frequencies is also shown in **Table 5.1**.<sup>43,58</sup>

**Table 5.1 SERS vibrational frequencies assignment of 4-MPBA and Cell**<sup>42, 43,58</sup>

4-MPBA SERS Peaks ( $\text{cm}^{-1}$ )	Assignment	Cell SERS Peaks ( $\text{cm}^{-1}$ )	Assignment
1000	$\delta_{\text{C-C-C}}$	1003	phenylalanine of protein and lipid
1020	$\nu_{\text{C-S}}$	1091	symmetric dioxy stretch of the phosphate backbone and $\nu_{\text{C-C}}$ of nucleic acids lipid
1074	$\nu_{\text{B-OH}}$	1448	$\delta_{\text{CH}_2}$ proteins and lipids
1182	$\nu_{\text{B-C}}$	1651	amide $\nu_{\text{C=O}}$ and $\nu_{\text{C=C}}$ of protein and unsaturated lipid
1472	$\nu_{\text{C=C}}$	2845	$\nu_{\text{CH}_2}$ of protein and lipid
		2875	
1574	$\nu_{\text{C-C}}$	2932	

$\delta$  (Bending);  $\nu$  (Stretching)

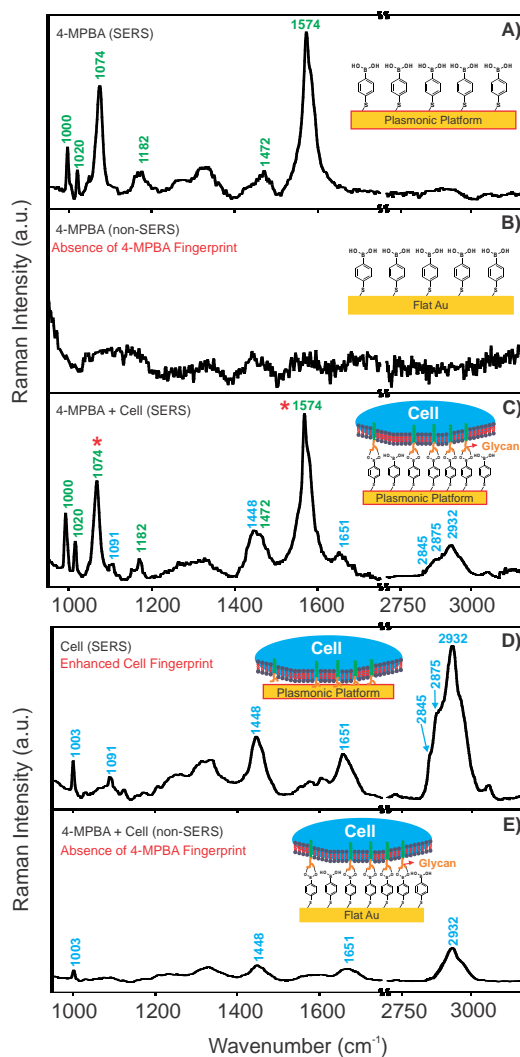


**Figure 5.6 SERS activity of 4-MPBA functionalized FC-patterned plasmonic platform representing 4-MPBA and HEK cell vibrational frequencies (A, C, and D); the non-SERS spectra are obtained on flat Au surface (B, and E) as a control compared to SERS signal obtained on SERS-active plasmonic regions containing nanotriangles within the fluoropolymer. A, B, C are normalized to the same scale. The same process is used for D, and E. Baseline correction is applied to all the spectra.**



### 5.3.5 Glycan expression of different cell lines probed by SERS

Boronic acids have the ability to form cyclic boronate esters with 1,2 and 1,3 diols, making them prime candidates for trapping and detecting saccharides.<sup>44</sup> The first SERS based sensor towards glucose sensing was introduced by the Van Duyne group.<sup>45</sup> A Ag film over a nanosphere pattern, where the Ag was functionalized with decanethiol was used in this study. More recently, boronic acid-based sensors have been used widely in newer glucose sensing applications using a variety of SERS and fluorescence methods.<sup>46-48</sup> Boronic acid moieties have also been used for aptasensing of glycoproteins,<sup>49</sup> and for the detection of glycans over the surface of a cell using fluorescence microscopy.<sup>50</sup> Glycan expression on the cell surface has further been studied with SERS using a bioorthogonal Raman reporter and lectin-based functionalized metallic nanoparticles.<sup>51,52</sup> However, metallic nanoparticles are hindered by their tendency for heterogeneous distribution and the formation of aggregates, especially on rough surfaces such as cells. As the distribution of glycans on the surface of a cell varies between different cells, it is important to provide a homogenous sensing area beneath or above the cell surface in order to provide more accurate mapping of the expression of glycans over the cell surface. The fabricated platform here provides this homogenous sensing surface beneath the cell which should afford reproducible and accurate maps of different cellular compartments and the biomolecule of interest on the surfaces of cells.

In the current study, 4-MPBA, having both a thiol for bonding to the plasmonic nanotriangles and a boronic acid moiety for interaction with sialoglycans on the cell surface serves as a Raman reporter. Upon binding to the surface glycans, a decrease to the intensities of the two main peaks of 4-MPBA as shown in **Figure 5.6 C** (1074 and 1574  $\text{cm}^{-1}$ ) is observed. The change of signal at 1074  $\text{cm}^{-1}$  (B-OH stretching) was used to map the locations of glycans over the cell surface. Sialoglycans are present on the surfaces of

mammalian cells. They play pivotal roles in the regulation of molecular and cellular interactions.<sup>53</sup> The elevated expression of sialic acid containing glycoproteins is indicative of disease and cancer progression.<sup>51</sup> The sialoglycan composition of a cell changes with progression of the cancer. This is attributed to the ability of sialoglycans to prevent cell coagulation and promote rapid entry into the bloodstream to facilitate cancer metastasis.<sup>51,54</sup> Thus, by tracking the expression of glycans over the plasmonic platform, it can potentially provide a tool to identify cancerous cells.

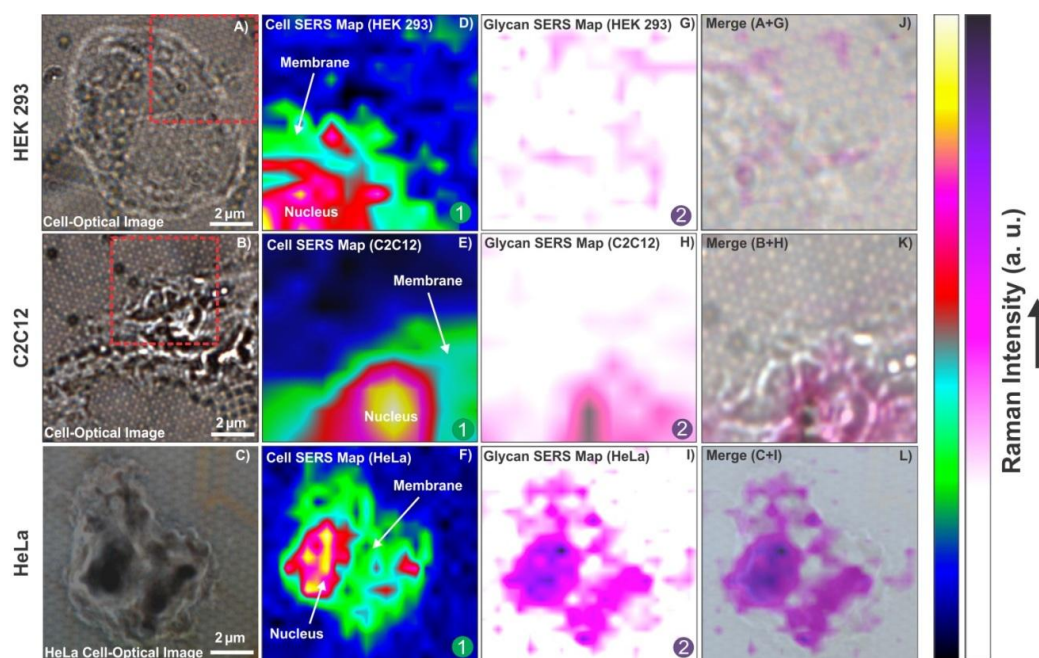


**Figure 5.7** Confocal SERS mapping of cell compartments and glycan expression on HEK 293, C2C12 and HeLa cells. Optical image of isolated single A) HEK 293, B) C2C12, C) HeLa cell. Confocal SERS map of cell compartments of selected regions in optical images for D) HEK 293 cell, E) C2C12 cell, F) HeLa cell; Confocal SERS map of glycan expression over the selected regions in optical images for G) HEK cell, H) C2C12 cell, I) HeLa cell; J) Overlay of A+G; K) Overlay of B+H; L) Overlay of C+I.

Having demonstrated the successful position of cells on the plasmonic platform as described above, three different cell lines were chosen for the evaluation of glycan expression. HEK 293 cells were chosen due to their vast usage in cell biology research for many years and their established cellular growth rate and easy maintenance.<sup>55</sup> This cell line serves as a control as it expresses no or minimal glycans.<sup>56</sup> We also used C2C12 mouse myoblast cells. This cell line was selected as a normal mammalian cell line representing a non-diseased state, where normal levels of glycan expression were expected. HeLa cells, the third selected cell line, are derived from cervical tumor cancer cells. This cell line is the oldest and most commonly used human cell line due to its remarkable durability and proliferation and is the first continuous human cancer cell line. Elevated glycan expression is known for cancer cell lines,<sup>57</sup> and has previously been observed for HeLa cells by SERS.<sup>51</sup> The optical images of selected isolated cells are shown in **Figures 5.7 A-C**. In the first step, regions of the isolated cells on the plasmonic platform were mapped by SERS. These maps revealed the different compartments of cells such as the nucleus and membrane as shown in **Figures 5.7 D-F**. There are a few overlaps between the Raman reporter and cell vibrational frequencies such as those at  $\sim 1000\text{ cm}^{-1}$  (**Figure 5.6C**). Regardless of these overlaps, by integrating the spectral range of  $2800\text{-}3000\text{ cm}^{-1}$ , one is able to map the cell compartments over the platform as shown in **Figures 5.7 D-F** using confocal SERS mapping.

The changes in the spectral fingerprint of the Raman reporter (4-MPBA) due to the interaction between 4-MPBA and glycans on the cell surface were used to map the glycan distribution over the cells. After baseline correction and normalization of the data contained within the maps, the average fingerprint of 4-MPBA based on each individual map was selected. This fingerprint was subtracted from each signal obtained on the cell area to map the changes over the cell. By analyzing the data based on the above

methodology, the SERS maps of the glycan expression over the cells were generated and are shown in **Figures 5.7 G, H, and I** for HEK 293, C2C12 and HeLa cells, respectively.

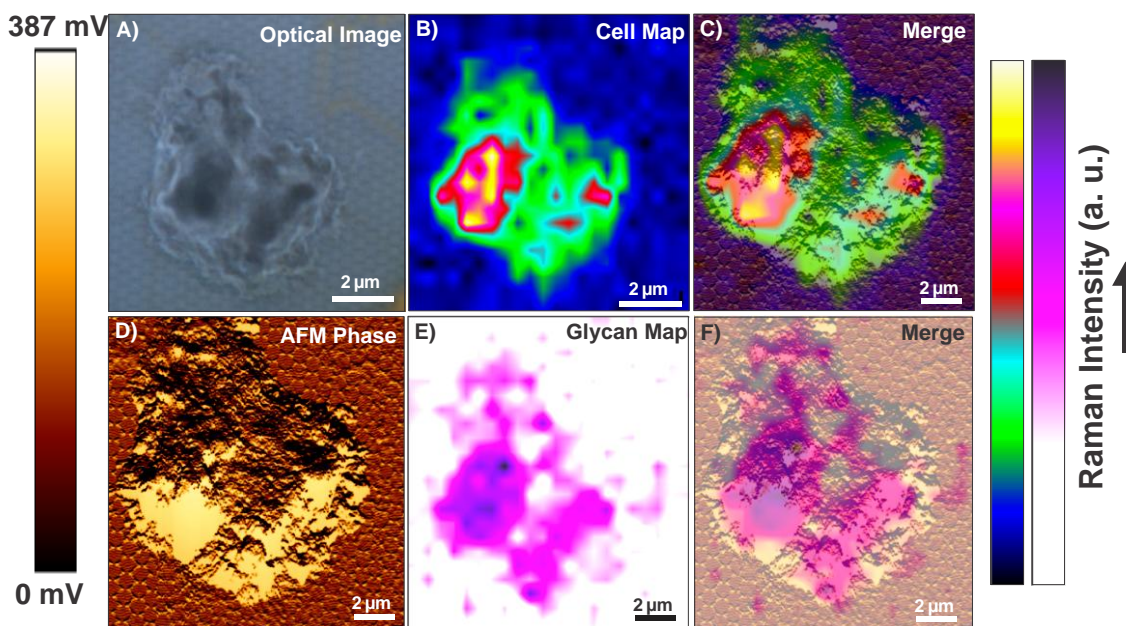


**Figure 5.8** Confocal SERS mapping of a single HeLa cell with nanoscale surface morphology obtained by AFM. **A)** Optical image of a single HeLa cell; **B)** SERS mapping of cell compartments; **C)** Overlay of SERS map in **B** with AFM morphology shown in **D**; **D)** AFM phase of the single cell shown in **D**. **E)** Glycan distribution on the same cell; **F)** Overlay of **D** and **E**.

As shown in **Figure 5.7G**, a minimal change was observed for HEK cells, indicating insignificant expression of glycans on the surface of the cell. The expression of glycans over the C2C12 cell surface is quite clear. In the HeLa cells, the level of glycan expression suggested by the SERS map is significantly higher than that for the C2C12 or HEK 293 cells. This is in agreement with the results of confocal SERS mapping using lectin-based nanoparticles where it was shown that HeLa cells express more glycans than

Chinese hamster ovarian (CHO) cells, a cell line also known to exhibit low levels of glycan expression.<sup>51</sup> The overlay of confocal SERS mapping of glycans over these three cell lines with the corresponding optical images of selected cell surface areas are shown in **Figures 5.7 J-L**.

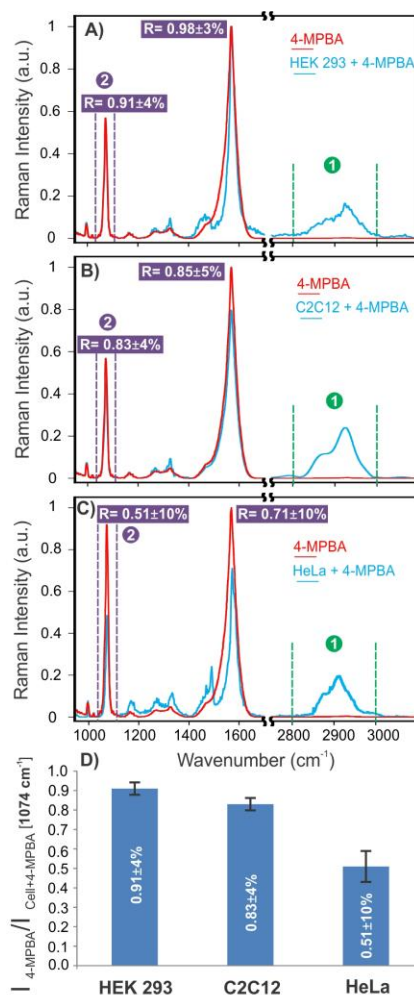


**Figure 5.9** Average SERS spectra of 4MPBA and isolated cells on 4-MPBA functionalized-plasmonic platform; A) HEK 293 cell; B) C2C12 cell; C) HeLa cell. D) Ratios of the average intensities of 4-MPBA/Cell+4MPBA for 15 cells at 1074 cm<sup>-1</sup>. <sup>1</sup>. Baseline corrections were applied to all spectra.

By combining AFM and subsequent SERS mapping on a single cell, it is also possible to obtain high resolution images of the cell morphology whilst providing high resolution confocal mapping of cell compartments or a molecule of interest such as glycans on the cell (See **Figure 5.8**). The corresponding SERS map-derived signals of 4-MPBA and cells over the platform functionalized with 4-MPBA were also shown for these three cell lines in **Figure 5.9**.

To quantify the changes observed for these three cell lines in terms of glycan expression, the ratio of the intensities of the SERS signals of 4-MPBA over the bare plasmonic platform and cells ( $\text{SERS}_{\text{intensity}}(4\text{-MPBA}) / \text{SERS}_{\text{intensity}}(4\text{-MPBA} + \text{Cell})$ ) were compared at 1074 and 1587  $\text{cm}^{-1}$ .

As shown in **Figure 5.9A**, the ratios of  $0.91 \pm 4\%$  and  $0.98 \pm 3\%$  were observed for the aforementioned signals, respectively. This leads to the insignificant change observed for the HEK 293 cells as a result of no or minimal glycan expression. The ratios obtained for the C2C12 cells were slightly decreased to  $0.83 \pm 4\%$  and  $0.85 \pm 5\%$  as shown in **Figure 5.9B**, corresponding to notable expression of glycans, as shown on the SERS map (**Figure 5.7H**). However, a significant change has been observed for HeLa cells representing the ratios of  $0.51 \pm 10\%$  and  $0.71 \pm 10\%$  as shown in **Figure 5.9C**. This leads to a distinct elevated expression of glycans over the cell surface compared to C2C12 and HEK 293 cells. Ratios of the average intensities of 4-MPBA/Cell+4MPBA for 15 cells at 1074  $\text{cm}^{-1}$  were also shown in **Figure 5.9 D** representing the quantified differentiation between cancerous cell line (HeLa) and non-cancerous cell lines (HEK 293 and C2C12). Similar observations in terms of the signal changes were reported previously for the 4-MPBA while interacting with glucose.<sup>58</sup> It has been previously reported that the discrepancies between prostate cancer and non-cancerous cells in terms of glycan expression were much more clearly resolved using SERS compared to fluorescence microscopy. Comparative fluorescence studies only demonstrated a slight

difference between the two cell subsets.<sup>51</sup> This introduces SERS as a critical non-invasive tool to differentiate cancer cells with high sensitivity. The statistical and error analysis of these signals are provided in **Figure 5.10** with respect to the observed median values.

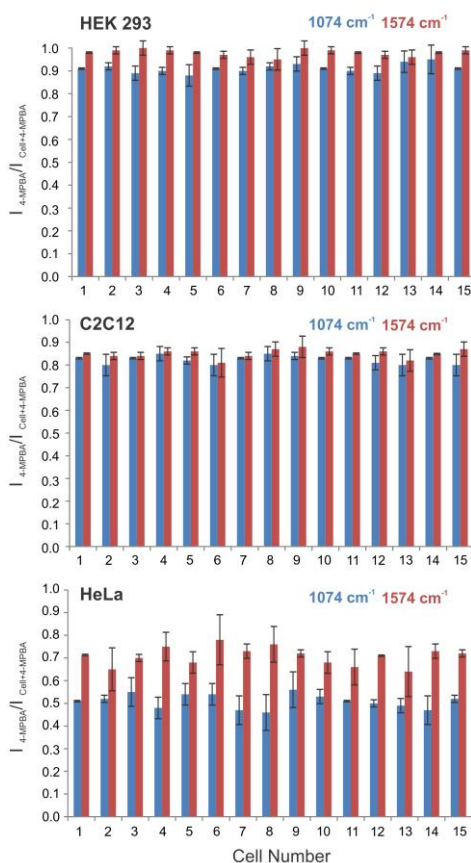


**Figure 5.10** Cell SERS analysis representing the ratios of the normalized average SERS (Intensity (4-MPBA)/Intensity (4-MPBA + Cell)) at 1074 and 1574 cm<sup>-1</sup> for 15 different cells for each cell line. The error bars are generated based on the percent deviation from the median ratio values. The obtained median values are 0.91± 4% (HEK 293 at 1074 cm<sup>-1</sup>), 0.98± 3% (HEK 293 at 1574 cm<sup>-1</sup>), 0.83± 4% (C2C12 at 1074 cm<sup>-1</sup>), 0.85± 5% (C2C12 at 1574 cm<sup>-1</sup>), 0.51± 10% (HeLa at 1074 cm<sup>-1</sup>), 0.71± 10% (HeLa at 1574 cm<sup>-1</sup>).

## 5.4 Conclusions

In conclusion, we have demonstrated the fabrication of a device that provides a promising plasmonic sensing platform for positionally-controlled surface-enhanced spectroscopy applications. This platform not only allows one to locate the analyte/reporter in defined positions, but also provides the opportunity to isolate a single cell for analysis of specific biomolecules on their surfaces. The SERS detection of glycan expression in different cell lines including HEK 293, C2C12, and HeLa cells was demonstrated. It was observed that the HeLa cell line derived from cervical cancer cells, expressed more glycans over its surface compared to noncancerous HEK 293 and C2C12 cells. This strategy may be further applied to detect proteins on cell surfaces. The SERS platform with ultra-sensitive detection capability will be pertinent to study membrane proteins. Raman and infrared vibrations<sup>59</sup> are sensitive to the local environment, leading to monitoring the conformational changes of cell surface receptors.<sup>52</sup> This provides the potential applications of the proposed platform to identify other types of cancer cells using SERS. Last but not least, the fabrication process of this platform is entirely compatible with other nanofabrication processes such as electron beam lithography. This only requires alignment control between two consecutive steps, which can be done easily with mask alignment technology. The inclusion of such modified platforms inside microfluidic channel is also possible, highlighting the versatility of the proposed method.<sup>60</sup>

## 5.5 References

- (1) Jeanmaire, D. L.; Van Duyne, R. P.; *J. Electroanal. Chem. Interfacial. Electrochem.* , (1977), 84, 1.
- (2) Fayyaz, S.; Tabatabaei, M.; Hou, R.; Lagugné-Labarthe, F.; *J. Phys. Chem. C*, (2012), 116, 11665.
- (3) Liu, N.; Pucci, A.; *Nat. Mater.*, (2012), 11, 9.



- (4) Aroca, R. F.; Ross, D. J.; Domingo, C.; *Appl. Spectrosc.*, **(2004)**, 58, 324A.
- (5) Hoffmann, J. M.; Yin, X.; Richter, J.; Hartung, A.; Maß, T. W. W.; Taubner, T.; *J. Phys. Chem. C*, **(2013)**, 117, 11311.
- (6) Kneipp, K.; Wang, Y.; Kneipp, H.; Perelman, L. T.; Itzkan, I.; Dasari, R. R.; Feld, M. S.; *Phys. Rev. Lett.*, **(1997)**, 78, 1667.
- (7) Nie, S.; Emory, S. R.; *Science*, **(1997)**, 275, 1102.
- (8) Sonntag, M. D.; Klingsporn, J. M.; Zrimsek, A. B.; Sharma, B.; Ruvuna, L. K.; Van Duyne, R. P.; *Chem. Soc. Rev.*, **(2014)**, 43, 1230.
- (9) Tabatabaei, M.; Najiminaini, M.; Davieau, K.; Kaminska, B.; Singh, M. R.; Carson, J. J. L.; Lagugné-Labarthe, F.; *ACS Photonics*, **(2015)**, DOI: 10.1021/acsp Photonics.5b00104.
- (10) Xu, L.; Yan, W.; Ma, W.; Kuang, H.; Wu, X.; Liu, L.; Zhao, Y.; Wang, L.; Xu, C.; *Adv. Mater.*, **(2015)**, 27, 1706.
- (11) Anker, J. N.; Hall, W. P.; Lyandres, O.; Shah, N. C.; Zhao, J.; Van Duyne, R. P.; *Nat. Mater.*, **(2008)**, 7, 442.
- (12) Sharma, B.; Fernanda Cardinal, M.; Kleinman, S. L.; Greeneltch, N. G.; Frontiera, R. R.; Blaber, M. G.; Schatz, G. C.; Van Duyne, R. P.; *MRS Bulletin*, **(2013)**, 38, 615.
- (13) Bantz, K. C.; Meyer, A. F.; Wittenberg, N. J.; Im, H.; Kurtulus, O.; Lee, S. H.; Lindquist, N. C.; Oh, S.-H.; Haynes, C. L.; *Phys. Chem. Chem. Phys.*, **(2011)**, 13, 11551.
- (14) Kang, J. W.; So, P. T. C.; Dasari, R. R.; Lim, D.-K.; *Nano Lett.*, **(2015)**, 15, 1766.
- (15) Henzie, J.; Lee, J.; Lee, M. H.; Hasan, W.; Odom, T. W.; *Annu. Rev. Phys. Chem.*, **(2009)**, 60, 147.
- (16) Aksu, S.; Yanik, A. A.; Adato, R.; Artar, A.; Huang, M.; Altug, H.; *Nano Lett.*, **(2010)**, 10, 2511.
- (17) Novotny, L.; van Hulst, N.; *Nat. Photon.*, **(2011)**, 5, 83.
- (18) Quake, S. R.; Scherer, A.; *Science*, **(2000)**, 290, 1536.

- (19) Vieu, C.; Carcenac, F.; Pépin, A.; Chen, Y.; Mejias, M.; Lebib, A.; Manin-Ferlazzo, L.; Couraud, L.; Launois, H.; *Appl. Surf. Sci.*, (2000), 164, 111.
- (20) Hulteen, J. C.; Treichel, D. A.; Smith, M. T.; Duval, M. L.; Jensen, T. R.; Van Duyne, R. P.; *J. Phys. Chem. B*, (1999), 103, 3854.
- (21) Tabatabaei, M.; Sangar, A.; Kazemi-Zanjani, N.; Torchio, P.; Merlen, A.; Lagugn -Labarthe, F.; *J. Phys. Chem. C*, (2013), 117, 14778.
- (22) Haynes, C. L.; Van Duyne, R. P.; *J. Phys. Chem. B*, (2001), 105, 5599.
- (23) Masson, J.-F.; Murray-Methot, M.-P.; Live, L. S.; *Analyst*, (2010), 135, 1483.
- (24) Lee, A.; Andrade, G. F. S.; Ahmed, A.; Souza, M. L.; Coombs, N.; Tumarkin, E.; Liu, K.; Gordon, R.; Brolo, A. G.; Kumacheva, E.; *J. Am. Chem. Soc.*, (2011), 133, 7563.
- (25) Galarreta, B.; Tabatabaei, M.; Guieu, V.; Peyrin, E.; Lagugn -Labarthe, F.; *Anal. Bioanal. Chem.*, (2013), 405, 1613.
- (26) Huang, J.-Y.; Zong, C.; Xu, L.-J.; Cui, Y.; Ren, B.; *Chem. Commun.*, (2011), 47, 5738.
- (27) Srivastava, S. K.; Shalabney, A.; Khalaila, I.; Gr ner, C.; Rauschenbach, B.; Abdulhalim, I.; *Small*, (2014), DOI: 10.1002/sml.201303218.
- (28) Wang, Y.; Deng, X.; Liu, J.; Tang, H.; Jiang, J.; *Chem. Commun.*, (2013), 49, 8489.
- (29) Potara, M.; Boca, S.; Licarete, E.; Damert, A.; Alupei, M.-C.; Chiriac, M. T.; Popescu, O.; Schmidt, U.; Astilean, S.; *Nanoscale*, (2013), 5, 6013.
- (30) Antonio, K. A.; Schultz, Z. D.; *Anal. Chem.*, (2014), 86, 30.
- (31) Jiang, C.; Liu, R.; Han, G.; Zhang, Z.; *Chem. Commun.*, (2013), 49, 6647.
- (32) Tabatabaei, M.; Caetano, F. A.; Vedraire, S.; Norton, P. R.; Ferguson, S. S. G.; Lagugn -Labarthe, F.; *Biomaterials*, (2013), 34, 10065.
- (33) Sniadecki, N.; Desai, R.; Ruiz, S.; Chen, C.; *Ann. Biomed. Eng.*, (2006), 34, 59.
- (34) Yap, F. L.; Zhang, Y.; *Biosens. Bioelect.*, (2007), 22, 775.
- (35) Hulteen, J. C.; Van Duyne, R. P.; *J. Vac. Sci. Technol. A*, (1995), 13, 1553.

- (36) Zhang, X.; Yonzon, C. R.; Van Duyne, R. P.; *J. Mat. Res.*, **(2006)**, *21*, 1083.
- (37) Wallace, G. Q.; Tabatabaei, M.; Lagugné-Labarthe, F.; *Can. J. Chem.*, **(2014)**, *92*, 1.
- (38) Kiran, V.; Sampath, S.; *ACS Appl. Mater. Interfaces*, **(2012)**, *4*, 3818.
- (39) Dong, B.; Fang, Y.; Xia, L.; Xu, H.; Sun, M.; *J. Raman Spectrosc.*, **(2011)**, *42*, 1205.
- (40) De Angelis, F.; Gentile, F.; Mecarini, F.; Das, G.; Moretti, M.; Candeloro, P.; Coluccio, M. L.; Cojoc, G.; Accardo, A.; Liberale, C.; Zaccaria, R. P.; Perozziello, G.; Tirinato, L.; Toma, A.; Cuda, G.; Cingolani, R.; Di Fabrizio, E.; *Nat. Photon.*, **(2011)**, *5*, 682.
- (41) Shao, M.-W.; Lu, L.; Wang, H.; Wang, S.; Zhang, M.-L.; Ma, D.-D.-D.; Lee, S.-T.; *Chem. Commun.*, **(2008)**, 2310.
- (42) Zhang, X.; Roeffaers, M. B. J.; Basu, S.; Daniele, J. R.; Fu, D.; Freudiger, C. W.; Holtom, G. R.; Xie, X. S.; *Chem. Phys. Chem.*, **(2012)**, *13*, 1054.
- (43) Sun, F.; Bai, T.; Zhang, L.; Ella-Menye, J.-R.; Liu, S.; Nowinski, A. K.; Jiang, S.; Yu, Q.; *Anal. Chem.*, **(2014)**, *86*, 2387.
- (44) Kong, K. V.; Lam, Z.; Lau, W. K. O.; Leong, W. K.; Olivo, M.; *J. Am. Chem. Soc.*, **(2013)**, *135*, 18028.
- (45) Shafer-Peltier, K. E.; Haynes, C. L.; Glucksberg, M. R.; Van Duyne, R. P.; *J. Am. Chem. Soc.*, **(2003)**, *125*, 588.
- (46) Fang, H.; Kaur, G.; Wang, B.; *J. Fluoresc.*, **(2004)**, *14*, 481.
- (47) Tang, Y.; Yang, Q.; Wu, T.; Liu, L.; Ding, Y.; Yu, B.; *Langmuir*, **(2014)**, *30*, 6324.
- (48) Sun, X.; Stagon, S.; Huang, H.; Chen, J.; Lei, Y.; *RSC Adv.*, **(2014)**, *4*, 23382.
- (49) Li, M.; Lin, N.; Huang, Z.; Du, L.; Altier, C.; Fang, H.; Wang, B.; *J. Am. Chem. Soc.*, **(2008)**, *130*, 12636.
- (50) Xu, X.-D.; Cheng, H.; Chen, W.-H.; Cheng, S.-X.; Zhuo, R.-X.; Zhang, X.-Z.; *Sci. Rep.*, **(2013)**, *3*.

- (51) Craig, D.; McAughtrie, S.; Simpson, J.; McCraw, C.; Faulds, K.; Graham, D.; *Anal. Chem.*, **(2014)**, *86*, 4775.
- (52) Lin, L.; Tian, X.; Hong, S.; Dai, P.; You, Q.; Wang, R.; Feng, L.; Xie, C.; Tian, Z.-Q.; Chen, X.; *Angew. Chem. Int. Ed.*, **(2013)**, *52*, 7266.
- (53) Varki, A.; *Nature*, **(2007)**, *446*, 1023.
- (54) Varki, N. M.; Varki, A.; *Lab. Inv.*, **(2007)**, *87*, 851.
- (55) Maus, L.; Dick, O.; Bading, H.; Spatz, J. P.; Fiammengo, R.; *ACS Nano*, **(2010)**, *4*, 6617.
- (56) Croset, A.; Delafosse, L.; Gaudry, J.-P.; Arod, C.; Glez, L.; Losberger, C.; Begue, D.; Krstanovic, A.; Robert, F.; Vilbois, F.; Chevalet, L.; Antonsson, B.; *J. Biotech.*, **(2012)**, *161*, 336.
- (57) Dube, D. H.; Bertozzi, C. R.; *Nat. Rev. Drug. Discov.*, **(2005)**, *4*, 477.
- (58) Torul, H.; Ciftci, H.; Dudak, F. C.; Adguzel, Y.; Kulah, H.; Boyac, I. H.; Tamer, U.; *Anal. Methods*, **(2014)**, *6*, 5097.
- (59) Ye, S.; Zaitseva, E.; Caltabiano, G.; Schertler, G. F. X.; Sakmar, T. P.; Deupi, X.; Vogel, R.; *Nature*, **(2010)**, *464*, 1386.
- (60) Brolo, A. G.; *Nat. Photon.*, **(2012)**, *6*, 709.

## Chapter 6

### 6 Optical Properties of Silver and Gold Tetrahedral Nanopyramid Arrays Prepared by Nanosphere Lithography<sup>3</sup>

In this chapter, tetrahedral nanopyramids made of silver and gold over ITO/glass surfaces are fabricated. Our protocol is making use of NSL method with the deposition of thicker metal layers. After removing the microspheres used in the NSL process, an array of metallic tetrahedral nanostructures of ~350-400 nm height is formed. The reported procedure avoids the use of any stabilizing surfactant molecules that are generally necessary to segregate the individual particles onto surfaces. We focus here on the optical and the physical properties of these plasmonic surfaces using near-field spectroscopy in conjunction with FDTD modeling of the electric field. Remarkably, FDTD shows that the localized surface plasmon resonance is confined along the sharp edges of the pyramids that are parallel to the input polarization of the impinging excitation laser. The variable gaps between the edges of two adjacent pyramids show a broader localized surface plasmon and larger specific surface as opposed to the usual nanotriangle array. Localized enhancement of the electric field is experimentally investigated by coating the plasmonic surface with a thin film of photosensitive azopolymer onto the surface of the nanopyramids. The reported deformation upon radiation of the surface topography is visualized by atomic force microscopy and suggests the potentiality of these 3D nanopyramids for near-field enhancement. This last feature is clearly confirmed by surface-enhanced Raman spectroscopy (SERS) measurement with 4-nitrothiophenol

---

<sup>3</sup> A version of this chapter has been published in [*J. Phys. Chem. C*, (2013), 117, 14778]. Reproduced with permission of the American Chemical Society (ACS) publishing group.

molecules deposited on the pyramid platforms. The potentiality of such 3D nanostructures in plasmonics and surface spectroscopy is thus clearly demonstrated.

## 6.1 Introduction

Plasmonic structures produced by advanced nanofabrication techniques open up new possibilities when the manipulation of a resonant optical field is of interest.<sup>1</sup> The current advances in plasmonics technology for active and passive photonic devices,<sup>2-4</sup> spectroscopic applications,<sup>5-7</sup> and the conception of photovoltaic devices<sup>8</sup> all arise from the possibility to fabricate metallic nanostructures into a short range arrangement over large surfaces. Electron-beam lithography,<sup>9,10</sup> and focused ion beam are particularly well suited for the fabrication of high resolution features (~10 nm) on small areas. Other approaches using nanoimprint lithography,<sup>8,11</sup> deep-UV lithography followed by epitaxial growth or atomic layer deposition or annealing<sup>8,12</sup> are common techniques used to make plasmonic surfaces with features as small as 10 nm over standard 4, 6 and 12 inch wafers.

Among the available nanofabrication methods, NSL is a versatile and economical approach to make sharp nanostructures organized onto large surfaces.<sup>13</sup> These nanostructures have various applications ranging from surface-enhanced spectroscopy, surface plasmon resonance measurements for biosensing applications<sup>14</sup> to solar cell applications with the ultimate goal to improve the photovoltaic conversion efficiency.<sup>15</sup> Initially reported by Fischer et al.,<sup>16</sup> NSL platforms use the properties of the localized surface plasmon resonance (LSPR) confined at the apices formed by two adjacent nanotriangles.<sup>14,17-21</sup> In NSL, a monolayer of silica or polystyrene nanoparticles is formed onto mica, silicon or glass wafer.<sup>22</sup> A thin layer of silver or gold with a thickness of around 30 nm is then deposited on this monolayer. Once the particles are removed, an array of metallic nanotriangles (Au, Ag) of 20-30 nm thicknesses is formed over the

substrate. However in most cases, only a thin layer of metal is deposited, leading to simple flat triangles array.

In this work, we show that the deposition of a thicker layer of metal with thickness of roughly half of the diameter of an individual particle lead to the formation of tetrahedral pyramids organized in a hexagonal pattern. The optical near-field and plasmonic properties of such nano-objects are investigated through EM field modeling and experimental measurements. More specifically, the optical properties of these arrays are first investigated using FDTD calculations for Ag and Au nanostructures along the transverse and longitudinal planes with respect to the polarization direction of 532 and 632.8 nm excitation wavelengths. In order to visualize the areas with maximum field enhancement we used the approach, developed by Hubert,<sup>23-25</sup> using a thin film of a photosensitive azobenzene polymer, and compared the topographical changes probed by AFM to the numerical calculations of the electric field.

Finally, the Raman surface enhancements of these platforms are systematically investigated for gold and silver nanopyramids at both 532 and 632.8 nm excitations. Silver nanopyramids demonstrated the highest enhancement of the Raman signal, leading to the photochemical transformation of 4-nitrothiophenol (4-NTP). Photogeneration of dimercaptoazobenzene appears to be effective for both excitation wavelengths, although 532 nm is always more efficient even under modest irradiation of 200  $\mu$ W.

Noteworthy, the proposed protocol can be used for a variety of other applications by changing the composition of deposited material. Such sharp nanopyramids could be used for hydrophobic surfaces, field emission, catalysis and many other applications.<sup>13</sup> Furthermore, these 3D individual objects can be further functionalized with guest molecules and being used as platform for enhanced optical sensing.

## 6.2 Experimental section

### 6.2.1 Materials

Microscope coverslips ( $22 \times 22 \times 0.15$  mm) were purchased from VWR International, Mississauga, Canada. Nochromix was purchased from Godax Laboratories Inc, Maryland, US. Hydrogen peroxide (30% v/v) was obtained from EMD Inc, Mississauga, Canada. Polystyrene microspheres (10% w/w) of 1  $\mu\text{m}$  diameter were purchased from ThermoScientific Co (California, US). Sodium dodecyl sulfate (SDS) was obtained from Sigma-Aldrich, Missouri, US. Glass slides coated with 110 nm indium thin oxide (ITO) were purchased from Lumtec (Taiwan).

### 6.2.2 Preparation of samples by nanosphere lithography

A detailed description of the preparation of the samples can be found elsewhere.<sup>26, 17</sup> Briefly, microscope coverslips used to prepare the monolayer of polystyrene particles at the water surface were first sonicated in acetone for 5 min followed by cleaning in nochromix solution in concentrated sulphuric acid for 15 mins. Subsequently, the slides were rinsed in Milli-Q ultrapure water (18.2 M $\Omega$ .cm) several times. These were sonicated for 1 hour in mixture of ammonium hydroxide: hydrogen peroxide: ultrapure water (18.2 M $\Omega$ .cm) in ratio of 5:1:1. Afterwards, the glass slides were sonicated for 15 mins in water. Polystyrene microspheres solution was equilibrated to room temperature prior to use. Thereafter, 30  $\mu\text{L}$  aliquot of polystyrene solution was mixed with 30  $\mu\text{L}$  of ethanol (100%). 20  $\mu\text{L}$  of the prepared solution was deposited on top of the dried coverslip. This was immediately introduced in the air-water interface of a 6 cm petri dish filled with ultrapure water (18.2 M $\Omega$ .cm). The coverslip floated on the air-water interface and the polystyrene colloidal solution spread out to the air-water interface. After the dispersion of the solution, the coverslip sank to the bottom of the petri dish. A few drops of 2% (w/v)



SDS solution in water were added to further group the nanospheres into an ordered monolayer. The nanosphere solution was finally picked up using a wet and clean glass slide coated with ITO and was allowed to dry overnight under a petri dish.

### 6.2.3 Metal deposition and characterization

After the samples dried, 350-400 nm of Au were deposited using electron beam evaporation (Hoser, Ottawa, Canada). The polystyrene particles were finally removed by sonicating the sample in ethanol for about a minute. The sample was then dried under the nitrogen gas. Scanning Electron Microscope (SEM) images were obtained using a LEO Zeiss 1540XB (Zeiss, Oberkochen, Germany). Atomic force microscopy measurements were performed with a NanoWizard II bioscience from JPK instruments (Berlin, Germany). AFM scans were conducted in non-contact mode using standard AFM tips (NCL20 Nano World Inc.; resonance frequency  $f=170$  kHz, force constant  $k = 48$  N/m or NSC15/AIBS Micromash; resonance frequency  $f=325$  kHz, force constant  $k=46$  N/m)

### 6.2.4 FDTD simulations

The distribution of the electric field intensity in close proximity of the silver and gold nanopillars was calculated using FDTD Solutions (Lumerical Solutions, Inc). The calculations were set up as a three dimensional system with a 0.15 nm resolution grid, for 1000 femtoseconds, including appropriate boundary conditions. A plane wave source was chosen at 532 or 632.8 nm working wavelengths, with a propagation axis perpendicular to the plane of the single or lattice of pillars, and with a polarization along the X axis. The physical parameters, such as size and height of the nanopillars, used in these calculations were obtained from the AFM and SEM data. The dielectric constant of the ITO, glass (silicon dioxide), silver and gold were described by the Drude model provided in the material database from the software. The calculation of the relative total electric

field intensity ( $|E|^2$ ) and its image plot was obtained from the contribution of its components ( $|E_x|^2 + |E_y|^2 + |E_z|^2$ ) and it was calculated at defined distances from the apex or the base of the pyramids.

### 6.2.5 Azopolymer thin film preparation and photoinduced surface deformation

A solution of poly{4'-[[[methacryloyloxy)ethyl]ethyl]amino]-4-nitroazobenzene-co-methyl methacrylate} with 11% molar azobenzene moieties (p(DR1M-co-MMA)-11%) as shown in **Figure 6.1** was prepared in chloroform (0.05 g in 5 ml of solvent) and spin-casted over the nanopyramids at a speed of 1000 rpm. The films were annealed 10 min at 100 °C. Resulting film thickness was of 80 nm as measured by atomic force microscopy on a small scratch made with the tip of a needle. To induce azobenzene surface deformation, irradiation was conducted at 532 nm (Coherent, Compass 315M Laser) with an expanded beam of about 6 mm, and an irradiance set to 100 mW/cm<sup>2</sup> for an irradiation time of 15 minutes.

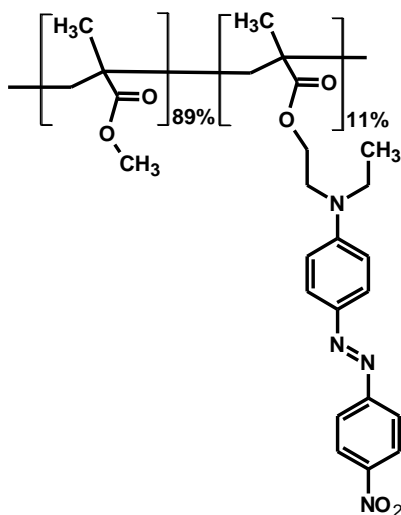


**Figure 6.1** Chemical Structure of p(DR1M-co-MMA) 11%

### 6.2.6 Raman SERS measurements

The Raman measurements were performed using a Horiba Jobin-Yvon Raman spectrometer equipped with a 600 grooves/mm grating and a 532 or 632.8 nm excitations with proper interference and edge filters. For both laser sources, intensities were adjusted to 2 mW or 200  $\mu$ W at the sample using neutral density filters. Microscope objective of x40, 0.7 N.A. was used for all experiments. Pinhole of the spectrometer was opened to 300  $\mu$ m. All Raman spectra are shown without baseline correction.

## 6.3 Results and discussion

A variety of methods have been reported for the fabrication of organized arrays of sharp nanotip structures for SERS applications. Conical<sup>27</sup> or pyramidal<sup>28-30</sup> structures have been made using top-down approaches with the desire to obtain very sharp apex at the extremity of the pyramids, leading to efficient SERS platforms. Although, these sharp structures are often distant by several microns from each other.<sup>31</sup> Other bottom-up approaches have also been reported with the intention to obtain sharp tips. However, due to the inhomogeneous distribution of such structures over a surface, their application for analytical purposes such as SERS is compromised.<sup>31,32</sup> In the present work, it is shown that the sharpness of the tip is not the dominant effect for the enhancement. The proximity of the pyramids edges is a much more important factor in particular when the irradiation source is polarized in the transverse direction with respect to the tip orientation. Inverted pyramids engraved on silicon and coated with gold that are commercially available for SERS measurements (Klarite TM, Renishaw diagnostic),<sup>33</sup> use the variable gaps between two opposed edges of the inverted pyramid. However, since they are opaque, they can be used only in reflection geometry. On the contrary, our structures can be used for both reflection/transmission measurements since the pyramids are deposited on a transparent ITO-coated glass substrate.

### 6.3.1 Characterization of nanopyramid arrays fabricated by NSL

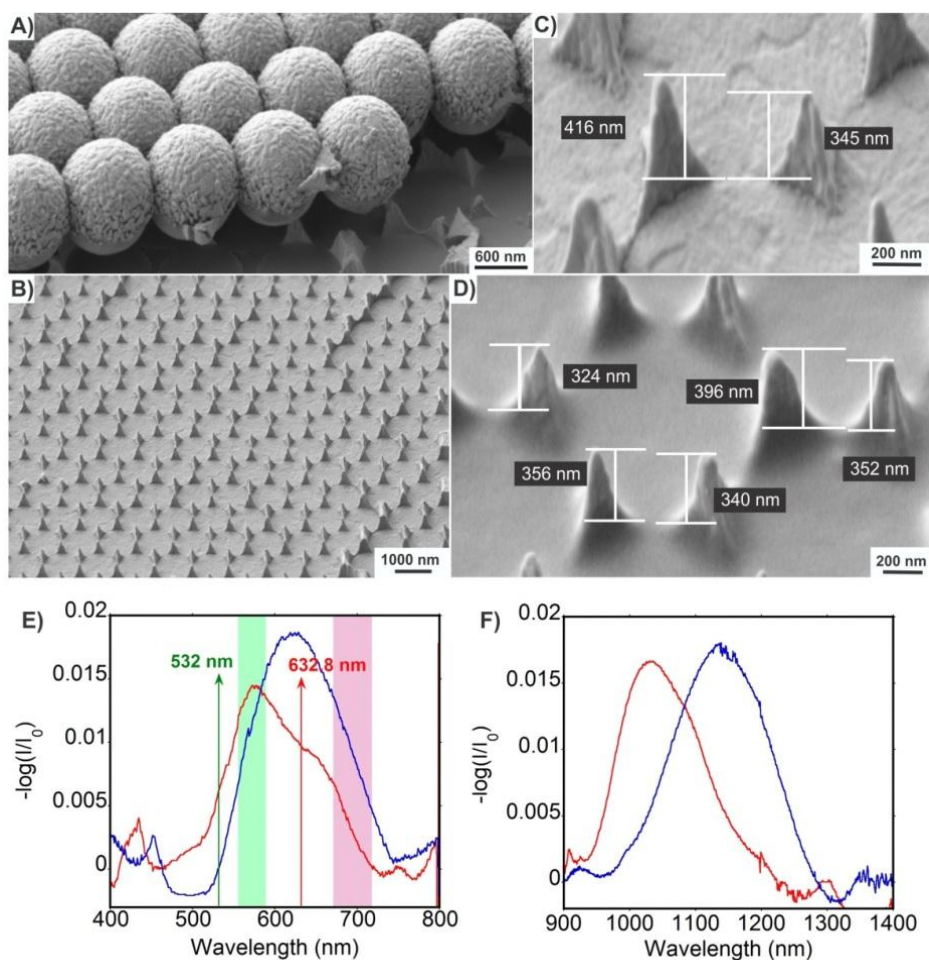


**Figure 6.2** A) SEM images of silver-coated polystyrene nanospheres. B) Array of silver nanopyramids. C, D) Individual silver nanopyramids before and after coating with an azopolymer thin film, respectively. E, F) Extinction spectra of the Silver (red) and gold(blue) nanopyramids. Excitation wavelengths as well as the [800-1800]  $\text{cm}^{-1}$  spectral ranges with respect to both excitations are indicated.

The resulting scanning electron microscopy (SEM) images of the nanopyrramids formed by NSL are shown in **Figure 6.2A-D** after deposition of 400 nm layer of silver over the 1  $\mu\text{m}$  diameter polystyrene spheres by electron-beam evaporation. Noteworthy, similar structures have been obtained for gold nanopyrramids (**Figure 6.3**). The triangular voids between three adjacent spheres in close contact get smaller during the deposition process, leading to the formation of pyramidal structures. ITO layer of 120 nm thickness over the glass slide forms an adhesive layer, avoiding further deposition of chromium or titanium deposition. It can be clearly seen that both deposited metal and the ITO layer demonstrated intrinsic roughness on the substrate (**Figure 6.2A**).

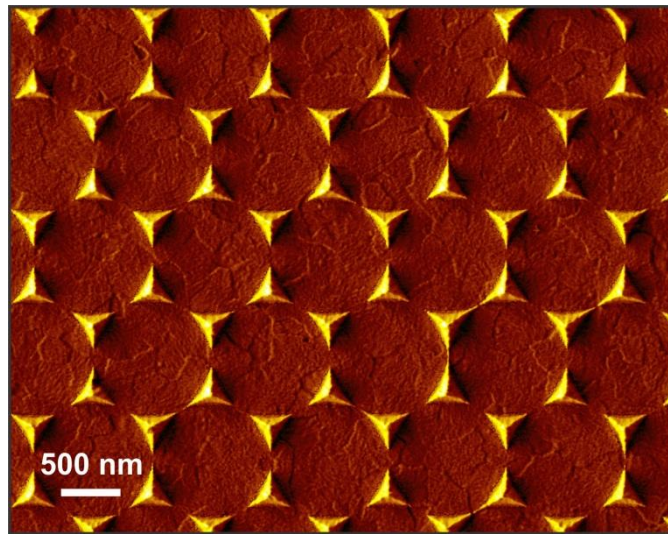


**Figure 6.3** False-colored SEM image showing arrays of gold nanopyrramids

Subsequent to the lift-off process of the polystyrene nanoparticles, a large surface ( $\text{mm}^2$ ) of homogeneous pyramids can be observed over the ITO substrate (**Figure 6.2B**). The extinction spectra of both silver and gold nanopyramid arrays (**Figure 6.2E-F**) show two

resonances corresponding to the quadrupolar and the dipolar contributions, respectively. For silver, the quadrupolar LSPR is expected at 550 nm, while for gold this resonance is red-shifted to 585 nm. The dipolar contributions are even further shifted in the near-infrared range at 1035 nm and 1100 nm, respectively.

### 6.3.2 FDTD calculations

In order to estimate the influence of the geometry on the localization of the LSPR, we have performed a series of finite difference time domain calculations for Au and Ag nanopillars irradiated with 532 and 632.8 nm wavelengths. The results of the normalized intensity enhancement,  $|E/E_0|^2$  depicted in logarithm scale are shown in **Figure 6.4** for Ag/532nm, while other cases (Ag/632.8, Au/632.8 and Au/532) are demonstrated in **Figure 6.5, 6.6 and 6.7**. In **Figure 6.4A-C**, a single isolated pillar was also investigated. The EM field was calculated in both longitudinal and transverse directions as shown in **Figure 6.4A-C**. In **Figure 6.4A**, the field is significantly confined along the edge of the pillars, which is also oriented along the polarization direction.

The typical field enhancement shown in log scale corresponds to 20 folds enhancement of the electric field, approximately. The field was calculated in the transverse plane with respect to light propagation 2 nm above the base of the pillar (**Figure 6.4B**) and 2 nm above the summit of the pillar (**Figure 6.4C**). Localized enhancement can be clearly seen at the three base corners of the pillars (Intensity enhancement of  $|E/E_0|^2 = 10^3$ ), while the enhancement at the summits of the pillar is limited (Intensity enhancement of  $10^{1.68} \sim 50$ ). This indicates that the polarization of the input light must have a component along the tip axis and no component in the orthogonal direction. Such observation was reported for nanoscale resolution tip-enhanced Raman spectroscopy (TERS), where the impinging field was ideally polarized along the tip axis to excite the

plasmon modes resonance of the metalized tip. This was then employed as a local nanoantennae to probe the surface of interest.<sup>34,35</sup>

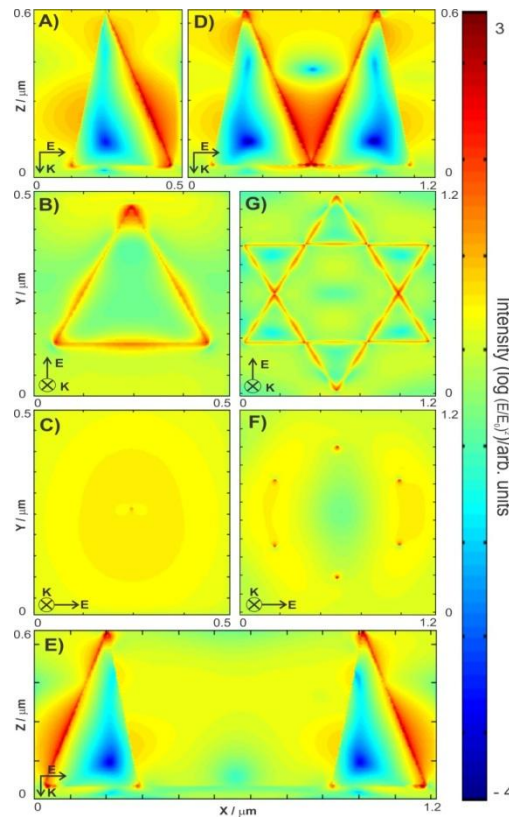


**Figure 6.4 FDTD calculation of the transverse (B,C,F,G) and longitudinal (A,D,E) components of the electric field ( $|E/E_0|^2$ , Log scale representation) for silver nanopylramids prepared on ITO and irradiated at 532 nm. The transverse field shown in C,F) are calculated 2 nm above the tip(s) of the pyramid(s). The transverse field shown in (B,G) are calculated 2 nm above the ITO base layer.**

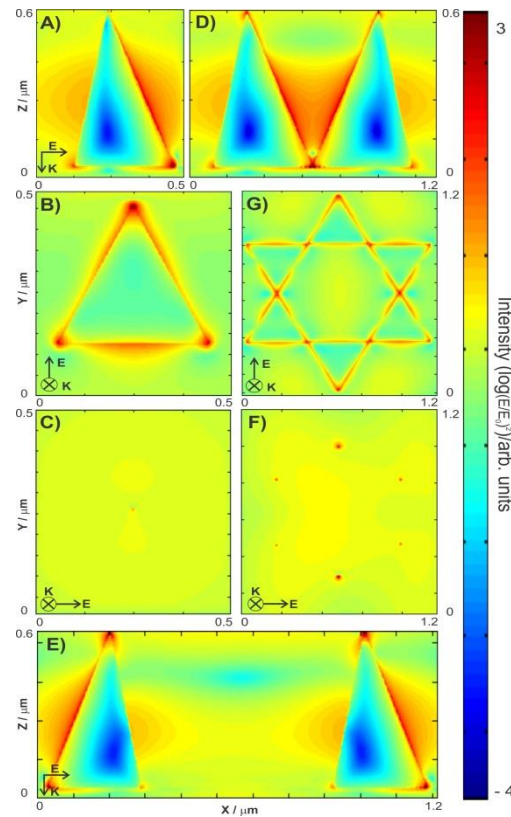


**Figure 6.5** FDTD calculation of the transverse (B,C,F,G) and longitudinal (A,D,E) components of the electric field ( $|E/E_0|^2$ , Log scale representation) for silver nanopillars prepared on ITO and irradiated at 632.8 nm. The transverse field shown in C,F) are calculated 2 nm above the tip(s) of the pyramid(s). The transverse field shown in (B,G) are calculated 2 nm above the ITO base layer

Further modeling was conducted on an array of pyramids arranged in a hexagonal lattice along the longitudinal and transverse planes with respect to the propagation direction  $\mathbf{k}$ . In **Figure 6.4D**, the field in the longitudinal plane of two facing pyramids was investigated. In this case, the field was also considerably confined along the facing edges of the pair of pyramids that formed variable gaps.



Typically, the field is confined from the base of the pyramids to about half the height of the pyramid array. This is as well observed for other material/wavelength configurations such as Ag/632.8 (**Figure 6.6 D**), and Au/632.8 (**Figure 6.7 D**) as opposed to Au/532 (**Figure 6.7 D**). In the later configuration, the field enhancement was confined along the edges of the pyramid pairs.

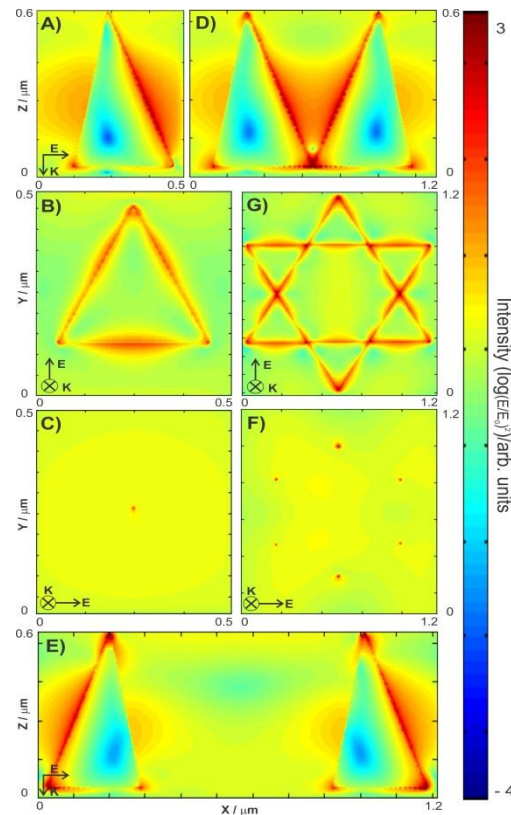


**Figure 6.6** FDTD calculation of the transverse (B,C,F,G) and longitudinal (A,D,E) components of the electric field ( $|E/E_0|^2$ , Log scale representation) for gold nanopillars prepared on ITO and irradiated at 632.8 nm. The transverse field shown in C,F) are calculated 2 nm above the tip(s) of the pyramid(s). The transverse field shown in (B,G) are calculated 2 nm above the ITO base layer.

However, no effective coupling was observed between the facing pyramids. The results clearly showed that the variable gap between opposed pyramids can be beneficial to applications in plasmon enhanced spectroscopy, since the matching between the plasmon resonance frequency and the excitation light frequency may not be critical. In other words, from calculations shown in **Figure 6.4** and **Figure 6.5**, silver nanopyramids are expected to be efficient for field enhancement at both 532 and 632.8 nm wavelengths. For gold pyramids, the scenario is different and coupling was mainly effective when 632.8 nm excitation was being used. As shown in **Figures 6.5 D**, and **6.6 D**, coupling between facing pyramids was only observed at 632.8 nm, while for 532 nm the enhanced field was mainly observed along the opposed edges of the nanopyramids, but without any coupling. Based on these calculations, we can then expect a much lower overall enhancement for gold pyramids exposed by 532 nm wavelengths, while silver pyramids will be effective for both wavelengths.

For surface-enhanced Raman, this is of interest but one must consider as well the enhancement of the Raman shifted frequencies. As shown in **Figure 6.2E**, ideally, both  $E_{Excitation}$  and  $E_{Raman}$  must be in resonance or pre-resonance with the extinction of the plasmon frequency to be enhanced. When these two conditions are fulfilled, the EM enhancement,  $F$ , is given by<sup>36</sup>

$$F = \left| \frac{E_{Excitation}}{E_0} \right|^2 \left| \frac{E_{Raman}}{E_0} \right|^2 \quad (1)$$

where  $E_0$  is the incident electric field before enhancement. This yields to a SERS intensity that can be described by Eq. (2):<sup>9</sup>

$$I_{SERS} = I_0 N \sigma_{SERS} \left| \frac{E_{Excitation}}{E_0} \right|^2 \quad (2)$$

where  $I_0$ ,  $N$  and  $\sigma$  are the intensity of the incident light, the number of scattering centers and the scattering cross section, respectively.

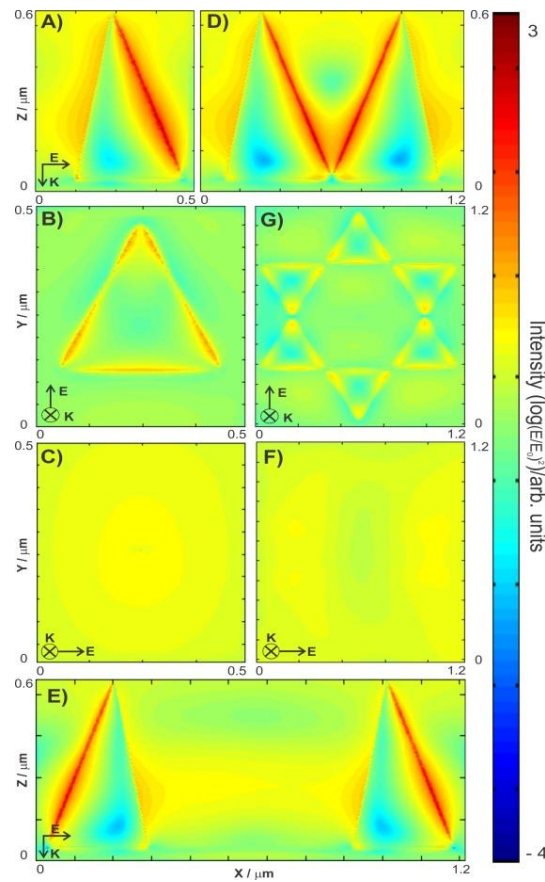


**Figure 6.7 FDTD calculation of the transverse (B,C,F,G) and longitudinal (A,D,E) components of the electric field ( $|E/E_0|^2$ , Log scale representation) for gold nanopillars prepared on ITO and irradiated at 532 nm. The transverse field shown in C,F) are calculated 2 nm above the tip(s) of the pyramid(s). The transverse field shown in (B,G) are calculated 2 nm above the ITO base layer.**

It appears that excitations at 532 and 632.8 nm are both resonant for the silver nanostructure, which gave rise to the enhancement of the Raman signal in the fingerprint region of the molecule of interest. From the FDTD calculation, assuming an intensity enhancement of  $10^3$  at both the excitation and Raman wavelengths for Ag/532 nm, equation (2) yields to an overall SERS EF of  $\sim 10^6$  which is comparable to reported values in literature.<sup>10</sup> However, for gold pyramids, since the excitation of 532 nm is weakly resonant with the quadrupolar contribution of pyramidal structure, a smaller Raman enhancement is therefore expected.

### 6.3.3 Mapping individual hot spots on photosensitive self-developing azopolymer

In order to visualize the confinement of the field over the whole plasmonic structure, experiments using a photosensitive polymer were conducted on the nanostructures. An azobenzene thin layer (80 nm) was spin coated over the whole silver nanopyramid arrays, leading to a smooth surface as shown in **Figure 6.2 D**. Azobenzene polymer is of particular interest since it undergoes surface migration and subsequent topographical changes upon irradiation by resonant light. In this study, we used p(DR1M-co-MMA) with a molar ratio in azobenzene moieties of 11% (**Figure 6.1**). The donor ( $\text{NH}_2$ ) and acceptor ( $\text{NO}_2$ ) groups located on opposite sides of the azobenzene core are responsible for the large charge density on the molecule, leading to a colorful thin film material with an absorption at maximum wavelength of  $\lambda=500$  nm and extinction coefficient of  $\epsilon=70000 \text{ l.mol}^{-1}.\text{cm}^{-1}$ . Therefore, excitation wavelength of 532 nm will be doubly resonant with i-the plasmon resonance of the silver pyramids array and ii- the absorption of the azobenzene polymer, leading to the most efficient surface deformation. Atomic force microscopy images were collected on the samples before and after irradiation at 532 nm with an irradiance of  $100 \text{ mW/cm}^2$  (**Figure 6.8 A-B**). Subtle changes in the

surface topography can be observed after irradiation during 15 min as shown by the indicated cross sections (1) and (2) on the AFM images. A topographical increase of  $7\pm 2$  nm can also be systematically measured at the center of a lattice (cross section (1)) over several individual lattices as shown in **Figure 6.8 B**, and **D**. The cross section shown in **Figure 6.8 B**, shows a bi-modal increases with two maxima separated by a smaller minimum. This change of topography is a very useful indicator of the field location knowing that azopolymers migrates from area where the field is large towards areas where the field is weaker. As shown in **Figure 6.4 G** for silver pyramids, the field calculated 2 nm above the pyramid base is indeed weaker at the center of the lattice, while the most intense field was observed at the apices between facing nanopillars. The azopolymer molecules migrated towards the center of the lattice as expected. Besides, the small minimum between the two maxima can be explained by the competition between the migration processes coming from both sides. Similar effect has been reported previously for studies where gratings were inscribed holographically onto thin films of azopolymers, leading to half periodic structures with respect to the interference fringe spacing.<sup>37</sup> This is result of photodriven mass transport from successive photoisomerization steps.<sup>38,39</sup> This photoinduced mechanism suggests possible strong alterations of the local viscoelastic properties of the polymer and changes of the local densities that further alter the migration of the polymer chains towards the center of the lattice.<sup>37</sup> Similar changes were obtained when the cross section was measured along closely facing triangles (cross section (2) on the AFM images). As shown in **Figure 6.8 E-F**, the topographical change is insignificant. It is less than 5 nm in height variation, but yet very clearly observable by AFM. Also, the change of the slopes is due to the migration of the photosensitive polymer mediated and amplified by the plasmonic resonance. The slope of the polymer thin film deposited over the pyramids was increased after irradiation, which indicated a mass flow from the area where enhancement of the

field is high towards regions where the field is weaker. In addition, the gap between the two facing pyramids indicated a weaker field enhancement at the exact center between the facing pyramids. Thus, the polymer migration was predominantly observed along the edge of the pyramids.

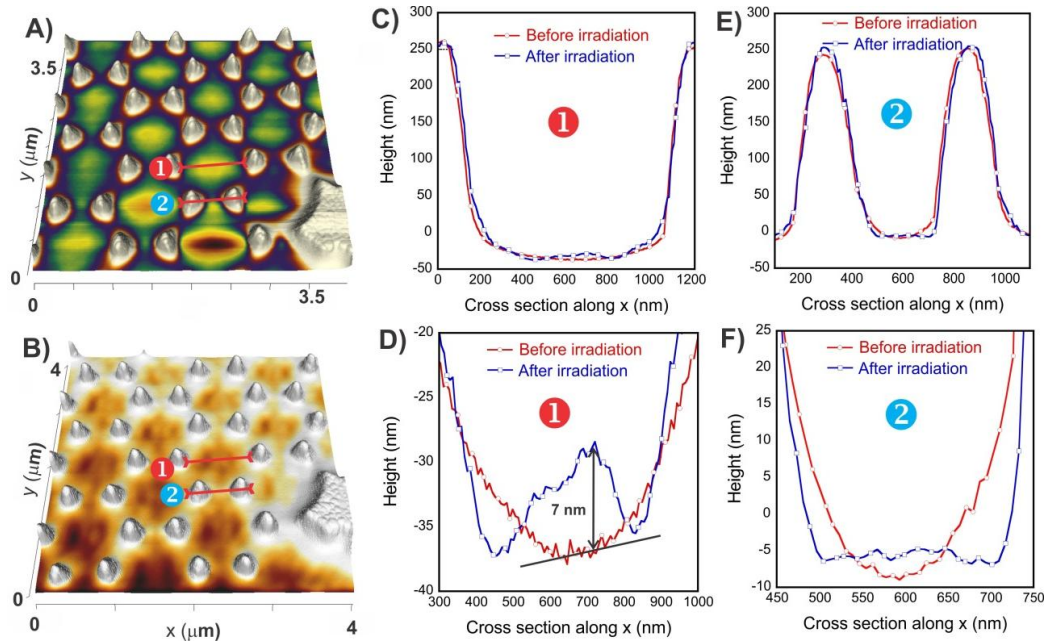


**Figure 6.8 A,B) AFM images of Ag nanopyramids prepared on ITO coated with a 80 nm azopolymer thin film layer before (A) and after (B) 15 min of irradiation with a irradiance of  $100 \text{ mW/cm}^2$ . C,D) topographical cross sections along the center of a hexagonal lattice (noted 1) of Ag nanopyramids before and after irradiation. E,F) AFM topographical cross sections along the closest facing silver pyramids (noted 2) before and after irradiation.**

### 6.3.4 SERS measurements

The capability of these pyramidal structures was further investigated for SERS application using a standard molecule. To perform this, the structures were immersed in a 1 mM solution of 4-NTP for 24 hours and subsequently rinsed with ethanol to remove non-adsorbed species. Both gold and silver pyramid arrays were investigated with excitation wavelengths of 532 and 632.8 nm. The Raman spectra measured on the pyramidal nanostructures are reported in **Figure 6.9** together with the reference spectra performed on flat portion of the deposited metal. None of the reference spectra measured on flat gold and silver areas showed spectral feature, emphasizing the interest of using the nanostructured surface for the study of adsorbed monolayers.

The spectra shown in **Figure 6.9A** demonstrated an intense signal for gold pyramids upon irradiation at 632.8 nm, whereas the Raman spectrum was weak for 532 nm. This confirms that the matching between the excitation wavelength and the plasmon resonance is critical and was fulfilled only for the Au/632.8 case. The main spectral features observed in **Figure 6.9A** at 1078, 1107, 1340 and 1572  $\text{cm}^{-1}$  are assigned to  $\nu_{7a}$  (coupled with C-S bond),  $\nu_{\phi-N}$ ,  $\nu_s \text{NO}_2$  and  $\nu_{8b}$  of the phenyl group, respectively.<sup>40</sup> The SERS spectra of silver nanopyramids irradiated by 632.8 nm laser with 0.2 and 2 mW intensities are shown in **Figure 6.9B**. Noticeably, the initial spectrum recorded with 0.2 mW was similar to the Au/632.8 case in terms of relative intensities and magnitude. Silver pyramidal nanostructures have therefore a plasmon that can be used in conjunction with both irradiation wavelengths since, as shown in **Figure 6.2E**, both 532 and 632.8 nm wavelengths are pre-resonant with the plasmon absorption. Considerably, the initial spectrum recorded with 0.2 mW was also similar to the Au/632.8 case in terms of relative intensities. However, when the laser power was increased to 2 mW, the collected spectra showed significant changes. This could be understood by considering the fact that 2 mW

laser focused with high N.A. microscope objective implies a typical irradiance in the MW/cm<sup>2</sup> range.

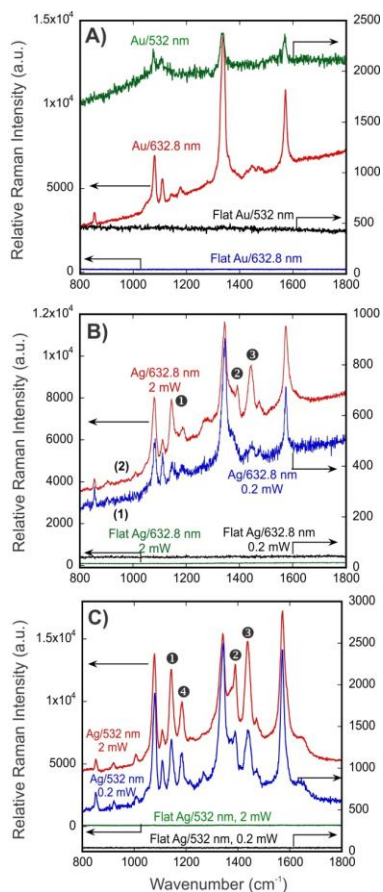


**Figure 6.9** Raman spectra of 4-NTP adsorbed on the nanopyramid arrays. The spectra were recorded with same acquisition time (10 s). No baseline correction was performed. Raman spectra acquired on flat metal portions (no structures) and functionalized the same conditions as shown. **A)** SERS spectra collected on Au nanopyrramids with 632.8 and 532 nm irradiations. **B)** SERS spectra collected on Ag nanopyrramids with 632.8 nm excitation under 0.2 mW (initial) and 2mW (final) irradiations. **C)** SERS spectra collected on Ag nanopyrramids with 532 nm excitation



**under 0.2 mW and 2mW irradiations. D) SERS spectra recorded at 632.8 nm on Ag nanopyramids at 2 mW (initial) and 0.2 mW (final).**

New bands at 1142, 1387 and 1437  $\text{cm}^{-1}$  (noted 1, 2 and 3 in **Figure 6.9B**) were assigned to  $\beta_{\text{C-H}}$ ,  $\nu_{\text{N=N}}+\nu_{\text{C=C}}+\nu_{\text{C-H}}$  and  $\nu_{\text{N=N}}+\nu_{\text{C=C}}+\beta_{\text{C-H}}$ , respectively, while the intensity of the 1340  $\text{cm}^{-1}$  band ( $\nu_{\text{s}} \text{NO}_2$ ) was decreased. Such observations were investigated by several groups and were assigned to photoinduced reduction of 4-NTP on Ag surfaces to form dimercaptoazobenzene (DMAB).<sup>40-42</sup> More recently, time resolved measurements using tip-enhanced spectroscopy were reported using a silver-coated AFM tip irradiated by a 532 nm excitation laser. Nonetheless, a non-resonant laser at 632.8 nm was used to probe the photoreduction as a function of irradiation time.<sup>43</sup>

Our results indicated that for these particular plasmonic platforms, even 632.8 nm can trigger the photoreduction of 4-NTP into DMAB as long as irradiation intensity is sufficiently high. The same condition was also applied to silver structures at 532 nm, which exhibited the highest enhancement as shown in **Figure 6.9C**. For both intensities of the excitation source, the spectra showed the new peaks assigned to the formation of DMAB as in the case of Ag/632.8. However, the peak associated with the symmetric stretching mode of  $\text{NO}_2$  was even further reduced in intensity, indicating a higher photoreduction yield upon 532 nm irradiation. Similarly, the Raman band at 1183  $\text{cm}^{-1}$  (noted 4) in **Figure 6.9C** was significantly increased which has not been addressed in other studies. This clearly indicates that Ag/532 offered the highest enhancement conditions even at low power.

We also compared side-by-side the SERS spectra from gold nanopyramids and nanotriangles made by NSL as shown in **Figure 6.10**. In the latter case (nanotriangles),

the thickness of gold was of 30 nm. At 632.8nm excitation, the SERS spectra are systematically more intense for the nanopyramids as compared to the nanotriangles by a typical factor of  $\sim 4$ . This gain confirms the interest of the nanopyramids compared to the nanotriangles for ultra-sensitive measurements.

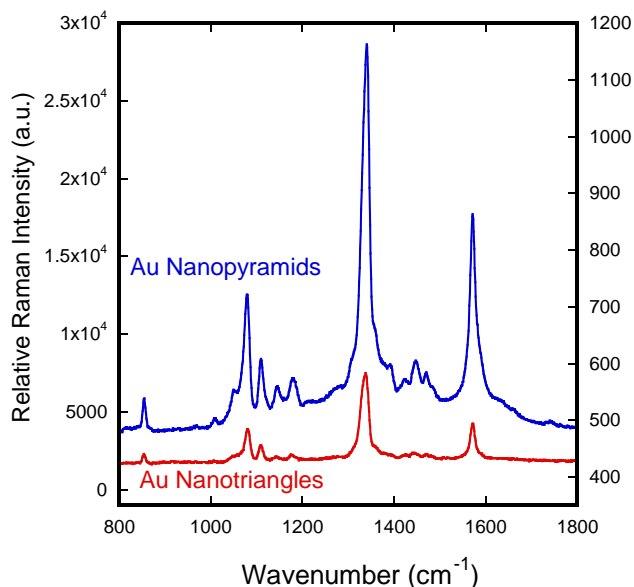


**Figure 6.10** Raman spectra of 4-NTP adsorbed on the nanotriangles (30 nm Au), and nanopyramid arrays (400 nm Au). The spectra were recorded with same acquisition time (10 s) and irradiation wavelength was 632.8 nm with  $I=2$  mW.

Significant relative intensity changes indicated the photoinduced transformation of the molecule of interest. Thus, a control experiment was performed to confirm the irreversibility of the photoinduced transformation. Using Ag/632.8 nm conditions, intensity of 2 mW was first used to collect the first spectrum shown in **Figure 6.11** (noted (1)). The second spectrum (noted (2) in **Figure 6.11**, was collected after irradiation with 0.2 mW similar to the conditions of **Figure 6.9B**. In such sequence the spectral features

recorded with the lowest intensity were identical to the spectra measured with higher intensity, confirming the irreversibility of the photoinduced reaction.

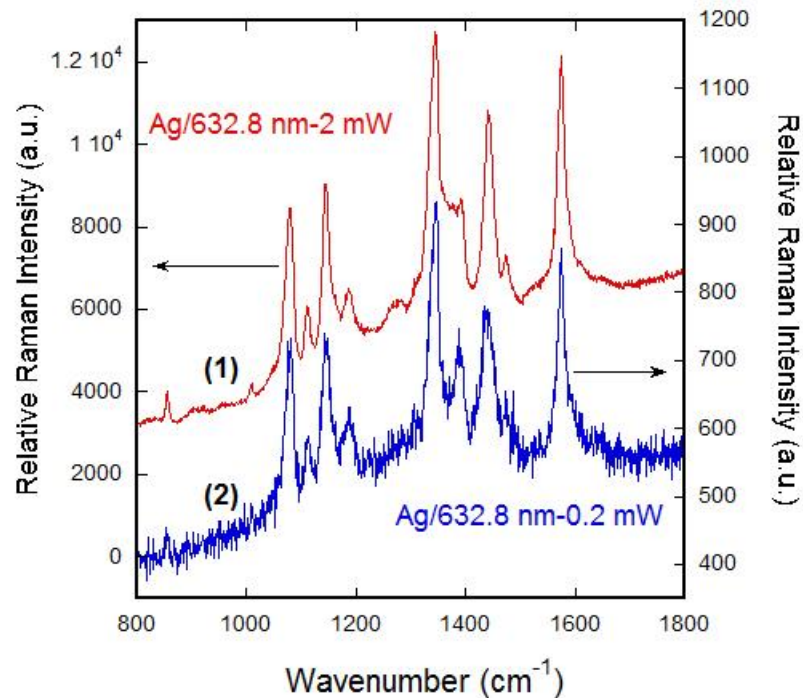


**Figure 6.11** SERS spectra of 4-NTP adsorbed onto silver nanopyramids recorded initially under 2 mW irradiance followed by a measurement under 0.2 mW with identical acquisition time (10 s).

## 6.4 Conclusion

In the present study, we have prepared arrays of metallic nanopyramids made of gold and silver using NSL. We focus our study on plamonics properties and near field enhancement of such real 3D nanostructure. Both platforms were investigated upon irradiation by 532 and 632.8 nm wavelengths, since the quadrupolar plasmon resonance of both structured metals have resonance close to these wavelengths. FDTD calculations

in the transverse and longitudinal planes with respect to the propagation direction of the excitation source were systematically conducted for the four cases, namely Au/532, Au/632.8 and Ag/532, Ag/632.8. These calculations clearly showed that the silver nanostructure can efficiently be excited at 532 and 632.8 nm, whereas gold nanostructure is not expected to be efficient at 532 nm. To complement these FDTD simulations, AFM characterization and Raman measurements were also conducted on the samples using photosensitive azopolymer thin film. This allows one to monitor topographical changes on the surface of silver nanostructure coated with a photo responsive film. In addition, this opens up the opportunity to indirectly locate the area of high field enhancement over the substrate. Finally, these structures were tested for SERS measurements with 4-NTP molecules. As a result, SERS was observed predominantly for Ag/532, Ag/632.8 and Au/632.8. For silver nanostructures, photoreduction of 4-NTP to DMAB was also observed. In the case of 632.8 nm irradiation, it was shown to be dependent on the laser intensity. Such changes were irreversible, emphasizing the interest of metallic plasmonic platforms not only for surface enhancement, but also for photoinduced chemical reaction at a monolayer of a material on the surface. These nanopyramid arrays fabricated on a conductive and transparent substrate can be further integrated in solar cells, benefiting from both the plasmon enhancement of the solar spectrum and the electronic conduction of the ITO layer, yielding to a higher photovoltaic conversion efficiency. Beyond optical applications, we suggest that these high aspect ratio structures have also potential as super-hydrophobic surfaces and field emission antennae. The extremely simple but efficient protocol proposed here based on the well-known NSL lithography can be applied to many materials for the preparation of real 3D sharp nanopyramids array on large surfaces.

## 6.5 References

(1) Brongersma, M. S.; Shalae, V. M.; *Science*, (2010), 328, 440.

- (2) Krasavin, A. V.; Zayats, A. V.; *Appl. Phys. Lett.*, **(2010)**, *97*, 041107.
- (3) Krasavin, A. V.; Zayats, A. V.; *Opt. Lett.*, **(2011)**, *36*, 3127.
- (4) Aydin, K.; Ferry, V. E.; Briggs, R. M.; Atwater, H. A.; *Nature Commun.*, **(2011)**, *2*, 1.
- (5) Brolo, A. G.; *Nature Photonics*, **(2012)**, *6*, 709.
- (6) Ahmed, A.; Gordon, R.; *Nano Letters*, **(2012)**, *12*, 2625.
- (7) Asiala, S. M.; Schultz, Z. D.; *Analyst*, **(2011)**, *136*, 4472.
- (8) Atwater, H. A.; Polman, A.; *Nature Mat.*, **(2010)**, *9*, 205.
- (9) Yokota, Y.; Ueno, K.; Misawa, H.; *Small*, **(2011)**, *7*, 252.
- (10) Marquestaut, N.; Martin, A.; Talaga, D.; Servant, L.; Ravaine, S.; Reculosa, S.; Bassani, D. M.; Gillies, E.; Lagugné-Labarthe, F.; *Langmuir*, **(2008)**, *24*, 11313.
- (11) Li, K.; Clime, L.; Cui, B.; Veres, T.; *Nanotechnology*, **(2008)**, *19*, 145305.
- (12) Dhawan, A.; Du, Y.; Batchelor, D.; Wang, D.; Leonard, D.; Misra, V.; Ozturk, M.; Gerhold, M. D.; Vo-Dinh, T.; *Small*, **(2011)**, *7*, 727.
- (13) Ye, X.; Qi, L.; *Nano Today*, **(2011)**, *6*, 608.
- (14) Correia-Ledo, D.; Gibson, K.; Dhawan, A.; Couture, M.; Graham, D.; Vo-Dinh, T.; Masson, J. F.; *J. Phys. Chem. C.*, **(2012)**, *116*, 6884.
- (15) Abass, A.; Shen, H.; Bienstman, P.; Maes, B.; *J. Appl. Phys.*, **(2011)**, *109*, 023111.
- (16) Fischer, U. C.; Zingsheim, H. P.; *J. Vac. Sci. Technol.*, **(1981)**, *19*, 881.
- (17) Huang, W.; Qian, W.; El-Sayed, M. A.; Ding, Y.; Wang, Z. L.; *J. Phys. Chem. C*, **(2007)**, *111*, 10751.
- (18) Haynes, C. L.; Van Duyne, R. P.; *J Phys. Chem. B*, **(2003)**, *107*, 7426.
- (19) Huang, W.; Qian, W.; El-Sayed, M. A.; *Nano Lett.*, **(2004)**, *4*, 1741.
- (20) Morarescu, R.; Shen, H.; Vallée, R. A. L.; Maes, B.; Kolaric, B.; Damman, P.; *J. Mater. Chem.*, **(2012)**, *22*, 11537.
- (21) Fayyaz, S.; Tabatabaei, M.; Hou, R.; Lagugné-Labarthe, F.; *J. Phys Chem. C*, **(2012)**, *27*, 1494.

- (22) Lenzmann, F.; Li, K.; Kitai, A. H.; Stöver, H. D. H.; *Chem. Mater.*, **(1994)**, *6*, 156.
- (23) Hubert, C.; Rumyantseva, A.; Lerondel, G.; Grand, J.; Kostcheev, S.; Billot, L.; Vial, A.; Bachelot, R.; Royer, P.; Chang, S.; *Nano Lett.*, **(2005)**, *5*, 615.
- (24) Hubert, C.; Bachelot, R.; Plain, J.; Kostcheev, S.; Lerondel, G.; Juan, M.; Royer, P.; Zou, S.; Schatz, G. C.; Wiederrecht, G. P.; *J. Phys. Chem. C*, **(2008)**, *112*, 4111.
- (25) Hubert, C.; Fiorini-Debuisschert, C.; Maurin, I.; Nunzi, J.-M.; Raimond, P.; *Adv. Mater.*, **(2002)**, *14*, 729.
- (26) Murray-Méthot, M.-P. M., N.; Masson, J.-F.; *Analyst*, **(2008)**, *133*, 1714.
- (27) Guieu, V.; Lagugné-Labarthe, F.; Servant, L.; Talaga, D.; Sojic, N.; *Small*, **(2008)**, *4*, 96.
- (28) Li, J. F.; Huang, Y. F.; Ding, Y.; Yang, Z. L.; Li, S. B.; Zhou, X. S.; Fan, F. R.; Zhang, W.; Zhou, Z. Y.; Wu, D. Y.; Ren, B.; Wang, Z. L.; Tian, Z. Q.; *Nature*, **(2010)**, *464*, 392.
- (29) Chung, P.-Y.; Lin, T.-H.; Schultz, G.; Batich, C.; Jiang, P.; *Appl. Phys. Lett.*, **(2010)**, *96*, 261108.
- (30) Lin, T.-H.; Linn, N. C.; Tarajano, L.; Jiang, B.; Jiang, P.; *J. Phys Chem. C*, **(2009)**, *113*, 1367.
- (31) Sun, C.-H.; Linn, N. C.; Jiang, P.; *Chem. Mater.*, **(2007)**, *19*, 4551.
- (32) Stoerzinger, K. A.; Hasan, W.; Lin, J. Y.; Robles, A.; Odom, T. W.; *J. Phys. Chem. Lett.*, **(2010)**, *1*, 1046.
- (33) Alexander, T. A.; *Proc. of SPIE*, **(2005)**, *6007*, 600703.
- (34) Hartschuh, A.; *Angew. Chem. Int. Ed.*, **(2008)**, *47*, 8178.
- (35) Cançado, L. G.; Jorio, A.; Ismach, A.; Joselevich, E.; Hartschuh, A.; Novotny, L.; *Phys. Rev. Lett.*, **(2009)**, *103*, 186101.

- (36) Schatz, G. C.; Young, M. A.; Van Duyne, R. P. In *Surface-Enhanced Raman Scattering*; Kneipp, K., Moskovits, M., Kneipp, H., Eds.; Springer-Verlag Berlin: Berlin/Heidelberg, 2006; Vol. 103, p 19.
- (37) Schaller, R. D.; Saykally, R. J.; Shen, Y. R.; Lagugné-Labarthet, F.; *Optics Letters*, **(2003)**, 28, 1296.
- (38) Viswanathan, N. K.; Balasubramanian, S.; L., L.; Tripathy, S. K.; Kumar, J.; *Jpn. J. Appl. Phys.*, **(1999)**, 38, 5928.
- (39) Lefin, P.; Fiorini, C.; Nunzi, J. M.; *Pure Appl. Opt.*, **(1998)**, 7, 71.
- (40) Kim, K.; Lee, Y. M.; Lee, H. B.; Park, Y.; Bae, T. Y.; Jung, Y. M.; Choi, C. H.; Shin, K. S.; *J. Raman Spectrosc.*, **(2010)**, 41, 187.
- (41) Kim, K.; Lee, I.; Lee, S. J.; *Chem. Phys. Lett.*, **(2003)**, 377, 201.
- (42) Sun, S.; Birke, R. L.; Lombardi, J. R.; Leung, K. P.; Genack, A. Z.; *J. Phys. Chem.*, **(1988)**, 92, 5965.
- (43) van Schrojenstein Lantman, E. M.; Deckert-Gaudig, T.; Mank, A. J. G.; Deckerts, V.; Weckhuysen, B. M.; *Nature Nanotechnology*, **(2012)**, 7, 583.

## Chapter 7

### 7 Tunable 3D plasmonic cavity nanosensors for surface-enhanced Raman spectroscopy with sub-femtomolar limit of detection<sup>4</sup>

Metallic nanohole arrays (NHAs) with a high hole density have emerged with potential applications for surface-enhanced Raman spectroscopy (SERS) including the detection of analytes at ultra-low concentrations. However, these NHA structures generally yield weak localized surface plasmon resonance (LSPR) which is a prerequisite for SERS measurements. In this chapter, a compact three-dimensional (3D) tunable plasmonic cavity with extraordinary optical transmission properties serves as a molecular sensor with sub-femtomolar detection. The 3D nanosensor consists of a gold film containing a NHA with an underlying cavity and a gold nanocone array at the bottom of the cavity. These nanosensors provide remarkable surface plasmon polariton (SPP) and LSPR coupling resulting in a significantly improved detection performance. The plasmonic tunability is evaluated both experimentally and theoretically. A SERS limit of detection of  $10^{-16}$  M for 4-Nitrothiophenol (4-NTP) is obtained along with distribution mapping of the molecule on the 3D plasmonic nanosensor. This results in an improved SERS EF of  $10^7$  obtained from a femtolitre plasmonic cavity volume. The tunability of these sensors can give rise to a potential opportunity for use in optical trapping while providing SERS sensing of a molecule of interest.

---

<sup>4</sup> A version of this chapter has been published in [*ACS Photonics*, (2015), 2, 752].  
Reproduced with permission of the American Chemical Society (ACS) publishing group.



## 7.1 Introduction

Molecular plasmonics has shown great promise for trace detection of molecules and biomolecules adsorbed onto rationally designed metallic platforms or particles.<sup>1-4</sup> Among the techniques benefiting from recent advances of plasmon-mediated optical measurements, SERS has pushed the limits for detection of even lower concentration of analytes. It yields chemical and biological sensing using a variety of surfaces and approaches that mainly relies on the drastic enhancement of the weak Raman signal through the enhancement of the local EM field in the vicinity of the metallic surface.<sup>5,6</sup> As an analytical technique, SERS provides label-free sensing with high sensitivity and chemical specificity.<sup>7,8</sup> Rational development of SERS platforms includes the production of reproducible engineered metallic platforms with arrays of well-defined structures that combine the functions of (i) trapping the analyte of interest, (ii) improving the sensitivity of the measurement by several orders of magnitude and (iii) providing quantitative measurements. As the enhancement of EM fields occurs in nanoscale regions, so-called plasmonic hot spots, integration of specific nanostructures for trapping the interested molecule in these hot spots can improve the sensitivity and reduce the detection time for SERS.<sup>9-13</sup>

Arrays of periodic nanoholes in a metallic film can act as a plasmonic substrate with diverse applications.<sup>14-17</sup> The nanohole array (NHA) structure in an optically thick metal film allows for momentum matching between an incident light on a NHA and the surface plasmon (SP) waves existing at the interface between a metal and a dielectric material.<sup>15</sup> The excitation of SPs, so-called surface plasmon polariton (SPP), by light incident on a metallic NHA results in extraordinary optical transmission (EOT) and optical resonances. The EOT properties of a NHA depend greatly on material composition and geometrical parameters of the structure.<sup>18-21</sup> Owing to scattering order of nanoholes, spacing between them and variable angle of incidence on the NHA, various EOTs related to different SPP

modes can be generated at different optical frequencies such as (1, 0) and (1, 1) transmission resonances.<sup>15</sup> NHAs have been widely used in various plasmonic applications ranging from optical trapping to sensing of biologically relevant molecules.<sup>20,22-28</sup> For instance, the array acts like a tunable filter since the wavelength selectivity of the array transmission can be adjusted simply by changing the periodicity.<sup>29,30</sup> Many studies have been performed to improve the performance of NHAs for sensing applications. For example, one of the most common applications of NHAs is surface plasmon resonance (SPR) refractive index sensing.<sup>22,25,31</sup> It has been shown that the most optimal performance was achieved in SPR sensing for a NHA structure consisting of an ultra-smooth NHA metal surface, elliptical nanohole shapes, and nearly SP energy matching between the top and bottom surfaces of the NHA.<sup>32</sup>

A localized surface plasmon resonance (LSPR) occurs when the incident light interacts with surface plasmon confined in the vicinity of a metallic nanoparticle, the size of which being comparable to or smaller than the excitation wavelength.<sup>33-35</sup> As a result, the EM field located in the near-field of the surface is greatly enhanced.<sup>36,37</sup> In this context, the aim is to design a plasmonic structure that will generate a strong LSPR coupling to further enhance the signal of the adsorbed molecule on a 2D or 3D plasmonic nanostructure.<sup>38</sup> Such LSPR plays a pivotal role in many surface-enhanced spectroscopic techniques such as surface-enhanced fluorescence, Raman and infrared spectroscopies, so-called SEF, SERS, and SEIRA, respectively.<sup>33,34,39</sup>

An individual nanohole can produce transmission based LSPR, which is associated to an interaction of the incident light with a LSPR around the nanohole.<sup>29</sup> The similar properties have been reported for a NHA with enhanced electric field intensity around each nanohole at the corresponding resonance wavelengths.<sup>23</sup> For SERS measurements, NHAs provide typical EFs below  $10^5$  which are weaker than other reliable SERS substrates.<sup>11,12,40</sup> More importantly, these EFs are not reported for very low

concentrations of the probe molecules. The reported range is between  $2-10^4$ , which is still comparable with some SERS substrates but not likely reliable compared to sensitive SERS substrates with EFs of over  $10^5$ .<sup>8,12,41</sup>

Herein, we evaluated the SERS performance of a 3D metallic nanostructure composed of an array of nanoholes and co-registered nanocones embedded in a single cavity. The optical properties of the nanosensors were investigated experimentally and using optical field modeling. Three major features of these sensors are highlighted in this work: i) plasmonic tunability; ii) SERS of 4-Nitrothiophenol (4-NTP) covalently attached on these sensors, and finally iii) limit of detection of 4-NTP adsorbed onto the sensors with fast acquisition time along with mapping the distribution of the molecules over the platform generating strong signals on the sensors based on the molecular fingerprint.

## 7.2 Experimental section

### 7.2.1 Fabrication of 3D plasmonic cavity nanosensors

The plasmonic cavities were fabricated using EBL methodology. First, electron-beam physical vapor deposition (EB-PVD) was used to deposit a 3 nm thin Ti layer on a Pyrex substrate. This ensured that the substrate surface was conductive for the EBL writing process. A 500 nm thick layer of photo-resist (negative tone photoresist ma-N 2403) was then spin-coated onto the Ti layer and soft baked at 90°C for 60 s. The sample was placed into an EBL instrument (LEO, 1530 e-beam lithography) where the nanohole array patterns were written on the photoresist layer. The sample was developed in MF 319 developer (Shipley, Marlborough, MA) for 40 s leaving behind photo-resist nano-pillars, which acted as a mask to create the nano-holes in the metal film. Another 3 nm thick Ti layer was deposited to create an adhesion layer followed by 80 nm deposition of Au using EB-PVD deposition instrument. Once the Au layer was deposited, the sample was

left in PG Remover solution at 80°C to lift-off the photoresist nano-pillars and leave behind the NHAs in the Au film. Once the NHAs were created, a TFT Ti etchant (Transene Company, Inc.) was used to etch away both Ti layer and Pyrex, forming a large cavity beneath the gold NHA. The sample was in Ti etchant for 70 s and resulted in a 250 nm deep cavity. Afterwards, 150 nm Au was deposited onto the structure to create a truncated nano-cone beneath each nanohole on the bottom surface of the cavity. The SEM images of the fabricated 3D plasmonic nanosensors with 500 nm periodicity are shown in Fig. 1(c). The presence of the 250 nm deep cavity and 150 nm tall truncated NCA beneath NHA the membrane structure are shown in these SEM images. Each 3D nanosensor had a dimension of approximately 5  $\mu\text{m}$  by 5  $\mu\text{m}$  and was repeated in a 7 by 7 square lattice arrangement with a periodicity of 10  $\mu\text{m}$ . In order to clean the platform for further use, O<sub>2</sub> plasma or UV-O<sub>3</sub> exposure are efficient methods. The substrate can also be cleaned by Nanostrip™ (90% sulfuric acid, 5% peroxymonosulfuric acid, <1% hydrogen peroxide, and 5% water) to remove all the impurities and subsequently washed with ultrapure MilliQ water and dried under nitrogen prior to O<sub>2</sub> or UV-O<sub>3</sub> cleaning.

### 7.2.2 Numerical simulation of 3D plasmonic cavity nanosensors

Modeling of the EM field was performed using FDTD method to numerically solve Maxwell's equations (FDTD Solutions, Lumerical Inc., Vancouver, Canada). As shown **Figure 7.1**, FDTD calculations were performed by creating a 3D unit cell that was simulated with periodic boundary conditions on the x- and y-axes, and a perfect match layer (PML) boundary condition in z axis. A rectangular, Cartesian style mesh was placed around the unit cell with a maximum mesh setting of 3 nm. The mesh settings can be altered to increase the accuracy of the simulation by increasing the number of points within the mesh.

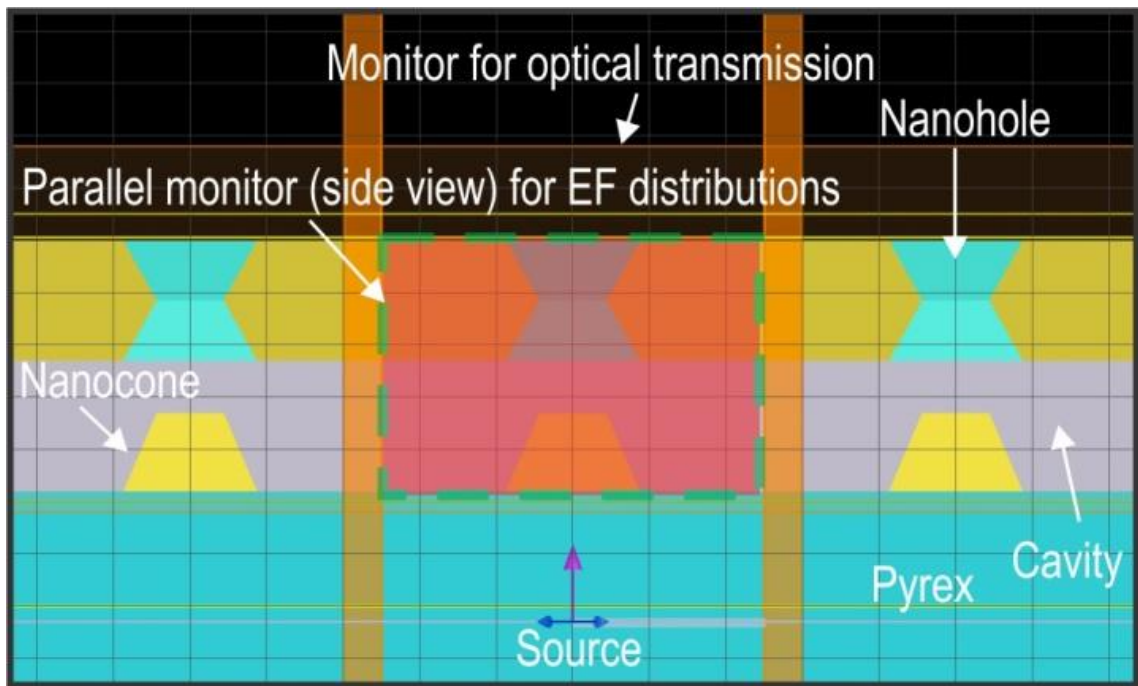


**Figure 7.1** Layout of FDTD simulation model including boundary conditions for optical properties and electromagnetic field distribution of 3D plasmonic nanosensors with a periodicity of 500 nm

### 7.2.3 Optical characterization setup

The extinction spectra of the platforms were measured, using an inverted microscope (Nikon, TE300) attached to a photometer (PTI, D104), monochromator (PTI, 101), and a photo-multiplier (PTI, 710). A 100 W halogen lamp produced unpolarized white light, which was focused onto the structure using a bright-field condenser lens (N.A. = 0.3) on the microscope. A X20 objective (N.A. = 0.45; Nikon, 93150) was used to collect the scattered light, which was then guided to the photometer using a beam splitter. Light from a desired region on the sample was selected by adjusting the apertures on the photometer. The light from this desired region was then guided to the monochromator for

spectral analysis. The optical transmission spectra were corrected for the background intensity (dark noise) and normalized by the intensity of the light source.

#### 7.2.4 SERS measurements and sample preparation

The Raman measurements were performed using a Horiba Jobin-Yvon Raman spectrometer equipped with a 600 g/mm grating and a 632.8 or 785 nm excitation with proper interference and edge filters. For both laser sources, intensities were set to 2 mW or 200  $\mu$ W at the sample using neutral density filters with 1.0 or 2.0 optical densities, respectively. Olympus microscope objectives of X20 (N.A.= 0.5), X40 (N.A.= 0.75), and X100 (N.A.= 0.9) were used for all experiments. The pinhole of the spectrometer was opened to 200  $\mu$ m. All of the Raman spectra collected for individual spots were the result of 3 s exposures; while the maps were the result of 1 s exposures. The maps were integrated within 1316 to 1354  $\text{cm}^{-1}$ . A stock solution of 4-NTP ( $10^{-3}$  M) in ethanol was made. This stock solution was then further diluted to yield 2 mL of solutions with concentrations ranging from  $10^{-6}$  to  $10^{-18}$  M. Two drops of the as-prepared solution ( $\sim 100$   $\mu$ L) were deposited onto one platform, and then placed into a petri-dish. All glassware used for functionalization and washing were new to avoid contamination. The petri-dish was sealed, and stored in the refrigerator for the duration of the functionalization. For the determination of limit of detection, the platforms were functionalized overnight (24 hours). Each platform was then washed into a beaker of ethanol (99.9%) 3 times to remove any excess of 4-NTP not adsorbed onto the surface. The platforms were then dried under nitrogen. Each SERS measurement was performed 3-5 times. The spectra of 10-15 spots were collected on each 3D nanosensor and the average value of the intensities was used in all relevant graphs.

## 7.3 Results and Discussion

### 7.3.1 Physical characterization of the fabricated 3D plasmonic cavity nanosensors

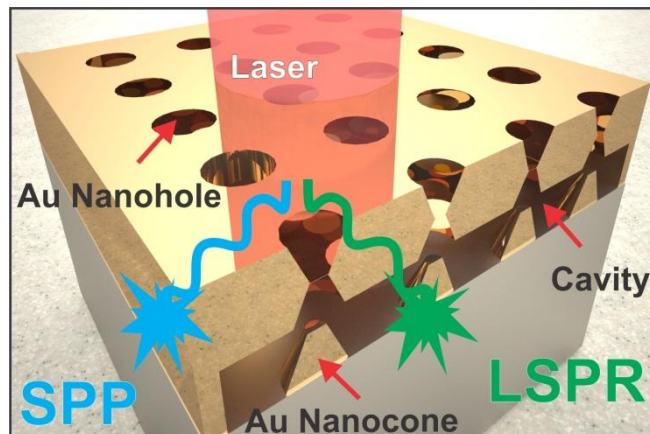


**Figure 7.2 Schematic of 3D plasmonic nanosensor displaying a cavity beneath the Au layer, and truncated nanocones at the bottom of the cavity.**

The schematic representation of 3D plasmonic cavity nanosensors is shown in **Figure 7.2**, generating SPP and LSPR couplings upon irradiation of the impinging light. Scanning electron microscopy (SEM) images of the nanosensors are shown in **Figure 7.3**. These sensors are composed of a NHA membrane with co-registered nanocone array (NCA). As shown in **Figure 7.3A**, this NHA-NCA platform consists of a NHA membrane in a 230 nm thick Au film on a Pyrex substrate with a 250 nm deep cavity, below the surface of the Au film. It can be seen in **Figure 7.3B** that at the bottom of the cavity, the co-registered truncated nanocones are aligned with the center of the nanoholes.

Demonstrated in **Figure 7.3**, a truncated cone has a height of 150 nm with an apex 100 nm away from the Au film. The hole sizes varied from 74 to 87 nm and the periodicities

varied from 425 to 500 nm with increments of 25 nm. A nanohole consists of two truncated nanocones with their apices connected at the center of the nanohole. The apex of the cone has a 1:2 ratio with respect to the cone base diameter. For the simulations, the complex refractive indices of Au were provided by Palik and a refractive index of 1.474 was used for Pyrex.<sup>42</sup>

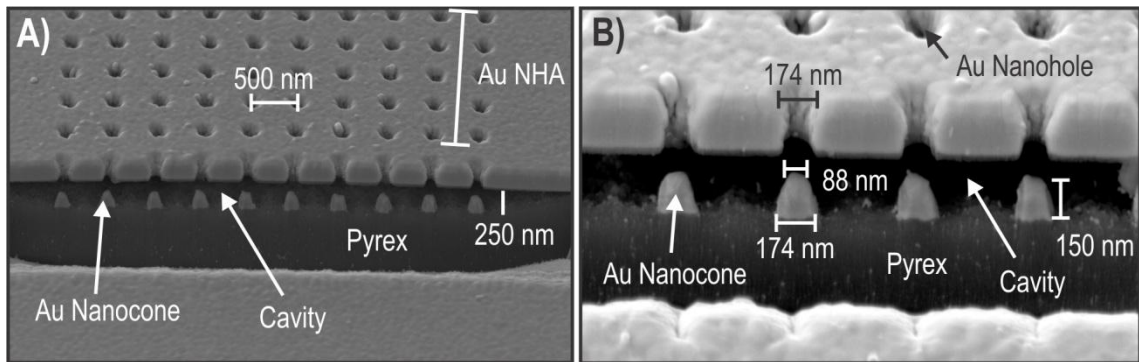


**Figure 7.3 SEM images of 3D plasmonic cavity nanosensors composed of a NHA membrane with co-registered NCA. a) A 230 nm thick Au NHA membrane with 500 nm periodicity and 87 nm hole radius fabricated on a Pyrex substrate with a single 250 nm deep cavity. b) Magnified image shown in (a) representing the dimensions of the truncated Au nanocones with an apex radius of 44 nm, a base radius of 87 nm, and a height of 150 nm.**

### 7.3.2 Tunable cavity 3D nanosensors

In both simulated and experimentally measured optical transmission spectra of the 3D nanosensors in **Figure 7.4**, multiple transmission resonances were observed due to the SPP corresponding to various scattering mode indices. A metallic NHA with a square lattice arrangement of nanoholes results in momentum matching between the in-plane wave-vectors of the incident light and the SP, when  $\vec{k}_{sp} = \frac{\omega}{c} \sin \theta \pm m\vec{u}_x \pm n\vec{u}_y$  is



satisfied. The expression  $\frac{\omega}{c} \sin \theta$  is the in-plane component of the wave vector of the incident light, where  $\omega$  is the frequency of the incident light,  $c$  is the speed of the light, and  $\theta$  is the incident angle of light.<sup>43</sup> The reciprocal lattice wave vectors  $\vec{u}_x$  and  $\vec{u}_y$  describe a square lattice when  $|\vec{u}_x| = |\vec{u}_y| = \frac{2\pi}{a}$ , where  $a$  is the spacing between adjacent nanoholes, and  $m$  and  $n$  are integers expressing the scattering mode indices. From the conservation of energy, the SP dispersion relationship on a smooth metal surface can be expressed as  $|\vec{k}_{sp}| = |\vec{k}_0| \sqrt{\frac{\epsilon_m \epsilon_d}{\epsilon_m + \epsilon_d}}$ , where  $\epsilon_d$  and  $\epsilon_m$  are the dielectric functions of the incident medium (at the top or bottom surface of nano-hole) and the metal film. By combining the momentum matching condition of the light-SP for light at normal incidence to the NHA and the dispersion relation of the SP, the EOT positions of a NHA associated to the SPP can be expressed by Equation 1:

$$\lambda_{max} \cong \frac{a}{\sqrt{m^2 + n^2}} \sqrt{\frac{\epsilon_m \epsilon_d}{\epsilon_m + \epsilon_d}} \quad (1)$$

The simulated and experimentally measured optical transmission spectra of the platforms for various periodicities are shown in **Figure 7.4** for platforms surrounded by air ( $n = 1.00$ ) or immersed in water ( $n = 1.33$ ). When the structures are in air, both simulation and experimental results showed a single transmission resonance, which can be associated to the  $(-1, 0)$  excitation of the SP on the top and bottom surface of the NHA membrane. However, this resonance has been also induced with the presence of truncated nanocone at the bottom of the cavity. The apex of the truncated nanocone and the bottom of the nanohole would generate nanoantenna effect at the resonance wavelength, which would generate localized SP between two afore-mentioned nanosensors. As a result,  $(-1, 0)$  resonance is related to not only SPPs but also LSPRs. As the periodicity of the hole

decreases, the resonance transmission of the 3D nanosensors are blue-shifted to shorter wavelengths (**Figures 7.4A and 7.4C**).

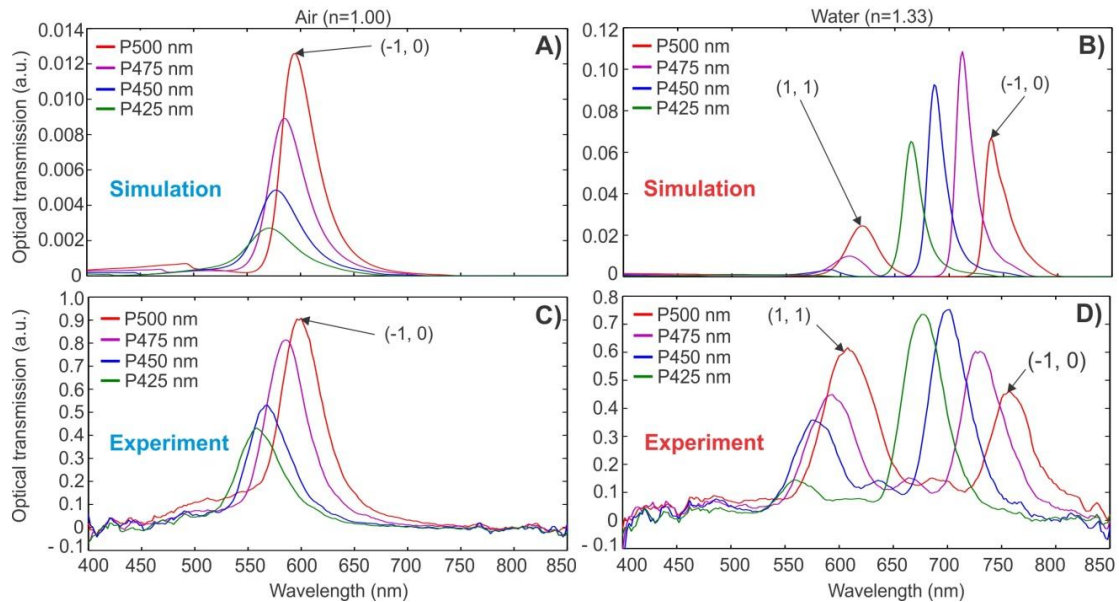


**Figure 7.4** Optical transmission spectra of 3D plasmonic nanosensors for simulated and experimental results. The periodicities range from 425 nm (green curve) to 500 nm (red curve) with increments of 25 nm. Simulated results for (a) air ( $n = 1.00$ ), (b) water ( $n = 1.33$ ), experimental results for (c) air ( $n = 1.00$ ), and (d) water ( $n = 1.33$ ). The existence of LSPR coupling was observed between the nanocone and nanohole in the simulation model, which resulted in generation of an antenna and strong hot spot within this area. Although a nanocone structure without the presence of nanohole could have two LSPRs located at the base and at the apex, the combination of both structures yields a strong local coupling of the respective LSPRs. The presence of a nanocone alters both the resonance frequency of the LSPRs and the transmission efficiency of a NHA due to the shadowing effect and optical absorption of the nanocone.<sup>23</sup> However, a NHA without nanocones cannot generate strong LSPR similar to the proposed structure and would have

more limited detection and sensitivity in the SERS applications according to the previous studies on NHAs.<sup>11,12,40</sup>

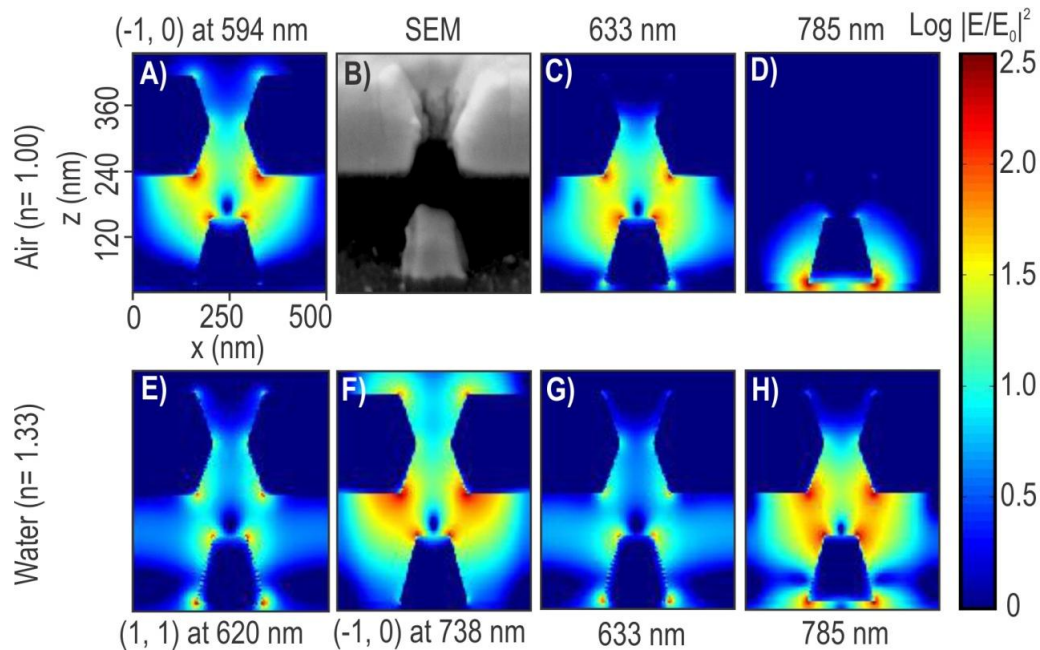


**Figure 7.5** Electric field ( $|E/E_0|^2$ , log scale representation) intensity of a unit cell in a 3D plasmonic nanosensor displayed on the  $xz$  plane. The electric field intensity for air ( $n = 1.00$ ) at (a)  $(-1,0)$  peak at 594 nm, (c) 633 nm, and (d) 780 nm. The SEM image of the actual structure represented simulated images has been shown in (b). The electric field intensity for water ( $n = 1.33$ ) at (e)  $(1,1)$  peak at 620 nm, (f)  $(-1,0)$  peak at 738 nm, (g) 633 nm, and (h) 785 nm.

Due to the bulk plasmon wavelength of Au at 500 nm, the resonance of the 3D nanosensors decays for smaller periodicity as the resonance blue-shifts towards 500 nm. When the 3D nanostructure is encapsulated in water, the LSPR-SPP mediated resonances of the 3D nanosensors are red-shifted towards longer wavelengths (**Figures 7.4B** and

7.4C). Two LSPR-SPP resonances were seen in the optical transmission spectra of the 3D nanosensors. The resonances were associated to  $(-1, 0)$  and  $(1, 1)$  scattering hole orders of the 3D nanosensors. The electric field intensity of 3D nanosensors with 500 nm periodicity is shown in **Figure 7.5** at the LSPR-SPP resonance wavelengths of 633 and 785 nm for both air and water surrounding media.

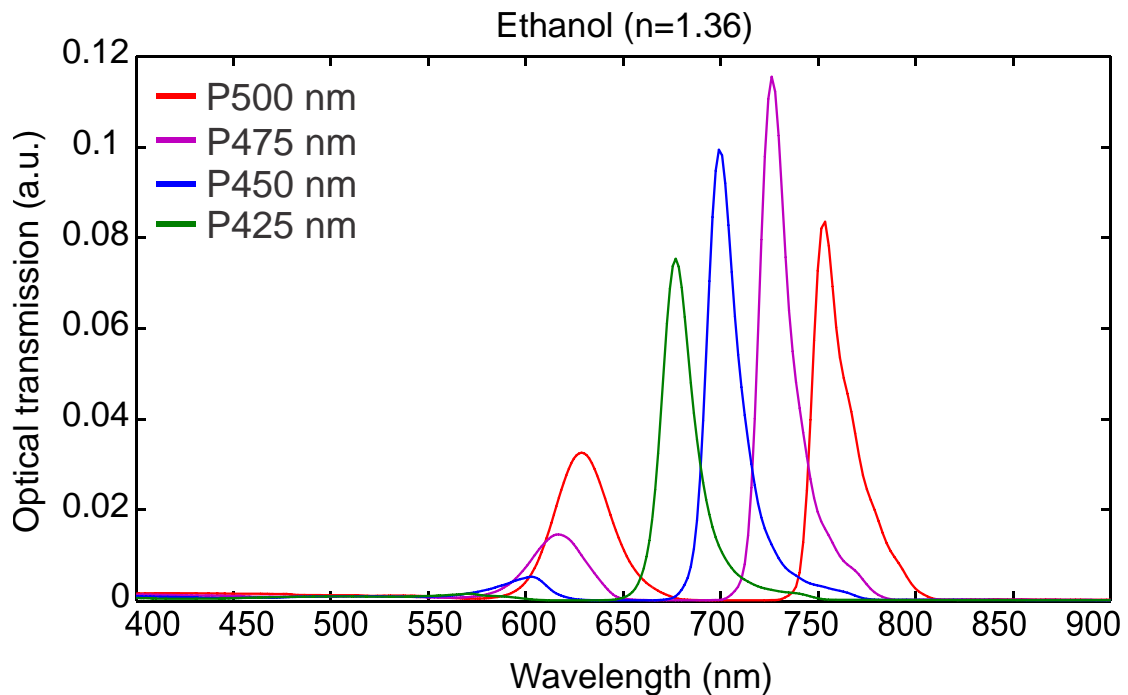


**Figure 7.6 Simulated optical transmission spectra of 3D cavity plasmonic nanosensors in Ethanol ( $n=1.36$ ). The periodicities range from 425 nm (green curve) to 500 nm (red curve) with increments of 25 nm.**

The electric field distributions at LSPR-SPP resonances for air and water confirm that there is a strong LSPR coupling between the bottom of the hole and the apex of the nanocone. This structure generates the highest electric field at the resonance peak.

However, the electric field at the (1, 1) LSPR-SPP resonance is of weaker intensity compared to the electric field at (-1, 0) resonance. The electric field at 633 nm appeared to be more intense in air, whereas it was lower when the platform was immersed in water. This was due to the presence of the (-1, 0) resonance peak close to 633 nm for a 3D nanosensor with 500 nm periodicity located in air. In contrast, the electric field at 785 nm was significantly higher within the apex of the truncated cone and the bottom surface of the hole compared to that obtained in air at 785 nm. There was a high absorption at the base of the truncated nanocone due to the LSPR absorption properties of the 3D nanosensor. Similar results are expected when the platform is immersed in a polar organic solvent such as ethanol ( $n=1.36$ ) based on its simulated optical transmission shown in **Figure 7.6**.

### 7.3.3 Effect of plasmonic tunability on SERS

As shown in **Figure 7.7**, the SERS spectra of the 4-NTP molecules (1 mM) were collected on different 3D nanosensors in two different media (air and water) and also for two wavelengths of incident light (633 and 785 nm). Using the 633 nm laser, the SERS signals of 4-NTP integrated for the  $\nu_s \text{NO}_2$  mode ( $1337 \text{ cm}^{-1}$ ) were stronger for 3D nanosensors with periodicities of 500 ( $3.2 \times 10^4$  counts) and 425 nm ( $2.5 \times 10^4$  counts) when the signal was collected in air compared to water (**Figures 7.7A and 7.7B**).

When the 785 nm laser was used, the SERS intensities of 4-NTP were stronger for both 3D nanosensors, P500 ( $5.4 \times 10^3$  counts) and P425 ( $4.1 \times 10^3$  counts) when collected in water compared to air (**Figures 7.7C and 7.7D**). These phenomena are also related to the tuned plasmonic bands of the 3D nanosensors in air and water as shown in **Figure 7.4**. We observed similar responses for 3D nanosensors with periodicities of 475 nm and 450 nm (**Figure 7.8**).

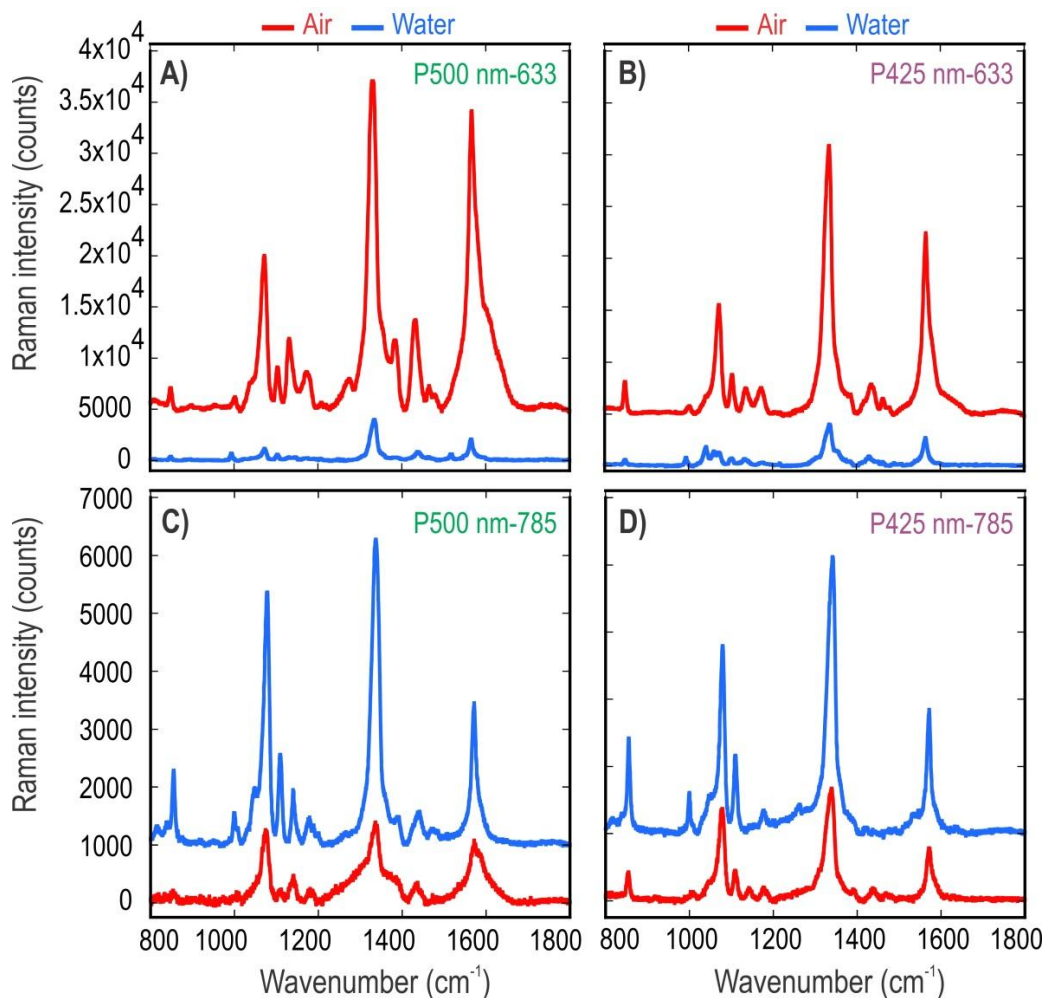


**Figure 7.7** SERS spectra of 4-NTP adsorbed on the 3D nanosensors with different periodicities, medium (air and water) and wavelength of incident light. a) P500 nm and b) P425 nm periodicities at 633 nm incident light in air (red) and water (blue); c) P500 nm and d) P425 nm periodicities at 785 nm in air (red) and water (blue). Acquisition time for each spectrum was 3 s with 5 accumulations. Base line correction was applied to all spectra. A +5000 a.u. offset was applied to both red spectra in a and b. A +1000 a.u. offset was applied to both blue spectra in c and d. These offsets were applied to represent the data in a more comparable fashion.

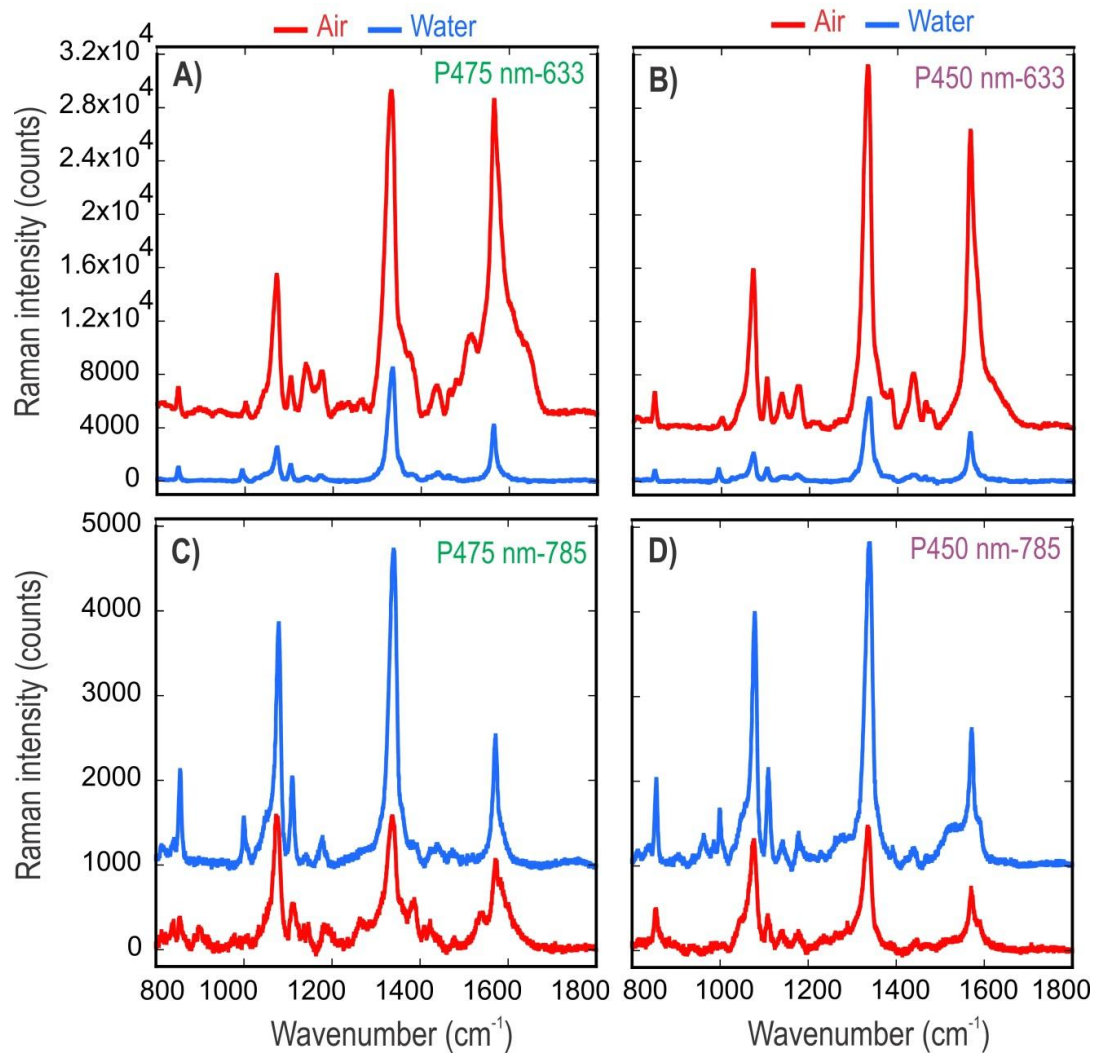


**Figure 7.8** SERS spectra of 4-NTP adsorbed on the 3D nanosensors with different periodicities, medium (air and water) and wavelength of incident light. a) P475 nm and b) P450 nm periodicities at 633 nm incident light in air (red) and water (blue); c) P475 nm and d) 450 nm periodicities at 785 nm in air (red) and water (blue). All the experimental conditions are the same as Figure 7.7.

We also observed a decrease in 4-NTP SERS signal when the periodicity was decreased from 500 nm to 425 nm, which was related to the dependence of the plasmonic bands on periodicity. For instance, from 500 nm to 425 nm, the plasmonic band is blue-shifted to the wavelengths below 600 nm in both simulations and experiment (**Figures 7.3A and 7.3C**).

### 7.3.4 SERS mapping of hot spots on 3D plasmonic nanosensors

In order to evaluate the detection limit of our 3D nanosensors, platforms were functionalized with a 100 attomolar (aM) solution of the 4-NTP. The transmission optical image of the array of P500 3D nanosensors is shown in **Figure 7.9A**. The SERS mapping was performed on the selected area in red shown in **Figure 7.9A**. The map was generated by integrating the intensity of the stretching mode of the nitro group ( $\nu_s \text{NO}_2$ ) in the 1282-1400  $\text{cm}^{-1}$  spectral range. A strong SERS intensity (bright regions) corresponded to the location of the 3D nanosensors, and therefore, the location of the hot spots. This is the case for spot 1 in **Figure 7.9B**. However, regions away from the 3D nanosensors (labelled spot 2 in **Figure 7.6**) show a considerably weaker SERS signal. This lack of enhancement was attributed to these positions containing only flat Au. As shown in the inset of **Figure 7.9A**, the relationship between the location of the 3D nanosensors in the optical image and the locations of strong SERS intensity was maintained.

As a result, the detection of 4-NTP drop casted onto the 3D nanosensors was possible even at a concentration of 100 aM, and with a rapid acquisition time of 1 second. The distinguishable locations of the 3D nanosensors based on the Raman map proved the reproducible ability of the sensors to generate a strong signal for low concentrations of molecules trapped in the nanoscale hot spots. Noteworthy, as stated previously, the engineered 3D nanosensors allow a generation of coupled SPP and LSPR, where generates strong hot spots between nanoholes and nanocones. In the meantime, the 3D



structure of nanosensors potentially increases the surface area for attachment of probe molecules to the surface of the nanostructure compared to a planar structure. This effect has been observed in other studies for SERS substrates compared to a 2D array of nanosensors.<sup>38</sup> For instance, in this case, the 3D nanosensors have surface area on both top and bottom surfaces of gold NHA membrane as well as on the nanocone itself compared to the planar NHA structure.

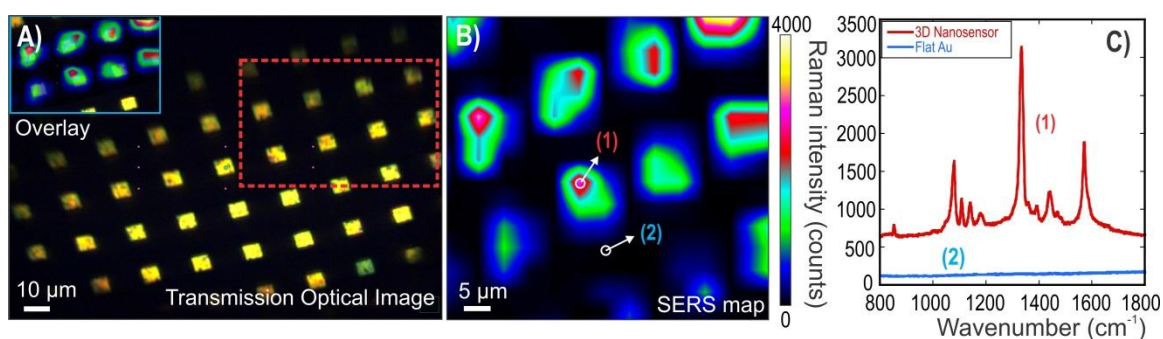


**Figure 7.9** Surface-enhanced Raman mapping of 4-NTP adsorbed on the 3D nanosensors with 500 nm periodicity in air with 633 nm incident light. Acquisition time for each spectrum was 1 s with 1  $\mu\text{m}$  step size. a) Transmission optical image of 3D nanosensors with overlaid SERS mapping (inset) for the area outlined with red dashed box. b) Raman mapping of the outlined area in panel (a). c) Spectra of the regions marked (1) and (2) in panel (b). No baseline correction was applied to spectra in panel (c).

### 7.3.5 Limit of detection for 3D nanosensors

In order to evaluate the limit of detection of such cavity-based sensors, the platforms were functionalized with 4-NTP at concentrations between 1  $\mu\text{M}$  to 1  $\text{mM}$ . In order to avoid cross contamination between high and low concentration experiments, each SERS experiment was repeated 3-5 times onto freshly prepared arrays of 3D nanosensors

(P500-P425). Furthermore, the experiments were conducted for an average of 10-15 spots on each platform. Standard error analysis of SERS signals for three main peaks of 4-NTP (100 aM) is shown in **Figure 7.10**. **Figure 7.11A** shows that all the main peaks of the 4-NTP were detectable between 1  $\mu\text{M}$  to 100 aM.<sup>44</sup>

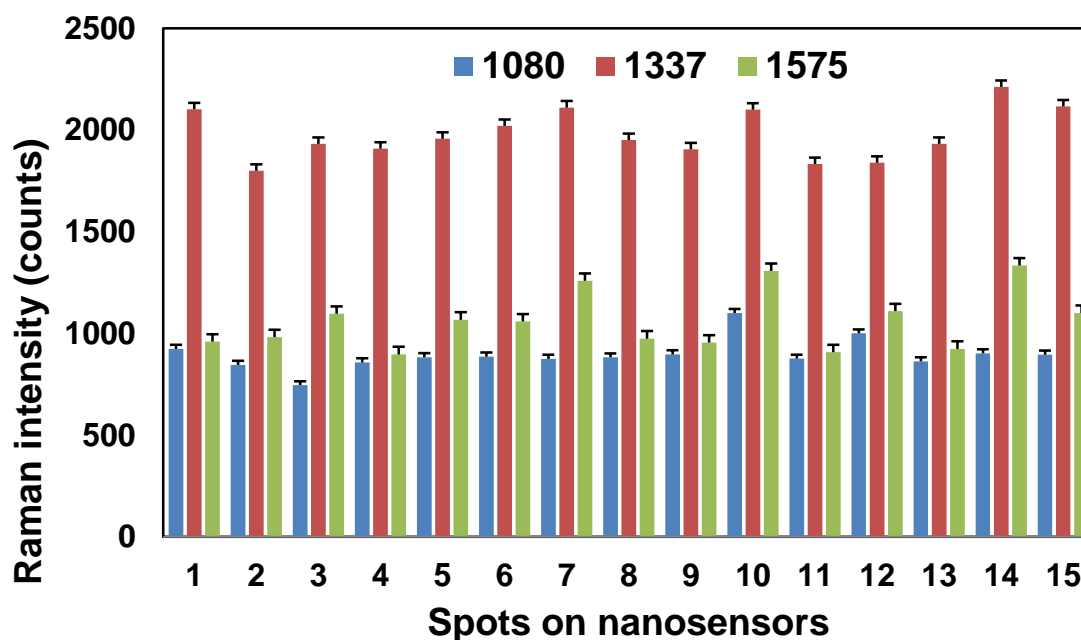


**Figure 7.10** Standard error analysis of SERS signals for three main peaks of 4-NTP (100 aM) at 1080 (vs C-H), 1337 (vs NO<sub>2</sub>), and 1575 (vs C-C) cm<sup>-1</sup> obtained on 15 spots (average of 3 experiments for each spot) of the P500 nanosensors. The standard error bars are generated based on the obtained mean values of 895.3, 1980.6, 1061.7 (a.u.) for the Raman intensities at 1080, 1337, and 1575 cm<sup>-1</sup>, respectively.

However, we observed a small but measurable change in the intensity of the SERS signal for 1aM 4-NTP, even though at this concentration, it was statistically unlikely to find a spot with a single or a few molecules trapped in the plasmonic cavity of the 3D nanosensors. Compared to higher concentrations of 4-NTP, there were fewer spots on the 3D nanosensors that provided SERS signal and the signals were not stable over long exposures. In most of the 2D plasmonic substrates for SERS, providing a reproducible global signal requires at least a homogeneous monolayer of the probe molecule attached onto the surface.<sup>38</sup> The advantage of nanostructures with an embedded cavity can be highlighted here as they provide a better opportunity to trap the molecule in the nanoscale hot spots compared to equivalent 2D structures.

Reliable Raman signal collected from these 3D nanosensors was obtained for concentrations down to 100 aM. This can be clearly observed by evaluating the intensity of the main peak of NO<sub>2</sub> (**Figure 7.11A** inset). Comparing the signal at 100 and 1 aM, it is apparent that the signal has mostly vanished for 1 aM. These measurements yield a limit of detection of ~100 aM (**Figure 7.11A**).

Due to the fact that altering the conditions of the experiment plays a key role in obtaining the SERS signal for different structures, the measurements for 100 aM 4-NTP were repeated with microscope objectives of different numerical apertures (N.A.). Increasing the N.A. of the objective resulted in an enhanced SERS signal (compare the main peak of NO<sub>2</sub> in **Figure 7.11B**). The SERS signals were enhanced almost two times when increasing the N.A. from 0.5 to 0.75 and three times when increasing the N.A. up to 0.9.

By increasing the N.A. of the microscope objective, the laser beam was more confined at the apex of the nanocone and the bottom of the nanohole resulting in a more efficient hot spot and LSPR. It can also be beneficial to decrease the laser spot even further to be more focused on the 3D nanosensors, thereby excluding the scattering from flat Au regions

around the hot spots. To evaluate the sensitivity of different 3D nanosensors based on their periodicities, the SERS signals have been collected with the same concentration of 100 aM. As shown in **Figure 7.11C**, a decremental trend is observed for the SERS signal when the periodicity of the platforms was decreased from 500 to 425 nm. These results have the similar trend as compared to measurements performed with 1 mM 4-NTP. This trend was clearly observed, as shown in the inset of **Figure 7.11C**.

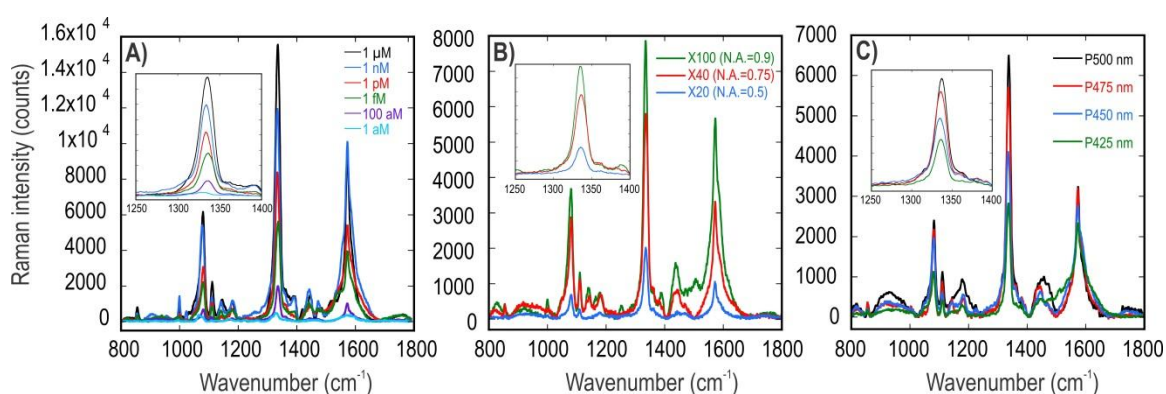


**Figure 7.11** SERS spectra of 4-NTP adsorbed onto 3D nanosensors collected by using 633 nm incident laser in air. a) Different concentrations (1 aM-1 mM) of 4-NTP adsorbed on the 3D nanosensors with 500 nm periodicity; b) The effect of numerical aperture and magnification on SERS spectra of 100 aM 4-NTP absorbed on the 3D nanosensors; c) SERS spectra of 100 aM 4-NTP adsorbed on to the 3D nanosensors. Baseline correction was applied to all spectra. SERS signals of the main  $\text{NO}_2$  peak are shown within each inset in each panel.

### 7.3.6 Estimation of a SERS enhancement factor

Generally speaking the definition of the SERS EF can be considered as the ratio between the SERS intensity per adsorbed molecule and the normal Raman intensity per bulk molecule. However, in SERS, the EF for a given molecule varies with the opto-geometric

conditions of the SERS measurement and corresponding reference measurement.<sup>45</sup> The determination of the number of molecules that yield the Raman signal and their contribution to the EF is not trivial and may lead to erroneous estimations. The ensemble of parameters that need to be considered when performing a SERS experiment, such as probing a single molecule or multiple molecules, the orientation of the molecules in the experimental system, the spatial distribution, or the experimental limitations in resolution, can only be used to approximate an EF.

The Raman signal is enhanced through both the excitation and the emission processes as shown in Equation 2:<sup>46</sup>

$$F = |E(\nu_{excitation})|^2 |E(\nu_{Raman})|^2 \quad (2)$$

where  $E(\nu_{excitation})$  and  $E(\nu_{Raman})$  are the local electric-field EFs at the incident frequency ( $\nu_{excitation}$ ) and at the Raman Stokes frequency ( $\nu_{Raman}$ ), respectively. However, since the plasmon frequency width is large compared to the Raman Stokes shift; both EM fields are often in resonance and/or pre-resonance with the plasmon band. Therefore, an approximation is to assume that  $E(\nu_{excitation})$  and  $E(\nu_{Raman})$  are the same, leading to an EF proportional to  $F = |E(\nu_{excitation})|^4$ . In such an approximation, the matching of the excitation laser line with the plasmon frequency is an essential condition to obtain large Raman surface enhancements. In order to establish the relationship between the nanostructured surface and the SERS activity of the platform, the EFs have been determined. The determination of the EF in SERS is a prerequisite to quantify the enhancement of the Raman signal. The surface Raman EF can be estimated by comparing the measured SERS intensities ( $I_{SERS}$ ) with the non-enhanced Raman scattering intensities ( $I_{NE}$ ) as shown in Equation 3:<sup>47,48</sup>

$$EF = \frac{N_{NE} \times I_{SERS}}{I_{NE} \times N_{SERS}} = \frac{6 \times 10^5 \times 8 \times 10^3}{2 \times 10^2 \times 2} = 1.2 \times 10^7 \quad (3)$$

The EF obtained in equation 3 is calculated based on the number of molecules that are statistically located in the confocal excitation volume and their associated SERS signals. The Raman intensity of the main peak of 4-NTP, the stretching mode of the nitro group (vs NO<sub>2</sub>), was used as the reference peak for these calculations. In order to obtain the surface Raman EF for the sensors, we obtained the Raman signals of 1 mM solution of 4-NTP on a blank (sensor-free) substrate. Based on the concentration, the number of molecules that will be placed in the confocal volume can be calculated as number of molecules = confocal volume × concentration × N<sub>A</sub> = 10<sup>-15</sup> L × 10<sup>-3</sup> mole/L × 6 × 10<sup>23</sup> molecules/mole = 6 × 10<sup>5</sup> molecules. This number represents  $N_{NE}$  with the Raman intensity of 2 × 10<sup>2</sup> ( $I_{NE}$ ) for vs NO<sub>2</sub>. The number of molecules in 100 μL of 100 aM solution of 4-NTP can be calculated as 10<sup>-16</sup> × 100 × 10<sup>-6</sup> = 10<sup>-20</sup> mole which represents 10<sup>-20</sup> × 6 × 10<sup>23</sup> = 6 × 10<sup>3</sup> molecules. For the similar situation one can calculate the number of molecules in 100 μL solution of 100 aM 4-NTP drop-casted onto the sensors to determine the number of adsorbed molecules in the confocal region for SERS measurement. For this, the surface area covered the used nanosensor (P500) is used which is around 2.5 × 10<sup>3</sup> μm<sup>2</sup>. Considering the number of molecules in the 100 μL, we can then estimate the number of molecules adsorbed in the confocal region (~1 μm<sup>2</sup>) to be 6 × 10<sup>3</sup> / 2.5 × 10<sup>3</sup> = 2 molecules ( $N_{SERS}$ ) with the SERS intensity of 8 × 10<sup>3</sup> ( $I_{SERS}$ ) for vs

$\text{NO}_2$ . In both cases a X100 (N.A.= 0.9) objective was used. Therefore, a surface Raman EF of  $1.2 \times 10^7$  was achieved for 100 aM 4-NTP from a femtoliter plasmonic focal volume.

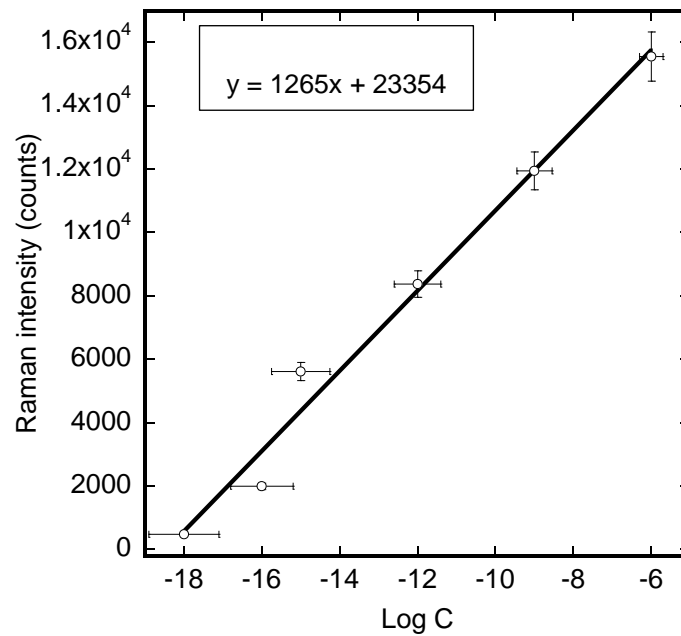


**Figure 7.12 Sensitivity of sensors represented by SERS signals of vs  $\text{NO}_2$  with respect to the Log [Concentration] between 1 aM and 1  $\mu\text{M}$ .**

For 100 aM concentration, there are about two or three molecules within the focal spot. Noteworthy, about four nanostructures are located within the same area. Therefore, to obtain a SERS signal, the molecules should be adsorbed within these hot spots. In our experiments performed with 100 aM concentration, most of our measurements have shown SERS activity as opposed to lower concentrations (1 aM). However, some

individual nanostructures appeared to be SERS inactive presumably due to the absence of the probe molecules or structural defects. Such EF obtained for a 100 aM solution in a femtoliter plasmonic cavity represents the promising chemical sensitivity of these 3D nanosensors (**Figure 7.12**).

Although the SERS intensities do not provide a linear relationship with respect to concentrations, as shown in **Figure 7.12**, there is a linear relationship between the intensities of signals and the logarithmic concentrations of the solutions between 1  $\mu\text{M}$  and 1 aM. This arises from the fact that SERS is a surface sensitive technique and is dependent on the number of molecules located in the hot spots to generate signal. Having said that, one molecule located at the hot spot can generate a strong signal, whereas a large amount of molecules located outside of the hot spots may generate no signal. In order to determine the sensitivity of the sensor, one can use the  $\frac{\Delta I}{\Delta \text{Log} C}$ , which can be the corresponding slope (1265) of the shown linear regression in **Figure 7.12**.

## 7.4 Conclusions

In this work, for the first time, the capability of cavity-based plasmonic nanosensors is demonstrated for SERS-based molecular sensing. These nanosensors provide extraordinary optical transmission properties, which can generate strong SPP and LSPR coupling. These phenomena have been shown here by simulated and experimental optical transmission measurements. The experimental results were also in good agreement with the FDTD calculations for EM field distributions at the plasmonic bands of the nanosensors. In the meantime, these structures represent a plasmonic tunability with respect to the media of the experiment and also the wavelength of the incident light.



These 3D nanosensors also provide a remarkable molecular limit of detection of  $10^{-16}$  M for a probe molecule (4-NTP) with a short acquisition time of 1 second. Consequently, a reliable EF of  $\sim 10^7$  is achieved for these sensors for an extreme low concentration of 100 aM from a femtoliter plasmonic probe volume. Reproducible SERS signals have been collected on the 3D nanosensors with concentrations down to 100 aM providing the spatial distribution of hot spots on the plasmonic substrate. It is also shown that by increasing the N.A. of the objectives, an enhancement occurs for the SERS signals obtained on these sensors proving the confined strong LSPR coupling in the NHA-NCA interface. The strong LSPR coupling of these nanosensors can introduce them to other spectroscopic techniques such as SEF, SEIRA, and even tip-enhanced Raman spectroscopy (TERS) in which there is better control over the polarization of light. Of even greater interest, the plasmonic tunability of these sensors can be used for simultaneous optical trapping and surface-enhanced detection.

## 7.5 References

- (1) Brolo, A. G.; *Nat. Photon.*, **(2012)**, 6, 709.
- (2) Passarelli, N.; Pérez, L. A.; Coronado, E. A.; *ACS Nano*, **(2014)**, 8, 9723.
- (3) Sonntag, M. D.; Klingsporn, J. M.; Zrimsek, A. B.; Sharma, B.; Ruvuna, L. K.; Van Duyne, R. P.; *Chem. Soc. Rev.*, **(2014)**, 43, 1230.
- (4) Baffou, G.; Quidant, R.; *Chem. Soc. Rev.*, **(2014)**, 43, 3898.
- (5) Fleischmann, M.; Hendra, P. J.; McQuillan, A. J.; *J. Chem. Phys. Lett.*, **(1974)**, 26, 163.
- (6) Jeanmaire, D. L.; Van Duyne, R. P.; *J. Electroanal. Chem.*, **(1997)**, 84, 1.
- (7) Nie, S.; Emory, S. R.; *Science*, **(1997)**, 275, 1102.
- (8) Kneipp, K.; Wang, Y.; Kneipp, H.; Perelman, L. T.; Itzkan, I.; Dasari, R. R.; Feld, M. S.; *Phys. Rev. Lett.*, **(1997)**, 78, 1667.
- (9) Sheehan, P. E.; Whitman, L. J.; *Nano Lett.*, **(2005)**, 5, 803.

- (10) Squires, T. M.; Messinger, R. J.; Manalis, S. R.; *Nat. Biotech.*, **(2008)**, *26*, 417.
- (11) Kumar, S.; Cherukulappurath, S.; Johnson, T. W.; Oh, S.-H.; *Chem. Mater.*, **(2014)**, *26*, 6523.
- (12) Brolo, A. G.; Arctander, E.; Gordon, R.; Leathem, B.; Kavanagh, K. L.; *Nano Lett.*, **(2004)**, *4*, 2015.
- (13) Im, H.; Sutherland, J. N.; Maynard, J. A.; Oh, S.-H.; *Anal. Chem.*, **(2012)**, *84*, 1941.
- (14) Barnes, W. L.; Dereux, A.; Ebbesen, T. W.; *Nature*, **(2003)**, *424*, 824.
- (15) Ebbesen, T. W.; Lezec, H. J.; Ghaemi, H. F.; Thio, T.; Wolff, P. A.; *Nature*, **(1998)**, *391*, 667.
- (16) Valsecchi, C.; Brolo, A. G.; *Langmuir*, **(2013)**, *29*, 5638.
- (17) Lee, M.; Kim, J.; Seo, W.; Hong, H.-G.; Song, Y.; Dasari, R. R.; An, K.; *Nat. Commun.*, **(2014)**, *5*.
- (18) Krishnan, A.; Thio, T.; Kim, T. J.; Lezec, H. J.; Ebbesen, T. W.; Wolff, P. A.; Pendry, J.; Martin-Moreno, L.; Garcia-Vidal, F. J.; *Optics Commun.*, **(2001)**, *200*, 1.
- (19) Najiminaini, M.; Vasefi, F.; Kaminska, B.; Carson, J. J. L.; *Appl. Phys. Lett.*, **(2012)**, *100*, 063110.
- (20) Najiminaini, M.; Vasefi, F.; Kaminska, B.; Carson, J. J. L.; *Appl. Phys. Lett.*, **(2012)**, *100*, 043105.
- (21) Przybilla, F.; Degiron, A.; Laluet, J.-Y.; Genet, C.; Ebbesen, T. W.; *J. Opt. A: Pure Appl. Opt.*, **(2006)**, *8*, 458.
- (22) Brolo, A. G.; Gordon, R.; Leathem, B.; Kavanagh, K. L.; *Langmuir*, **(2004)**, *20*, 4813.
- (23) Najiminaini, M.; Ertorer, E.; Kaminska, B.; Mittler, S.; Carson, J. J. L.; *Analyst*, **(2014)**, *139*, 1876.
- (24) Gordon, R.; Sinton, D.; Kavanagh, K. L.; Brolo, A. G.; *Acc. Chem. Res.*, **(2008)**, *41*, 1049.

- (25) Im, H.; Wittenberg, N. J.; Lesuffleur, A.; Lindquist, N. C.; Oh, S.-H.; *Chem. Sci.*, **(2010)**, *1*, 688.
- (26) Im, H.; Lee, S. H.; Wittenberg, N. J.; Johnson, T. W.; Lindquist, N. C.; Nagpal, P.; Norris, D. J.; Oh, S.-H.; *ACS Nano*, **(2011)**, *5*, 6244.
- (27) Wang, Y.; Kar, A.; Paterson, A.; Kourentzi, K.; Le, H.; Ruchhoeft, P.; Willson, R.; Bao, J.; *ACS Photon.*, **(2014)**, *1*, 241.
- (28) Ricciardi, A.; Consales, M.; Quero, G.; Crescitelli, A.; Esposito, E.; Cusano, A.; *ACS Photon.*, **(2014)**, *1*, 69.
- (29) Genet, C.; Ebbesen, T. W.; *Nature*, **(2007)**, *445*, 39.
- (30) Yokogawa, S.; Burgos, S. P.; Atwater, H. A.; *Nano Lett.*, **(2012)**, *12*, 4349.
- (31) Yanik, A. A.; Cetin, A. E.; Huang, M.; Artar, A.; Mousavi, S. H.; Khanikaev, A.; Connor, J. H.; Shvets, G.; Altug, H.; *Proc. Nat. Acad. Sci.*, **(2011)**, *108*, 11784.
- (32) Cervantes Tellez, G. A.; Hassan, S. a.; Tait, R. N.; Berini, P.; Gordon, R.; *Lab Chip*, **(2013)**, *13*, 2541.
- (33) Fayyaz, S.; Tabatabaei, M.; Hou, R.; Lagugné-Labarthe, F.; *J. Phys. Chem. C*, **(2012)**, *116*, 11665.
- (34) Aroca, R. F.; Ross, D. J.; Domingo, C.; *Appl. Spectrosc.*, **(2004)**, *58*, 324A.
- (35) Jensen, T.; Kelly, L.; Lazarides, A.; Schatz, G.; *J. Cluster Sci.*, **(1999)**, *10*, 295.
- (36) Merlen, A.; Lagugné-Labarthe, F.; *Appl. Spectrosc.*, **(2014)**, *68*, 1307.
- (37) Bukasov, R.; Ali, T. A.; Nordlander, P.; Shumaker-Parry, J. S.; *ACS Nano*, **(2010)**, *4*, 6639.
- (38) Tabatabaei, M.; Sangar, A.; Kazemi-Zanjani, N.; Torchio, P.; Merlen, A.; Lagugné-Labarthe, F.; *J. Phys. Chem. C*, **(2013)**, *117*, 14778.
- (39) Brown, L. V.; Yang, X.; Zhao, K.; Zheng, B. Y.; Nordlander, P.; Halas, N. J.; *Nano Lett.*, **(2015)**, *15*, 1272.
- (40) Yu, Q.; Guan, P.; Qin, D.; Golden, G.; Wallace, P. M.; *Nano Lett.*, **(2008)**, *8*, 1923.

- (41) Zheng, P.; Cushing, S. K.; Suri, S.; Wu, N.; *Phys. Chem. Chem. Phys.*, **(2015)**.
- (42) Palik, E. D., Handbook of Optical Constants of Solids, Academic Press, New York, 1985.
- (43) Thio, T.; Ghaemi, H. F.; Lezec, H. J.; Wolff, P. A.; Ebbesen, T. W.; *J. Opt. Soc. Am. B*, **(1999)**, *16*, 1743.
- (44) Skadtchenko, B. O.; Aroca, R.; *Spectrochim. Acta A Mol. Biomol. Spectrosc.*, **(2001)**, *57*, 1009.
- (45) Marquestaut, N.; Martin, A.; Talaga, D.; Servant, L.; Ravaine, S.; Reculosa, S.; Bassani, D. M.; Gillies, E.; Lagugné-Labarthet, F.; *Langmuir*, **(2008)**, *24*, 11313.
- (46) Schatz, G. C.; Young, M. A.; Van Duyne, R. P. In Surface-enhanced Raman scattering; Kneipp, K., Moskovits, M., Kneipp, H., Eds.; Springer-Verlag: Berlin, **(2006)**; *Vol. 103*, pp 19–46.
- (47) Félidj, N.; Truong, S. L.; Aubard, J.; Lévi, G.; Krenn, J. R.; Hohenau, A.; Leitner, A.; Aussenegg, F. R.; *J. Chem. Phys.*, **(2004)**, *120*, 7141.
- (48) Félidj, N.; Aubard, J.; Lévi, G.; Krenn, J. R.; Salerno, M.; Schider, G.; Lamprecht, B.; Leitner, A.; Aussenegg, F. R.; *Phys. Rev. B*, **(2002)**, *65*, 075419.

## Chapter 8

### 8 Conclusions and outlook

Plasmon-mediated surface-enhanced detection techniques in particular surface-enhanced Raman spectroscopy (SERS), have opened a wide spectrum of applications, especially in the ultra-sensitive detection of biomolecules.<sup>1-8</sup> In the present thesis, we have investigated new developments towards fabrication of ultra-sensitive plasmonic platforms designed for SERS measurements, and more importantly, the integration of these platforms into organized micropatterns providing a tool for controlled study of a biomolecule of interest over the cells surfaces.

An introduction summarizes the principles of plasmon-mediated surface-enhanced techniques and the fundamental principles of the distinct enhancement mechanisms of SERS are developed in Chapter 2. Subsequently, two commonly-used fabrication techniques namely NSL and EBL, and the advantages and limitations of these techniques have been discussed in detail in Chapter 3.

With the desire to enable the controlled positioning and growth of cells over a substrate, a newly-developed micropatterning technique of biocompatible thin films of fluorocarbon polymer has been introduced in Chapter 4. These micropatterns have shown successful controlled positioning of both conventional cell lines and those that were transfected with a variety of receptors. The potential programming capabilities of these substrates has been further investigated for complex neuronal networks to provide promising isolation and controlled connection not only for the projections of neurons, but also for the spines, the small regions within the projections where neurons communicate. This was evidenced by high resolution imaging using atomic force microscopy.

We also used a sensitive plasmonic platform fabricated by NSL, as a low-cost and high throughput technique to be integrated with the micropatterns for the first time for biosensing of glycans over the cells using a Raman reporter (Chapter 5). Micropatterns have been employed to provide single cells trapped onto the homogenous sensitive plasmonic windows fabricated by NSL. This approach was used for accurate confocal SERS mapping of glycans over the cells to differentiate cancerous from non-cancerous cells based on the level of glycan expression over the cells surfaces. By applying slight alterations for these plasmonic platforms, they can also be used for other advanced spectroscopic techniques such as surface-enhanced spectroscopy (SEF) or TERS. For instance, by adding a thin dielectric layer over these plasmonic structures, one is able to perform SEF of a probe molecule over this platform. Moreover, due to the high spatial resolutions provided by TERS, these platforms can also potentially be used for mapping the protein distributions at small biological structures such as neuronal spines. These patterns not only surpass the difficulty of isolating the neuronal connections due to their intrinsic random connections, they also provide new alternatives to probe biomolecules of interest present at spines using TERS, which provides high resolution topographical images and chemical information.

The second goal of the thesis was focused on development of new plasmonic structures for ultra-sensitive detections. In Chapter 6, we demonstrated the fabrication of homogenous tetrahedral nanopyramids using NSL to generate stronger plasmonic hot spots and more surface area for a molecule of interest to adsorb over the surface of the plasmonic structure. A complete theoretical description and experimental optical characterization of these nanostructures were provided in Chapter 6 in addition to their SERS activity. Since the nanostructures were fabricated on a conductive substrate, ITO, they would be beneficial for electrochemical studies. This advantage was later employed for the biosensing application of probing electrochemical characteristics of a protein over

the surface of these plasmonic structures.<sup>9</sup> These nanostructures can easily be tuned to be fabricated with different metals or a mixture of metals to generate new plasmonic bands. This provides a fine tunability of this structure to detect a probe molecule in a specific spectral region based on the newly-generated plasmonic bands caused by the presence of the heterometallic nanostructure. Moreover, NSL provides a simple method for fabrication of different plasmonic nanostructures with high efficiency. These platforms offer potential applications for industrial scale-up in order to be used in different fields. A promising example of a large-area nanosphere self-assembly has been reported recently for high throughput periodic surface nanostructures over a 1 m<sup>2</sup> glass substrate.<sup>10</sup> This process reached also a throughput of 3000 wafers/h.<sup>10</sup> This opens up a full compatibility of this process with large requested volume in photovoltaic manufacturing and the fabrication of periodic nanostructures on different plasmonic devices. The aim is to use plasmonic resonances to enhance the efficiency of photovoltaic cells.<sup>10</sup>

EBL is a commonly-used fabrication technique for complex plasmonic nanostructures. In Chapter 7, this technique has been employed to fabricate novel plasmonic nanocavities involving 3D nanostructures consisting of the arrays of nanoholes and co-registered nanocones. This specific tunable plasmonic nanostructure has shown the ability not only to generate a strong SPP, but also a promising localized SP compared to conventional nanoholes arrays. Strong generated LSPRs within this structure introduce this 3D structure as a reliable platform for ultra-sensitive SERS measurements. This platform also offers the plasmonic tunability in the presence of distinct media, leading to versatile plasmonic domains of detections for different water-soluble molecules and also those are soluble in organic solvents such as ethanol. Using this platform, ultra-sensitive detection of 4-NTP was possible at a concentration of 10<sup>-16</sup> M. At such a low concentration only a few molecules were trapped in the nanoscale hot spots of the nanocavities. Therefore, this platform can be applied to detection of more complex molecules and biomolecules at low

concentrations, and can also be used for optical trapping while detecting a probe molecule using a plasmon-mediated spectroscopic technique such as SERS.<sup>11</sup>

It is worthwhile to mention that the developed plasmonic platforms demonstrated in both Chapter 6 and 7 can also be integrated with TERS measurements for detection of a variety of molecules. A strong tip-tip LSPR can be generated with the presence of a metallic TERS tip over the sharp apex of nanopillars shown in Chapter 6 or inside a nanohole over a nanocone within a single nanocavity that has been demonstrated in Chapter 7. Furthermore, these structures can also be integrated within the micropatterns described in Chapters 4 and 5, or microfluidic devices for providing sensing windows within these channels for dynamic or static chemical and biochemical measurements.<sup>7,12</sup>

Aside from that, recent ultrafast SERS methods have been also introduced using pico- and femtosecond excitation sources. This includes surface-enhanced femtosecond stimulated Raman spectroscopy (SE-FSRS), surface-enhanced coherent anti-Stokes Raman spectroscopy (SE-CARS), and time-resolved SE-CARS (TR-SE-CARS). These recently developed techniques have convincingly demonstrated the compatibility of ultrafast pulses with highly enhancing plasmonic substrates. Molecular-plasmonic studies on the femtosecond time scale of nuclear motion has been enabled using these newly-developed techniques. More importantly, as plasmons induce new chemical changes in proximal molecular species, bond-making and -breaking processes can also be closely examined by these techniques.<sup>13</sup> It is worthwhile to mention that by combining these ultrafast spectroscopic techniques with TERS, one would be able to obtain nanoscale-resolution topographical images along with ultrafast chemical information with high signal-to-noise ratios. This opens up new alternatives for real-time detections with high spatial resolution.



Plasmon-mediated surface-enhanced techniques, in particular SERS, are capable of providing ultra-sensitive chemical information of various samples with high signal-to-noise ratio. SERS has emerged as a significantly matured technique over the past decades since its discovery,<sup>14,15</sup> with a general agreement upon the enhancement mechanism.<sup>16-18</sup> SERS also provides clear proof of ultra-sensitive detections down to single-molecule sensitivity.<sup>19-22</sup> The development of recent commercial substrates for SERS also leads to diverse range of applications with easy-to-access platforms.<sup>23,24</sup> Thus, SERS appears to play a more significant role as detection techniques in future for a variety of applications ranging from materials science to life sciences and surface chemistry.<sup>2,25-28</sup> All these techniques involve the use, the tunability and the tailoring of surface plasmon by developing novel surface nanostructures. This is the key element for further improvement in such techniques towards ultra-high sensitivity for both *in vitro* and *in vivo* detections.

## 8.1 References

- (1) Yamamoto, Y.; Ishikawa, M.; Ozaki, Y.; Itoh, T.; *Front. Phys.*, **(2014)**, *9*, 31.
- (2) Sharma, B.; Frontiera, R. R.; Henry, A.-I.; Ringe, E.; Van Duyne, R. P.; *Mater. Today*, **(2012)**, *15*, 16.
- (3) Xu, H.; Bjerneld, E. J.; Käll, M.; Börjesson, L.; *Phys. Rev. Lett.*, **(1999)**, *83*, 4357.
- (4) Cao, Y. C.; Jin, R.; Mirkin, C. A.; *Science*, **(2002)**, *297*, 1536.
- (5) Qian, X.; Peng, X.-H.; Ansari, D. O.; Yin-Goen, Q.; Chen, G. Z.; Shin, D. M.; Yang, L.; Young, A. N.; Wang, M. D.; Nie, S.; *Nat. Biotech.*, **(2008)**, *26*, 83.
- (6) Anker, J. N.; Hall, W. P.; Lyandres, O.; Shah, N. C.; Zhao, J.; Van Duyne, R. P.; *Nat. Mater.*, **(2008)**, *7*, 442.
- (7) Brolo, A. G.; *Nat. Photon.*, **(2012)**, *6*, 709.
- (8) Li, J. F.; Huang, Y. F.; Ding, Y.; Yang, Z. L.; Li, S. B.; Zhou, X. S.; Fan, F. R.; Zhang, W.; Zhou, Z. Y.; WuDe, Y.; Ren, B.; Wang, Z. L.; Tian, Z. Q.; *Nature*, **(2010)**, *464*, 392.

- (9) Cheng, X. R.; Wallace, G. Q.; Lagurné-Labarthe, F.; Kerman, K.; *ACS Appl. Mater. Interfaces*, **(2015)**, 7, 4081.
- (10) Gao, P.; He, J.; Zhou, S.; Yang, X.; Li, S.; Sheng, J.; Wang, D.; Yu, T.; Ye, J.; Cui, Y.; *Nano Lett.*, **(2015)**.
- (11) Tabatabaei, M.; Najiminaini, M.; Davieau, K.; Kaminska, B.; Singh, M. R.; Carson, J. J. L.; Lagurné-Labarthe, F.; *ACS Photonics*, **(2015)**, 2, 752.
- (12) Galarreta, B.; Tabatabaei, M.; Guieu, V.; Peyrin, E.; Lagurné-Labarthe, F.; *Anal. Bioanal. Chem.*, **(2013)**, 405, 1613.
- (13) Keller, E. L.; Brandt, N. C.; Cassabaum, A. A.; Frontiera, R. R.; *Analyst*, **(2015)**.
- (14) Jeanmaire, D. L.; Van Duyne, R. P.; *J. Electroanal. Chem.*, **(1977)**, 84, 1.
- (15) Albrecht, M. G.; Creighton, J. A.; *J. Am. Chem. Soc.*, **(1977)**, 99, 5215.
- (16) Moskovits, M.; *J. Raman Spectrosc.*, **(2005)**, 36, 485.
- (17) Kleinman, S. L.; Frontiera, R. R.; Henry, A.-I.; Dieringer, J. A.; Van Duyne, R. P.; *Phys. Chem. Chem. Phys.*, **(2013)**, 15, 21.
- (18) Ausman, L. K.; Li, S.; Schatz, G. C.; *J. Phys. Chem. C*, **(2012)**, 116, 17318.
- (19) Moskovits, M. T., L. L.; Yang, J.; Haslett, T. *SERS and the single molecule. In Optical properties of Nanostructured Random Media*; Springer: Berlin, 2002; p 215.
- (20) Emory, S. R.; Haskins, W. E.; Nie, S.; *J. Am. Chem. Soc.*, **(1998)**, 120, 8009.
- (21) Kneipp, K.; Wang, Y.; Kneipp, H.; Perelman, L. T.; Itzkan, I.; Dasari, R.; Feld, M. S.; *Phys. Rev. Lett.*, **(1997)**, 78, 1667.
- (22) Le Ru, E. C.; Meyer, M.; Etchegoin, P. G.; *J. Phys. Chem. B*, **(2006)**, 110, 1944.
- (23) Ko, H.; Singamaneni, S.; Tsukruk, V. V.; *Small*, **(2008)**, 4, 1576.
- (24) Hoppmann, E. P.; Yu, W. W.; White, I. M.; *Methods* **(2013)**, 63, 219.
- (25) El-Ansary, A.; Faddah, L. M.; *Nanotechnol., Sci. Appl.*, **(2010)**, 3, 65.
- (26) Hudson, S. D.; Chumanov, G.; *Anal. Bioanal. Chem.*, **(2009)**, 394, 679.
- (27) Tripp, R. A.; Dluhy, R. A.; Zhao, Y.; *Nano Today*, **(2008)**, 3, 31.

(28) Ling, X.; Huang, S.; Deng, S.; Mao, N.; Kong, J.; Dresselhaus, M. S.; Zhang, J.; *Acc. Chem. Res.*, (2015), Ahead of Print.

## Appendix A.

## Copyrights



RightsLink®

Home

Account Info

Help



ACS Publications  
Most Trusted. Most Cited. Most Read.

**Title:**

Tunable 3D Plasmonic Cavity Nanosensors for Surface-Enhanced Raman Spectroscopy with Sub-femtomolar Limit of Detection

**Author:**

Mohammadali Tabatabaei, Mohamadreza Najiminaini, Kieffer Davieau, et al

**Publication:** ACS Photonics

**Publisher:** American Chemical Society

**Date:** Jun 1, 2015

Copyright © 2015, American Chemical Society

Logged in as:

Mohammadali Tabatabaei

LOGOUT

#### PERMISSION/LICENSE IS GRANTED FOR YOUR ORDER AT NO CHARGE

This type of permission/license, instead of the standard Terms & Conditions, is sent to you because no fee is being charged for your order. Please note the following:

- Permission is granted for your request in both print and electronic formats, and translations.
- If figures and/or tables were requested, they may be adapted or used in part.
- Please print this page for your records and send a copy of it to your publisher/graduate school.
- Appropriate credit for the requested material should be given as follows: "Reprinted (adapted) with permission from (COMPLETE REFERENCE CITATION). Copyright (YEAR) American Chemical Society." Insert appropriate information in place of the capitalized words.
- One-time permission is granted only for the use specified in your request. No additional uses are granted (such as derivative works or other editions). For any other uses, please submit a new request.

BACK

CLOSE WINDOW

Copyright © 2015 [Copyright Clearance Center, Inc.](#) All Rights Reserved. [Privacy statement.](#) [Terms and Conditions.](#)  
Comments? We would like to hear from you. E-mail us at [customer@copyright.com](mailto:customer@copyright.com)



RightsLink®

Home

Account Info

Help



ACS Publications  
Most Trusted. Most Cited. Most Read.

**Title:** Optical Properties of Silver and Gold Tetrahedral Nanopyramid Arrays Prepared by Nanosphere Lithography

**Author:** Mohammadali Tabatabaei, Alexandre Sangar, Nastaran Kazemi-Zanjani, et al

**Publication:** The Journal of Physical Chemistry C

**Publisher:** American Chemical Society

**Date:** Jul 1, 2013

Copyright © 2013, American Chemical Society

Logged in as:

Mohammadali Tabatabaei

LOGOUT

#### PERMISSION/LICENSE IS GRANTED FOR YOUR ORDER AT NO CHARGE

This type of permission/license, instead of the standard Terms & Conditions, is sent to you because no fee is being charged for your order. Please note the following:

- Permission is granted for your request in both print and electronic formats, and translations.
- If figures and/or tables were requested, they may be adapted or used in part.
- Please print this page for your records and send a copy of it to your publisher/graduate school.
- Appropriate credit for the requested material should be given as follows: "Reprinted (adapted) with permission from (COMPLETE REFERENCE CITATION). Copyright (YEAR) American Chemical Society." Insert appropriate information in place of the capitalized words.
- One-time permission is granted only for the use specified in your request. No additional uses are granted (such as derivative works or other editions). For any other uses, please submit a new request.

BACK

CLOSE WINDOW

Copyright © 2015 Copyright Clearance Center, Inc. All Rights Reserved. [Privacy statement](#). [Terms and Conditions](#).  
Comments? We would like to hear from you. E-mail us at [customer@copyright.com](mailto:customer@copyright.com)



# RightsLink®

[Home](#)
[Account Info](#)
[Help](#)


**Title:** Directing GPCR-transfected cells and neuronal projections with nano-scale resolution

**Author:** Mohammadali Tabatabaei, Fabiana A. Caetano, Sylvain Vedraïne, Peter R. Norton, Stephen S.G. Ferguson, François Lagugn -Labarthe

**Publication:** Biomaterials

**Publisher:** Elsevier

**Date:** December 2013

Copyright   2013 Elsevier Ltd. All rights reserved.

Logged in as:  
Mohammadali Tabatabaei  
Account #:  
3000933040

[LOGOUT](#)

## Order Completed

Thank you very much for your order.

This is a License Agreement between Mohammadali Tabatabaei ("You") and Elsevier ("Elsevier"). The license consists of your order details, the terms and conditions provided by Elsevier, and the [payment terms and conditions](#).

[Get the printable license.](#)

License Number	3663250958682
License date	Jul 06, 2015
Licensed content publisher	Elsevier
Licensed content publication	Biomaterials
Licensed content title	Directing GPCR-transfected cells and neuronal projections with nano-scale resolution
Licensed content author	Mohammadali Tabatabaei, Fabiana A. Caetano, Sylvain Vedraïne, Peter R. Norton, Stephen S.G. Ferguson, François Lagugn�-Labarthe
Licensed content date	December 2013
Licensed content volume number	34
Licensed content issue number	38
Number of pages	10
Type of Use	reuse in a thesis/dissertation
Portion	full article
Format	both print and electronic
Are you the author of this Elsevier article?	Yes
Will you be translating?	No
Title of your thesis/dissertation	Integrated Plasmonics to Directing Cellular Connections and Biosensing Applications
Expected completion date	Aug 2015
Estimated size (number of pages)	23
Elsevier VAT number	GB 494 6272 12

**ELSEVIER LICENSE  
TERMS AND CONDITIONS**

Jul 06, 2015

---

This is a License Agreement between Mohammadali Tabatabaei ("You") and Elsevier ("Elsevier") provided by Copyright Clearance Center ("CCC"). The license consists of your order details, the terms and conditions provided by Elsevier, and the payment terms and conditions.

**All payments must be made in full to CCC. For payment instructions, please see information listed at the bottom of this form.**

Supplier	Elsevier Limited The Boulevard, Langford Lane Kidlington, Oxford, OX5 1GB, UK
Registered Company Number	1982084
Customer name	Mohammadali Tabatabaei
Customer address	1151 Richmond Street London, ON N6A5B7
License number	3663250958682
License date	Jul 06, 2015
Licensed content publisher	Elsevier
Licensed content publication	Biomaterials
Licensed content title	Directing GPCR-transfected cells and neuronal projections with nano-scale resolution
Licensed content author	Mohammadali Tabatabaei, Fabiana A. Caetano, Sylvain Vedraïne, Peter R. Norton, Stephen S.G. Ferguson, François Lagugné-Labarthet
Licensed content date	December 2013
Licensed content volume number	34
Licensed content issue number	38
Number of pages	10
Start Page	10065
End Page	10074
Type of Use	reuse in a thesis/dissertation
Portion	full article



Rightslink Printable License

2015-07-06, 4:47 PM

Format	both print and electronic
Are you the author of this Elsevier article?	Yes
Will you be translating?	No
Title of your thesis/dissertation	Integrated Plasmonics to Directing Cellular Connections and Biosensing Applications
Expected completion date	Aug 2015
Estimated size (number of pages)	23
Elsevier VAT number	GB 494 6272 12
Permissions price	0.00 CAD
VAT/Local Sales Tax	0.00 CAD / 0.00 GBP
Total	0.00 CAD
Terms and Conditions	

### INTRODUCTION

1. The publisher for this copyrighted material is Elsevier. By clicking "accept" in connection with completing this licensing transaction, you agree that the following terms and conditions apply to this transaction (along with the Billing and Payment terms and conditions established by Copyright Clearance Center, Inc. ("CCC"), at the time that you opened your Rightslink account and that are available at any time at <http://myaccount.copyright.com>).

### GENERAL TERMS

2. Elsevier hereby grants you permission to reproduce the aforementioned material subject to the terms and conditions indicated.

3. Acknowledgement: If any part of the material to be used (for example, figures) has appeared in our publication with credit or acknowledgement to another source, permission must also be sought from that source. If such permission is not obtained then that material may not be included in your publication/copies. Suitable acknowledgement to the source must be made, either as a footnote or in a reference list at the end of your publication, as follows:

"Reprinted from Publication title, Vol /edition number, Author(s), Title of article / title of chapter, Pages No., Copyright (Year), with permission from Elsevier [OR APPLICABLE SOCIETY COPYRIGHT OWNER]." Also Lancet special credit - "Reprinted from The Lancet, Vol. number, Author(s), Title of article, Pages No., Copyright (Year), with permission from Elsevier."

4. Reproduction of this material is confined to the purpose and/or media for which permission is hereby given.

<https://s100.copyright.com/App/PrintableLicenseFrame.jsp?publisherID=70&...f=e3b5c8ee-0a13-41e4-8605-eb1e5b4c75e3%20%20&targetPage=printablelicense> Page 2 of 8

5. Altering/Modifying Material: Not Permitted. However figures and illustrations may be altered/adapted minimally to serve your work. Any other abbreviations, additions, deletions and/or any other alterations shall be made only with prior written authorization of Elsevier Ltd. (Please contact Elsevier at [permissions@elsevier.com](mailto:permissions@elsevier.com))

6. If the permission fee for the requested use of our material is waived in this instance, please be advised that your future requests for Elsevier materials may attract a fee.

7. Reservation of Rights: Publisher reserves all rights not specifically granted in the combination of (i) the license details provided by you and accepted in the course of this licensing transaction, (ii) these terms and conditions and (iii) CCC's Billing and Payment terms and conditions.

8. License Contingent Upon Payment: While you may exercise the rights licensed immediately upon issuance of the license at the end of the licensing process for the transaction, provided that you have disclosed complete and accurate details of your proposed use, no license is finally effective unless and until full payment is received from you (either by publisher or by CCC) as provided in CCC's Billing and Payment terms and conditions. If full payment is not received on a timely basis, then any license preliminarily granted shall be deemed automatically revoked and shall be void as if never granted. Further, in the event that you breach any of these terms and conditions or any of CCC's Billing and Payment terms and conditions, the license is automatically revoked and shall be void as if never granted. Use of materials as described in a revoked license, as well as any use of the materials beyond the scope of an unrevoked license, may constitute copyright infringement and publisher reserves the right to take any and all action to protect its copyright in the materials.

9. Warranties: Publisher makes no representations or warranties with respect to the licensed material.

10. Indemnity: You hereby indemnify and agree to hold harmless publisher and CCC, and their respective officers, directors, employees and agents, from and against any and all claims arising out of your use of the licensed material other than as specifically authorized pursuant to this license.

11. No Transfer of License: This license is personal to you and may not be sublicensed, assigned, or transferred by you to any other person without publisher's written permission.

12. No Amendment Except in Writing: This license may not be amended except in a writing signed by both parties (or, in the case of publisher, by CCC on publisher's behalf).

13. Objection to Contrary Terms: Publisher hereby objects to any terms contained in any purchase order, acknowledgment, check endorsement or other writing prepared by you, which terms are inconsistent with these terms and conditions or CCC's Billing and Payment terms and conditions. These terms and conditions, together with CCC's Billing and Payment terms and conditions (which are incorporated herein), comprise the entire agreement between you and publisher (and CCC) concerning this licensing transaction. In the event of any conflict between your obligations established by these terms and conditions and those

established by CCC's Billing and Payment terms and conditions, these terms and conditions shall control.

14. **Revocation:** Elsevier or Copyright Clearance Center may deny the permissions described in this License at their sole discretion, for any reason or no reason, with a full refund payable to you. Notice of such denial will be made using the contact information provided by you. Failure to receive such notice will not alter or invalidate the denial. In no event will Elsevier or Copyright Clearance Center be responsible or liable for any costs, expenses or damage incurred by you as a result of a denial of your permission request, other than a refund of the amount(s) paid by you to Elsevier and/or Copyright Clearance Center for denied permissions.

#### LIMITED LICENSE

The following terms and conditions apply only to specific license types:

15. **Translation:** This permission is granted for non-exclusive world **English** rights only unless your license was granted for translation rights. If you licensed translation rights you may only translate this content into the languages you requested. A professional translator must perform all translations and reproduce the content word for word preserving the integrity of the article. If this license is to re-use 1 or 2 figures then permission is granted for non-exclusive world rights in all languages.

16. **Posting licensed content on any Website:** The following terms and conditions apply as follows: Licensing material from an Elsevier journal: All content posted to the web site must maintain the copyright information line on the bottom of each image; A hyper-text must be included to the Homepage of the journal from which you are licensing at <http://www.sciencedirect.com/science/journal/xxxxx> or the Elsevier homepage for books at <http://www.elsevier.com>; Central Storage: This license does not include permission for a scanned version of the material to be stored in a central repository such as that provided by Heron/XanEdu.

Licensing material from an Elsevier book: A hyper-text link must be included to the Elsevier homepage at <http://www.elsevier.com>. All content posted to the web site must maintain the copyright information line on the bottom of each image.

**Posting licensed content on Electronic reserve:** In addition to the above the following clauses are applicable: The web site must be password-protected and made available only to bona fide students registered on a relevant course. This permission is granted for 1 year only. You may obtain a new license for future website posting.

17. **For journal authors:** the following clauses are applicable in addition to the above:

#### Preprints:

A preprint is an author's own write-up of research results and analysis, it has not been peer-reviewed, nor has it had any other value added to it by a publisher (such as formatting,

copyright, technical enhancement etc.).

Authors can share their preprints anywhere at any time. Preprints should not be added to or enhanced in any way in order to appear more like, or to substitute for, the final versions of articles however authors can update their preprints on arXiv or RePEc with their Accepted Author Manuscript (see below).

If accepted for publication, we encourage authors to link from the preprint to their formal publication via its DOI. Millions of researchers have access to the formal publications on ScienceDirect, and so links will help users to find, access, cite and use the best available version. Please note that Cell Press, The Lancet and some society-owned have different preprint policies. Information on these policies is available on the journal homepage.

**Accepted Author Manuscripts:** An accepted author manuscript is the manuscript of an article that has been accepted for publication and which typically includes author-incorporated changes suggested during submission, peer review and editor-author communications.

Authors can share their accepted author manuscript:

- immediately
  - o via their non-commercial person homepage or blog
  - o by updating a preprint in arXiv or RePEc with the accepted manuscript
  - o via their research institute or institutional repository for internal institutional uses or as part of an invitation-only research collaboration work-group
  - o directly by providing copies to their students or to research collaborators for their personal use
  - o for private scholarly sharing as part of an invitation-only work group on commercial sites with which Elsevier has an agreement
- after the embargo period
  - o via non-commercial hosting platforms such as their institutional repository
  - o via commercial sites with which Elsevier has an agreement

In all cases accepted manuscripts should:

- link to the formal publication via its DOI
- bear a CC-BY-NC-ND license - this is easy to do
- if aggregated with other manuscripts, for example in a repository or other site, be

shared in alignment with our hosting policy not be added to or enhanced in any way to appear more like, or to substitute for, the published journal article.

**Published journal article (JPA):** A published journal article (PJA) is the definitive final record of published research that appears or will appear in the journal and embodies all value-adding publishing activities including peer review co-ordination, copy-editing, formatting, (if relevant) pagination and online enrichment.

Policies for sharing publishing journal articles differ for subscription and gold open access articles:

**Subscription Articles:** If you are an author, please share a link to your article rather than the full-text. Millions of researchers have access to the formal publications on ScienceDirect, and so links will help your users to find, access, cite, and use the best available version.

Theses and dissertations which contain embedded PJAs as part of the formal submission can be posted publicly by the awarding institution with DOI links back to the formal publications on ScienceDirect.

If you are affiliated with a library that subscribes to ScienceDirect you have additional private sharing rights for others' research accessed under that agreement. This includes use for classroom teaching and internal training at the institution (including use in course packs and courseware programs), and inclusion of the article for grant funding purposes.

**Gold Open Access Articles:** May be shared according to the author-selected end-user license and should contain a [CrossMark logo](#), the end user license, and a DOI link to the formal publication on ScienceDirect.

Please refer to Elsevier's [posting policy](#) for further information.

**18. For book authors** the following clauses are applicable in addition to the above: Authors are permitted to place a brief summary of their work online only. You are not allowed to download and post the published electronic version of your chapter, nor may you scan the printed edition to create an electronic version. **Posting to a repository:** Authors are permitted to post a summary of their chapter only in their institution's repository.

**19. Thesis/Dissertation:** If your license is for use in a thesis/dissertation your thesis may be submitted to your institution in either print or electronic form. Should your thesis be published commercially, please reapply for permission. These requirements include permission for the Library and Archives of Canada to supply single copies, on demand, of the complete thesis and include permission for Proquest/UMI to supply single copies, on demand, of the complete thesis. Should your thesis be published commercially, please reapply for permission. Theses and dissertations which contain embedded PJAs as part of the formal submission can be posted publicly by the awarding institution with DOI links back to the formal publications on ScienceDirect.

### **Elsevier Open Access Terms and Conditions**

You can publish open access with Elsevier in hundreds of open access journals or in nearly 2000 established subscription journals that support open access publishing. Permitted third party re-use of these open access articles is defined by the author's choice of Creative Commons user license. See our [open access license policy](#) for more information.

#### **Terms & Conditions applicable to all Open Access articles published with Elsevier:**

Any reuse of the article must not represent the author as endorsing the adaptation of the article nor should the article be modified in such a way as to damage the author's honour or reputation. If any changes have been made, such changes must be clearly indicated.

The author(s) must be appropriately credited and we ask that you include the end user license and a DOI link to the formal publication on ScienceDirect.

If any part of the material to be used (for example, figures) has appeared in our publication with credit or acknowledgement to another source it is the responsibility of the user to ensure their reuse complies with the terms and conditions determined by the rights holder.

#### **Additional Terms & Conditions applicable to each Creative Commons user license:**

**CC BY:** The CC-BY license allows users to copy, to create extracts, abstracts and new works from the Article, to alter and revise the Article and to make commercial use of the Article (including reuse and/or resale of the Article by commercial entities), provided the user gives appropriate credit (with a link to the formal publication through the relevant DOI), provides a link to the license, indicates if changes were made and the licensor is not represented as endorsing the use made of the work. The full details of the license are available at <http://creativecommons.org/licenses/by/4.0>.

**CC BY NC SA:** The CC BY-NC-SA license allows users to copy, to create extracts, abstracts and new works from the Article, to alter and revise the Article, provided this is not done for commercial purposes, and that the user gives appropriate credit (with a link to the formal publication through the relevant DOI), provides a link to the license, indicates if changes were made and the licensor is not represented as endorsing the use made of the work. Further, any new works must be made available on the same conditions. The full details of the license are available at <http://creativecommons.org/licenses/by-nc-sa/4.0>.

**CC BY NC ND:** The CC BY-NC-ND license allows users to copy and distribute the Article, provided this is not done for commercial purposes and further does not permit distribution of the Article if it is changed or edited in any way, and provided the user gives appropriate credit (with a link to the formal publication through the relevant DOI), provides a link to the license, and that the licensor is not represented as endorsing the use made of the work. The full details of the license are available at <http://creativecommons.org/licenses/by-nc-nd/4.0>. Any commercial reuse of Open Access articles published with a CC BY NC SA or CC BY NC ND license requires permission from Elsevier and will be subject to a fee.

Commercial reuse includes:

- Associating advertising with the full text of the Article
- Charging fees for document delivery or access
- Article aggregation
- Systematic distribution via e-mail lists or share buttons

Posting or linking by commercial companies for use by customers of those companies.

**20. Other Conditions:**

v 1.7

---

---

Page

Subject: **Re: Copyright Permission Request**  
To: Mohammadali Tabatabaei

Date: 07/08/15 13:05  
From: Joanne Paterson

---

good news! see below.  
cheers,  
Joanne

---

--  
Joanne Paterson, BMus BA MA MScILS  
Coordinator, Scholarship@Western  
Metadata Management Librarian  
Library Information Resources Management  
Western University, Western Libraries  
London, ON N6A 3K7

---

Dear Joanne,

Hereby I permit the corresponding PhD student to use an adapted version of Figure 2.9 in my thesis entitled as "*Tip-Enhances Raman Spectroscopy Enabling Spectroscopy at the Nanoscale*".

*Regards,*  
Nastaran Kazemi-Zanjani

On 08/07/2015 10:41 AM, Joanne Paterson wrote:

---

Dear Mohammadali,

I have contacted the two researchers for their permission and have so far received one confirmation as below

I will let you know when I hear from the other request :)



Page

Joanne Paterson, BMus BA MA MScILS  
Coordinator, Scholarship@Western  
Metadata Management Librarian  
Library Information Resources Management  
Western University, Western Libraries  
London, ON N6A 3K7

---

Hi Joanne,

No problem at all. The candidate has my permission to use those two figures.

Kind regards,

Betty Galarreta, Ph.D.  
Chemistry Department  
Pontificia Universidad Católica del Perú  
Av. Universitaria 1801, San Miguel  
Lima, Peru

On 06/07/2015 12:11 PM, Mohammadali Tabatabaei wrote:

---

Hello,

I am Mohammadali Tabatabaei, a Ph.D. candidate at department of chemistry. This email is to acquire the permission to use an adapted version of Figure 2.9 in the entitled thesis of "*Tip-Enhances Raman Spectroscopy Enabling Spectroscopy at the Nanoscale*" by N. Kazemi-Zanjani, and also the Figure 1.2 and Figure 2.2 of "*Rational Design and Advanced Fabrication of Metallic Nanostructures for Surface-Enhanced Raman Spectroscopy*" by B. C. Galarreta. The original/adapted mentioned figures are intended to be used in my Ph.D. thesis with this permission.

I appreciate if you could guide me in this regard.

Kind Regards,

Mohammadali

-

Mohammadali Tabatabaei  
Ph.D. Candidate  
Dr. Lasuené-Labarthe Research Group

Thank you Mohamadreza.

Mohammadali, the email below from Mohamadreza qualifies as his permission for you to adapt two of his images for use in your thesis.

Regards,  
Don

---

Donald Taylor  
University Copyright Officer  
Head, Interlibrary Loans & Research Repository Coordinator  
SFU Library, Burnaby BC

---

**From:** "Mohamadreza Najiminaini"  
**To:** "Donald Taylor"  
**Cc:** "Mohammadali Tabatabaei"  
**Sent:** Tuesday, 7 July, 2015 13:03:02  
**Subject:** Re: Request from Western University to use 2 figures from your 2012 PhD The

Hi Don,

It is fine if Mohammadali wants to use my thesis images.

Best Regards,

Mohamadreza

On Tue, Jul 7, 2015 at 11:35 AM, Donald Taylor wrote:  
> Dear Mohamadreza,  
> A PhD candidate at Western University in London Ontario would like to use  
> some figures from your PhD thesis in his thesis. His contact information and  
> request is below. Could you please contact him and let him know if he may  
> reproduce two adapted versions of your figures in his thesis?  
>  
> The student's name is Mohammadali Tabatabaei and his email is

Page

> -----  
> Donald Taylor  
> University Copyright Officer  
> Head, Interlibrary Loans & Research Repository Coordinator  
> SFU Library, Burnaby BC  
>  
>  
> \_\_\_\_\_  
>  
>  
> Sent: Monday, 6 July, 2015 09:30:42  
> Subject: [Rights and permissions questions for materials in Summit]  
> Copyright Permission Request  
>  
> Mohammadali sent a message using the contact form at  
> <http://summit.sfu.ca/contact>.  
>  
> Hello,  
>  
> I am Mohammadali Tabatabaei, a Ph.D. candidate at department of chemistry of  
> Western university in London, ON, Canada. This email is to acquire the  
> permission to use the adapted versions of Figures 1.4 and 1.5 from the  
> thesis  
> mentioned below. These are intended to be used for my Ph.D. thesis.  
>  
> "Development of 3D metallic nano-structures for sensing applications" by  
> Najiminaini, Mohamadreza;  
>  
> Identifier:etd7291  
>  
> I appreciate if you could guide me in this regard.  
>  
> Kind Regards,  
>  
> Mohammadali Tabatabaei  
>

--  
Mohamadreza Najiminaini, Ph.D.  
Postdoctoral Fellow  
Department of Medical Biophysics  
Western University

## Curriculum Vitae

**Name:** Mohammadali Tabatabaei

**Post-secondary Education and Degrees:** Shahid Beheshti University (National University of Iran)  
Tehran, Iran  
2006-2010 B.Sc.

The University of Western Ontario  
London, Ontario, Canada  
2011-2015 Ph.D.

### Honours and Awards:

1. 98<sup>th</sup> Canadian Chemistry Conference Travel Award, August 2015
2. Highlighted Research in [Faculty of Science News](#) at Western University, London, ON, Canada, February 2015.
3. Second Prize in Poster Competition, [5<sup>th</sup> Nano Ontario Conference](#). University of Windsor, Windsor, ON, Canada, November 2014.
4. Second Prize in Poster Competition, [24<sup>th</sup> Canadian Materials Science Conference \(CMSC\)](#), Western University, London, ON, Canada, June 2012.
5. *Western Graduate Research Scholarship*, Western University 2011-Present.
6. Annual *International Student Scholarship* Western University 2011-Present.

**Related Work Experience** Teaching and Research Assistant  
The University of Western Ontario  
2011-2015

### Publications:

1. Wallace, G. Q.; Tabatabaei, M.; Zuin, M. S.; Workentin, M. S.; Lagagné-Labarthet, F. (2015), submitted.
2. Tabatabaei, M.; Wallace, G. Q.; Caetano, F. A.; Gillies, E. R.; Ferguson, S. S. G.; Lagagné-Labarthet, F. (2015), submitted.

3. Wallace, G. Q.; Zuin, M. S.; Tabatabaei, M.; Gobbo, P.; Lagugné-Labarthe, F.; Workentin, M. S. *Analyst* (2015), Accepted Manuscript; DOI: 10.1039/C5AN01127B.
4. Tabatabaei, M.; Najiminaini, M.; Davieau, K.; Kaminska, B.; Singh, M.; Carson, J. J.L.; Lagugné-Labarthe, F. *ACS Photonics* (2015), 2, 752.
5. Wallace, G. Q.; Pashae, F.; Hou, R.; Tabatabaei, M.; Lagugné-Labarthe, F. *Proc. SPIE*, (2014), 9126, Nanophotonics V, 912610, doi:10.1117/12.2054391
6. Wallace, G. Q.; Tabatabaei, M.; Lagugné-Labarthe, F. *Can. J. Chem.*, (2014), 92, 1.
7. Tabatabaei, M.; Caetano, F. A.; Vedraïne, S.; Norton, P.; Ferguson, S. S. G.; Lagugné-Labarthe, F. *Biomaterials*, (2013), 34, 10065.
8. Tabatabaei, M.; Sangar, A.; Kazemi-Zanjani, N.; Torchio, P.; Merlen, A.; Lagugné-Labarthe, F. *J. Phys. Chem. C*, (2013), 117, 14778.
9. Galarreta, B.C.; Tabatabaei, M.; Guieu, V.; Peyrin, E.; Lagugné-Labarthe, F. *Anal. Bioanal. Chem.* (2013), 405, 1613. [Front Cover]
10. Fayyaz, S.\*; Tabatabaei, M.\*; Hou, R.; Lagugné-Labarthe, F. *J. Phys. Chem. C* (2012), 116, 11665. [\*Contributed equally to this work]
11. Davarani, S. S. H.; Najarian, A. M.; Nojavan, S.; Tabatabaei, M. *Analytica. Chimica. Acta.* (2012), 725, 51.
12. Davarani, S. S. H.; Shejjooni-Foomani, N.; Najarian, A. M.; Tabatabaei, M.; Vahidi, S. *Am. J. Anal. Chem.* (2011), 2, 626.
13. Davarani, S. S. H.; Shejjooni-Foomani, N.; Vahidi, S.; Tabatabaei, M.; Arvin-Nezhad, H. *J. Heterocyclic. Chem.* (2010), 47, 40.